Abstract

DEL ROSARIO, RICARDO CRUZ-HERRERA. Computational Methods for Feedback Control in Structural Systems. (Under the direction of Prof. H.T. Banks)

Numerical methods, LQR control, an abstract formulation and reduced basis techniques for a system consisting of a thin cylindrical shell with surface-mounted piezoceramic actuators are investigated. Donnell-Mushtari equations, modified to include Kelvin-Voigt damping and passive patch contributions, are used to model the system dynamics. The voltage-induced piezoceramic patch contributions, used as input in the control regime, enter the equations as external forces and moments. Existence and uniqueness of solutions are demonstrated through variational and semigroup formulations of the system equations. The semigroup formulation is also used to establish theoretical control results and illustrate convergence of the finite dimensional controls and Riccati operators. The spatial components of the state are discretized using a Galerkin expansion resulting in an ordinary differential equation that can be readily marched in time by existing ordinary differential equation solvers. Full order approximation methods which employ standard basis elements such as cubic or linear splines result in large matrix dimensions rendering the system computationally expensive for real-time simulations. To lessen on-line computational requirements, reduced basis methods employing snapshots of the full order model as basis functions are investigated. As a first step in validating the model, a shell with obtainable analytic natural frequencies and modes was considered. The derived frequencies and modes were then compared with numerical approximations using full order basis functions. Further testing on the static and dynamic performance of the full order model was carried out through the following steps: (i) choose true state solutions, (ii) solve for the forces in the equations that would lead to these known solutions, and (iii) compare numerical results excited by the derived forces with the true solutions. Reduced order methods employing the Lagrange and the Karhunen-Loève proper orthogonal

decomposition (POD) basis functions are implemented on the model. Finally, a state feedback method was developed and investigated computationally for both the full order and reduced order models.

COMPUTATIONAL METHODS FOR FEEDBACK CONTROL IN STRUCTURAL SYSTEMS

BY

RICARDO C.H. DEL ROSARIO

A DISSERTATION SUBMITTED TO THE GRADUATE FACULTY OF
NORTH CAROLINA STATE UNIVERSITY
IN PARTIAL FULFILLMENT OF THE
REQUIREMENTS FOR THE DEGREE OF
DOCTOR OF PHILOSOPHY

DEPARTMENT OF MATHEMATICS

RALEIGH

August 26, 1998

APPROVED BY:

— dedicated to my parents Cecinio and Lourdes —

Biography

Ricardo Cruz-Herrera del Rosario was born in Olongapo City, Philippines on January 26, 1970, where he spent the first 12 years of his life. In June 1982, he moved to Manila to study at Philippine Science High School in Diliman, Quezon City. He later attended the University of the Philippines in Diliman from June 1986 to October 1989 where he graduated Cum Laude with a Bachelor of Science in Mathematics. For the next two years he worked as an instructor in the Department of Mathematics at the University of the Philippines while taking graduate courses in actuarial and computer science. Tokyo Denshi Sekkei Philippines, Inc. then hired him as a software engineer from November 1991 to July 1993. In August 1993, he moved to the United States to continue his graduate studies. He obtained his M.S. degree in Mathematics from Iowa State University in May 1995 and afterwards spent two months as a summer intern at NASA Langley Research Center. He started his doctoral studies in Applied Mathematics at North Carolina State University in August 1995.

Acknowledgements

A lot of people made it possible for me to finish this dissertation. For guidance and support through my graduate studies at NC State, I thank my advisor Prof. H. T. Banks. For continued advice and friendship since I was a masters student at Iowa State University, I am grateful to Prof. Ralph Smith. I also express sincere appreciation to Professors Hien Tran and Kazufumi Ito for valuable input on various aspects of my research.

I gratefully acknowledge the Air Force Office of Scientific Research for financial support under grants AFSOR F49620-95-1-0236 and AFSOR F49620-98-1-0180. Additional support was also provided in part by the National Aeronautics and Space Administration under NASA Contract Number NAS1-19480 and NASA grant NAG-1-1600.

I extend deepest gratitude to all my friends who encouraged and helped me throughout the process. Special thanks to Melissa Choi, Laura Potter, Cindy Musante, Mike Jeffris, Yue Zhang, Rebecca Segal, John Peach, Rory Schnell, Hung Ly, Gerald Guanga, Karyna Ventura, Jennifer Pizarro and Myrene Santos.

I am indebted to Jose and Tessie Chua, Lorrie and Wyda Chua, Francis and Sony Jao, and Ricky and Arlete Chua for making me a part of their family.

Finally, I would like to thank my parents Cecinio and Lourdes, my brother Dante and his wife Peeya, and my sisters Belinda, Laura and Melissa for their unconditional love and support.

Table of Contents

List of Tables

List of Figures

List of Symbols

u	longitudinal displacement
v	circumferential displacement
w	transverse displacement
R	shell radius
E	shell Young's Modulus
ℓ	shell length
ρ	shell density
h	shell thickness
c_D	shell Kelvin-Voigt damping
ν	shell Poisson ratio
d_{31}	patch proportionality constant
$1i$, pe_{1i}	subscripts to identify i^{th} outer patch
$2i$, pe_{2i}	subscripts to identify i^{th} inner patch
$\hat{q}_x$	surface force in longitudinal direction
$\hat{q}_\theta$	surface force in circumferential direction
$\hat{q}_n$	surface force in transverse direction
V, $\mathcal{V}$	test function spaces; $\mathcal{V} = V \times V$
H, $\mathcal{H}$	state spaces; $\mathcal{H} = H \times V$
$\mathcal{U}$	control space ($\mathbb{R}^{2s}$)
$\mathcal{Y}$	observation space
N_u, N_v, N_w	no. of standard splines in u, v, w directions

N	indicates the same no. of standard splines $N = N_u = N_v = N_w$
M_u, M_v, M_w	no. of Fourier limits in circumferential direction
M	indicates the same no. of Fourier limits $M = M_u = M_v = M_w$
$\mathcal{N}_u$,$\mathcal{N}_v$,$\mathcal{N}_w$	no. of basis functions in u, v, w directions
$\mathcal{N}$	dimension of subspace $V^{\mathcal{N}} \subset V$ $(\mathcal{N} = \mathcal{N}_u + \mathcal{N}_v + \mathcal{N}_w)$
$2\mathcal{N}$	dimension of subspace $\mathcal{V}^{2\mathcal{N}} = V^{\mathcal{N}} \times V^{\mathcal{N}} \subset \mathcal{V}$
$\mathcal{A}, \mathcal{A}^{2\mathcal{N}}$	infinite and finite dimensional system operators
$\mathcal{B}, \mathcal{B}^{2\mathcal{N}}$	infinite and finite dimensional control operators
$\mathcal{C}, \mathcal{C}^{2\mathcal{N}}$	infinite and finite dimensional observation operators
$A^{2\mathcal{N}}$	matrix representation of $\mathcal{A}^{2\mathcal{N}}$
$B^{2\mathcal{N}}$	matrix representation of $\mathcal{B}^{2\mathcal{N}}$

Chapter 1

Introduction

Advances in smart material technologies have produced a number of lightweight materials whose sensing and actuating capabilities are promising in control applications (for a general discussion on current smart materials used in smart material structures, see [14]). Control methodologies have kept pace by considering the physical properties of the structure/sensor system thereby establishing control authority with less hardware and control input. Recent demands in smart material control applications include faster methods to compute feedback control gains. We aim to address this by presenting a numerical approximation method which (i) captures the essential dynamics of the system to be controlled, (ii) is easily adaptable to different boundary conditions, (iii) allows material changes when smart materials are incorporated into the system, and (iv) concentrates most numerical computations off-line for faster control gain calculations. We focus on a system consisting of a thin cylindrical shell bonded with piezoceramic patches as actuators but the numerical methods and control methodologies we present are readily implementable for other structures such as plates or beams, employing different types of smart actuators such as electrostrictives or magnetostrictives.

Piezoceramic patches, as actuators, produce strains in response to applied voltages; as sensors, material deformations of the structure to which they are bonded or in which they are embedded generate voltages. These smart materials are preferred for

control applications in thin shell dynamics since they are lightweight, cost effective, easily manufactured in different sizes and shapes, produce significant strains, and the voltage-strain relations are nearly linear for small electric fields. It must be noted that at higher fields, nonlinear responses occur which can degrade the control design if the nonlinearities are not part of the design. For current applications, the voltage limits are within the linear range of the piezoceramic patch. High temperatures can change the constant relation between generated strain and patch input. Hence for systems subjected to above normal temperatures, parameter identification must be performed (see [14]) once the constant has changed.

Active control of shell vibrations has been a growing research area for a number of years due to its vast number of applications such as noise and fatigue reduction in aircraft cabins, vibration suppression for the cylindrical support coils in magnetic resonance image equipments, and flow control in flexible pipes. Mathematical models of thin shells, accepted as the primary tool in this field, abound in literature. The existing models differ on assumptions made to express the strain-displacement equations of linear elasticity. In [34, 38], a summary and comparison of the theories of Donnell-Mushtari, Love-Timoshenko, Byrne-Flügge-Goldenveizer-Lur'ye-Novozhilov, Reissner-Naghdi-Berry and Vlasov and Sanders are given. The model of Koiter is one of the latest improvements to the Love-Kirchhoff family of thin shell models (see [17]). We chose to express shell dynamics through the Donnell-Mushtari equations because this framework, aside from providing ease in exposition while capturing the essential dynamics of relatively short shells (i.e., the ratio of the length ℓ over the radius R is less than $1/4$), has the advantage of being easily extended to more accurate models (Naghdi or Sanders) or longer shells (Flügge).

A variety of numerical methods to approximate shell structures are currently available. Finite-difference methods (see [49, 50]), one of the earliest to be used in computation, are not generally accurate and result in large matrices. Furthermore, boundary conditions are difficult to implement. Finite element methods, on the other hand, are

easily adaptable to different boundary conditions and a number of books and software packages have been written for thin shell approximation (see [4, 17, 27, 26, 28, 53]). Discontinuities in shell constants and parameters which arise when piezoceramic patches are bonded to the shell pose difficulties in the creation of the elements. In such cases, the elements must be aligned with the boundaries of the patches. Another difficulty with finite element methods is the *locking* phenomena which can be exhibited when elements are not able to handle the Kirchhoff-Love constraint of vanishing transverse shear strains as the shell thickness h tends to zero ([3, 15]). Another more serious type of locking arises when the approximation method is not capable of handling purely bending deformation energies (see [5, 6, 33, 45]). In this case, mesh sizes must be decreased significantly smaller than the shell thickness to accommodate higher order finite elements in bending dominated simulations. Modal approximation methods are useful only in applications where analytic expressions for the modes can be obtained. For most applications, however, mode shapes must be first approximated or experimentally determined before being used in the modal expansions.

We present a Galerkin type approximation method employing spline bases in the axial direction and Fourier polynomials in the circumferential (θ) direction. Although we show in Chapter 5 that several of the issues in numerical approximation are successfully resolved with this method, a need still exists for faster calculations. Hence we investigate the Lagrange and Karhunen-Loève proper orthogonal decomposition (POD) reduced basis methods in an attempt to decrease the size of the finite dimensional system. The first attempts at reduced basis methods in structures appear to have been by Almroth [2] and Nagy [39]. Preliminary applications in structures can also be found in [40, 41, 42], while implementation in incompressible viscous flows were pioneered by Peterson [44]. In open loop control of fluids, we believe that the Lagrange reduced basis method was first employed in [30, 31] and POD was first used in [37]. To our knowledge, this thesis (and [7]) represent the first time Lagrange or POD reduced basis functions are employed in *feedback control* of structures.

Lagrange reduced basis methods use parameter dependent "solutions" as basis

functions, where the "solutions" could come either from numerical simulations or experimental data. The idea is based on the hope that solutions at other parameter values could be approximated in terms of the few chosen representative parameters. Proper orthogonal reduced basis methods initially use the same parameter dependent "solutions" but an optimal way of capturing the features in the "solutions" is obtained through an orthogonalization procedure. Out of the initial set of parameter dependent solutions, a smaller set of orthogonal solutions containing most of the information in the first set, are used as basis functions.

In Chapter 2, we present the governing equations of the thin shell model as developed elsewhere. Existence and uniqueness of solutions to these equations, optimal control, and convergence of finite dimensional approximations are addressed in Chapter 3. General finite dimensional approximation methods, together with the ideas behind Lagrange and POD reduced basis functions are discussed in Chapter 4. Our extensive numerical results are presented in Chapter 5, and conclusions are summarized in Chapter 6.

Chapter 2

Shell Equations

The system we consider in this dissertation is a thin cylindrical shell with surface-mounted piezoceramic patches as actuators. In accordance with thin shell theory, the shell is assumed to satisfy four basic assumptions, known as Love's postulates, namely (i) the thickness h of the shell is small compared to the radius R, i.e., $h/R \ll 1$; (ii) shell deflections are assumed to be small; (iii) the stress in the direction normal to the thin dimensions is assumed negligible, and (iv) a line originally normal to the shell reference surface will remain normal to the deformed reference surface, and unstrained (see [14, 34, 35]). Shell dynamics are modeled using the Donnell-Mushtari equations and hence it is assumed that the ratio of the length ℓ of the shell to its radius is less than 4. Furthermore, it is assumed that the shell thickness is uniform. Bonded to the inner and outer surfaces of the shell are s pairs of piezoceramic patches which will be used as actuators in this work. The actuating capabilities of the patches derive from material deformations which occur in response to applied voltages. The patches also produce voltages in response to mechanical strains but the sensing capacity is not exploited here. Piezoceramic patches can be molded in a variety of shapes and so, as in many applications, we assume that the patches are molded to have the same curvature as the shell. This does not cause pre-stressing on the structure but significantly alters the material properties as well as the thickness of the structure in regions covered by the patches. These passive patch contributions enter the equations by changing the

internal moments and forces of the shell. Contributions to the structural dynamics due to the glue bonding layer are ignored. It is demonstrated in [14] that these contributions can be combined with passive patch contributions, and the resulting coefficients can be obtained using parameter estimation techniques.

According to assumption (ii) above, shell deflections are small hence all displacements are measured from the original, undeformed state of the shell. The fourth assumption (iv) assumes that displacements in the thickness direction are linear hence every point on the shell surface can be described by the corresponding point on the reference surface. We choose the unperturbed middle surface of the shell to be the reference surface. All forces and moments are thus given in terms of middle surface resultants.

As illustrated in Figure 2.1, we orient the shell such that its longitudinal axis is aligned with the x-axis. The displacements of the middle surface in the longitudinal, circumferential and transverse directions are denoted by u, v and w, respectively. The region occupied by the middle surface is denoted by Γ_0 where $\Gamma_0 = \{(x, \theta) : 0 \leq x \leq \ell, 0 \leq \theta \leq 2\pi\}$; the density, Young's modulus, Poisson ratio and Kelvin-Voigt damping coefficient of the shell are denoted by ρ_s, E, ν and c_D, respectively. Also indicated in Figure 2.1 is the location of the i^{th} outer patch with center located at $(\bar{x}_{1i}, \bar{\theta}_{1i})$ and edge coordinates $x_{1_{1i}}, x_{2_{1i}}, \theta_{1_{1i}}, \theta_{1_{1i}}$. The center of the i^{th} inner patch will be denoted similarly by $(\bar{x}_{2i}, \bar{\theta}_{2i})$ with edge coordinates $x_{1_{2i}}, x_{2_{2i}}, \theta_{1_{2i}}, \theta_{1_{2i}}$. For the rest of this paper, the subscripts $1i$ and $2i$ will be used to identify the i^{th} outer and inner patches, respectively. It is assumed that for the i^{th} patch pair, the outer patch has thickness $h_{pe_{1i}}$, density $\rho_{pe_{1i}}$, Young's modulus $E_{pe_{1i}}$, Poisson ratio $\nu_{pe_{1i}}$, Kelvin-Voigt damping coefficient $c_{Dpe_{1i}}$ and proportionality constant $d_{31_{1i}}$. Similarly, the inner patch properties will be denoted by $h_{pe_{2i}}$, $\rho_{pe_{2i}}$, $E_{pe_{2i}}$, $\nu_{pe_{2i}}$, $c_{Dpe_{2i}}$ and d_{31}. The proportionality constant $d_{31_{1i}}$ (see [14, 29]) relates the strain generated by the patch in response to the voltage input. The model we present allows differing patch characteristics (for the $2s$ patches) to give flexibility in

the design of the smart material system, and to account for inconsistencies in current manufacturing methods for piezoceramic patches. Furthermore, the model and control formulation permit different voltage inputs to the $2s$ patches.

Shell equations are derived in [14, 34] by considering strain-displacement relations, stress-strain relations, internal force and moment resultants, and equations of motion. By neglecting higher order terms, one obtains the modified Donnell-Mushtari equations

$$\begin{aligned}
&R\rho h\frac{\partial^2 u}{\partial t^2} - R\frac{\partial N_x}{\partial x} - \frac{\partial N_{\theta x}}{\partial \theta} = R\hat{q}_x \\
&\quad -R\sum_{i=1}^{s}\left[\frac{\partial (N_x)_{pe_{1i}}}{\partial x}\mathcal{S}_{pe_{1i}}(x,\theta) + \frac{\partial (N_x)_{pe_{2i}}}{\partial x}\mathcal{S}_{pe_{2i}}(x,\theta)\right] \\
&R\rho h\frac{\partial^2 v}{\partial t^2} - \frac{\partial N_\theta}{\partial \theta} - R\frac{N_{x\theta}}{\partial x} = R\hat{q}_\theta \\
&\quad -\sum_{i=1}^{s}\left[\frac{\partial (N_\theta)_{pe_{1i}}}{\partial \theta}\mathcal{S}_{pe_{1i}}(x,\theta) + \frac{\partial (N_\theta)_{pe_{2i}}}{\partial \theta}\mathcal{S}_{pe_{2i}}(x,\theta)\right] \\
&R\rho h\frac{\partial^2 w}{\partial t^2} - R\frac{\partial^2 M_x}{\partial x^2} - \frac{1}{R}\frac{\partial^2 M_\theta}{\partial \theta^2} - 2\frac{\partial^2 M_{x\theta}}{\partial x \partial \theta} + N_\theta = R\hat{q}_n \\
&\quad -\sum_{i=1}^{s}\left[R\frac{\partial^2}{\partial x^2}\Big((M_x)_{pe_{1i}} + (M_x)_{pe_{2i}}\Big) + \frac{1}{R}\frac{\partial^2}{\partial \theta^2}\Big((M_\theta)_{pe_{1i}} + (M_\theta)_{pe_{2i}}\Big)\right].
\end{aligned} \tag{2.1}$$

External resultant forces in the longitudinal, circumferential and transverse directions are modeled by the functions $\hat{q}_x, \hat{q}_\theta$ and $\hat{q}_n$, respectively (see [14]).

The composite density ρ consists of the shell density ρ_s in regions devoid of patches and a linear combination of ρ_s and the patch densities $\rho_{pe_{1i}}, \rho_{pe_{2i}}$ in regions covered by the patches. Hence ρ is piecewise constant with discontinuities at the patch edges.

As detailed in [14], the internal force and moment middle surface resultants

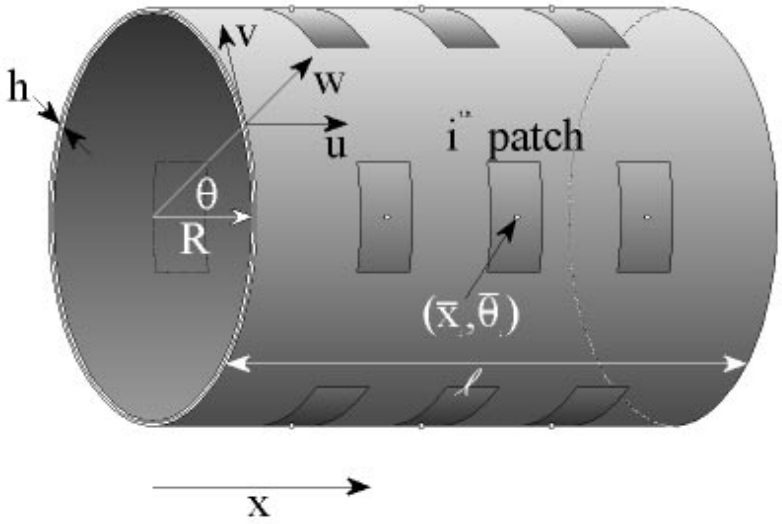

Figure 2.1: Thin cylindrical shell with piezoceramic patch configuration.

$N_x, N_\theta, N_{x\theta}, N_{\theta x}, M_x, M_\theta, M_{x\theta}$ incorporating Kelvin-Voigt damping but *without* passive patch contributions have the form

$$
\begin{aligned}
N_x &= \frac{Eh}{(1-\nu^2)}\left[\frac{\partial u}{\partial x}+\nu\left(\frac{1}{R}\frac{\partial v}{\partial \theta}+\frac{w}{R}\right)\right]+\frac{c_D h}{(1-\nu^2)}\frac{\partial}{\partial t}\left[\frac{\partial u}{\partial x}+\nu\left(\frac{1}{R}\frac{\partial v}{\partial \theta}+\frac{w}{R}\right)\right]\\
N_\theta &= \frac{Eh}{(1-\nu^2)}\left[\frac{1}{R}\frac{\partial v}{\partial \theta}+\frac{w}{R}+\nu\frac{\partial u}{\partial x}\right]+\frac{c_D h}{(1-\nu^2)}\frac{\partial}{\partial t}\left[\frac{1}{R}\frac{\partial v}{\partial \theta}+\frac{w}{R}+\nu\frac{\partial u}{\partial x}\right]\\
N_{x\theta} = N_{\theta x} &= \frac{Eh}{2(1+\nu)}\left[\frac{\partial v}{\partial x}+\frac{1}{R}\frac{\partial u}{\partial \theta}\right]+\frac{c_D h}{2(1+\nu)}\frac{\partial}{\partial t}\left[\frac{\partial v}{\partial x}+\frac{1}{R}\frac{\partial u}{\partial \theta}\right]\\
M_x &= -\frac{Eh^3}{12(1-\nu^2)}\left[\frac{\partial^2 w}{\partial x^2}+\frac{\nu}{R^2}\frac{\partial^2 w}{\partial \theta^2}\right]-\frac{c_D h^3}{12(1-\nu^2)}\frac{\partial}{\partial t}\left[\frac{\partial^2 w}{\partial x^2}+\frac{\nu}{R^2}\frac{\partial^2 w}{\partial \theta^2}\right]\\
M_\theta &= -\frac{Eh^3}{12(1-\nu^2)}\left[\frac{1}{R^2}\frac{\partial^2 w}{\partial \theta^2}+\nu\frac{\partial^2 w}{\partial x^2}\right]-\frac{c_D h^3}{12(1-\nu^2)}\frac{\partial}{\partial t}\left[\frac{1}{R^2}\frac{\partial^2 w}{\partial \theta^2}+\nu\frac{\partial^2 w}{\partial x^2}\right]\\
M_{x\theta} = M_{\theta x} &= -\frac{Eh^3}{12R(1+\nu)}\frac{\partial^2 w}{\partial x\partial \theta}-\frac{c_D h^3}{12R(1+\nu)}\frac{\partial}{\partial t}\left[\frac{\partial^2 w}{\partial x\partial \theta}\right].
\end{aligned}
\tag{2.2}
$$

We point out that these resultants yield the classical Donnell-Mushtari equations if the damping terms are dropped, i.e., set $c_D = 0$ (see [34]). Incorporation of passive patch contributions in the model leads to the addition of more terms in the resultant expressions. In this case, the internal force N_x is now given by

$$\begin{aligned}
N_x &= \frac{Eh}{(1-\nu^2)}\left[\frac{\partial u}{\partial x} + \nu\left(\frac{1}{R}\frac{\partial v}{\partial \theta} + \frac{w}{R}\right)\right] \\
&+ \sum_{i=1}^{s} \frac{E_{pe_{1i}}}{(1-\nu_{pe_{1i}}^2)}\left[h_{pe_{1i}}\left(\frac{\partial u}{\partial x} + \nu_{pe_{1i}}\left(\frac{1}{R}\frac{\partial v}{\partial \theta} + \frac{w}{R}\right)\right)\right. \\
&\qquad \left. -\frac{a_{2_{1i}}}{2}\left(\frac{\partial^2 w}{\partial x^2} + \frac{\nu_{pe_{1i}}}{R^2}\frac{\partial^2 w}{\partial \theta^2}\right)\right]\chi_{pe_{1i}}(x,\theta) \\
&+ \sum_{i=1}^{s} \frac{E_{pe_{2i}}}{(1-\nu_{pe_{2i}}^2)}\left[h_{pe_{2i}}\left(\frac{\partial u}{\partial x} + \nu_{pe_{2i}}\left(\frac{1}{R}\frac{\partial v}{\partial \theta} + \frac{w}{R}\right)\right)\right. \\
&\qquad \left. +\frac{a_{2_{2i}}}{2}\left(\frac{\partial^2 w}{\partial x^2} + \frac{\nu_{pe_{2i}}}{R^2}\frac{\partial^2 w}{\partial \theta^2}\right)\right]\chi_{pe_{2i}}(x,\theta) \\
&+ \frac{c_D h}{(1-\nu^2)}\frac{\partial}{\partial t}\left[\frac{\partial u}{\partial x} + \nu\left(\frac{1}{R}\frac{\partial v}{\partial \theta} + \frac{w}{R}\right)\right] \\
&+ \sum_{i=1}^{s} \frac{c_{D_{pe_{1i}}}}{(1-\nu_{pe_{1i}}^2)}\frac{\partial}{\partial t}\left[h_{pe_{1i}}\left(\frac{\partial u}{\partial x} + \nu_{pe_{1i}}\left(\frac{1}{R}\frac{\partial v}{\partial \theta} + \frac{w}{R}\right)\right)\right. \\
&\qquad \left. -\frac{a_{2_{1i}}}{2}\left(\frac{\partial^2 w}{\partial x^2} + \frac{\nu_{pe_{1i}}}{R^2}\frac{\partial^2 w}{\partial \theta^2}\right)\right]\chi_{pe_{1i}}(x,\theta) \\
&+ \sum_{i=1}^{s} \frac{c_{D_{pe_{2i}}}}{(1-\nu_{pe_{2i}}^2)}\frac{\partial}{\partial t}\left[h_{pe_{2i}}\left(\frac{\partial u}{\partial x} + \nu_{pe_{2i}}\left(\frac{1}{R}\frac{\partial v}{\partial \theta} + \frac{w}{R}\right)\right)\right. \\
&\qquad \left. +\frac{a_{2_{2i}}}{2}\left(\frac{\partial^2 w}{\partial x^2} + \frac{\nu_{pe_{2i}}}{R^2}\frac{\partial^2 w}{\partial \theta^2}\right)\right]\chi_{pe_{2i}}(x,\theta)\ .
\end{aligned} \tag{2.3}$$

Expressions for $N_\theta, N_{x\theta}, N_{\theta x}, M_x, M_\theta$ and $M_{x\theta}$ with passive patch contributions are given in Appendix A and details of the derivation are found in [14]. Note that

in the expressions above, the presence of the characteristic function $\chi_{pe_{1i}}(x,\theta)$ with value 1 in the region covered by the i^{th} outer patch and zero elsewhere indicates the patch contributions to regions of the shell covered by the patch, with $\chi_{pe_{2i}}(x,\theta)$ defined analogously. Furthermore, the constants $a_{2_{1i}} = (h/2 + h_{pe_{1i}})^2 - h^2/4$, $a_{2_{2i}} = (h/2 + h_{pe_{2i}})^2 - h^2/4$, $a_{3_{1i}} = (h/2 + h_{pe_{1i}})^3 - h^3/8$ and $a_{3_{2i}} = (h/2 + h_{pe_{2i}})^3 - h^3/8$ arise from integrating across the thickness of the patch.

Denoting the outer and inner input voltages by $V_{1i}(t)$ and $V_{2i}(t)$, respectively, the external line force and moment resultants due to the i^{th} patch pair, as derived in [14], are given by

$$
\begin{aligned}
(M_x)_{pe_{1i}} &= \frac{-E_{pe_{1i}} d_{31_{1i}}}{(1-\nu_{pe_{1i}})h_{pe_{1i}}}\left[\frac{1}{2}a_{2_{1i}} + \frac{1}{3R}a_{3_{1i}}\right]\chi_{pe_{1i}}(x,\theta)V_{1i} \\
(M_x)_{pe_{2i}} &= \frac{E_{pe_{2i}} d_{31_{2i}}}{(1-\nu_{pe_{2i}})h_{pe_{2i}}}\left[\frac{1}{2}a_{2_{2i}} - \frac{1}{3R}a_{3_{2i}}\right]\chi_{pe_{2i}}(x,\theta)V_{2i} \\
(M_\theta)_{pe_{1i}} &= \frac{-E_{pe_{1i}} d_{31_{1i}} a_{2_{1i}}}{2(1-\nu_{pe_{1i}})h_{pe_{1i}}}\chi_{pe_{1i}}(x,\theta)V_{1i} \\
(M_\theta)_{pe_{2i}} &= \frac{E_{pe_{2i}} d_{31_{2i}} a_{2_{2i}}}{2(1-\nu_{pe_{2i}})h_{pe_{2i}}}\chi_{pe_{2i}}(x,\theta)V_{2i} \\
(N_x)_{pe_{1i}} &= \frac{-E_{pe_{1i}} d_{31_{1i}}}{(1-\nu_{pe_{1i}})h_{pe_{1i}}}\left[h_{pe_{1i}} + \frac{1}{2}a_{2_{1i}}\right]\chi_{pe_{1i}}(x,\theta)\mathcal{S}_{pe_{1i}}(x,\theta)V_{1i} \\
(N_x)_{pe_{2i}} &= \frac{-E_{pe_{2i}} d_{31_{2i}}}{(1-\nu_{pe_{2i}})h_{pe_{2i}}}\left[h_{pe_{2i}} - \frac{1}{2}a_{2_{2i}}\right]\chi_{pe_{2i}}(x,\theta)\mathcal{S}_{pe_{2i}}(x,\theta)V_{2i} \\
(N_\theta)_{pe_{1i}} &= \frac{-E_{pe_{1i}} d_{31_{1i}}}{1-\nu_{pe_{1i}}}\chi_{pe_{1i}}(x,\theta)\mathcal{S}_{pe_{1i}}(x,\theta)V_{1i} \\
(N_\theta)_{pe_{2i}} &= \frac{-E_{pe_{2i}} d_{31_{2i}}}{1-\nu_{pe_{2i}}}\chi_{pe_{2i}}(x,\theta)\mathcal{S}_{pe_{2i}}(x,\theta)V_{2i}
\end{aligned}
\tag{2.4}
$$

The patch-induced external resultants $(N_x)_{pe_{1i}}$ and $(N_\theta)_{pe_{1i}}$ produce forces which are opposite in direction at points symmetric to the center $(\bar{x}_{1i}, \bar{\theta}_{1i})$ of the i^{th} outer patch. This is modeled by the the outer-patch indicator function $\mathcal{S}_{pe_{1i}}(x,\theta) =$

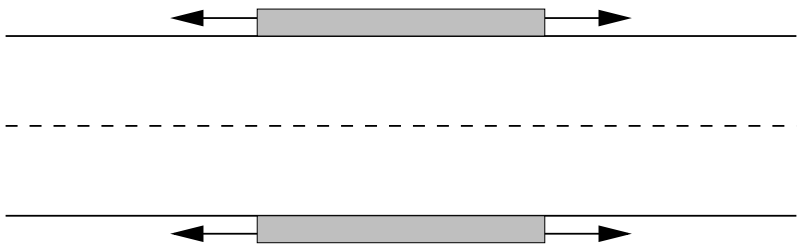

Figure 2.2: In-phase patch excitation producing predominantly planar vibrations.

$S_{pe_{1i}}(x)\hat{S}_{pe_{1i}}(\theta)$, where

$$S_{pe_{1i}}(x) = \begin{cases} 1 & , \quad x < (x_{1_{1i}} + x_{2_{1i}})/2 \\ 0 & , \quad x = (x_{1_{1i}} + x_{2_{1i}})/2 \\ -1 & , \quad x > (x_{1_{1i}} + x_{2_{1i}})/2 \end{cases} ,$$

and

$$\hat{S}_{pe_{1i}}(\theta) = \begin{cases} 1 & , \quad \theta < (\theta_{1_{1i}} + \theta_{2_{1i}})/2 \\ 0 & , \quad \theta = (\theta_{1_{1i}} + \theta_{2_{1i}})/2 \\ -1 & , \quad \theta > (\theta_{1_{1i}} + \theta_{2_{1i}})/2 \end{cases} .$$

The indicator function $\mathcal{S}_{pe_{2i}}(x,\theta) = S_{pe_{2i}}(x)\hat{S}_{pe_{2i}}(\theta)$ for the inner patches is similarly defined by replacing the subscripts $i1$ with $2i$ in the definitions above.

If predominantly planar vibrations are needed, we model identical voltages applied to the i^{th} patch pair as indicated in Figure 2.2. To obtain predominantly bending deformations, we model voltages with the same magnitude but opposite signs, as depicted in Figure 2.3. As indicated later in Chapter 5, the control methods we employ to stabilize an externally excited shell necessitate voltage inputs to the inner and outer patches which are nearly diametrically out-of-phase but exhibit magnitude differences. This indicates that both in-plane forces and bending moments are generated.

To accommodate commonly employed experimental edge clamps, we consider

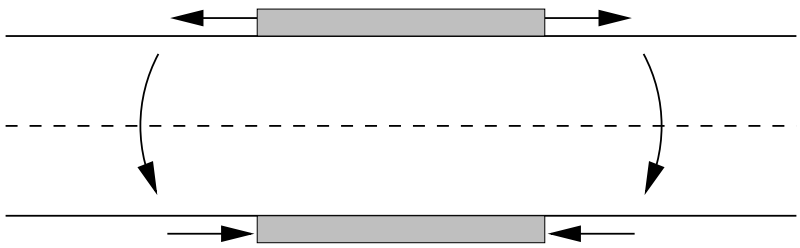

Figure 2.3: Out-of-phase patch excitation producing predominantly bending moments.

clamped edge and simply supported boundary conditions. The clamped edge conditions are expressed as

$$u(t,0,\theta) = u(t,\ell,\theta) = v(t,0,\theta) = v(t,\ell,\theta) \quad = \quad 0 \tag{2.5a}$$

$$w(t,0,\theta) = w(t,\ell,\theta) = \frac{\partial w(t,0,\theta)}{\partial x} = \frac{\partial w(t,\ell,\theta)}{\partial x} \quad = \quad 0\ , \tag{2.5b}$$

(see [14]), while simply supported boundary conditions are given by

$$v(t,0,\theta) = v(t,\ell,\theta) = w(t,0,\theta) = w(t,\ell,\theta) \quad = \quad 0 \tag{2.6a}$$

$$M_x(t,0,\theta) = M_x(t,\ell,\theta) = N_x(t,0,\theta) = N_x(t,\ell,\theta) \quad = \quad 0 \tag{2.6b}$$

(see [34]).

For approximation and theoretical analysis (see [24, 25]) we consider the weak form of the equations

$$\begin{aligned}
&\int_{\Gamma_0} R\left\{\rho h\frac{\partial^2 u}{\partial t^2}\overline{\eta_1} + N_x\overline{\frac{\partial \eta_1}{\partial x}} + \frac{1}{R}N_{\theta x}\overline{\frac{\partial \eta_1}{\partial \theta}} - \hat{q}_x\overline{\eta_1} - \sum_{i=1}^{s}\left[(N_x)_{pe_{1i}} + (N_x)_{pe_{2i}}\right]\overline{\frac{\partial \eta_1}{\partial x}}\right\} d\gamma = 0\\
&\int_{\Gamma_0}\left\{R\rho h\frac{\partial^2 v}{\partial t^2}\overline{\eta_2} + N_\theta\overline{\frac{\partial \eta_2}{\partial \theta}} + RN_{x\theta}\overline{\frac{\partial \eta_2}{\partial x}} - R\hat{q}_\theta\overline{\eta_2} - \sum_{i=1}^{s}\left[(N_\theta)_{pe_{1i}} + (N_\theta)_{pe_{2i}}\right]\overline{\frac{\partial \eta_2}{\partial \theta}}\right\} d\gamma = 0\\
&\int_{\Gamma_0}\left\{R\rho h\frac{\partial^2 w}{\partial t^2}\overline{\eta_3} + N_\theta\overline{\eta_3} - R\hat{q}_n\overline{\eta_3} - RM_x\overline{\frac{\partial^2 \eta_3}{\partial x^2}} - \frac{1}{R}M_\theta\overline{\frac{\partial^2 \eta_3}{\partial \theta^2}} - 2M_{x\theta}\overline{\frac{\partial^2 \eta_3}{\partial x \partial \theta}}\right.\\
&\qquad\left. + R\sum_{i=1}^{s}\left[(M_x)_{pe_{1i}} + (M_x)_{pe_{2i}}\right]\overline{\frac{\partial^2 \eta_3}{\partial x^2}} + \frac{1}{R}\sum_{i=1}^{s}\left[(M_\theta)_{pe_{1i}} + (M_\theta)_{pe_{2i}}\right]\overline{\frac{\partial^2 \eta_3}{\partial \theta^2}}\right\} d\gamma = 0
\end{aligned} \tag{2.7}$$

for all test functions $\Psi = (\eta_1, \eta_2, \eta_3)$ (see [14] for details in derivation). Here, the state variables for the system are taken to be $y = (u, v, w)$ in the state space

$$H = L^2(\Gamma_0) \times L^2(\Gamma_0) \times L^2(\Gamma_0) \ . \tag{2.8}$$

Test functions are chosen to satisfy essential boundary conditions and smoothness criteria. For the fixed edge or clamped boundary conditions (2.5), we take the space of test and trial functions to be

$$V = H_0^1(\Gamma_0) \times H_0^1(\Gamma_0) \times H_0^2(\Gamma_0) \ , \tag{2.9}$$

where

$$\begin{aligned} H_0^1(\Gamma_0) &= \Big\{ \eta \in H^1(\Gamma_0) : \eta(0, \cdot) = \eta(\ell, \cdot) = 0 \Big\} \\ H_0^2(\Gamma_0) &= \left\{ \eta \in H^2(\Gamma_0) : \eta(0, \cdot) = \frac{\partial \eta(0, \cdot)}{\partial x} = \eta(\ell, \cdot) = \frac{\partial \eta(\ell, \cdot)}{\partial x} = 0 \right\} . \end{aligned}$$

On the other hand, the test and trial function space for the simply supported boundary conditions (2.6) is

$$V = H^1(\Gamma_0) \times H_0^1(\Gamma_0) \times H^2(\Gamma_0) \cap H_0^1(\Gamma_0) \ . \tag{2.10}$$

Here note that the boundary conditions (2.6b) are natural boundary conditions and hence are not imposed on the test or trial functions.

Chapter 3

Abstract Formulation and Feedback Control

In this section, we show well-posedness of the shell model using variational and semigroup formulations. The abstract variational form is useful in parameter estimation and numerical approximation methods, while the semigroup formulations are suitable for control applications. We illustrate well-posedness by invoking existence and uniqueness theorems given in [14, Chapter 4]. The equivalence of the variational and semigroup solutions is also verified. We then briefly state control results on the infinite dimensional system and discuss convergence of Galerkin approximations. Existence, uniqueness and convergence of the Riccati solutions and the approximate LQR controls are illustrated following the ideas in [11, 14].

3.1 Variational Formulation

As indicated in [11, 14], we start the abstract formulation by considering Hilbert spaces $\mathbf{V}$ and $\mathbf{H}$ such that $\mathbf{V}$ is continuously and densely embedded in $\mathbf{H}$. We then identify $\mathbf{H}^*$ with $\mathbf{H}$ through the Riesz map, and consider the Gelfand triple $\mathbf{V} \hookrightarrow \mathbf{H} \hookrightarrow \mathbf{V}^*$ (see [14, p. 97], [52, p. 25] or [54, p. 261]). Here $\mathbf{V}^*$ and $\mathbf{H}^*$ are the dual spaces to $\mathbf{V}$ and $\mathbf{H}$, respectively. We take the duality product $\langle \cdot, \cdot \rangle_{\mathbf{V}^* \times \mathbf{V}}$ on $\mathbf{V}^* \times \mathbf{V}$ to be the unique extension by continuity of the scalar product $\langle \cdot, \cdot \rangle_{\mathbf{H}}$ of $\mathbf{H}$

defined on $\mathbf{H} \times \mathbf{V}$.

It can be readily shown that the test function space V (given in (2.9) or (2.10)) and state space H (given in (2.8)) satisfy the continuous and dense embedding conditions above, hence for the shell system, we let $\mathbf{V} \equiv V$, $\mathbf{H} \equiv H$ with $V \hookrightarrow H \hookrightarrow V^*$. Furthermore, the embedding of V into H and H^* into V^* are compact (for details regarding the embedding of V in H, see for example, [1, 54]).

We now define the inner products on H and V to abstractly formulate the mass, stiffness and damping terms in (2.7). To this end, we define the inner product on H to be

$$\langle \phi, \psi \rangle_H = \int_{\Gamma_0} \rho h u \bar{\eta}_1 d\gamma + \int_{\Gamma_0} \rho h v \bar{\eta}_2 d\gamma + \int_{\Gamma_0} \rho h w \bar{\eta}_3 d\gamma \ , \tag{3.1}$$

where $\phi = (u, v, w), \psi = (\eta_1, \eta_2, \eta_3) \in H$ and $d\gamma = R d\theta dx$. It can be readily seen that the norm induced by this inner product is equivalent to the usual norm in H. We next define the stiffness inner product $\langle \cdot, \cdot \rangle_{V_E}$ on V to be

$$\langle \phi, \psi \rangle_{V_E} \ = \ \sum_{i=1}^{16} I_i(\phi, \psi) \ , \tag{3.2}$$

where the I_i are terms in the weak form containing the stiffness coefficients $E, E_{pe_{1i}}$ and $E_{pe_{2i}}$, obtained by the substitution of the internal force and moments resultants (i.e., (2.3), (A.1), (A.2), (A.3),(A.4) and (A.5) substituted in the weak form (2.7)). To illustrate, I_1 and I_2 have the form

$$I_1(\phi, \psi) \ = \ \int_0^{2\pi} \int_0^{\ell} \frac{EhR}{(1-\nu^2)} \left[\frac{\partial u}{\partial x} + \nu \left(\frac{1}{R} \frac{\partial v}{\partial \theta} + \frac{w}{R} \right) \right] \overline{\frac{\partial \eta_1}{\partial x}} dx d\theta \tag{3.3}$$

$$\begin{aligned} I_2(\phi, \psi) \ = \ & \sum_{i=1}^{s} \int_{\theta_{1_{1i}}}^{\theta_{2_{1i}}} \int_{x_{1_{1i}}}^{x_{2_{1i}}} \frac{E_{pe_{1i}} R}{(1-\nu_{pe_{1i}}^2)} \left[h_{pe_{1i}} \left(\frac{\partial u}{\partial x} + \nu_{pe_{1i}} \left(\frac{1}{R} \frac{\partial v}{\partial \theta} + \frac{w}{R} \right) \right) \right. \\ & \left. - \frac{a_{2_{1i}}}{2} \left(\frac{\partial^2 w}{\partial x^2} + \frac{\nu_{pe_{1i}}}{R^2} \frac{\partial^2 w}{\partial \theta^2} \right) \right] \overline{\frac{\partial \eta_1}{\partial x}} dx d\theta \\ + \ & \sum_{i=1}^{s} \int_{\theta_{1_{2i}}}^{\theta_{2_{2i}}} \int_{x_{1_{2i}}}^{x_{2_{2i}}} \frac{E_{pe_{2i}} R}{(1-\nu_{pe_{2i}}^2)} \left[h_{pe_{2i}} \left(\frac{\partial u}{\partial x} + \nu_{pe_{2i}} \left(\frac{1}{R} \frac{\partial v}{\partial \theta} + \frac{w}{R} \right) \right) \right. \\ & \left. + \frac{a_{2_{2i}}}{2} \left(\frac{\partial^2 w}{\partial x^2} + \frac{\nu_{pe_{2i}}}{R^2} \frac{\partial^2 w}{\partial \theta^2} \right) \right] \overline{\frac{\partial \eta_1}{\partial x}} dx d\theta \ . \end{aligned} \tag{3.4}$$

Expressions for $I_i, i = 4, \ldots, 16$ are given in Appendix B. The damping inner product on V, denoted by $< \cdot, \cdot >_{V_{c_D}}$, is obtained by replacing E by c_D, $E_{pe_{1i}}$ by $c_{D_{pe_1 i}}$ and $E_{pe_{2i}}$ by $c_{D_{pe_2 i}}$ in the expression for the stiffness inner product $\langle \cdot, \cdot \rangle_{V_E}$ given in (3.2). As in the H inner product, the norms on V induced by $\langle \cdot, \cdot \rangle_{V_E}$ and $\langle \cdot, \cdot \rangle_{V_{c_D}}$ are equivalent to the standard norm in V.

We now define the stiffness and damping sesquilinear forms $\sigma_1 : V \times V \to \mathbb{C}$ and $\sigma_2 : V \times V \to \mathbb{C}$, respectively, by

$$\begin{aligned} \sigma_1(\phi, \psi) &= \langle \phi, \psi \rangle_{V_E} \\ \sigma_2(\phi, \psi) &= \langle \phi, \psi \rangle_{V_{c_D}} + \int_{\Gamma_0} \mu w \bar{\eta}_3 d\gamma \ . \end{aligned} \tag{3.5}$$

It is readily verified that the stiffness form σ_1 satisfies

(H1) $|\sigma_1(\phi, \psi)| \leq c_1 |\phi|_V |\psi|_V$, for some $c_1 \in \mathbb{R}$ (Bounded)

(H2) $Re\sigma_1(\phi, \phi) \geq c_2 |\phi|_V^2$, for some $c_2 > 0$ (V-Elliptic)

(H3) $\sigma_1(\phi, \psi) = \overline{\sigma_1(\psi, \phi)}$ (Symmetric)

for all $\phi, \psi \in V$. Furthermore, the damping term σ_2 has the properties

(H4) $|\sigma_2(\phi, \psi)| \leq c_3 |\phi|_V |\psi|_V$, for some $c_3 \in \mathbb{R}$ (Bounded)

(H5) $Re\sigma_2(\phi, \phi) \geq c_4 |\phi|_V^2$, for some $c_4 > 0$ (V-Elliptic) .

From the continuity properties (H1) and (H4), it follows that we can define operators $\mathcal{A}_1, \mathcal{A}_2 \in \mathcal{L}(V, V^*)$ such that

$$\begin{aligned} \langle \mathcal{A}_1 \phi, \psi \rangle_{V^*, V} &= \sigma_1(\phi, \psi), \quad \forall \phi, \psi \in V \\ \langle \mathcal{A}_2 \phi, \psi \rangle_{V^*, V} &= \sigma_2(\phi, \psi), \quad \forall \phi, \psi \in V \ . \end{aligned} \tag{3.6}$$

To abstractly formulate the control input and external forcing function contributions, we take the control input space to be the space $\mathcal{U} = \mathbb{R}^{2s}$. The control input

operator $\tilde{\mathcal{B}} \in \mathcal{L}(\mathcal{U}, V^*)$ is defined by

$$\begin{aligned}\left\langle \tilde{\mathcal{B}}U(t), \psi \right\rangle_{V^*,V} &= \sum_{i=1}^{s} \int_{\Gamma_0} \left[(N_x)_{pe_{1i}} + (N_x)_{pe_{2i}}\right] \overline{\frac{\partial \eta_1}{\partial x}} d\gamma \\ &+ \sum_{i=1}^{s} \int_{\Gamma_0} \frac{1}{R} \left[(N_\theta)_{pe_{1i}} + (N_\theta)_{pe_{2i}}\right] \overline{\frac{\partial \eta_2}{\partial \theta}} d\gamma \\ &- \sum_{i=1}^{s} \int_{\Gamma_0} \left[(M_x)_{pe_{1i}} + (M_x)_{pe_{2i}}\right] \overline{\frac{\partial^2 \eta_3}{\partial x^2}} d\gamma \\ &- \sum_{i=1}^{s} \int_{\Gamma_0} \frac{1}{R^2} \left[(M_\theta)_{pe_{1i}} + (M_\theta)_{pe_{2i}}\right] \overline{\frac{\partial^2 \eta_3}{\partial \theta^2}} d\gamma \ ,\end{aligned} \tag{3.7}$$

for all $\psi = (\eta_1, \eta_2, \eta_3) \in V$ and $U(t) \in \mathcal{U}$. Note that the vector $U(t)$ represents the time varying voltage input to each patch employed in (2.4), i.e.,

$$U(t) = (V_{11}(t), V_{21}(t), \ldots, V_{1i}(t), V_{2i}(t), \ldots, V_{1s}(t), V_{2s}(t)) \ .$$

The external forcing function will be denoted by $\tilde{g} = \dfrac{1}{\rho h}[\hat{q}_x, \hat{q}_\theta, \hat{q}_\eta]^T$. Finally, we let $y(t) = [u(t), v(t), w(t)]^T$ and the weak form (2.7) is written in the second order abstract variational form

$$\begin{aligned}&\langle \ddot{y}(t), \psi \rangle_{V^*,V} + \sigma_2(\dot{y}(t), \psi) + \sigma_1(y(t), \psi) = \left\langle \tilde{\mathcal{B}}U(t) + \tilde{g}(t), \psi \right\rangle_{V^*,V} \quad \forall \psi \in V \\ &y(0) = y_0, \qquad \dot{y}(0) = y_1 \ .\end{aligned} \tag{3.8}$$

Equivalently

$$\begin{aligned}&\ddot{y}(t) + \mathcal{A}_2 \dot{y}(t) + \mathcal{A}_1 y(t) = \tilde{\mathcal{B}}U(t) + \tilde{g}(t) \quad \text{in } V^* \\ &y(0) = y_0, \qquad \dot{y}(0) = y_1 \ .\end{aligned} \tag{3.9}$$

We assume the following regularity condition for the forcing function $\tilde{g}(t)$ in (3.9):

(H6) The input function $\tilde{\mathcal{B}}U(t) + \tilde{g}$ satisfies $\tilde{\mathcal{B}}U(t) + \tilde{g} \in L^2(0, T; V^*)$.

It should be noted that this force condition is sufficiently general to encompass most forces in applications.

The following theorem first proven in [12] (see also [14, Chapter 4]) provides the existence, uniqueness and continuous dependence on data of the solution to (3.8) (equivalently (3.9)).

Theorem 3.1.1 *Suppose that σ_1, σ_2 and $\tilde{\mathcal{B}}U(t) + \tilde{g}(t)$ satisfy (H1)-(H6) and that $y_0 \in V, y_1 \in H$. Then there exists a unique solution y of (3.8) (equivalently (3.9)) with $y \in L^2((0,T);V), \dot{y} \in L^2((0,T);V)$ and $\ddot{y} \in L^2((0,T);V^*)$. Moreover, solutions of (3.8) depend continuously on the data $(y_0, y_1, \tilde{\mathcal{B}}U + \tilde{g})$ in that the map $(y_0, y_1, \tilde{\mathcal{B}}U + \tilde{g}) \to (y, \dot{y})$ is continuous from $V \times H \times L^2((0,T);V^*)$ to $L^2((0,T);V) \times L^2((0,T);V)$.*

3.2 Semigroup Formulation

To formulate the solutions of (3.8) in a semigroup fashion, we first rewrite (3.8) in first order form. To this end, we define the spaces

$$\begin{aligned} \mathcal{H} &= V \times H \\ \mathcal{V} &= V \times V \end{aligned} \tag{3.10}$$

with norms

$$\begin{aligned} \|(\phi_1, \phi_2)\|_{\mathcal{H}}^2 &= \|\phi_1\|_V^2 + \|\phi_2\|_H^2 \\ \|(\phi_1, \phi_2)\|_{\mathcal{V}}^2 &= \|\phi_1\|_V^2 + \|\phi_2\|_V^2 \ . \end{aligned}$$

It can be readily verified that these product spaces also form a Gelfand triple $\mathcal{V} \hookrightarrow \mathcal{H} \hookrightarrow \mathcal{V}^*$, where $\mathcal{V}^* = V \times V^*$. The forcing terms are then reformulated as

$$g(t) = \begin{bmatrix} 0 \\ \\ \tilde{g}(t) \end{bmatrix} \quad , \quad \mathcal{B}U(t) = \begin{bmatrix} 0 \\ \\ \tilde{\mathcal{B}}U(t) \end{bmatrix} \ , \tag{3.11}$$

and we define the sesquilinear form $\sigma : \mathcal{V} \times \mathcal{V} \to \mathbb{C}$ by

$$\sigma(\Phi, \Psi) = -\langle \phi_2, \psi_1 \rangle_V + \sigma_1(\phi_1, \psi_2) + \sigma_2(\phi_2, \psi_2)$$

for $\Phi = (\phi_1, \phi_2), \Psi = (\psi_1, \psi_2) \in \mathcal{V}$. Finally, we take the state to be $z(t) = (y(t), \dot{y}(t)) \in \mathcal{H}$, and the second-order system (3.8) formulated in first-order form is

$$\begin{aligned} &\langle \dot{z}(t), \Psi \rangle_{\mathcal{V}^*, \mathcal{V}} + \sigma(z(t), \Psi) = \langle \mathcal{B}U(t) + g(t), \Psi \rangle_{\mathcal{V}^*, \mathcal{V}} \ , \qquad \forall \Psi \in \mathcal{V} \\ &z(0) = z_0 = (y_0, y_1) \ . \end{aligned} \tag{3.12}$$

The $\mathcal{V}$-continuity of σ and $\mathcal{V}$-ellipticity of $\sigma(\cdot,\cdot) + \lambda \langle \cdot, \cdot \rangle_{\mathcal{H}}$ for $\lambda > 0$ is easy to show and this is done in [14, p. 109]. Hence we can define an operator $\tilde{\mathcal{A}} \in \mathcal{L}(\mathcal{V}, \mathcal{V}^*)$ by

$$\sigma(\Phi, \Psi) = \left\langle \tilde{\mathcal{A}}\Phi, \Psi \right\rangle_{\mathcal{V}^*, \mathcal{V}} \ .$$

To write (3.12) in an equivalent strong form, we restrict $\tilde{\mathcal{A}}$ to the system operator

$$\begin{aligned} \mathrm{dom}\mathcal{A} &= \{(\phi_1, \phi_2) \in \mathcal{H} | \phi_2 \in V, \mathcal{A}_1\phi_1 + \mathcal{A}_2\phi_2 \in H\} \\ \mathcal{A} &= \begin{bmatrix} 0 & I \\ -\mathcal{A}_1 & -\mathcal{A}_2 \end{bmatrix}, \end{aligned} \tag{3.13}$$

where $\mathcal{A}_1$ and $\mathcal{A}_2$ are defined in (3.6). It should be noted that $\mathcal{A}$ is the negative of the restriction to $\mathrm{dom}\mathcal{A}$ of the operator $\tilde{\mathcal{A}}$ so that $\sigma(\Phi, \Psi) = \langle -\mathcal{A}\Phi, \Psi \rangle_{\mathcal{H}}$ for $\Phi \in \mathrm{dom}\mathcal{A}, \Psi \in \mathcal{V}$. A strong form of the abstract system model (3.12) is given by

$$\begin{aligned} \dot{z}(t) &= \mathcal{A}z(t) + \mathcal{B}U(t) + g(t) \quad \text{in } \mathcal{V}^* \\ z(0) &= z_0 \ . \end{aligned} \tag{3.14}$$

The following theorems proven in [14, Chapter 4] give existence of the solution to (3.14) and establishes its equivalence to the variational solution given by Theorem 3.1.1.

Theorem 3.2.1 *Under Hypotheses (H1)-(H5) on σ_1 and σ_2, $\tilde{\mathcal{A}}$ generates an analytic semigroup $\mathcal{T}(t)$ on $\mathcal{V}, \mathcal{H}$ and $\mathcal{V}^*$. In terms of this semigroup, the representation*

$$z(t) = \mathcal{T}(t)z_0 + \int_0^t \mathcal{T}(t-s)\left[\mathcal{B}U(s) + g(s)\right] ds \tag{3.15}$$

defines a mild solution to (3.14) for $z_0 \in \mathcal{V}^*$ and $\mathcal{B}U + g \in L^2((0,T); \mathcal{V}^*)$. Furthermore, this semigroup is (uniformly) exponentially stable on $\mathcal{V}, \mathcal{H}$ and $\mathcal{V}^*$.

Theorem 3.2.2 *Let z_{sg} denote the semigroup solution to (3.14) given by (3.15) and let z_{var} denote the weak solution to (3.12). Under hypotheses (H1)-(H5), it follows that $z_{sg}(z_0, \mathcal{F}) = z_{var}(z_0, \mathcal{F})$ for $z_0 \in \mathcal{H}$ and $\mathcal{F} \equiv \mathcal{B}U + g \in L^2((0,T); \mathcal{V}^*)$.*

3.3 Control Problem

In this section, we discuss infinite dimensional control methods to attenuate shell vibrations modeled by (3.14). We consider transient shell vibrations ($g \equiv 0$) and systems driven by a periodic exogenous force ($g \neq 0$). The first case with $g \equiv 0$ could be useful in applications where the shell or patches undergoes initial deformations and vibrates to a steady state. Control methods for this case are designed to attenuate only the transient state responses. Systems driven by a persistent exogenous force are appropriate for applications in which the disturbance is due to rotating or oscillating components, where examples include vibration suppression due to engine noises. In this case, both transient and periodic state responses must be considered in designing control methodologies. As will be discussed later, we control the periodic state responses through a tracking variable.

The state observations in the observation space $\mathcal{Y}$ are given by

$$z_{ob} = \mathcal{C}z(t)$$

where $\mathcal{C} \in \mathcal{L}(\mathcal{H}, \mathcal{Y})$ is bounded. The operator $\mathcal{C}$ is often unbounded in applications due to the discrete nature of the sensing devices but we only consider the bounded case here. We also make the simplifying assumption that the full state $z = (y, \dot{y})$ is available for the computation of the feedback control $U(t)$. This assumption was made since numerical calculations which allow full state measurements are much easier to use to demonstrate our ideas. In many practical applications, current measuring devices can only deliver partial state measurements hence compensators must be included in the control design. The reader is referred to [11] and [14, Chapters 7.5 and 8] for discussions regarding compensators and unbounded observation operators $\mathcal{C}$.

No Exogenous Input:

The quadratic functional we minimize in order to determine the optimal control $\bar{U}$

for the infinite horizon control problem is

$$J(U, z_0) = \int_0^\infty \left\{ \|\mathcal{C}z(t)\|_{\mathcal{H}}^2 + \left\|\mathcal{R}^{1/2}U(t)\right\|_{\mathcal{U}}^2 \right\} dt \tag{3.16}$$

subject to

$$\begin{aligned} \dot{z}(t) &= \mathcal{A}z(t) + \mathcal{B}U(t) \\ z(0) &= z_0 \ . \end{aligned}$$

Here, the positive, self-adjoint operator $\mathcal{R} = (\mathcal{R}^{1/2})^2 \in \mathcal{L}(\mathcal{U},\mathcal{U})$ is used to limit voltage input to the patches. We do not state results for the finite horizon problem but the reader is referred to discussions in [11, Theorem 3.1] and [14, Chapter 7.2.1].

We first give the definitions for the pair $(\mathcal{A}, \mathcal{B})$ to be stabilizable and $(\mathcal{A}, \mathcal{C})$ to be detectable before stating Theorem 7.5 in [14], which uses these conditions to indicate the existence of optimal controls minimizing (3.16). The proof of this theorem can be found in [11].

Definition 3.3.1 *The pair $(\mathcal{A}, \mathcal{B})$ is said to be stabilizable if there exists an operator $\mathcal{K} \in \mathcal{L}(\mathcal{V}^*,\mathcal{U})$ such that $\mathcal{A} - \mathcal{B}\mathcal{K}$ generates an exponentially stable semigroup on $\mathcal{V}^*$ (i.e., $\left\|e^{t(\mathcal{A}-\mathcal{B}\mathcal{K})}\right\|_{\mathcal{L}(\mathcal{V}^*)} \leq Me^{-\omega t}$ for $M \geq 1, \omega > 0$).*

Definition 3.3.2 *The pair $(\mathcal{A}, \mathcal{C})$ is said to be detectable if there exists an operator $\mathcal{F} \in \mathcal{L}(\mathcal{Y}, \mathcal{V}^*)$ such that $\mathcal{A} - \mathcal{F}\mathcal{C}$ generates an exponentially stable semigroup on $\mathcal{V}^*$.*

Theorem 3.3.1 *(Theorem 7.5 in [14].) If $(\mathcal{A}, \mathcal{B})$ is stabilizable and $(\mathcal{A}, \mathcal{C})$ is detectable, then the algebraic Riccati equation*

$$\left(\mathcal{A}^*\Pi + \Pi\mathcal{A} - \Pi\mathcal{B}\mathcal{R}^{-1}\mathcal{B}^*\Pi + \mathcal{C}^*\mathcal{C}\right) z = 0 \qquad \forall z \in \mathcal{V} \tag{3.17}$$

has a unique non-negative solution $\Pi \in \mathcal{L}(\mathcal{V}^*, \mathcal{V})$, $\mathcal{A} - \mathcal{B}\mathcal{R}^{-1}\mathcal{B}^*\Pi$ generates an exponentially stable closed loop semigroup $\mathcal{S}(t)$ on $\mathcal{H}, \mathcal{V}, \mathcal{V}^*$, and the optimal control that minimizes (3.16) is given by

$$\bar{U}(t) = -\mathcal{R}^{-1}\mathcal{B}^*\Pi\bar{z}(t)$$

where $\bar{z}(t) = \mathcal{S}(t)z_0$ for $z_0 \in \mathcal{V}^*$.

Periodic Exogenous Input:

In this control problem, we seek the optimal control $\bar{U}$ minimizing the cost functional

$$J(U, z_0) = \frac{1}{2}\int_0^\tau \left\{ \|\mathcal{C}z(t)\|_{\mathcal{Y}}^2 + \left\|\mathcal{R}^{1/2}U(t)\right\|_{\mathcal{U}}^2 \right\} dt \tag{3.18}$$

subject to the evolution equation

$$\begin{aligned} \dot{z}(t) &= \mathcal{A}z(t) + \mathcal{B}z(t) + g(t) \\ z(0) &= z(\tau)\ , \end{aligned} \tag{3.19}$$

where $g \in L^2(0, \tau; \mathcal{H})$ is τ-periodic in time.

The control of the persistent state dynamics is provided through the tracking variable $r(t)$ which is a solution of the operator equation

$$\begin{aligned} \dot{r}(t) &= -\left[\mathcal{A} - \mathcal{B}\mathcal{R}^{-1}\mathcal{B}^*\Pi\right]^* r(t) + \Pi g(t) \\ r(0) &= r(\tau)\ , \end{aligned} \tag{3.20}$$

where Π is the solution to the algebraic Riccati equation (3.17).

The existence and uniqueness of the Riccati solutions, together with the existence of optimal controls is guaranteed in [21] – see also [14, Theorem 7.16], where and $(\mathcal{A}, \mathcal{B})$ and $(\mathcal{A}, \mathcal{C})$ are assumed to be stabilizable and detectable in the space $\mathcal{H}$ (i.e., we replace $\mathcal{V}^*$ by $\mathcal{H}$ in Definitions 3.3.1 and 3.3.2).

Theorem 3.3.2 *([21] and Theorem 7.16 in [14]) Consider the system (3.19) which is assumed to have a unique mild solution. A bounded control operator $\mathcal{B} \in \mathcal{L}(\mathcal{U}, \mathcal{H})$ is considered and $g \in L^2(0, \tau; \mathcal{H})$ is taken to be $\tau-$periodic. Moreover, we suppose that $(\mathcal{A}, \mathcal{B})$ and $(\mathcal{A}, \mathcal{C})$ are stabilizable and detectable in $\mathcal{H}$.*

The Riccati equation (3.17) then has a unique nonnegative solution Π. Furthermore, if r denotes the $\tau-$periodic tracking solution of (3.20) and $\bar{z}$ is the closed loop solution of

$$\begin{aligned} \dot{\bar{z}}(t) &= \left[\mathcal{A} - \mathcal{B}\mathcal{R}^{-1}\mathcal{B}^*\Pi\right]\bar{z}(t) - \mathcal{B}\mathcal{R}^{-1}\mathcal{B}^* r(t) + g(t) \\ \bar{z}(0) &= \bar{z}(\tau)\ , \end{aligned} \tag{3.21}$$

then the optimal control is given by

$$\bar{U}(t) = -\mathcal{R}^{-1}\mathcal{B}^* \left[\Pi \bar{z}(t) - r(t)\right] \ . \tag{3.22}$$

3.4 Convergence of Finite Dimensional Approximations

The solutions given by Theorem 3.1.1 and Theorem 3.2.1, together with the optimal controls given by Theorem 3.3.1 and Theorem 3.3.2 are infinite dimensional. For numerical applications, we use Galerkin approximation to obtain solutions in finite dimensional subspaces $\mathcal{V}^{\mathcal{N}} \subset \mathcal{V} \subset \mathcal{H}$. The bases for these subspaces can consist of modes, splines, polynomials, finite elements, or reduced basis elements. Specific bases used in the approximation methods will be discussed in Chapter 4.

Since $\mathcal{V} = V \times V$, we use the superscript $\mathcal{N}$ to denote $\mathcal{N}$-dimensional subspaces of V and use the superscript $2\mathcal{N}$ to denote the $2\mathcal{N}$-dimensional subspace $\mathcal{V}^{2\mathcal{N}} = V^{\mathcal{N}} \times V^{\mathcal{N}}$. The following approximation condition is necessary for the convergence of the finite dimensional solutions to the infinite dimensional solutions given by Theorem 3.1.1 and Theorem 3.2.1.

(H1N) Let $\mathbf{V}$ be a Hilbert space. For any $z \in \mathbf{V}$, there exists a sequence $\tilde{z}^{\mathcal{N}} \in \mathbf{V}^N$ such that $\left|z - \tilde{z}^{\mathcal{N}}\right|_{\mathbf{V}} \to 0$ as $N \to \infty$.

It is easy to show that if $\mathcal{V}^{2\mathcal{N}} = V^{\mathcal{N}} \times V^{\mathcal{N}} \subset \mathcal{V}$ satisfies (H1N), then $V^{\mathcal{N}} \subset V$ also satisfies (H1N). Conversely, if $V^{\mathcal{N}} \subset V$ satisfies (H1N), then we can set $\mathcal{V}^{2\mathcal{N}} = V^{\mathcal{N}} \times V^{\mathcal{N}}$ with $\mathcal{V}^{2\mathcal{N}}$ satisfying (H1N).

We now define the operators $\mathcal{A}_1^{\mathcal{N}} : V^{\mathcal{N}} \to V^{\mathcal{N}}$ and $\mathcal{A}_2^{\mathcal{N}} : V^{\mathcal{N}} \to V^{\mathcal{N}}$ which approximate $\mathcal{A}_1$ and $\mathcal{A}_2$, respectively, by restricting σ_1 and σ_2 to $V^{\mathcal{N}} \times V^{\mathcal{N}}$, i.e.,

$$\begin{aligned} \left\langle \mathcal{A}_1^{\mathcal{N}}\phi, \psi \right\rangle_H &= \sigma_1(\phi, \psi) \quad \forall \phi, \psi \in V^{\mathcal{N}} \\ \left\langle \mathcal{A}_2^{\mathcal{N}}\phi, \psi \right\rangle_H &= \sigma_2(\phi, \psi) \quad \forall \phi, \psi \in V^{\mathcal{N}} \ . \end{aligned} \tag{3.23}$$

Similarly, the operator $\mathcal{A}^{2\mathcal{N}} : \mathcal{V}^{2\mathcal{N}} \to \mathcal{V}^{2\mathcal{N}}$ is the restriction of σ on $\mathcal{V}^{2\mathcal{N}} \times \mathcal{V}^{2\mathcal{N}}$ with definition

$$\left\langle -\mathcal{A}^{2\mathcal{N}}\Phi, \Psi \right\rangle_{\mathcal{H}} = \sigma(\Phi, \Psi) \quad \forall \Phi, \Psi \in \mathcal{V}^{2\mathcal{N}} \ . \tag{3.24}$$

It readily follows that

$$\mathcal{A}^{2\mathcal{N}} = \begin{bmatrix} 0 & I \\ -\mathcal{A}_1^{\mathcal{N}} & -\mathcal{A}_2^{\mathcal{N}} \end{bmatrix} \ . \tag{3.25}$$

The usual projection operators from H onto $V^{\mathcal{N}}$ and from $\mathcal{H}$ onto $\mathcal{V}^{2\mathcal{N}}$ are denoted by $\mathcal{P}^{\mathcal{N}}$ and $\mathcal{P}^{2\mathcal{N}}$, respectively, satisfying

$$\begin{aligned} &\mathcal{P}^{\mathcal{N}}\phi \in V^{\mathcal{N}} \text{ and } \left\langle \mathcal{P}^{\mathcal{N}}\phi - \phi, \psi \right\rangle_{H} = 0 \ \forall \psi \in V^{\mathcal{N}} \\ &\mathcal{P}^{2\mathcal{N}}\Phi \in \mathcal{V}^{2\mathcal{N}} \text{ and } \left\langle \mathcal{P}^{2\mathcal{N}}\Phi - \Phi, \Psi \right\rangle_{\mathcal{H}} = 0 \ \forall \Psi \in \mathcal{V}^{2\mathcal{N}} \ . \end{aligned} \tag{3.26}$$

The control operator $\mathcal{B}$ (3.7) is approximated by $\mathcal{B}^{2\mathcal{N}}$ by restricting it to the finite dimensional subspace using its adjoint

$$\left\langle \mathcal{B}^{2\mathcal{N}}U, \Psi \right\rangle_{\mathcal{H}} = \langle U, \mathcal{B}^*\Psi \rangle_{\mathcal{U}} \ , \quad \forall \Psi \in \mathcal{V}^{2\mathcal{N}} \ ,$$

and $\mathcal{C}^{2\mathcal{N}}$ is the restriction of $\mathcal{C}$ to $\mathcal{V}^{2\mathcal{N}}$. The approximating operators $\mathcal{A}_1^{\mathcal{N}}, \mathcal{A}_2^{\mathcal{N}}, \mathcal{B}^{2\mathcal{N}}$ and $\mathcal{C}^{2\mathcal{N}}$ will be employed in the discussion regarding convergence of finite dimensional suboptimal controls in Chapter 3.5. The following is Lemma 4.1 in [11] which gives the convergence of the finite dimensional Galerkin solutions.

Theorem 3.4.1 *(Lemma 4.1 in [11]) Suppose (H1N) is satisfied and let* $\mathcal{B}U + g \in L^2(0, T; \mathcal{V}^*)$ *and* $z_0 \in \mathcal{H}$. *If* $z(t) \in \mathcal{V}$ *is defined by (3.15) and* $z^{2\mathcal{N}}(t) \in \mathcal{V}^{2\mathcal{N}}, t \geq 0$ *satisfies*

$$\begin{aligned} &\frac{d}{dt}\left\langle z^{2\mathcal{N}}(t), \Psi \right\rangle_{\mathcal{H}} + \sigma(z^{2\mathcal{N}}(t), \Psi) = \langle g(t) + \mathcal{B}U(t), \psi \rangle_{\mathcal{V}^*, \mathcal{V}} \ , \quad \forall \Psi \in \mathcal{V}^{2\mathcal{N}} \\ &z^{2\mathcal{N}}(0) = \mathcal{P}^{2\mathcal{N}} z_0 \ , \end{aligned} \tag{3.27}$$

then the error function $e^{2\mathcal{N}}(t) = z^{2\mathcal{N}}(t) - z(t)$ *satisfies*

$$\left\| e^{2\mathcal{N}}(t) \right\|_{\mathcal{H}} \to 0$$

and

$$\int_0^t \left\| e^{2\mathcal{N}}(s) \right\|_{\mathcal{V}}^2 ds \to 0 \quad as\ \mathcal{N} \to \infty$$

uniformly in $t \in [0, T]$.

3.5 Finite Dimensional Control and Convergence of Riccati Solutions

The theory for convergence of Riccati and optimal control solutions for systems with no exogenous force and bounded observation operator $\mathcal{C}$ is essentially complete. The essential hypothesis which requires that $(\mathcal{A}^{2\mathcal{N}}, \mathcal{B}^{2\mathcal{N}})$ be stabilizable for systems incorporating passive patch contributions, is currently being investigated by the author. The stabilizability condition is a sufficient assumption for the convergence theorems. For systems with periodic exogenous disturbance, the theory is less complete. For this case, we merely present the finite dimensional control methods we implemented computationally. Numerical results in Chapter 5 suggest the controllability of the finite dimensional system and existence of finite dimensional controls.

No Exogenous Input:

The approximate infinite horizon control problem for the system with no exogenous force involves finding $U \in L^2(0, \infty; \mathcal{U})$ which minimizes

$$J^{2\mathcal{N}}(U, z_0^{2\mathcal{N}}) = \int_0^\infty \left\{ \left\| \mathcal{C}^{2\mathcal{N}} z^{2\mathcal{N}}(t) \right\|_{\mathcal{Y}}^2 + \left\| \mathcal{R}^{1/2} U(T) \right\|_{\mathcal{U}}^2 \right\} dt \tag{3.28}$$

subject to $z^{2\mathcal{N}}$ satisfying

$$\begin{aligned} \dot{z}^{2\mathcal{N}}(t) &= \mathcal{A}^{2\mathcal{N}} z^{2\mathcal{N}} + \mathcal{B}^{2\mathcal{N}} U(t)\ , \quad t > 0 \\ z^{2\mathcal{N}}(0) &= \mathcal{P}^{2\mathcal{N}} z_0 = z_0^{2\mathcal{N}}\ . \end{aligned} \tag{3.29}$$

The analogous definition of stabilizable and detectable matrix pairs for finite dimensional systems will be defined before we state the theorem which gives convergence results.

Definition 3.5.1 *The pair* $(\mathcal{A}^{2\mathcal{N}}, \mathcal{B}^{2\mathcal{N}})$ *is said to be uniformly stabilizable if there exist constants* $M_1 \geq 1, \omega_1 > 0$ *independent of* $\mathcal{N}$ *and a sequence of operators* $\mathcal{K}^{2\mathcal{N}} \in \mathcal{L}(\mathcal{V}^{2\mathcal{N}}, \mathcal{U})$ *such that* $\sup_{\mathcal{N}} \left|\mathcal{K}^{2\mathcal{N}}\right| < \infty$ *and*

$$\left\| e^{t\left(\mathcal{A}^{2\mathcal{N}} - \mathcal{B}^{2\mathcal{N}}\mathcal{K}^{2\mathcal{N}}\right)} \mathcal{P}^{2\mathcal{N}} z \right\|_{\mathcal{H}} \leq M_1 e^{-\omega_1 t} \left\| z \right\|_{\mathcal{H}}$$

for $z \in \mathcal{H}$.

Definition 3.5.2 *The pair* $(\mathcal{A}^{2\mathcal{N}}, \mathcal{C}^{2\mathcal{N}})$ *is said to be uniformly detectable if there exist constants* $M_2 \geq 1, \omega_2 > 0$ *independent of* $\mathcal{N}$ *and a sequence of operators* $\mathcal{F}^{2\mathcal{N}} \in \mathcal{L}(\mathcal{Y}, \mathcal{V}^{2\mathcal{N}})$ *such that* $\sup_{\mathcal{N}} \left|\mathcal{F}^{2\mathcal{N}}\right| < \infty$ *and*

$$\left\| e^{t\left(\mathcal{A}^{2\mathcal{N}} - \mathcal{F}^{2\mathcal{N}}\mathcal{C}^{2\mathcal{N}}\right)} \mathcal{P}^{2\mathcal{N}} z \right\|_{\mathcal{H}} \leq M_2 e^{-\omega_2 t} \left\| z \right\|_{\mathcal{H}}$$

for $z \in \mathcal{H}$.

Theorem 3.5.1 *([11] and Theorem 7.10, [14]) Suppose* $V \overset{i}{\hookrightarrow} H$, *where the embedding* i *is compact. Let the sesquilinear form* σ *associated with the first-order system (3.12) be continuous and* $\mathcal{V}$*-elliptic. Assume that the operators* $\mathcal{A}, \mathcal{B}, \mathcal{C}$ *are such that* $(\mathcal{A}, \mathcal{B})$ *is stabilizable and* $(\mathcal{A}, \mathcal{C})$ *is detectable where* $\mathcal{B} \in \mathcal{L}(\mathcal{U}, \mathcal{V}^*)$ *is unbounded and* $\mathcal{C} \in \mathcal{L}(\mathcal{H}, \mathcal{Y})$ *is bounded. Consider an approximation method which satisfies* $(H1N)$. *Finally, suppose that for fixed* $\mathcal{N}_0$ *and* $\mathcal{N} > \mathcal{N}_0$, *the pair* $(\mathcal{A}^{2\mathcal{N}}, \mathcal{B}^{2\mathcal{N}})$ *is uniformly stabilizable and* $(\mathcal{A}^{2\mathcal{N}}, \mathcal{C}^{2\mathcal{N}})$ *is uniformly detectable.*

Then for $\mathcal{N}$ *sufficiently large, there exists a unique nonnegative self-adjoint solution* $\Pi^{2\mathcal{N}} \in \mathcal{L}(\mathcal{V}^*, \mathcal{V})$ *to the* $\mathcal{N}^{th}$ *approximate algebraic Riccati equation (3.17) in* $\mathcal{V}^{2\mathcal{N}}$ *with* $\mathcal{A}, \mathcal{B}, \mathcal{C}$ *replaced by* $\mathcal{A}^{2\mathcal{N}}, \mathcal{B}^{2\mathcal{N}}, \mathcal{C}^{2\mathcal{N}}$, *respectively. There also exist constants* $M_3 \geq 1$ *and* $\omega_3 > 0$ *independent of* $\mathcal{N}$ *such that* $\mathcal{S}^{2\mathcal{N}}(t) = e^{\left(\mathcal{A}^{2\mathcal{N}} - \mathcal{B}^{2\mathcal{N}}\mathcal{R}^{-1}\mathcal{B}^{2\mathcal{N}*}\Pi^{2\mathcal{N}}\right)t}$ *satisfies*

$$\left\| \mathcal{S}^{2\mathcal{N}}(t) \right\|_{\mathcal{V}^{2\mathcal{N}}} \leq M_3 e^{-\omega_3 t} \ , t > 0$$

or equivalently

$$\left\| e^{t\left(\mathcal{A}^{2\mathcal{N}} - \mathcal{B}^{2\mathcal{N}}\mathcal{R}^{-1}\mathcal{B}^{2\mathcal{N}*}\right)} \mathcal{P}^{2\mathcal{N}} z_0 \right\|_{\mathcal{H}} \leq M_3 e^{-\omega_3 t} \left\| z_0 \right\|_{\mathcal{H}} \ , t > 0, z_0 \in \mathcal{H} \ .$$

Additionally, the convergences

$$\Pi^{2\mathcal{N}}\mathcal{P}^{2\mathcal{N}}z \xrightarrow{s} \Pi z \text{ in } \mathcal{V} \text{ for every } z \in \mathcal{V}^*$$
$$\left\|\mathcal{B}^{2\mathcal{N}^*}\Pi^{2\mathcal{N}}\mathcal{P}^{2\mathcal{N}} - \mathcal{B}^*\Pi\right\|_{\mathcal{L}(\mathcal{H},\mathcal{U})} \to 0 \ ,$$

as $\mathcal{N} \to \infty$, of the Riccati and control operators are obtained. Moreover, the feedback system operator $\mathcal{A} - \mathcal{B}\mathcal{R}^{-1}\mathcal{B}^{2\mathcal{N}^*}\Pi^{2\mathcal{N}}$ generates an exponentially stable analytic semigroup on $\mathcal{H}$ and for every $z_0 \in \mathcal{H}$,

$$J^{2\mathcal{N}}\left(-\mathcal{B}^{2\mathcal{N}^*}\Pi^{2\mathcal{N}}z(\cdot), z_0\right) - J(\bar{u}, z_0) \leq \varepsilon(\mathcal{N})\,\|z_0\|^2_{\mathcal{H}}$$

where $\varepsilon(\mathcal{N}) \to$ as $\mathcal{N} \to \infty$.

The assumptions of uniform stabilizability of $(\mathcal{A}^{2\mathcal{N}}, \mathcal{B}^{2\mathcal{N}})$ and uniform detectability of $(\mathcal{A}^{2\mathcal{N}}, \mathcal{C}^{2\mathcal{N}})$ in Theorem 3.5.1 can be difficult to directly verify. Hence we need results relying on easily confirmed assumptions. For first-order systems, Lemma 4.7 in [11] (which is restated as Lemma 7.12 in [14]) guarantees that $(\mathcal{A}^{2\mathcal{N}}, \mathcal{B}^{2\mathcal{N}})$ is stabilizable provided $(\mathcal{A}, \mathcal{B})$ is stabilizable and the injection $\mathcal{V} \hookrightarrow \mathcal{H}$ is compact. For the second-order system we consider, the creation of the product spaces $\mathcal{V} = V \times V$ and $\mathcal{H} = H \times V$ prohibits the compactness of $i : \mathcal{V} \hookrightarrow \mathcal{H}$, even when $V \hookrightarrow H$ is compact. Hence we need the following lemma to obtain uniform exponential bounds on the approximating semigroups $\mathcal{S}^{2\mathcal{N}}(t)$.

Lemma 3.5.1 *(Lemma 6.2 in [11]) Suppose $V \xhookrightarrow{i} H$, where i is compact. Moreover, suppose that the damping sesquilinear form σ_2 can be decomposed as $\sigma_2 = \gamma\sigma_1 + \tilde{\sigma}_2$, for some $\gamma > 0$, where the continuous sesquilinear form $\tilde{\sigma}_2$ satisfies for some $\mu \in \mathbb{R}$*

$$Re\tilde{\sigma}_2(\phi, \phi) \geq -\frac{c_2\gamma}{2}\|\phi\|^2_V - \mu\|\phi\|^2_H \text{ for all } \phi \in V \ .$$

Finally, suppose that the operator $\mathcal{A}_1^{-1}\tilde{\mathcal{A}}_2$, where $\tilde{\mathcal{A}}_2 \in \mathcal{L}(V, V^*)$ is defined by

$$\left\langle \tilde{\mathcal{A}}_2\phi, \eta \right\rangle_{V^*,V} = \tilde{\sigma}_2(\phi, \eta) \tag{3.30}$$

is compact on V.

Let $\mathcal{T}$ *denote the open loop semigroup generated by the product space operator* $\mathcal{A}$ *and let* $\mathcal{T}^{2\mathcal{N}}$ *be generated by* $\mathcal{A}^{2\mathcal{N}}$. *If for some* $\nu \geq \mu$ *and* $M \geq 1$

$$\|\mathcal{T}(t)\|_{\mathcal{L}(\mathcal{H})} \leq Me^{\nu t} \ , \quad t \geq 0 \ , \tag{3.31}$$

then for any $\varepsilon > 0$ *there exists an integer* $\mathcal{N}_\varepsilon$ *such that for* $\mathcal{N} \geq \mathcal{N}_\varepsilon$

$$\left\|\mathcal{T}^{2\mathcal{N}}(t)\mathcal{P}^{2\mathcal{N}}\right\|_{\mathcal{L}(\mathcal{H})} \leq \tilde{M}e^{(\nu+\varepsilon)t} \ , \quad t \geq 0 \ ,$$

for some constant $\tilde{M} > 0$ *independent of* $\mathcal{N}$.

Since the proof of Lemma 6.2 in [11] is given in sketchy form, we give a detailed proof here. We first state and prove the following lemmas which will be used in proving Lemma 3.5.1 below.

Lemma 3.5.2 $\left(\mathcal{A}_1^{\mathcal{N}}\right)^{-1} \equiv P_{V_1}^{\mathcal{N}}\mathcal{A}_1^{-1}$ *on* $V^{\mathcal{N}}$, *where* $P_{V_1}^{\mathcal{N}} : V \to V^{\mathcal{N}}$ *is defined by*

$$\sigma_1\left(P_{V_1}^{\mathcal{N}}\phi - \phi, \psi^{\mathcal{N}}\right) = 0 \quad \textit{for all } \psi^{\mathcal{N}} \in V^{\mathcal{N}} \ , \phi \in V \ . \tag{3.32}$$

Proof:

- Since $\sigma_1(\cdot,\cdot)$ gives rise to an inner product on V whose induced norm is equivalent to the usual norm in V, then a closer inspection of (3.32) reveals that $P_{V_1}^{\mathcal{N}}$ is the projection operator from V into $V^{\mathcal{N}}$ under the $\sigma_1(\cdot,\cdot)$ inner product, i.e., the projection of V_1 onto $V^{\mathcal{N}}$ where V_1 is V with the σ_1 inner product. It follows immediately that $P_{V_1}^{\mathcal{N}}$ from V onto $V^{\mathcal{N}}$ is well defined and linear. Now let $\phi^{\mathcal{N}}$ be any arbitrary element of $V^{\mathcal{N}}$. Then for any $\psi^{\mathcal{N}} \in V^{\mathcal{N}}$,

$$\begin{aligned}
\sigma_1\left(\mathcal{A}_1^{-1}\phi^{\mathcal{N}}, \psi^{\mathcal{N}}\right) &= \left\langle \phi^{\mathcal{N}}, \psi^{\mathcal{N}} \right\rangle_{V^*,V} \ , \quad \text{(from (3.6))} \\
&= \left\langle \phi^{\mathcal{N}}, \psi^{\mathcal{N}} \right\rangle_{H} \ , \quad \text{(since } \phi^{\mathcal{N}} \in V\text{)} \\
&= \left\langle \mathcal{A}_1^{\mathcal{N}}\left(\mathcal{A}_1^{\mathcal{N}}\right)^{-1}\phi^{\mathcal{N}}, \psi^{\mathcal{N}} \right\rangle_{H} \\
&= \sigma_1\left(\left(\mathcal{A}_1^{\mathcal{N}}\right)^{-1}\phi^{\mathcal{N}}, \psi^{\mathcal{N}}\right) \ , \quad \text{(from (3.23))} \ .
\end{aligned}$$

We note that $\mathcal{A}_1^{\mathcal{N}}$ is invertible in $V^{\mathcal{N}}$ follows from (3.23) and the V-ellipticity of σ_1. Thus, $\sigma_1\left(\mathcal{A}_1^{-1}\phi^{\mathcal{N}} - \left(\mathcal{A}_1^{\mathcal{N}}\right)^{-1}\phi^{\mathcal{N}}, \psi^{\mathcal{N}}\right) = 0$ for every $\psi^{\mathcal{N}} \in V^{\mathcal{N}}$. But by the defining the relationships (3.32) we have

$$\sigma_1\left(P_{V_1}^{\mathcal{N}}\mathcal{A}_1^{-1}\phi^{\mathcal{N}} - \mathcal{A}_1^{-1}\phi^{\mathcal{N}}, \psi^{\mathcal{N}}\right) = 0 \text{ for all } \phi^{\mathcal{N}}, \psi^{\mathcal{N}} \in V^{\mathcal{N}} .$$

It follows that $P_{V_1}^{\mathcal{N}}\mathcal{A}_1^{-1}\phi^{\mathcal{N}} = \left(\mathcal{A}_1^{\mathcal{N}}\right)^{-1}\phi^{\mathcal{N}}$ and this completes the proof. ■

Lemma 3.5.3 $\left(\mathcal{A}_1^{\mathcal{N}}\right)^{-1}\tilde{\mathcal{A}}_2^{\mathcal{N}} \equiv P_{V_1}^{\mathcal{N}}\mathcal{A}_1^{-1}\tilde{\mathcal{A}}_2$ *on* $V^{\mathcal{N}}$, *where* $\tilde{\mathcal{A}}_2^{\mathcal{N}}$ *is the restriction of* $\tilde{\sigma}_2$ *on* $V^{\mathcal{N}}$, *i.e.,* $\tilde{\mathcal{A}}_2^{\mathcal{N}} : V^{\mathcal{N}} \to V^{\mathcal{N}}$ *is defined by*

$$\left\langle \tilde{\mathcal{A}}_2^{\mathcal{N}}\phi, \psi \right\rangle_H = \tilde{\sigma}_2(\phi, \psi) \quad \forall \phi, \psi \in V^{\mathcal{N}} . \tag{3.33}$$

Proof:

- Let $\phi^{\mathcal{N}} \in V^{\mathcal{N}}$. Then for all $\psi^{\mathcal{N}} \in V^{\mathcal{N}}$

$$\begin{aligned}
\sigma_1\left(\left(\mathcal{A}_1^{\mathcal{N}}\right)^{-1}\tilde{\mathcal{A}}_2^{\mathcal{N}}\phi^{\mathcal{N}}, \psi^{\mathcal{N}}\right) &= \left\langle \tilde{\mathcal{A}}_2^{\mathcal{N}}\phi^{\mathcal{N}}, \psi^{\mathcal{N}} \right\rangle_{V^*,V} \text{ (from Lemma 3.5.2,} \\
&\qquad \text{(3.32) and (3.6))} \\
&= \left\langle \tilde{\mathcal{A}}_2^{\mathcal{N}}\phi^{\mathcal{N}}, \psi^{\mathcal{N}} \right\rangle_H \text{ (since } \tilde{\mathcal{A}}_2^{\mathcal{N}}\phi^{\mathcal{N}} \in V^{\mathcal{N}}) \\
&= \tilde{\sigma}_2(\phi^{\mathcal{N}}, \psi^{\mathcal{N}}) \text{ (from (3.33))} \\
&= \left\langle \tilde{\mathcal{A}}_2\phi^{\mathcal{N}}, \psi^{\mathcal{N}} \right\rangle_{V^*,V} \text{ (from (3.30))} \\
&= \left\langle \mathcal{A}_1\mathcal{A}_1^{-1}\tilde{\mathcal{A}}_2\phi^{\mathcal{N}}, \psi^{\mathcal{N}} \right\rangle_{V^*,V} \\
&= \sigma_1\left(\mathcal{A}_1^{-1}\tilde{\mathcal{A}}_2\phi^{\mathcal{N}}, \psi^{\mathcal{N}}\right) \text{ (from (3.6))}
\end{aligned}$$

Therefore, $\sigma_1\left(\left(\mathcal{A}_1^{\mathcal{N}}\right)^{-1}\tilde{\mathcal{A}}_2^{\mathcal{N}}\phi^{\mathcal{N}} - \mathcal{A}_1^{-1}\tilde{\mathcal{A}}_2\phi^{\mathcal{N}}, \psi^{\mathcal{N}}\right) = 0$, $\forall \psi^{\mathcal{N}} \in V^{\mathcal{N}}$. We then conclude from (3.32) that $\left(\mathcal{A}_1^{\mathcal{N}}\right)^{-1}\tilde{\mathcal{A}}_2^{\mathcal{N}}\phi^{\mathcal{N}} = P_{V_1}^{\mathcal{N}}\mathcal{A}_1^{-1}\tilde{\mathcal{A}}_2\phi^{\mathcal{N}}$ $\forall \phi^{\mathcal{N}} \in V^{\mathcal{N}}$. ■

Lemma 3.5.4 $\left\|\mathcal{A}_1^{-1} - P_{V_1}^{\mathcal{N}}\mathcal{A}_1^{-1}\right\|_{\mathcal{L}(V,V)} \to 0$

Proof:

- First we consider $\mathcal{A}_1^{-1}$ as a compact operator from V to V by using the compact injections $i : V \hookrightarrow H$ and $i^* : H^* \hookrightarrow V^*$ and setting $\mathcal{A}_1^{-1} = \mathcal{A}_1^{-1} i^* i$. Next, note that the convergence $P_{V_1}^{\mathcal{N}} w \to Iw \ , \forall w \in V$ is evident from (H1N) where $P_{V_1}^{\mathcal{N}}$ is, as introduced above, the projection operator from V_1 onto $V^{\mathcal{N}}$ (again V_1 is V with the the norm induced by the $\sigma_1(\cdot,\cdot)$ inner product). Thus convergence follows from $\left|P_{V_1}^{\mathcal{N}} z - z\right|_{V_1} \leq \left|\tilde{z}^{\mathcal{N}} - z\right|_{V_1} \leq k \left|\tilde{z}^{\mathcal{N}} - z\right|_V$. Then

$$\begin{aligned}
\left\|\mathcal{A}_1^{-1} - P_{V_1}^{\mathcal{N}} \mathcal{A}_1^{-1}\right\|_{\mathcal{L}(V,V)} &= \sup_{\|v\|_V \leq 1} \left\| \left(\mathcal{A}_1^{-1} - P_{V_1}^{\mathcal{N}} \mathcal{A}_1^{-1}\right) v \right\|_V \\
&= \sup_{\|v\|_V \leq 1} \left\| (I - P_{V_1}^{\mathcal{N}}) \mathcal{A}_1^{-1} v \right\|_V \\
&= \sup_{w \in U} \left\| (I - P_{V_1}^{\mathcal{N}}) w \right\|_V
\end{aligned}$$

where $U = \mathcal{A}_1^{-1}\Big(\{\|v\|_V \leq 1\}\Big)$ is a relatively compact subset in V since $\mathcal{A}_1^{-1}$ is a compact operator from V to V. Thus, by Chatelin's Theorem[1],

$$\sup_{w \in U} \left\| (I - P_{V_1}^{\mathcal{N}}) w \right\|_V \to 0 \ .$$

This gives us the desired result

$$\left\|\mathcal{A}_1^{-1} - P_{V_1}^{\mathcal{N}} \mathcal{A}_1^{-1}\right\|_{\mathcal{L}(V,V)} \to 0 \ .$$

■

Lemma 3.5.5 $\left\|\mathcal{A}_1^{-1}\tilde{\mathcal{A}}_2 - P_{V_1}^{\mathcal{N}} \mathcal{A}_1^{-1}\tilde{\mathcal{A}}_2\right\|_{\mathcal{L}(V,V)} \to 0$ *where* $\mathcal{A}_1^{-1}\tilde{\mathcal{A}}_2$ *is compact on* V.

Proof:

- The proof of this lemma is similar to the proof given for the previous lemma. ■

[1]Theorem 3.2 in [20]: Suppose that $T_n x \to Tx, x \in X$. Then for any relatively compact set U, $\sup_{x \in U} \|(T_n - T)x\| \to 0$.

We now give the proof of Lemma 3.5.1.

Proof of Lemma 3.5.1:

- We first express the sesquilinear form σ in terms of components,

$$\sigma(\Phi, \Psi) = -\langle \phi_2, \psi_1 \rangle_{V_1} + \sigma_1(\phi_1, \psi_2) + \sigma_2(\phi_2, \psi_2) \ ,$$

then

$$\begin{aligned}
Re\sigma(\Phi, \Phi) &= Re\left\{ -\langle \phi_2, \phi_1 \rangle_{V_1} + \sigma_1(\phi_1, \phi_2) + \sigma_2(\phi_2, \phi_2) \right\} \\
&= Re\sigma_2(\phi_2, \phi_2) \ , \quad \text{since } \langle \cdot, \cdot \rangle_{V_1} \text{ is equivalent to } \sigma_1(\cdot, \cdot) \\
&= \gamma Re\sigma_1(\phi_2, \phi_2) + Re\tilde{\sigma}_2(\phi_2, \phi_2) \ , \quad \text{since} \\
&\qquad \sigma_2(\psi, \psi) = \gamma\sigma_1(\psi, \psi) + \tilde{\sigma}_2(\psi, \psi) \text{ for some } \gamma > 0 \\
&\geq \gamma c_2 \|\phi_2\|_V^2 - \frac{c_2}{2}\gamma\|\phi_2\|_V^2 - \mu\|\phi_2\|_H^2 \ , \quad \text{since} \\
&\qquad Re\sigma_1(\phi, \phi) \geq c_2\|\phi\|_V^2 \text{ (see (H2)), and} \\
&\qquad Re\tilde{\sigma}_2(\psi, \psi) \geq -\frac{c_2\gamma}{2}\|\psi\|_V^2 - \mu\|\psi\|_H^2 \\
&= \frac{c_2}{2}\gamma\|\phi_2\|_V^2 - \mu\|\phi_2\|_H^2 \\
&= \frac{c_2}{2}\gamma\|\phi_2\|_V^2 + \mu\|\phi_1\|_H^2 - \mu\left\{ \|\phi_2\|_H^2 + \|\phi_1\|_H^2 \right\} \\
&\geq \min\left\{ \frac{\gamma c_2}{2}, \mu \right\} \|\Phi\|_V^2 - \mu \|\Phi\|_H^2 \ .
\end{aligned}$$

It follows that the linear operator $\mathcal{A}$ associated with σ (see (3.13)) is the infinitesimal generator of a C_0 semigroup $\mathcal{T}(t)$ satisfying

$$\|\mathcal{T}(t)\|_{\mathcal{L}(\mathcal{H})} \leq Me^{\mu t} \ , \tag{3.34}$$

and thus (3.31) holds with $\nu = \mu$. Now suppose (3.31) holds for any $\nu \geq \mu$, i.e., suppose $\|\mathcal{T}(t)\|_{\mathcal{L}(\mathcal{H})} \leq Me^{\nu t}$ is satisfied. To prove the lemma, we show $\forall \varepsilon > 0$, there exists N_ε such that for $N \geq N_\varepsilon$

$$\left\| \mathcal{T}^{2\mathcal{N}}(t)\mathcal{P}^{2\mathcal{N}} \right\|_{\mathcal{L}(\mathcal{H})} \leq \tilde{M}e^{(\nu+\varepsilon)t} \ , \quad t \geq 0 \ . \tag{3.35}$$

The next step involves writing the semigroup $\mathcal{T}(t)$ in terms of the generator $\mathcal{A}$ using the inverse of the Laplace transform. From the result above that $\mathcal{A}$ is the infinitesimal generator of a C_0 semigroup satisfying (3.31), it follows that $\mathcal{A} - \nu I$ generates a C_0 semigroup of contractions $\mathcal{S}(t)$ satisfying $\|\mathcal{S}(t)\|_{\mathcal{L}(\mathcal{H})} \leq M$, where $\mathcal{T}(t) = \mathcal{S}(t)e^{\nu t}$. Theorem 6.A in [48] guarantees the existence of δ such that $0 < \delta < \pi/4$ and

$$\rho(\mathcal{A} - \nu I) \supset \Sigma_\delta = \{z \in \mathbb{C} : |\arg(z)| < \pi/2 + \delta\} \ .$$

By Theorem 7.7 in [43], we can express $\mathcal{S}(t)$ as

$$\begin{aligned} \mathcal{S}(t) &= \frac{1}{2\pi i}\int_\Gamma e^{\lambda t}(\lambda I - (\mathcal{A} - \nu I))^{-1}d\lambda \\ &= \frac{1}{2\pi i}\int_\Gamma e^{\lambda t}((\lambda + \nu)I - \mathcal{A})^{-1}d\lambda \ , \end{aligned}$$

where Γ is a smooth curve in $\Sigma_\delta \cup \{0\}$ running from $\infty e^{-i\vartheta}$ to $\infty e^{i\vartheta}$ for $\pi/2 < \vartheta < \pi/2 + \delta$. Since $\mathcal{T}(t) = e^{\nu t}\mathcal{S}(t)$, we have

$$\mathcal{T}(t) = \frac{1}{2\pi i}\int_\Gamma e^{\nu t}e^{\lambda t}((\lambda + \nu)I - \mathcal{A})^{-1}d\lambda \ .$$

Shifting the path of integration Γ by ν and denoting it by Γ' yields

$$\mathcal{T}(t) = \frac{1}{2\pi i}\int_{\Gamma'} e^{\lambda t}(\lambda I - \mathcal{A})^{-1}d\lambda \ . \tag{3.36}$$

The finite dimensional semigroup can similarly be written as

$$\mathcal{T}^{2\mathcal{N}}(t) = \frac{1}{2\pi i}\int_{\Gamma'} e^{\lambda t}\left(\lambda I - \mathcal{A}^{2\mathcal{N}}\right)^{-1} d\lambda \ .$$

Multiplying by $\mathcal{P}^{2\mathcal{N}}$ and obtaining the norm of both sides yields

$$\left\|\mathcal{T}^{2\mathcal{N}}(t)\mathcal{P}^{2\mathcal{N}}\right\|_{\mathcal{L}(\mathcal{H})} \leq \left|\frac{1}{2\pi i}\right| \int_{\Gamma'} \left|e^{\lambda t}\right| \left\|\left(\lambda I - \mathcal{A}^{2\mathcal{N}}\right)^{-1}\mathcal{P}^{2\mathcal{N}}\right\|_{\mathcal{L}(\mathcal{H})} |d\lambda| \ .$$

Thus, if we find M_0 and N_ε such that whenever $Re\lambda \geq \nu + \varepsilon$ and $N \geq N_\varepsilon$, $\left\|\left(\lambda I - \mathcal{A}^{2\mathcal{N}}\right)^{-1}\mathcal{P}^{\mathcal{N}}\right\|_{\mathcal{L}(\mathcal{H})} \leq M_0$, then we establish (3.35). This uniform

boundedness will be shown by decomposing the resolvent $\left(\lambda I - \mathcal{A}^{2\mathcal{N}}\right)^{-1}$ into its components. To this end, consider the resolvent equation

$$\left(\lambda I - \mathcal{A}^{2\mathcal{N}}\right)^{-1} \mathcal{P}^{2\mathcal{N}} \begin{pmatrix} f \\ g \end{pmatrix} = \begin{pmatrix} z_1^{\mathcal{N}} \\ z_2^{\mathcal{N}} \end{pmatrix} ,$$

where $(f, g) \in \mathcal{H}$ and $(z_1^{\mathcal{N}}, z_2^{\mathcal{N}}) \in \mathcal{V}^{2\mathcal{N}}$. Using the components of $\mathcal{A}$ given in (3.25), and letting $\mathcal{P}^{2\mathcal{N}}(f, g) = (f^{\mathcal{N}}, g^{\mathcal{N}})$, we obtain

$$\begin{aligned} f^{\mathcal{N}} &= \lambda z_1^{\mathcal{N}} - z_2^{\mathcal{N}} \\ g^{\mathcal{N}} &= \lambda z_2^{\mathcal{N}} + \mathcal{A}_1^{\mathcal{N}} z_2^{\mathcal{N}} + \mathcal{A}_1^{\mathcal{N}} z_1^{\mathcal{N}}. \end{aligned}$$

Eliminating $z_2^{\mathcal{N}}$ in the system of equations above and using the assumption $\mathcal{A}_2 = \gamma \mathcal{A}_1 + \tilde{\mathcal{A}}_2$ yields

$$\begin{aligned} &\left(I + \frac{\lambda^2}{\lambda\gamma + 1} (\mathcal{A}_1^{\mathcal{N}})^{-1} + \frac{\lambda}{\lambda\gamma + 1} (\mathcal{A}_1^{\mathcal{N}})^{-1} \tilde{\mathcal{A}}_2^{\mathcal{N}} \right) z_1^{\mathcal{N}} = \\ &\frac{\gamma f^{\mathcal{N}}}{\lambda\gamma + 1} + \frac{(\mathcal{A}_1^{\mathcal{N}})^{-1}}{\lambda\gamma + 1} \left(g^{\mathcal{N}} + \lambda f^{\mathcal{N}} + \tilde{\mathcal{A}}_2^{\mathcal{N}} f^{\mathcal{N}} \right) . \end{aligned} \tag{3.37}$$

To simplify notation, let

$$G = I + \frac{\lambda^2}{\lambda\gamma + 1} \mathcal{A}_1^{-1} + \frac{\lambda}{\lambda\gamma + 1} \mathcal{A}_1^{-1} \tilde{\mathcal{A}}_2 \in \mathcal{L}(V, V) ,$$

and

$$\xi = \frac{\gamma f}{\lambda\gamma + 1} + \frac{(\mathcal{A}_1)^{-1}}{\lambda\gamma + 1} \left(g + \lambda f + \tilde{\mathcal{A}}_2 f \right) \in V ,$$

and denote the corresponding finite dimensional expressions by $G^{\mathcal{N}}$ and $\xi^{\mathcal{N}}$, respectively. If we show that $\|z_1^{\mathcal{N}}\|_V$ is bounded, then (3.35) is satisfied where $z_1^{\mathcal{N}}$ is given by $G^{\mathcal{N}} z_1^{\mathcal{N}} = \xi^{\mathcal{N}}$, for $\|(f, g)\|_{\mathcal{H}} \leq 1$, $Re\lambda \geq \nu + \varepsilon$ and $\mathcal{N} \geq \mathcal{N}_\varepsilon$. The next step is then to show that the inverse of G exists and is bounded in $\mathcal{L}(V, V)$ whenever $Re\lambda > \nu$. Since $(\lambda I - \mathcal{A})^{-1}$ exists and is bounded in $\mathcal{L}(\mathcal{H}, \mathcal{H})$ whenever $Re\lambda > \nu$, then for every $(f, g) \in \mathcal{H}$, we can solve for $(z_1, z_2) \in \mathcal{H}$ such that

$$(\lambda I - \mathcal{A}) \begin{pmatrix} z_1 \\ z_2 \end{pmatrix} = \begin{pmatrix} f \\ g \end{pmatrix} .$$

Solving for z_1 yields

$$z_1 = \left(I + \frac{\lambda}{\lambda\gamma+1}\mathcal{A}_1^{-1}(\lambda + \tilde{\mathcal{A}}_2)\right)^{-1}\left(\frac{\gamma f}{\lambda\gamma+1} + \frac{\mathcal{A}_1^{-1}}{\lambda\gamma+1}\left(g + \lambda f + \tilde{\mathcal{A}}_2 f\right)\right)$$

and $\|z_1\|_V \leq M_1$ whenever $\|(f,g)\|_{\mathcal{H}} \leq 1$. Thus, G^{-1} exists and is bounded in $\mathcal{L}(V,V)$ whenever $Re\lambda > \nu$. Now, we consider the finite dimensional operators and show boundedness of $\|z_1^{\mathcal{N}}\|_V$. Note first that $G^{\mathcal{N}} z_1^{\mathcal{N}}$ can be expressed as

$$\begin{aligned} G^{\mathcal{N}} z_1^{\mathcal{N}} &= \left(I + \frac{\lambda^2}{\lambda\gamma+1}(\mathcal{A}_1^{\mathcal{N}})^{-1} + \frac{\lambda}{\lambda\gamma+1}(\mathcal{A}_1^{\mathcal{N}})^{-1}\tilde{\mathcal{A}}_2^{\mathcal{N}}\right) z_1^{\mathcal{N}} \\ &= \left(I + \frac{\lambda^2}{\lambda\gamma+1}\mathcal{A}_1^{-1} + \frac{\lambda}{\lambda\gamma+1}\mathcal{A}_1^{-1}\tilde{\mathcal{A}}_2\right) z_1^{\mathcal{N}} \\ &\quad -\frac{\lambda^2}{\lambda\gamma+1}\left(\mathcal{A}_1^{-1} - (\mathcal{A}_1^{\mathcal{N}})^{-1}\right) z_1^{\mathcal{N}} \\ &\quad -\frac{\lambda}{\lambda\gamma+1}\left(\mathcal{A}_1^{-1}\tilde{\mathcal{A}}_2 - (\mathcal{A}_1^{\mathcal{N}})^{-1}\tilde{\mathcal{A}}_2^{\mathcal{N}}\right) z_1^{\mathcal{N}} \ . \end{aligned}$$

Since $G^{\mathcal{N}} z_1^{\mathcal{N}} = \xi^{\mathcal{N}}$, we have

$$\xi^{\mathcal{N}} = G z_1^{\mathcal{N}} - \frac{\lambda^2}{\lambda\gamma+1}\left(\mathcal{A}_1^{-1} - (\mathcal{A}_1^{\mathcal{N}})^{-1}\right) z_1^{\mathcal{N}} - \frac{\lambda}{\lambda\gamma+1}\left(\mathcal{A}_1^{-1}\tilde{\mathcal{A}}_2 - (\mathcal{A}_1^{\mathcal{N}})^{-1}\tilde{\mathcal{A}}_2^{\mathcal{N}}\right) z_1^{\mathcal{N}} .$$

Equivalently,

$$\begin{aligned} z_1^{\mathcal{N}} &= G^{-1}\left\{\xi^{\mathcal{N}} + \frac{\lambda^2}{\lambda\gamma+1}\left(\mathcal{A}_1^{-1} - (\mathcal{A}_1^{\mathcal{N}})^{-1}\right) z_1^{\mathcal{N}}\right. \\ &\quad + \left.\frac{\lambda}{\lambda\gamma+1}\left(\mathcal{A}_1^{-1}\tilde{\mathcal{A}}_2 - (\mathcal{A}_1^{\mathcal{N}})^{-1}\tilde{\mathcal{A}}_2^{\mathcal{N}}\right) z_1^{\mathcal{N}}\right\} \ . \end{aligned}$$

Taking the V norm of both sides and using Lemma 3.5.2 and Lemma 3.5.3, we obtain

$$\begin{aligned} \|z_1^{\mathcal{N}}\|_V \leq \|G^{-1}\|_{\mathcal{L}(V,V)} \Bigg(&\|\xi^{\mathcal{N}}\|_V + \left|\frac{\lambda^2}{\lambda\gamma+1}\right| \left\|\mathcal{A}_1^{-1} - P_{V_1}^{\mathcal{N}}\mathcal{A}_1^{-1}\right\|_{\mathcal{L}(V,V)} \left\|z_1^{\mathcal{N}}\right\|_V \\ &+ \left|\frac{\lambda}{\lambda\gamma+1}\right| \left\|(\mathcal{A}_1^{-1}\tilde{\mathcal{A}}_2 - P_{V_1}^{\mathcal{N}}\mathcal{A}_1^{-1}\tilde{\mathcal{A}}_2)\right\|_{\mathcal{L}(V,V)} \left\|z_1^{\mathcal{N}}\right\|_V \Bigg) . \end{aligned}$$

From the convergences in Lemma 3.5.4 and Lemma 3.5.5, it can be seen that $\|z_1^{\mathcal{N}}\|_V$ is bounded and this completes the proof. ■

Periodic Exogenous Input:

Here the finite dimensional control problem for a system excited by a periodic exogenous force $g^{2\mathcal{N}}(t) = \mathcal{P}^{2\mathcal{N}} g(t)$, $g \in L^2(0,\tau;\mathcal{H})$ is given by: Find $\bar{U}$ minimizing the cost functional

$$J(U, z_0^{\mathcal{N}}) = \frac{1}{2}\int_0^\tau \left\{ \left\| \mathcal{C}^{2\mathcal{N}} z^{2\mathcal{N}}(t) \right\|_{\mathcal{Y}}^2 + \left\| \mathcal{R}^{1/2} U(t) \right\|_{\mathcal{U}}^2 \right\} dt \tag{3.38}$$

subject to

$$\begin{aligned} \dot{z}^{2\mathcal{N}}(t) &= \mathcal{A}^{2\mathcal{N}} z^{2\mathcal{N}}(t) + \mathcal{B}^{2\mathcal{N}} z^{2\mathcal{N}}(t) + g^{2\mathcal{N}}(t) \\ z^{2\mathcal{N}}(0) &= z^{2\mathcal{N}}(\tau) \ . \end{aligned} \tag{3.39}$$

The existence of finite dimensional approximating Riccati solutions $\Pi^{2\mathcal{N}}$ is guaranteed by Theorem 3.5.1. If r is the τ-periodic solution of the adjoint or tracking equation

$$\begin{aligned} \dot{r}^{2\mathcal{N}}(t) &= -\left[\mathcal{A}^{2\mathcal{N}} - \mathcal{B}^{2\mathcal{N}} \mathcal{R}^{-1} \left(\mathcal{B}^{2\mathcal{N}}\right)^* \Pi^{2\mathcal{N}}\right]^* r^{2\mathcal{N}}(t) + \Pi^{2\mathcal{N}} g^{2\mathcal{N}}(t) \\ r^{2\mathcal{N}}(0) &= r^{2\mathcal{N}}(\tau) \ , \end{aligned} \tag{3.40}$$

and $\bar{z}^{2\mathcal{N}}$ is the closed loop solution of

$$\begin{aligned} \dot{\bar{z}}(t) &= \left[\mathcal{A}^{2\mathcal{N}} - \mathcal{B}^{2\mathcal{N}} \mathcal{R}^{-1} \left(\mathcal{B}^{2\mathcal{N}}\right)^* \Pi^{2\mathcal{N}}\right] \bar{z}^{2\mathcal{N}}(t) - \mathcal{B}^{2\mathcal{N}} \mathcal{R}^{-1} \left(\mathcal{B}^{2\mathcal{N}}\right)^* r^{2\mathcal{N}}(t) + g^{2\mathcal{N}}(t) \\ \bar{z}^{2\mathcal{N}}(0) &= \bar{z}^{2\mathcal{N}}(\tau) \ , \end{aligned} \tag{3.41}$$

then the optimal control is given by

$$\bar{U}(t) = -\mathcal{R}^{-1} \left(\mathcal{B}^{2\mathcal{N}}\right)^* \left[\Pi^{2\mathcal{N}} \bar{z}^{2\mathcal{N}}(t) - r^{2\mathcal{N}}(t)\right] \ . \tag{3.42}$$

Chapter 4

Approximation Methods

In order to pose the previously described systems in a form that can be solved through computational means, we restrict the solution space to finite dimensional subspaces. It has been shown in Section 3.4 that if the chosen finite dimensional approximating subspaces satisfy (H1N), the resulting numerical solutions converge to the infinite dimensional solution as the dimension of the finite dimensional subspace becomes unbounded.

In this chapter, we describe the Galerkin methods employed to numerically approximate the system (2.7). The convergence, accuracy and efficiency of the methods depend heavily on the type of basis elements used in creating the finite dimensional system. As we shall see, standard basis functions such as cubic or linear splines result in large dimensional systems requiring intensive computations and thus are not suitable for real-time implementation. To address the issue, we investigate two reduced basis methods, the Lagrange and proper orthogonal decomposition methods, which give a 97% reduction in the dimension of the finite dimensional system. Numerical results illustrating the features of the methods are presented in Chapter 5.

The general approximation strategy can be summarized as follows. We approximate the solution $y = (u, v, w)$ by restricting the state space to a finite dimensional subset $V^{\mathcal{N}} \subset V \subset H$. The $\mathcal{N}$-dimensional subspace $V^{\mathcal{N}}$ is then formed by choosing

basis functions $\{\mathcal{B}_{u_i}\}_{i=1}^{\mathcal{N}_u}$, $\{\mathcal{B}_{v_i}\}_{i=1}^{\mathcal{N}_v}$ and $\{\mathcal{B}_{w_i}\}_{i=1}^{\mathcal{N}_w}$ and setting

$$V^{\mathcal{N}} = \text{span}\{\mathcal{B}_{u_i}\}_{i=1}^{\mathcal{N}_u} \times \text{span}\{\mathcal{B}_{v_i}\}_{i=1}^{\mathcal{N}_v} \times \text{span}\{\mathcal{B}_{w_i}\}_{i=1}^{\mathcal{N}_w} \ , \tag{4.1}$$

where $\mathcal{N} = \mathcal{N}_u + \mathcal{N}_v + \mathcal{N}_w$. Basis functions will be chosen according to rate of convergence, flexibility to different boundary conditions, smoothness, accuracy, and dimension of the finite dimensional system. Finally, we form the Galerkin expansions

$$y^{\mathcal{N}}(t,x,\theta) = \begin{bmatrix} u^{\mathcal{N}}(t,x,\theta) \\ v^{\mathcal{N}}(t,x,\theta) \\ w^{\mathcal{N}}(t,x,\theta) \end{bmatrix} = \begin{bmatrix} \sum_{i=1}^{\mathcal{N}_u} u_i(t)\mathcal{B}_{u_i}(x,\theta) \\ \sum_{i=1}^{\mathcal{N}_v} v_i(t)\mathcal{B}_{v_i}(x,\theta) \\ \sum_{i=1}^{\mathcal{N}_w} w_i(t)\mathcal{B}_{w_i}(x,\theta) \end{bmatrix} , \tag{4.2}$$

and the approximating system is determined by restricting the weak form (2.7) to $V^{\mathcal{N}}$ with basis functions used as test functions. This is equivalent to orthogonalizing the residual with respect to elements from $V^{\mathcal{N}}$.

Details regarding the creation of matrix components for the longitudinal displacement are summarized below. Creation of submatrices for the other two directions v and w is described in Appendix C. The matrix system is created by first substituting the force and moment resultants into the weak form (2.7). Then, the displacements u, v and w are approximated by $u^{\mathcal{N}}$, $v^{\mathcal{N}}$ and $w^{\mathcal{N}}$, respectively, and the j^{th} basis function $\mathcal{B}_{u_j}$ is substituted to the test function η_1 in (2.7). The resulting weak form of the first equation in (2.7) *without* damping contributions is given below.

$$\begin{aligned}
& \int_{\Gamma_0} \rho_s h R \frac{\partial^2 u^{\mathcal{N}}}{\partial t^2} \mathcal{B}_{u_j} d\gamma \\
+ \ & \sum_{i=1}^{s} \int_{\Gamma_{pe_{1i}}} \rho_{pe_{1i}} h_{pe_{1i}} R \frac{\partial^2 u^{\mathcal{N}}}{\partial t^2} \mathcal{B}_{u_j} d\gamma + \sum_{i=1}^{s} \int_{\Gamma_{pe_{2i}}} \rho_{pe_{2i}} h_{pe_{2i}} R \frac{\partial^2 u^{\mathcal{N}}}{\partial t^2} \mathcal{B}_{u_j} d\gamma \\
+ \ & \int_{\Gamma_0} \frac{EhR}{(1-\nu^2)} \left[\frac{\partial u^{\mathcal{N}}}{\partial x} + \nu \left(\frac{1}{R} \frac{\partial v^{\mathcal{N}}}{\partial \theta} + \frac{w^{\mathcal{N}}}{R} \right) \right] \frac{\partial \mathcal{B}_{u_j}}{\partial x} d\gamma \\
+ \ & \sum_{i=1}^{s} \int_{\Gamma_{pe_{1i}}} \frac{E_{pe_{1i}} R}{(1-\nu_{pe_{1i}}^2)} \left[h_{pe_{1i}} \left(\frac{\partial u^{\mathcal{N}}}{\partial x} + \nu_{pe_{1i}} \left(\frac{1}{R} \frac{\partial v^{\mathcal{N}}}{\partial \theta} + \frac{w^{\mathcal{N}}}{R} \right) \right) \right.
\end{aligned}$$

$$
\begin{aligned}
& - \frac{a_{2_{1i}}}{2}\left(\frac{\partial^2 w^{\mathcal{N}}}{\partial x^2} + \frac{\nu_{pe_{1i}}}{R^2}\frac{\partial^2 w^{\mathcal{N}}}{\partial \theta^2}\right)\Bigg] \frac{\partial \mathcal{B}_{u_j}}{\partial x} d\gamma \\
+ & \sum_{i=1}^{s} \int_{\Gamma_{pe_{2i}}} \frac{E_{pe_{2i}} R}{(1-\nu_{pe_{2i}}^2)} \Bigg[h_{pe_{2i}} \left(\frac{\partial u^{\mathcal{N}}}{\partial x} + \nu_{pe_{2i}}\left(\frac{1}{R}\frac{\partial v^{\mathcal{N}}}{\partial \theta} + \frac{w^{\mathcal{N}}}{R}\right)\right) \\
& + \frac{a_{2_{2i}}}{2}\left(\frac{\partial^2 w^{\mathcal{N}}}{\partial x^2} + \frac{\nu_{pe_{2i}}}{R^2}\frac{\partial^2 w^{\mathcal{N}}}{\partial \theta^2}\right)\Bigg] \frac{\partial \mathcal{B}_{u_j}}{\partial x} d\gamma \qquad (4.3) \\
+ & \int_{\Gamma_0} \frac{Eh}{2(1+\nu)} \left[\frac{\partial v^{\mathcal{N}}}{\partial x} + \frac{1}{R}\frac{\partial u^{\mathcal{N}}}{\partial \theta}\right] \frac{\partial \mathcal{B}_{u_j}}{\partial \theta} d\gamma \\
+ & \sum_{i=1}^{s} \int_{\Gamma_{pe_{1i}}} E_{pe_{1i}} \Bigg[\frac{h_{pe_{1i}}}{2(1+\nu_{pe_{1i}})} \left(\frac{\partial v^{\mathcal{N}}}{\partial x} + \frac{1}{R}\frac{\partial u^{\mathcal{N}}}{\partial \theta}\right) \\
& - \frac{a_{2_{1i}}}{2R(1+\nu_{pe_{1i}})} \frac{\partial^2 w^{\mathcal{N}}}{\partial x \partial \theta}\Bigg] \frac{\partial \mathcal{B}_{u_j}}{\partial \theta} d\gamma \\
+ & \sum_{i=1}^{s} \int_{\Gamma_{pe_{2i}}} E_{pe_{2i}} \Bigg[\frac{h_{pe_{2i}}}{2(1+\nu_{pe_{2i}})} \left(\frac{\partial v^{\mathcal{N}}}{\partial x} + \frac{1}{R}\frac{\partial u^{\mathcal{N}}}{\partial \theta}\right) \\
& + \frac{a_{2_{2i}}}{2R(1+\nu_{pe_{2i}})} \frac{\partial^2 w^{\mathcal{N}}}{\partial x \partial \theta}\Bigg] \frac{\partial \mathcal{B}_{u_j}}{\partial \theta} d\gamma \\
= & \int_{\Gamma_0} q_x \mathcal{B}_{u_j} R d\gamma + R\sum_{i=1}^{s} \int_{\Gamma_{pe_{1i}}} (N_x)_{pe_{1i}} \frac{\partial \mathcal{B}_{u_j}}{\partial x} d\gamma + R\sum_{i=1}^{s} \int_{\Gamma_{pe_{2i}}} (N_x)_{pe_{2i}} \frac{\partial \mathcal{B}_{u_j}}{\partial x} d\gamma \ ,
\end{aligned}
$$

where $\Gamma_{pe_{1i}}$ and $\Gamma_{pe_{2i}}$ are the regions covered by the i^{th} outer and inner patches, respectively. To complete the expression above with damping, more terms are created by replacing the stiffness constants E, E_{pe1i} or E_{pe2i} with c_D, $c_{D_{pe1i}}$ or $c_{D_{pe2i}}$, respectively, and replacing the approximations $u^{\mathcal{N}}, v^{\mathcal{N}}, w^{\mathcal{N}}$ with $\dot{u}^{\mathcal{N}}, \dot{v}^{\mathcal{N}}, \dot{w}^{\mathcal{N}}$, respectively. We also point out that if passive contributions are dropped, terms with summations are neglected.

Each term in the equation above gives rise to a component matrix of the finite dimensional system. By letting the basis elements $\mathcal{B}_{u_j}$ range from $j = 1, \ldots, \mathcal{N}_u$, the component matrices are created in the manner below. Note that the superscripts in the matrix element definitions below indicate the size of the resulting matrix, and was given to simplify notation.

1. $$[U_M]_{l,k}^{\mathcal{N}_u\times\mathcal{N}_u} = \int_0^{2\pi}\int_0^{\ell} \rho h R \mathcal{B}_{u_k}(x,\theta)\mathcal{B}_{u_l}(x,\theta)dxd\theta + \sum_{i=1}^{s}\int_{\theta_{1_{1i}}}^{\theta_{2_{1i}}}\int_{x_{1_{1i}}}^{x_{2_{1i}}} \rho_{pe_{1i}} h_{pe_{1i}} R\mathcal{B}_{u_k}(x,\theta)\mathcal{B}_{u_l}(x,\theta)dxd\theta + \sum_{i=1}^{s}\int_{\theta_{1_{2i}}}^{\theta_{2_{2i}}}\int_{x_{1_{2i}}}^{x_{2_{2i}}} \rho_{pe_{2i}} h_{pe_{2i}} R\mathcal{B}_{u_k}(x,\theta)\mathcal{B}_{u_l}(x,\theta)dxd\theta$$

2. $$[U_{11}]_{l,k}^{\mathcal{N}_u\times\mathcal{N}_u} = \int_0^{2\pi}\int_0^{\ell} \frac{EhR}{1-\nu^2}\frac{\partial}{\partial x}\mathcal{B}_{u_k}(x,\theta)\frac{\partial}{\partial x}\mathcal{B}_{u_l}(x,\theta)dxd\theta$$

3. $$[V_{11}]_{l,k}^{\mathcal{N}_u\times\mathcal{N}_v} = \int_0^{2\pi}\int_0^{\ell} \frac{Eh\nu}{1-\nu^2}\frac{\partial}{\partial \theta}\mathcal{B}_{v_k}(x,\theta)\frac{\partial}{\partial x}\mathcal{B}_{u_l}(x,\theta)dxd\theta$$

4. $$[W_{11}]_{l,k}^{\mathcal{N}_u\times\mathcal{N}_w} = \int_0^{2\pi}\int_0^{\ell} \frac{Eh\nu}{1-\nu^2}\mathcal{B}_{w_k}(x,\theta)\frac{\partial}{\partial x}\mathcal{B}_{u_l}(x,\theta)dxd\theta$$

5. $$[V_{12}]_{l,k}^{\mathcal{N}_u\times\mathcal{N}_v} = \int_0^{2\pi}\int_0^{\ell} \frac{Eh}{2(1+\nu)}\frac{\partial}{\partial x}\mathcal{B}_{v_k}(x,\theta)\frac{\partial}{\partial \theta}\mathcal{B}_{u_l}(x,\theta)dxd\theta$$

6. $$[U_{12}]_{l,k}^{\mathcal{N}_u\times\mathcal{N}_u} = \int_0^{2\pi}\int_0^{\ell} \frac{Eh}{2R(1+\nu)}\frac{\partial}{\partial \theta}\mathcal{B}_{u_k}(x,\theta)\frac{\partial}{\partial \theta}\mathcal{B}_{u_l}(x,\theta)dxd\theta$$

7. $$[U_{13}]_{l,k}^{\mathcal{N}_u\times\mathcal{N}_u} = \sum_{i=1}^{s}\int_{\theta_{1_{1i}}}^{\theta_{2_{1i}}}\int_{x_{1_{1i}}}^{x_{2_{1i}}} \frac{E_{pe_{1i}}h_{pe_{1i}}R}{1-\nu_{pe_{1i}}^2}\frac{\partial}{\partial x}\mathcal{B}_{u_k}(x,\theta)\frac{\partial}{\partial x}\mathcal{B}_{u_l}(x,\theta)dxd\theta$$

8. $$[V_{13}]_{l,k}^{\mathcal{N}_u\times\mathcal{N}_v} = \sum_{i=1}^{s}\int_{\theta_{1_{1i}}}^{\theta_{2_{1i}}}\int_{x_{1_{1i}}}^{x_{2_{1i}}} \frac{E_{pe_{1i}}h_{pe_{1i}}\nu_{pe_{1i}}}{1-\nu_{pe_{1i}}^2}\frac{\partial}{\partial \theta}\mathcal{B}_{v_k}(x,\theta)\frac{\partial}{\partial x}\mathcal{B}_{u_l}(x,\theta)dxd\theta$$

9. $$[W_{12}]_{l,k}^{\mathcal{N}_u\times\mathcal{N}_w} = \sum_{i=1}^{s}\int_{\theta_{1_{1i}}}^{\theta_{2_{1i}}}\int_{x_{1_{1i}}}^{x_{2_{1i}}} \frac{E_{pe_{1i}}h_{pe_{1i}}\nu_{pe_{1i}}}{1-\nu_{pe_{1i}}^2}\mathcal{B}_{w_k}(x,\theta)\frac{\partial}{\partial x}\mathcal{B}_{u_l}(x,\theta)dxd\theta$$

10. $$[W_{13}]_{l,k}^{\mathcal{N}_u\times\mathcal{N}_w} = -\sum_{i=1}^{s}\int_{\theta_{1_{1i}}}^{\theta_{2_{1i}}}\int_{x_{1_{1i}}}^{x_{2_{1i}}} \frac{E_{pe_{1i}}Ra_{2_{1i}}}{2(1-\nu_{pe_{1i}}^2)}\frac{\partial^2}{\partial x^2}\mathcal{B}_{w_k}(x,\theta)\frac{\partial}{\partial x}\mathcal{B}_{u_l}(x,\theta)dxd\theta$$

11. $$[W_{14}]_{l,k}^{\mathcal{N}_u\times\mathcal{N}_w} = -\sum_{i=1}^{s}\int_{\theta_{1_{1i}}}^{\theta_{2_{1i}}}\int_{x_{1_{1i}}}^{x_{2_{1i}}} \frac{E_{pe_{1i}}\nu_{pe_{1i}}a_{2_{1i}}}{2R(1-\nu_{pe_{1i}}^2)}\frac{\partial^2}{\partial \theta^2}\mathcal{B}_{w_k}(x,\theta)\frac{\partial}{\partial x}\mathcal{B}_{u_l}(x,\theta)dxd\theta$$

12. $$[U_{14}]_{l,k}^{\mathcal{N}_u\times\mathcal{N}_u} = \sum_{i=1}^{s}\int_{\theta_{1_{2i}}}^{\theta_{2_{2i}}}\int_{x_{1_{2i}}}^{x_{2_{2i}}} \frac{E_{pe_{2i}}h_{pe_{2i}}R}{1-\nu_{pe_{2i}}^2}\frac{\partial}{\partial x}\mathcal{B}_{u_k}(x,\theta)\frac{\partial}{\partial x}\mathcal{B}_{u_l}(x,\theta)dxd\theta$$

13. $$[V_{14}]_{l,k}^{\mathcal{N}_u\times\mathcal{N}_v} = \sum_{i=1}^{s}\int_{\theta_{1_{2i}}}^{\theta_{2_{2i}}}\int_{x_{1_{2i}}}^{x_{2_{2i}}} \frac{E_{pe_{2i}}h_{pe_{2i}}\nu_{pe_{2i}}}{1-\nu_{pe_{2i}}^2}\frac{\partial}{\partial \theta}\mathcal{B}_{v_k}(x,\theta)\frac{\partial}{\partial x}\mathcal{B}_{u_l}(x,\theta)dxd\theta$$

14. $$[W_{15}]_{l,k}^{\mathcal{N}_u\times\mathcal{N}_w} = \sum_{i=1}^{s}\int_{\theta_{1_{2i}}}^{\theta_{2_{2i}}}\int_{x_{1_{2i}}}^{x_{2_{2i}}} \frac{E_{pe_{2i}}h_{pe_{2i}}\nu_{pe_{2i}}}{1-\nu_{pe_{2i}}^2}\mathcal{B}_{w_k}(x,\theta)\frac{\partial}{\partial x}\mathcal{B}_{u_l}(x,\theta)dxd\theta$$

15. $$[W_{16}]_{l,k}^{\mathcal{N}_u\times\mathcal{N}_w} = \sum_{i=1}^{s}\int_{\theta_{1_{2i}}}^{\theta_{2_{2i}}}\int_{x_{1_{2i}}}^{x_{2_{2i}}} \frac{E_{pe_{2i}}Ra_{2_{2i}}}{2(1-\nu_{pe_{2i}}^2)}\frac{\partial^2}{\partial x^2}\mathcal{B}_{w_k}(x,\theta)\frac{\partial}{\partial x}\mathcal{B}_{u_l}(x,\theta)dxd\theta$$

16. $$[W_{17}]_{l,k}^{\mathcal{N}_u\times\mathcal{N}_w} = \sum_{i=1}^{s}\int_{\theta_{1_{2i}}}^{\theta_{2_{2i}}}\int_{x_{1_{2i}}}^{x_{2_{2i}}} \frac{E_{pe_{2i}}\nu_{pe_{2i}}a_{2_{2i}}}{2R(1-\nu_{pe_{2i}}^2)}\frac{\partial^2}{\partial\theta^2}\mathcal{B}_{w_k}(x,\theta)\frac{\partial}{\partial x}\mathcal{B}_{u_l}(x,\theta)dxd\theta$$

17. $$[V_{15}]_{l,k}^{\mathcal{N}_u\times\mathcal{N}_v} = \sum_{i=1}^{s}\int_{\theta_{1_{1i}}}^{\theta_{2_{1i}}}\int_{x_{1_{1i}}}^{x_{2_{1i}}} \frac{E_{pe_{1i}}h_{pe_{1i}}}{2(1+\nu_{pe_{1i}})}\frac{\partial}{\partial x}\mathcal{B}_{v_k}(x,\theta)\frac{\partial}{\partial\theta}\mathcal{B}_{u_l}(x,\theta)dxd\theta$$

18. $$[U_{15}]_{l,k}^{\mathcal{N}_u\times\mathcal{N}_u} = \sum_{i=1}^{s}\int_{\theta_{1_{1i}}}^{\theta_{2_{1i}}}\int_{x_{1_{1i}}}^{x_{2_{1i}}} \frac{E_{pe_{1i}}h_{pe_{1i}}}{2R(1+\nu_{pe_{1i}})}\frac{\partial}{\partial\theta}\mathcal{B}_{u_k}(x,\theta)\frac{\partial}{\partial\theta}\mathcal{B}_{u_l}(x,\theta)dxd\theta$$

19. $$[W_{18}]_{l,k}^{\mathcal{N}_u\times\mathcal{N}_w} = -\sum_{i=1}^{s}\int_{\theta_{1_{1i}}}^{\theta_{2_{1i}}}\int_{x_{1_{1i}}}^{x_{2_{1i}}} \frac{E_{pe_{1i}}a_{2_{1i}}}{2R(1+\nu_{pe_{1i}})}\frac{\partial^2}{\partial x\partial\theta}\mathcal{B}_{w_k}(x,\theta)\frac{\partial}{\partial\theta}\mathcal{B}_{u_l}(x,\theta)dxd\theta$$

20. $$[V_{16}]_{l,k}^{\mathcal{N}_u\times\mathcal{N}_v} = \sum_{i=1}^{s}\int_{\theta_{1_{2i}}}^{\theta_{2_{2i}}}\int_{x_{1_{2i}}}^{x_{2_{2i}}} \frac{E_{pe_{2i}}h_{pe_{2i}}}{2(1+\nu_{pe_{2i}})}\frac{\partial}{\partial x}\mathcal{B}_{v_k}(x,\theta)\frac{\partial}{\partial\theta}\mathcal{B}_{u_l}(x,\theta)dxd\theta$$

21. $$[U_{16}]_{l,k}^{\mathcal{N}_u\times\mathcal{N}_u} = \sum_{i=1}^{s}\int_{\theta_{1_{2i}}}^{\theta_{2_{2i}}}\int_{x_{1_{2i}}}^{x_{2_{2i}}} \frac{E_{pe_{2i}}h_{pe_{2i}}}{2R(1+\nu_{pe_{2i}})}\frac{\partial}{\partial\theta}\mathcal{B}_{u_k}(x,\theta)\frac{\partial}{\partial\theta}\mathcal{B}_{u_l}(x,\theta)dxd\theta$$

22. $$[W_{19}]_{l,k}^{\mathcal{N}_u\times\mathcal{N}_w} = \sum_{i=1}^{s}\int_{\theta_{1_{2i}}}^{\theta_{2_{2i}}}\int_{x_{1_{2i}}}^{x_{2_{2i}}} \frac{E_{pe_{2i}}a_{2_{2i}}}{2R(1+\nu_{pe_{2i}})}\frac{\partial^2}{\partial x\partial\theta}\mathcal{B}_{w_k}(x,\theta)\frac{\partial}{\partial\theta}\mathcal{B}_{u_l}(x,\theta)dxd\theta$$

23. $$[F_u(t)]_l^{\mathcal{N}_u\times 1} = \int_0^{2\pi}\int_0^{\ell} R\hat{q}_x(t,\theta,x)\mathcal{B}_{u_l}(\theta,x)dxd\theta$$

24. $$[B_u]_l^{\mathcal{N}_u\times 1} = \sum_{i=1}^{s}\int_{\theta_{1_{1i}}}^{\theta_{2_{1i}}}\int_{x_{1_{1i}}}^{x_{2_{1i}}} R(N_x)_{pe_{1i}}\frac{\partial\mathcal{B}_{ul}}{\partial x}dxd\theta + \sum_{i=1}^{s}\int_{\theta_{1_{2i}}}^{\theta_{2_{2i}}}\int_{x_{1_{2i}}}^{x_{2_{2i}}} R(N_x)_{pe_{2i}}\frac{\partial\mathcal{B}_{ul}}{\partial x}$$

The matrices $\tilde{U}_{1k}, k = 1,\ldots,6; \tilde{V}_{1k}, k = 1,\ldots,6; \tilde{W}_{1k}, k = 1,\ldots,9$ which contain the internal damping contributions are created by replacing E by c_D, $E_{pe_{1i}}$ with $c_{D_{pe_{1i}}}$ and $E_{pe_{2i}}$ with $c_{D_{pe_{2i}}}$, in the expressions above. The remaining matrices arising from the second and third equations of the weak form (2.7) are detailed in Appendix C.

We point out that by using the weak form in the discretization method, derivatives are transferred to the test functions hence decreasing smoothness requirements. Moreover, the method treats incorporation of discontinuous characteristic and indicator functions without added difficulties since these affect only the region of integration.

With the submatrices defined this way, the mass, stiffness and control input matrices and the forcing vector can now be constructed as follows

$$M^{\mathcal{N}} = \left[\begin{array}{c|c|c} U_M & & \\ \hline & V_M & \\ \hline & & W_M \end{array}\right] ,$$

$$K_E^{\mathcal{N}} = \left[\begin{array}{c|c|c} \sum_{k=1}^{6} U_{1k} & \sum_{k=1}^{6} V_{1k} & \sum_{k=1}^{9} W_{1k} \\ \hline \sum_{k=1}^{6} U_{2k} & \sum_{k=1}^{6} V_{2k} & \sum_{k=1}^{9} W_{2k} \\ \hline \sum_{k=1}^{9} U_{3k} & \sum_{k=1}^{9} V_{3k} & \sum_{k=1}^{26} W_{3k} \end{array}\right] , \tag{4.4}$$

$$K_{C_D}^{\mathcal{N}} = \left[\begin{array}{c|c|c} \sum_{k=1}^{6} \tilde{U}_{1k} & \sum_{k=1}^{6} \tilde{V}_{1k} & \sum_{k=1}^{9} \tilde{W}_{1k} \\ \hline \sum_{k=1}^{6} \tilde{U}_{2k} & \sum_{k=1}^{6} \tilde{V}_{2k} & \sum_{k=1}^{9} \tilde{W}_{2k} \\ \hline \sum_{k=1}^{9} \tilde{U}_{3k} & \sum_{k=1}^{9} \tilde{V}_{3k} & \sum_{k=1}^{26} \tilde{W}_{3k} \end{array}\right] ,$$

$$\hat{F}^{\mathcal{N}}(t) = \begin{bmatrix} F_u(t) \\ F_v(t) \\ F_w(t) \end{bmatrix} \tag{4.5}$$

and

$$\hat{B}^{\mathcal{N}} = \begin{bmatrix} B_u \\ B_v \\ B_w \end{bmatrix} . \tag{4.6}$$

To write the approximating system in first-order form, we consolidate the generalized coefficients $u_i(t), v_i(t)$ and $w_i(t)$ into one vector

$$\vartheta^{\mathcal{N}}(t) = (u_1(t), \ldots, u_{\mathcal{N}_u}(t), v_1(t), \ldots, v_{\mathcal{N}_v}(t), w_1(t), \ldots, w_{\mathcal{N}_w}(t)) \in \mathbb{R}^{\mathcal{N}} , \tag{4.7}$$

and form the control vector

$$U(t) = (V_{11}(t), V_{21}(t), \ldots, V_{1s}(t), V_{2s}(t)) \in \mathbb{R}^{2s} \ , \tag{4.8}$$

where s is the number of patch pairs. The finite dimensional system is then described by

$$\begin{aligned}
\begin{bmatrix} K_E^{\mathcal{N}} & 0 \\ 0 & M^{\mathcal{N}} \end{bmatrix} \begin{bmatrix} \dot{\vartheta}^{\mathcal{N}}(t) \\ \ddot{\vartheta}^{\mathcal{N}}(t) \end{bmatrix} &= \begin{bmatrix} 0 & K_E^{\mathcal{N}} \\ -K_E^{\mathcal{N}} & -K_{C_D}^{\mathcal{N}} \end{bmatrix} \begin{bmatrix} \vartheta^{\mathcal{N}}(t) \\ \dot{\vartheta}^{\mathcal{N}}(t) \end{bmatrix} \\
&\quad + \begin{bmatrix} 0 \\ \hat{B}^{\mathcal{N}} \end{bmatrix} U(t) + \begin{bmatrix} 0 \\ \hat{F}^{\mathcal{N}}(t) \end{bmatrix} \qquad (4.9) \\
\begin{bmatrix} K_E^{\mathcal{N}} & 0 \\ 0 & M^{\mathcal{N}} \end{bmatrix} \begin{bmatrix} \vartheta^{\mathcal{N}}(0) \\ \dot{\vartheta}^{\mathcal{N}}(0) \end{bmatrix} &= \begin{bmatrix} \vartheta_1^{\mathcal{N}} \\ \vartheta_2^{\mathcal{N}} \end{bmatrix} .
\end{aligned}$$

To pose the system in a form suitable for simulations, parameter estimation and control applications, the mass and stiffness matrices are inverted yielding a Cauchy equation of the form

$$\begin{aligned}
\dot{z}^{2\mathcal{N}}(t) &= A^{2\mathcal{N}} z^{2\mathcal{N}}(t) + B^{2\mathcal{N}} U(t) + G^{2\mathcal{N}}(t) \\
z^{2\mathcal{N}}(0) &= z_0^{2\mathcal{N}} = \begin{bmatrix} K_E^{\mathcal{N}} & 0 \\ 0 & M^{\mathcal{N}} \end{bmatrix}^{-1} \begin{bmatrix} \vartheta_1^{\mathcal{N}} \\ \vartheta_2^{\mathcal{N}} \end{bmatrix} ,
\end{aligned} \tag{4.10}$$

where $z^{2\mathcal{N}}(t) = \left[\vartheta^{\mathcal{N}}(t), \dot{\vartheta}^{\mathcal{N}}(t)\right]^T \in R^{2\mathcal{N}}$.

4.1 Full Order Methods

Use of standard Galerkin basis elements such as cubic splines, linear splines or Legendre polynomials will be referred to as *full order methods*. To exploit the tensor nature of the cylindrical shell domain Γ_0 and periodicity in θ, the basis for the three displacements are constructed with Fourier components in θ and spline components

in x. The choice of splines in the axial variable is motivated by the following criteria: efficiency, flexibility with regard to internal and external patch contributions, adaptability with respect to various boundary conditions, and accuracy.

Let B_{u_n}, B_{v_n} and B_{w_n} denote the spline components in the longitudinal, circumferential and tangential directions, respectively. Furthermore, denote the Fourier limits by M_u, M_v and M_w and the number of basis splines by $\hat{N}_u, \hat{N}_v, \hat{N}_w$. Then in terms of complex Fourier expansions, the approximate solutions (4.2) are expressed as

$$\begin{aligned} u^{\mathcal{N}}(t,x,\theta) &= \sum_{m=-M_u}^{M_u} \sum_{n=1}^{\hat{N}_u} u_{mn}(t) e^{im\theta} B_{u_n}(x) \\ v^{\mathcal{N}}(t,x,\theta) &= \sum_{m=-M_v}^{M_v} \sum_{n=1}^{\hat{N}_v} v_{mn}(t) e^{im\theta} B_{v_n}(x) \\ w^{\mathcal{N}}(t,x,\theta) &= \sum_{m=-M_w}^{M_w} \sum_{n=1}^{\hat{N}_w} w_{mn}(t) e^{im\theta} B_{w_n}(x) \ . \end{aligned}$$

The complex expansions above are expressed in real components using the Euler identities $e^{\pm im\theta} = \cos(m\theta) \pm i \sin(m\theta)$ yielding

$$\begin{aligned} u^{\mathcal{N}}(t,x,\theta) &= \sum_{n=1}^{\hat{N}_u} u_{0n}(t) B_{u_n}(x) \\ &+ \sum_{m=1}^{M_u} \sum_{n=1}^{\hat{N}_u} u_{mn}(t) \cos(m\theta) B_{u_n}(x) + \sum_{m=1}^{M_u} \sum_{n=1}^{\hat{N}_u} \tilde{u}_{mn}(t) \sin(m\theta) B_{u_n}(x) \\ v^{\mathcal{N}}(t,x,\theta) &= \sum_{n=1}^{\hat{N}_v} v_{0n}(t) B_{v_n}(x) \\ &+ \sum_{m=1}^{M_v} \sum_{n=1}^{\hat{N}_v} v_{mn}(t) \cos(m\theta) B_{v_n}(x) + \sum_{m=1}^{M_v} \sum_{n=1}^{\hat{N}_v} \tilde{v}_{mn}(t) \sin(m\theta) B_{v_n}(x) \\ w^{\mathcal{N}}(t,x,\theta) &= \sum_{n=1}^{\hat{N}_w} w_{0n}(t) B_{w_n}(x) \\ &+ \sum_{m=1}^{M_w} \sum_{n=1}^{\hat{N}_w} w_{mn}(t) \cos(m\theta) B_{w_n}(x) + \sum_{m=1}^{M_w} \sum_{n=1}^{\hat{N}_w} \tilde{w}_{mn}(t) \sin(m\theta) B_{w_n}(x) \ . \end{aligned}$$

The total number of basis functions for each displacement is $\mathcal{N}_u = \hat{N}_u(2M_u+1), \mathcal{N}_v = \hat{N}_v(2M_v+1)$ and $\mathcal{N}_w = \hat{N}_w(2M_w+1)$.

For the longitudinal and circumferential displacements, we investigate the use of both linear and cubic spline bases. Due to differentiability requirements, only cubic splines are used when approximating the transverse displacement. To start defining the splines, we partition the interval $[0, \ell]$ along the x-axis with grid points $x_n = nh_x$, $h_x = \ell/N, n = 0, \ldots, N$. For $n = -1, 0, 1, \ldots, N+1$, the standard cubic splines are then defined by

$$b_n(x) = \frac{1}{h_x^3} \begin{cases} (x - x_{n-2})^3, & x \in [x_{n-2}, x_{n-1}] \\ h_x^3 + 3h_x^2(x - x_{n-1}) + 3h_x(x - x_{n-1})^2 - 3(x - x_{n-2})^3, & x \in [x_{n-1}, x_n] \\ h_x^3 + 3h_x^2(x_{n+1} - x) + 3h_x(x_{n+1} - x)^2 - 3(x_{n+1} - x)^3, & x \in [x_n, x_{n+1}] \\ (x_{n+2} - x)^3, & x \in [x_{n+1}, x_{n+2}] \\ 0, & \text{otherwise} \end{cases} \tag{4.11}$$

(see [47]). On the other hand, the standard linear splines are given by

$$l_n(x) = \frac{1}{h_x} \begin{cases} (x - x_{n-1}, & x \in [x_{n-1}, x_n] \\ (x_{n+1} - x), & x \in [x_n, x_{n+1}] \\ 0, & \text{otherwise} , \end{cases} \tag{4.12}$$

for $n = 0, \ldots, N$.

Both standard linear and cubic splines must be modified to satisfy the essential boundary conditions and ensure the approximate solutions are in V. Appropriate bases for the two boundary conditions are then formed by combining the modified axial bases with Fourier components in θ. Modification of the splines are carried out as follows.

(i) *Fixed displacements at* $x = 0, \ell$. To construct basis functions satisfying fixed displacements (but unspecified slopes) at $x = 0, \ell$, the modified cubic splines

are taken to be

$$\hat{b}_n(x) = \begin{cases} b_0(x) - 4b_{-1}(x) & , \quad n = 0 \\ b_1(x) - b_{-1}(x) & , \quad n = 1 \\ b_n(x) & , \quad n = 2, \cdots, N-2 \\ b_{N-1}(x) - b_{N+1} & , \quad n = N-1 \\ b_N(x) - 4b_{N+1}(x) & , \quad n = N \end{cases} , \tag{4.13}$$

for a total of $N+1$ modified cubic spline axial basis functions. The linear splines are modified by omitting the first and last linear splines from the set and setting

$$\hat{l}_n(x) = l_n(x), n = 1, \ldots, N_1 \ . \tag{4.14}$$

With the bases defined this way, note that the boundary conditions are satisfied, i.e., $\hat{b}_n(0) = \hat{b}_n(\ell) = 0$ and $\hat{l}_n(0) = \hat{l}_n(\ell) = 0$.

(ii) *Fixed displacements and slope at* $x = 0, \ell$. This condition is imposed only on the transverse displacement and only cubic splines are used here. The modified cubic splines satisfying the zero slope zero displacements are given by

$$\tilde{b}_n(x) = \begin{cases} b_0(x) - 2b_{-1}(x) - 2b_1(x) & , \quad n = 1 \\ b_n(x) & , \quad n = 2, \cdots, N-2 \\ b_N(x) - 2b_{N-1}(x) - 2b_{N+1}(x) & , \quad n = N-1 \end{cases} , \tag{4.15}$$

with $n = 1, \cdots, N-1$ for a total of $N-1$ basis functions. This basis now satisfies

$$\hat{b}_n(0) = \hat{b}'_n(0) = \hat{b}(\ell) = \hat{b}'_n(\ell) = 0 \ .$$

The bases used for simply supported shells must satisfy the conditions $B_{v_k}(0) = B_{v_k}(\ell) = 0, B_{w_k}(0) = B_{w_k}(\ell) = 0$ (the moment and shear conditions are natural and hence do not need to be explicitly enforced). To illustrate the use of cubic splines, we combine standard cubic splines (4.11) with Fourier components to construct bases for the longitudinal direction, and use a combination of Fourier polynomials and modified

Basis Function	Definition	Axial Limit
longitudinal $B_{u_{mn}}(x,\theta)$ – linear	$e^{im\theta}l_n(x)$ (4.12)	$\hat{N}_u = N_u + 1$
– cubic	$e^{im\theta}b_n(x)$ (4.11)	$\hat{N}_u = N_u + 3$
circumferential $B_{v_{mn}}(x,\theta)$ – linear	$e^{im\theta}\hat{l}_n(x)$ (4.14)	$\hat{N}_v = N_v - 1$
– cubic	$e^{im\theta}\hat{b}_n(x)$ (4.13)	$\hat{N}_v = N_v + 1$
transverse $B_{w_{mn}}(x,\theta)$ – cubic	$e^{im\theta}\hat{b}_n(x)$ (4.13)	$\hat{N}_w = N_w + 1$

Table 4.1: Basis function definitions for models with simply-supported boundary conditions

Basis Function	Definition	Axial Limit
longitudinal $B_{u_{mn}}(x,\theta)$ – linear	$e^{im\theta}\hat{l}_n(x)$ (4.14)	$\hat{N}_u = N_u - 1$
– cubic	$e^{im\theta}\hat{b}_n(x)$ (4.13)	$\hat{N}_u = N_u + 1$
circumferential $B_{v_{mn}}(x,\theta)$ – linear	$e^{im\theta}\hat{l}_n(x)$ (4.14)	$\hat{N}_v = N_v - 1$
– cubic	$e^{im\theta}\hat{b}_n(x)$ (4.13)	$\hat{N}_v = N_v + 1$
transverse $B_{w_{mn}}(x,\theta)$ – cubic	$e^{im\theta}\tilde{b}_n(x)$ (4.15)	$\hat{N}_w = N_w - 1$

Table 4.2: Basis function definitions for models with fixed-edge boundary conditions

cubic splines (4.13) for the circumferential and transverse basis functions. Choices for shell models with simply supported edge conditions are given in Table 4.1, while bases for fixed-edge conditions are summarized in Table 4.2. The last column in each table summarizes the total number of axial functions in each expansion.

We point out that the linear and cubic spline bases described here are but two choices from among many that can be made for the axial components. For the applications considered here, cubic splines provided a good balance between accuracy, efficiency and adaptability with regard to patches and boundary conditions. If higher accuracy is desired, however, quintic splines may be employed. Similarly, spectral expansions employing Legendre, Chebyshev or sinc functions can be employed once modifications have been made for boundary conditions.

4.2 Lagrange Reduced Basis Method

Full order discretizations result in system matrices with large dimension and hence are not readily implementable in real time computations. As shown in [24, 25] and later in Chapter 5, a large number of basis functions was needed to resolve the system (4.10), where $\mathcal{N}_u = \mathcal{N}_v = 117$ and $\mathcal{N}_w = 99$ basis functions were used for a total of $2\mathcal{N} = 666$ coefficients in the ODE system (4.10). Thus, the investigation of model reduction techniques is a necessary next step in this study to develop practical methods.

The method we investigate involves the use of a reduced basis subspace to approximate the displacements u, v and w. Three ways to choose the reduced basis subspaces were discussed in [30], namely the Taylor, the Lagrange and the Hermite reduced basis methods.

The basis elements in the Lagrange subspace are snapshots (i.e., solutions evaluated at N_R times $\{t_1, \dots t_{N_R}\}$) of the model obtained by solving the system (2.7) using a full order method. If experimental data is available, measurements of the displacements could also be used as reduced basis elements. Thus, the basis elements in the u, v and w directions are taken to be $\{\mathcal{B}_{u_i}(x,\theta)\}_{i=1}^{\mathcal{N}_u} = \{u^{\mathcal{N}}(t_i,x,\theta)\}_{i=1}^{\mathcal{N}_u}$, $\{\mathcal{B}_{v_i}(x,\theta)\}_{i=1}^{\mathcal{N}_v} = \{v^{\mathcal{N}}(t_i,x,\theta)\}_{i=1}^{\mathcal{N}_v}$ and $\{\mathcal{B}_{w_i}(x,\theta)\}_{i=1}^{\mathcal{N}_w} = \{w^{\mathcal{N}}(t_i,x,\theta)\}_{i=1}^{\mathcal{N}_w}$, respectively.

As an alternative to the Lagrange reduced basis method, discussed in [30, 31], the Hermite subspace could be formed by taking as basis elements the full order solutions and their first derivatives. This gives us the subspace

$$V^{\mathcal{N}} = \text{span}\left\{\mathcal{B}_{u_i}, \dot{\mathcal{B}}_{u_i}\right\}_{i=1}^{\mathcal{N}_u/2} \times \text{span}\left\{\mathcal{B}_{v_i}, \dot{\mathcal{B}}_{v_i}\right\}_{i=1}^{\mathcal{N}_v/2} \times \text{span}\left\{\mathcal{B}_{w_i}, \dot{\mathcal{B}}_{w_i}\right\}_{i=1}^{\mathcal{N}_w/2}$$

with dimension $\mathcal{N} = \mathcal{N}_u + \mathcal{N}_v + \mathcal{N}_w$. Another alternative is the Taylor reduced basis method where basis elements are taken to be a solution together with its $\mathcal{N} - 1$ time derivatives at one time instance.

4.3 POD Reduced Basis Method

Given N_s snapshots of the model

$$\{y^{\mathcal{N}}(t_j, x, \theta)\} = \{(u^{\mathcal{N}}(t_j, x, \theta), v^{\mathcal{N}}(t_j, x, \theta), w^{\mathcal{N}}(t_j, x, \theta))\}$$

at time instances $t_j, j = 1, \ldots, N_s$, we seek basis elements of the form

$$\begin{aligned} \mathcal{B}_{u_i}(x, \theta) &= \sum_{j=1}^{N_s} \bar{\alpha}_j^i u^{\mathcal{N}}(t_j, x, \theta) \\ \mathcal{B}_{v_i}(x, \theta) &= \sum_{j=1}^{N_s} \bar{\beta}_j^i v^{\mathcal{N}}(t_j, x, \theta) \\ \mathcal{B}_{w_i}(x, \theta) &= \sum_{j=1}^{N_s} \bar{\gamma}_j^i w^{\mathcal{N}}(t_j, x, \theta) \ . \end{aligned} \tag{4.16}$$

We require each basis function $\mathcal{B}_{u_i}$ to resemble the snapshots $\{u^{\mathcal{N}}\}_{j=1}^{N_s}$ in the sense that it maximizes

$$\frac{1}{N_s} \sum_{j=1}^{N_s} \left| \left\langle u^{\mathcal{N}}(t_j, \cdot, \cdot), \mathcal{B}_{u_i}(\cdot, \cdot) \right\rangle \right|^2 \tag{4.17}$$

subject to $\langle \mathcal{B}_{u_i}, \mathcal{B}_{u_i} \rangle = \|\mathcal{B}_{u_i}\|^2 = 1$. The POD basis functions in the circumferential and transverse directions are taken to resemble the snapshots in the v and w directions in a similar manner.

For the rest of this section, we discuss POD basis elements in the u direction, but all ideas similarly apply to basis functions in the v and w directions.

As a first step in obtaining the maximum to (4.17), we denote the time average by $\ll \cdot \gg$, i.e.,

$$\ll u^{\mathcal{N}} \gg = \frac{1}{N_s} \sum_{j=1}^{N_s} u^{\mathcal{N}}(t_j, \cdot, \cdot) \ .$$

We next define $R_u : L^2(\Gamma_0) \to L^2(\Gamma_0)$ by

$$(R_u \eta)(x, \theta) = \left\langle \frac{1}{N_s} \sum_{j=1}^{N_s} u^{\mathcal{N}}(t_j, x, \theta) u^{\mathcal{N}}(t_j, \cdot, \cdot), \eta(\cdot, \cdot) \right\rangle .$$

Note that

$$\begin{aligned}\Big\langle R\eta(*,*),\eta(*,*)\Big\rangle &= \Big\langle\Big\langle\frac{1}{N_s}\sum_{j=1}^{N_s}u^{\mathcal{N}}(t_j,*,*)u^{\mathcal{N}}(t_j,\cdot,\cdot),\eta(\cdot,\cdot)\Big\rangle,\eta(*,*)\Big\rangle \\ &= \frac{1}{N_s}\sum_{j=1}^{N_s}\Big\langle u^{\mathcal{N}}(t_j,*,*),\eta(*,*)\Big\rangle\Big\langle u^{\mathcal{N}}(t_j,\cdot,\cdot),\eta(\cdot,\cdot)\Big\rangle \\ &= \frac{1}{N_s}\sum_{j=1}^{N_s}\Big|\Big\langle u^{\mathcal{N}}(t_j,\cdot,\cdot),\eta(\cdot,\cdot)\Big\rangle\Big|^2 \ ,\end{aligned}$$

hence maximizing (4.17) involves finding the largest eigenvalue to

$$R_u\eta = \lambda\eta \quad \text{subject to} \ \ \|\eta\|^2 = 1 \ . \tag{4.18}$$

As detailed in [37], by substituting $\eta = \sum_{j=1}^{N_s}\bar{\alpha}_j^i u^{\mathcal{N}}$ into (4.18), we obtain the matrix eigenvalue problem

$$C_u\alpha = \lambda\alpha \ ,$$

where the covariant matrix C_u is defined by

$$[C_u]_{k\ell} = \frac{1}{N_s}\Big\langle u^{\mathcal{N}}(t_k,\cdot,\cdot),u^{\mathcal{N}}(t_\ell,\cdot,\cdot)\Big\rangle \ , \quad k,\ell = 1,\ldots,N_s \ . \tag{4.19}$$

The vector of coefficients $\bar{\alpha}^i \in \mathbb{R}^{N_s}$ in (4.16) is then taken to be the i^{th} eigenvector of the matrix C_u. The matrices C_v and C_w together with the vectors $\bar{\beta}^i$ and $\bar{\gamma}^i$ are obtained similarly.

Since the matrix C_u is nonnegative (this is easily seen by arguing $\xi^T C_u\xi \geq 0$ for $\xi \in \mathbb{R}^{N_s}$) and Hermitian, it has a complete set of orthogonal eigenvectors with corresponding eigenvalues $\lambda_1 \geq \lambda_2 \geq \ldots \geq \lambda_{N_s} \geq 0$. We choose the eigenvectors $\bar{\alpha}^i$ such that

$$\bar{\alpha}^k \cdot \bar{\alpha}^\ell = \begin{cases} 0 \ , & k \neq \ell \\ \dfrac{1}{N_s\lambda_k} \ , & k = \ell \ . \end{cases}$$

The eigenvectors $\bar{\beta}^i$ and $\bar{\gamma}^i$ of C_v and C_w are chosen similarly.

The basis elements $\mathcal{B}_{u_i}$ given by (4.16) are shown to be orthonormal in [37]. Furthermore, the lemma given below from [16] establishes the optimality of the basis in the sense that the approximation $u^{\mathcal{N}}$ using the POD basis to the solution

$u \in L^2(0,T;L^2(\Gamma_0))$ contains the most "displacement energy" possible in a time average sense. (For a full discussion of this measure of optimality of the POD method, see for example, [16]).

Lemma 4.3.1 *Let* $\left\{\mathcal{B}_{u_1}, \mathcal{B}_{u_2}, \ldots, \mathcal{B}_{u_{N_s}}\right\}$ *denote the orthonormal set of POD basis elements and* $\lambda_1 \geq \ldots \geq \lambda_{N_s}$ *denote the corresponding set of eigenvalues. If* $u^{N_s} = \sum_{i=1}^{N_s} b_i(t)\mathcal{B}_{u_i}$ *denotes the approximation to* u *with respect to this basis, then for any arbitrary orthonormal basis* $\{\psi_1, \psi_2, \ldots, \psi_{N_s}\}$*, the following hold*

1. $\ll b_i(t)b_j^*(t) \gg = \lambda_i \delta_{ij}$,
2. *for every* N_s, $\displaystyle\sum_{i=1}^{N_s} \ll b_i(t)b_i^*(t) \gg = \sum_{i=1}^{N_s} \lambda_i \geq \sum_{i=1}^{N_s} \ll a_i(t)a_i^*(t) \gg$,

where the $a_i(t)$ *are coefficients of the approximation to* u, $u_\psi^{N_s} = \sum_{i=1}^{N_s} a_i(t)\psi_i$, *using the arbitrary orthonormal basis* $\{\psi_j\}_{j=1}^{N_s}$.

Proof:

- To prove (1), we let $u^{N_s} = \sum_{i=1}^{N_s} b_i(t)\mathcal{B}_{u_i}$ be the approximation to u with respect to the POD basis elements. Then the coefficients $b_i(t)$ are given by $b_i(t) = \left\langle u^{N_s}(t,\cdot,\cdot), \mathcal{B}_{u_i}(\cdot,\cdot)\right\rangle$ and we have

$$\begin{aligned}
\ll b_i(t)b_j^*(t) \gg &= \ll \left\langle u^{N_s}(t,*,*), \mathcal{B}_{u_i}(*,*)\right\rangle \left\langle u^{N_s}(t,\cdot,\cdot), \mathcal{B}_{u_j}(\cdot,\cdot)\right\rangle \gg \\
&= \frac{1}{N_s}\sum_{k=1}^{N_s} \left\langle u^{\mathcal{N}}(t_k,*,*), \mathcal{B}_{u_i}(*,*)\right\rangle \left\langle u^{\mathcal{N}}(t_k,\cdot,\cdot), \mathcal{B}_{u_j}(\cdot,\cdot)\right\rangle \\
&= \left\langle \frac{1}{N_s}\sum_{k=1}^{N_s} \left\langle u^{\mathcal{N}}(t_k,\cdot,\cdot), \mathcal{B}_{u_j}(\cdot,\cdot)\right\rangle u^{\mathcal{N}}(t_k,*,*), \mathcal{B}_{u_i}(*,*)\right\rangle \\
&= \left\langle R_u\mathcal{B}_{u_j}, \mathcal{B}_{u_i}\right\rangle \\
&= \left\langle \lambda_j\mathcal{B}_{u_j}, \mathcal{B}_{u_i}\right\rangle \\
&= \lambda_i\delta_{ij} \ .
\end{aligned}$$

The proof of (2) is straightforward from the maximality of the POD elements in (4.17):

$$\begin{aligned} \ll a_i(t)a_i^*(t) \gg &= \ll \left|\left\langle u_\psi^{N_s}(t,\cdot,\cdot), \psi_i(\cdot,\cdot)\right\rangle\right|^2 \gg \\ &= \frac{1}{N_s}\sum_{k=1}^{N_s}\left|\left\langle u^{\mathcal{N}}(t_k,\cdot,\cdot), \psi_i(\cdot,\cdot)\right\rangle\right|^2 \\ &\leq \frac{1}{N_s}\sum_{k=1}^{N_s}\left|\left\langle u^{\mathcal{N}}(t_k,\cdot,\cdot), \mathcal{B}_{u_i}(\cdot,\cdot)\right\rangle\right|^2 \\ &= \ll b_i(t)b_i^*(t) \gg \ . \end{aligned}$$

■

Note that (1) indicates that POD coefficients are uncorrelated. Furthermore, for a decomposition with respect to any arbitrary orthonormal basis $\{\psi_j\}_{j=1}^{N_s}$ (i.e., $u^{N_s} = \sum_{i=1}^{N_s} a_i(t)\psi_i$), the quantity $\ll a_i(t)a_i^*(t) \gg$ represents the average "energy" in the i^{th} mode in the sense that

$$\begin{aligned} \ll \left\langle u^{N_s}, u^{N_s}\right\rangle \gg &= \ll \left\langle \sum_{i=1}^{N_s} a_i(t)\psi_i, \sum_{j=1}^{N_s} a_j(t)\psi_j\right\rangle \gg \\ &= \ll \sum_{i=1}^{N_s} a_i(t)\sum_{j=1}^{N_s} a_j^*(t)\left\langle \psi_i, \psi_j\right\rangle \gg \\ &= \ll \sum_{i=1}^{N_s} a_i(t)a_i^*(t) \gg . \end{aligned}$$

To determine the dimension of the reduced basis space in the u direction, we determine the integer $\mathcal{N}_u$ such that the sum of the first $\mathcal{N}_u$ eigenvalues gives a good approximation to the sum of all the eigenvalues, i.e., $\sum_{i=1}^{\mathcal{N}_u}\lambda_i \simeq \sum_{i=1}^{N_s}\lambda_i$. The ratio $\sum_{i=1}^{\mathcal{N}_u}\lambda_i \big/ \sum_{i=1}^{N_s}\lambda_i$ gives the percentage of the "energy" in the N_s POD elements contained by the first $\mathcal{N}_u$ POD basis elements. The dimensions $\mathcal{N}_v$ and $\mathcal{N}_w$ are determined by considering the eigenvalue ratios of the matrices C_v and C_w, respectively.

We reiterate that due to the three component nature of the state, i.e., $y = (u, v, w)$, all discussions above involve only the circumferential direction but the ideas must be extended in a similar manner to the v and w directions.

Chapter 5

Numerical Examples

Our experiences with numerical approximation and control of the shell system will be presented in this chapter. We begin by employing the full order method in modal analysis, static and dynamic simulations, and LQR control. Then we implement the Lagrange and POD reduced basis methods in uncontrolled and controlled simulations of the shell. To facilitate comparison between the three methods, the same conditions were used in all control simulations. We end the chapter by implementing POD reduced order model computed gains in the full order model.

The model and code we developed allows different characteristics for each individual patch, but to simplify exposition, we assumed uniform parameters for all the patches. Thus, the subscripts $1i$ and $2i$ are dropped in the modeling equations, and we denote the patch thickness, patch density, patch Young's modulus, patch Kelvin-Voigt damping, patch Poisson ratio and patch proportionality constant by h_{pe}, ρ_{pe}, E_{pe}, $C_{D_{pe}}$, ν_{pe} and d_{31}, respectively. Two sets of physical constants were used in the approximations. The English system constants, reported in Table 5.1, were used in the modal (Chapter 5.1.1) and uncontrolled shell examples (Chapter 5.1.2). These constants are consistent with the physical parameters used at the Acoustics Division of NASA Langley Research center. For all the control examples, the metric system was chosen and values are given in Table 5.2.

For the time-dependent problems, the ordinary differential equations arising from

	Dimensions	Parameters
Shell	$h = .01\ in$ $R = 3.0\ in$ $\ell = 12.0\ in$	$\rho = .283\ lb/in^3$ $E = 3 \times 10^7\ lb/in^2$ $c_D = 15.099 \times lb\ in\ s$ $\nu = .3$
Patches (1 pair)	$h_{pe} = .001\ in$ Center $(\hat{x}, \hat{\theta})$: $(6, \pi/12)$ $x_1 = 4.5\ in$, $x_2 = 7.5\ in$ $\theta_1 = 0$, $\theta_2 = \pi/6$	$E_{pe} = 9.137 \times 10^6 lb/in^2$ $\nu_{pe} = .31$ $d_31 = 7.4 \times 10^{-9} in/V$

Table 5.1: English system dimensions and physical parameters for the shell and patch.

	Dimensions	Parameters
Shell	$h = .00127\ m$ $R = .4\ m$ $\ell = 1\ m$	$\rho = 2700\ kg/m^3$ $E = 7.1 \times 10^{10} N/m^2$ $c_D = 1.47 \times 10^5 Nms$ $\nu = .33$
Patches (12 pairs)	$h_{pe} = .0001778\ m$ Centers $(\hat{x}, \hat{\theta})$: (.25,0), (.5,0), (.75,0) $(.25, \pi/2)$, $(.5, \pi/2)$, $(.75, \pi/2)$ $(.25, \pi)$, $(.5, \pi)$, $(.75, \pi)$ $(.25, 3\pi/2)$, $(.5, 3\pi/2)$, $(.75, 3\pi/2)$	$\rho_{pe} = 7600\ kg/m^3$ $E_{pe} = 6.3 \times 10^{10} N/m^2$ $c_{D_{pe}} = 1.7 \times 10^5 Nms$ $\nu_{pe} = .31$ $d_{31} = 190 \times 10^{-12} m/V$

Table 5.2: Metric system dimensions and physical parameters for the shell and patches.

the Galerkin expansions in the spatial variables (4.10) were marched in time using the ordinary differential equation solver presented in [19].

In all simulations, double precision was used in the computations and numerical approximation of the integrals was performed using a four point Gaussian quadrature of the form

$$\int_0^\ell f(x)dx \approx \sum_{k=1}^{4N_q} c_k f(x_k) \ ,$$

where N_q is the number of nodes which we assumed to be 16 (hence 64 quadrature points are obtained). The four point quadrature rule was chosen to obtain exact values when integrating cubic spline basis functions against cubic spline basis functions. The quadrature weights c_k and points x_k, on the interval $(0, h_q)$, are given by

$$\begin{aligned}
c_1 &= \frac{49}{6(18+\sqrt{30})} \cdot \frac{h_q}{2} \quad , \quad x_1 = h_q \left[\frac{1}{2} - \frac{\sqrt{15+2\sqrt{30}}}{2\sqrt{35}} \right] \\
c_2 &= \frac{49}{6(18-\sqrt{30})} \cdot \frac{h_q}{2} \quad , \quad x_2 = h_q \left[\frac{1}{2} - \frac{\sqrt{15-2\sqrt{30}}}{2\sqrt{35}} \right] \\
c_3 &= \frac{49}{6(18-\sqrt{30})} \cdot \frac{h_q}{2} \quad , \quad x_3 = h_q \left[\frac{1}{2} + \frac{\sqrt{15-2\sqrt{30}}}{2\sqrt{35}} \right] \\
c_4 &= \frac{49}{6(18+\sqrt{30})} \cdot \frac{h_q}{2} \quad , \quad x_4 = h_q \left[\frac{1}{2} + \frac{\sqrt{15+2\sqrt{30}}}{2\sqrt{35}} \right] \ ,
\end{aligned}$$

where $h_q = \ell / N_q$ (see [51]).

5.1 Full Order Methods

Computations with full order methods employing the spline/Fourier basis functions as discussed in Chapter 4.1 will be reported on here. In Chapter 5.1.1, we consider a simply supported shell in which analytic values of natural frequencies and modes could be derived. Approximations of the natural frequencies and modes using spline/Fourier elements are then compared with analytic values. Computational validation of the $\mathcal{O}(h_x^2)$ convergence of linear splines and $\mathcal{O}(h_x^4)$ convergence with cubic splines is demonstrated below (note that h_x is the size of the uniform intervals along the x-axis when creating standard linear or cubic splines). The natural frequencies and modes of a fixed-edge shell were also computed but analytic expressions are not available for this case hence we only present the numerical results.

In Chapter 5.1.2, the static and dynamic behavior of the model were tested by considering known displacements, numerically forcing the shell to exhibit the known solutions, and comparing the true and approximate displacements. Since fixed-edge boundary conditions are more common in experimental setups, these conditions are used for the rest of the chapter. The $\mathcal{O}(h_x^2)$ convergence of linear splines and $\mathcal{O}(h_x^4)$ convergence with cubic splines were are again demonstrated by the method.

Control laws in Theorem 3.3.1 (no exogenous force) and Theorem 3.3.2 (periodic exogenous force) are implemented in Chapter 5.1.3. The effect of patch sizes and passive patch contributions were considered. For the shell with periodic exogenous input, single and multiple frequency external excitation forces with normal distribution along the spatial components were investigated.

5.1.1 Modal Solutions

Simply supported shell with no damping, devoid of patches and constant parameters

As mentioned earlier, this is one of the few cases where modal expressions could be obtained analytically. It is evident that very few experimental or actual implementation

would benefit from these conditions, but the analytic solutions provide an excellent means of testing the approximation methods. Once the methods are verified, they can be employed to approximate the natural frequencies and modes of more physically realistic shell systems.

Analytic natural frequencies and modes for the shell model we consider in this report have been investigated by the authors in [24, 22], and references could be found in [34, 38]. We begin by letting ρ, ν and E have the constant values given in Table 5.1, assuming no damping ($c_D = 0$), and considering zero external force, i.e., $\hat{q}_x = \hat{q}_\theta = \hat{q}_n = 0$. In operator format, the Donnell-Mushtari equations (2.1) can now be written in the form

$$\rho h \frac{\partial^2 \vec{u}}{\partial t^2} = L\vec{u} \ , \tag{5.1}$$

where $\vec{u} = [u \ v \ w]^T$ and the operator L is given by

$$L = \frac{Eh}{1-\nu^2} \begin{bmatrix} \frac{\partial^2}{\partial x^2} + \frac{(1-\nu)}{2R^2}\frac{\partial^2}{\partial \theta^2} & \frac{(1+\nu)}{2R}\frac{\partial^2}{\partial x \partial \theta} & \frac{\nu}{R}\frac{\partial}{\partial x} \\ \frac{(1+\nu)}{2R}\frac{\partial^2}{\partial x \partial \theta} & \frac{(1-\nu)}{2}\frac{\partial}{\partial x^2} + \frac{1}{R^2}\frac{\partial^2}{\partial \theta^2} & \frac{1}{R^2}\frac{\partial}{\partial \theta} \\ -\frac{\nu}{R}\frac{\partial}{\partial x} & -\frac{1}{R^2}\frac{\partial}{\partial \theta} & -\frac{1}{R^2} - k\left[\frac{\partial^2}{\partial x^2} + \frac{1}{R^2}\frac{\partial^2}{\partial \theta^2}\right]^2 \end{bmatrix} .$$

Here $k = h^2/12$ and the boundary conditions are $B\vec{u} = \vec{0}$. We consider simply supported boundary conditions hence $B = \begin{bmatrix} B_1 & 0 \\ 0 & B_2 \end{bmatrix}$, where

$$B_1 = \frac{Eh}{1-\nu^2} \begin{bmatrix} 0 & 1 & 0 \\ 0 & 0 & 1 \\ \frac{\partial}{\partial x} & \frac{\nu}{R}\frac{\partial}{\partial \theta} & \frac{\nu}{R} \\ 0 & 0 & \frac{-h^2}{12}\left[\frac{\partial^2}{\partial x^2} + \nu\frac{\partial^2}{R^2 \partial \theta^2}\right] \end{bmatrix}_{x=0} ,$$

and B_2 is similar to B_1 except evaluation is at $x = \ell$.

We next write the displacements in separated form

$$\begin{aligned} u(t,x,\theta) &= T(t)U(x,\theta) \\ v(t,x,\theta) &= T(t)V(x,\theta) \\ w(t,x,\theta) &= T(t)W(x,\theta) \ , \end{aligned} \tag{5.2}$$

and perform separation of variables in (5.1) to obtain

$$\begin{aligned} &L\vec{Y} + \rho h\omega^2\vec{Y} = \vec{0} \\ &B\vec{Y} = \vec{0} \end{aligned} \quad , \quad T'' + \omega^2 T = 0 \ . \tag{5.3}$$

Here ω is the angular frequency of vibration and we consolidated the longitudinal, circumferential and transverse vibration modes in the vector $\vec{Y} = [U, V, W]^T$. Due to availability of simple analytic solutions (5.3), it is very popular in thin shell analysis. One modal solution, as given in [34, 38], has the form

$$\begin{aligned} U(x,\theta) &= A_1 \cos\left(\frac{n\pi x}{\ell}\right)\cos(m\theta) \\ V(x,\theta) &= B_1 \sin\left(\frac{n\pi x}{\ell}\right)\sin(m\theta) \\ W(x,\theta) &= C_1 \sin\left(\frac{n\pi x}{\ell}\right)\cos(m\theta) \end{aligned} \tag{5.4}$$

(the U component of the modes should not be confused with the control vector defined in (4.8) since control input is ignored in this section). The relationship of ω with the wave numbers m and n is obtained by substituting (5.4) in (5.2) and utilizing the resulting expression in (5.1). We then obtain a matrix system of the form

$$D \begin{bmatrix} A_1 \\ A_2 \\ A_3 \end{bmatrix} = 0 \ ,$$

whose solution is guaranteed if the determinant of D is nonzero (see [24, 34, 38] for the detailed expression of D). Setting the determinant to zero yields

$$\Omega^6 - K_2\Omega^4 + K_1\Omega^2 - K_0 = 0 \ , \tag{5.5}$$

where $\Omega^2 = \rho(1-\nu^2)\omega^2 R/E$ and

$$\begin{aligned} K_2 &= 1 + \frac{1}{2}(3-\nu)(m^2+\lambda^2) + \tilde{k}\left(m^2+\lambda^2\right)^2 \\ K_1 &= \frac{1}{2}(1-\nu)\left[(3+2\nu)\lambda^2 + m^2 + \left(m^2+\lambda^2\right)^2 + \frac{3-\nu}{1-\nu}\tilde{k}\left(m^2+\lambda^2\right)^2\right] \\ K_0 &= \frac{1}{2}(1-\nu)\left[(1-\nu^2)\lambda^4 + \tilde{k}\left(m^2+\lambda^2\right)^4\right] . \end{aligned}$$

Here $\lambda = n\pi R/\ell$ and $\tilde{k} = h^2/(12R^2)$. The solutions to the cubic equation (5.5) are given by

$$\Omega^2_{mnj} = -\frac{2}{3}\sqrt{K_2^2 - 3K_1}\cos\left(\frac{\alpha + 2(j-1)\pi}{3}\right) + \frac{K_2}{3}, \quad j = 1,2,3$$

where

$$\alpha = \cos^{-1}\left(\frac{-27K_0 - 2K_2^3 + 9K_1K_2}{2\sqrt{(K_2^2 - 3K_1)^2}}\right) .$$

Therefore, for each set of wave numbers m, n, three natural frequencies of the shell arise. Written in units of hertz, the frequencies are

$$f_{mnj} = \frac{\Omega_{mnj}}{2\pi R}\sqrt{\frac{E}{\rho(1-\nu^2)}} \quad , \quad j = 1,2,3 . \tag{5.6}$$

A second set of modes satisfying the eigenvalue problem in (5.3) has the form

$$\begin{aligned} U(x,\theta) &= A_2\cos\left(\frac{n\pi x}{\ell}\right)\sin(m\theta) \\ V(x,\theta) &= B_2\sin\left(\frac{n\pi x}{\ell}\right)\cos(m\theta) \\ W(x,\theta) &= C_2\cos\left(\frac{n\pi x}{\ell}\right)\sin(m\theta) . \end{aligned} \tag{5.7}$$

Although frequencies corresponding to this mode are also given by the first set (5.4), linearly independent modes could be produced by (5.7) and is therefore needed to obtain a complete basis when using modal approximation. We retain the second set (5.7) to have a complete set when comparing approximated modes.

We now turn to the approximation of the eigenvalue problem. The approximate system (4.9) with no external force input reduces to

$$K_E^{\mathcal{N}}\vartheta^{\mathcal{N}} = \omega^2 M^{\mathcal{N}}\vartheta^N , \tag{5.8}$$

where $K_E^{\mathcal{N}}$ and $M^{\mathcal{N}}$ (defined in (4.4)) are created using splines modified to satisfy the simply supported boundary conditions and without patch contributions. The approximate frequencies, in hertz, are obtained by dividing the numerically obtained eigenvalues with 2π. Modes corresponding to the frequency ω_j are constructed by forming linear combinations of the basis functions with elements of the j^{th} eigenvector ϑ as coefficients. Approximate modes will be denoted by $U^{\mathcal{N}}(x,\theta), V^{\mathcal{N}}(x,\theta), W^{\mathcal{N}}(x,\theta)$.

We group vibrational modes in three classes to facilitate comparison between analytic and computed solutions: (i) purely axisymmetric modes ($m = 0, n \geq 1$), (ii) purely extensional modes ($m \geq 1, n = 0$), and (iii) general shell modes ($m \geq 1, n \geq 1$).

(i) Purely Axisymmetric modes ($\mathbf{m = 0, n \geq 1}$)

The first set of analytic modes (5.4) for this case reduces to

$$\begin{aligned} U(x,\theta) &= A_1 \cos\left(\frac{n\pi x}{\ell}\right) \\ V(x,\theta) &= 0 \\ W(x,\theta) &= C_1 \sin\left(\frac{n\pi x}{\ell}\right) , \end{aligned} \tag{5.9}$$

where it can be seen that the longitudinal and radial components of the mode are coupled. For each value of n, solving the determinant equation (5.5) and converting the solution to units of hertz yields two frequencies

$$f_{0n} = \frac{\sqrt{2}}{4\pi R}\sqrt{\lambda^2 + 1 \pm \sqrt{(\lambda^2+1)^2 - 4\lambda^2(1-\nu^2)}}\sqrt{\frac{E}{\rho(1-\nu^2)}}$$

(again, $\lambda = n\pi R/\ell$). The second set (5.7) yields torsional modes (i.e., primarily circumferential modes)

$$\begin{aligned} U(x,\theta) &= 0 \\ V(x,\theta) &= B_2 \sin\left(\frac{n\pi x}{\ell}\right) \\ W(x,\theta) &= 0 , \end{aligned} \tag{5.10}$$

with the third frequency corresponding to n given by

$$f_{0n3} = \frac{n}{2\ell}\sqrt{\frac{E}{2\rho(1+\nu)}} .$$

Thus, three frequencies are associated with each wave number n. It can also be seen from (5.9) and (5.10) that the longitudinal-radial modes (from set 1)are uncoupled with the torsional modes (from set 2).

For $n = 1, \ldots, 5$, the three corresponding analytic frequencies together with cubic spline and mixed linear/cubic spline approximate frequencies (see Table 4.1) are tabulated in Table 5.3. Cubic spline approximations are obtained using $N = N_u = N_v = N_w = 8$ standard splines while $N = N_u = N_v = N_w = 32$ standard splines were used for the linear/cubic spline case. For both cases $M = M_u = M_v = M_w = 0$. Note that in all simulations, we employ the same partition along the x axis when creating splines for the u, v, w, directions, hence N will be used to denote the uniform discretization levels. The same is true for the the equal Fourier limits on the θ-axis where we denote all Fourier limits by M. Frequencies corresponding to torsional modes are boxed to facilitate comparison with torsional frequencies of the fixed-edge shell.

To illustrate the quadratic rate of convergence of mixed linear/cubic spline basis functions, additional approximations were done using $N = 8$ and $N = 16$ standard linear splines. For the three frequencies corresponding to $n = 1$ (266.05, 406.80, 603.83 Hz), the relative error was divided by the relative error when N was doubled. In Table 5.4, it is seen that each of the three frequencies exhibit a ratio of almost four indicating $\mathcal{O}(h_x^2)$ convergence rate of the method. We point out that the cubic spline method converges at a $\mathcal{O}(h_x^4)$ convergence rate leading to the highly accurate values with $N = 8$ in Table 5.3.

To illustrate the expected trigonometric properties of modes and uncoupling of the torsional modes with the longitudinal-radial modes, we plot cross sections of the nonzero components of (5.9) and (5.10) along the line $\theta = 0$ in Figure 5.1 and Figure 5.2. Frequencies corresponding to $n = 1$ are in Figure 5.1 while $n = 2$ frequencies are plotted in Figure 5.2; in both cases, modes are approximated using purely cubic spline bases with $M = 0$ and $N = 16$. The figures illustrate that torsional modes corresponding to the 266.05 and 532.11 frequencies are linearly independent with the

n	Analytic Frequencies			Cubic Spline Approx			Linear Spline Approx		
1	266.05	406.80	603.83	266.06	406.80	603.83	266.19	406.99	603.87
2	531.53	532.11	924.29	531.53	532.11	924.29	531.71	533.18	925.95
3	541.03	798.16	1362.11	541.03	798.22	1362.19	541.25	801.79	1368.07
4	543.53	1064.22	1807.86	543.58	1064.82	1808.81	543.85	1072.81	1822.21
5	544.60	1330.27	2255.52	544.85	1333.95	2262.44	545.06	1347.10	2283.78

Table 5.3: Simply supported analytic and approximate frequencies (obtained using $N = 8$ cubic splines and $N = 32$ linear splines) with $m = 0$. The frequencies of the torsional modes are boxed.

longitudinal-radial modes. Figures corresponding to the remaining frequencies indicate the same linear independence, and furthermore, that U and V components obey the phase shift in (5.9). We point out that *cross section* plots of the remaining modes illustrate similar results (for the rest of the plots, see [22]).

(ii) Purely Extensional Modes ($\mathbf{m \geq 1, n = 0}$)

For each wave number m, the two sets (5.4) and (5.7) yield the analytic modes

$$\begin{aligned} U(x,\theta) &= A_1 \cos(m\theta) & & U(x,\theta) &= A_2 \sin(m\theta) \\ V(x,\theta) &= 0 \qquad , \text{ and} & & V(x,\theta) &= 0 \\ W(x,\theta) &= 0 & & W(x,\theta) &= 0 \ , \end{aligned} \tag{5.11}$$

with frequencies

$$f_{mo} = \frac{m}{R}\sqrt{\frac{E}{2\rho(1+\nu)}} \ . \tag{5.12}$$

Note that the modes have purely longitudinal components.

Approximation was performed using $N = 8$ standard cubic splines. In Table 5.5, we compare analytic frequencies (obtained from (5.12)) corresponding to wave numbers $m = 1, 2, 3$ with approximate frequencies. For each frequency, cross sections of the two resulting modes along the left end of the shell ($x = 0, 0 \leq \theta \leq 2\pi$) are plotted

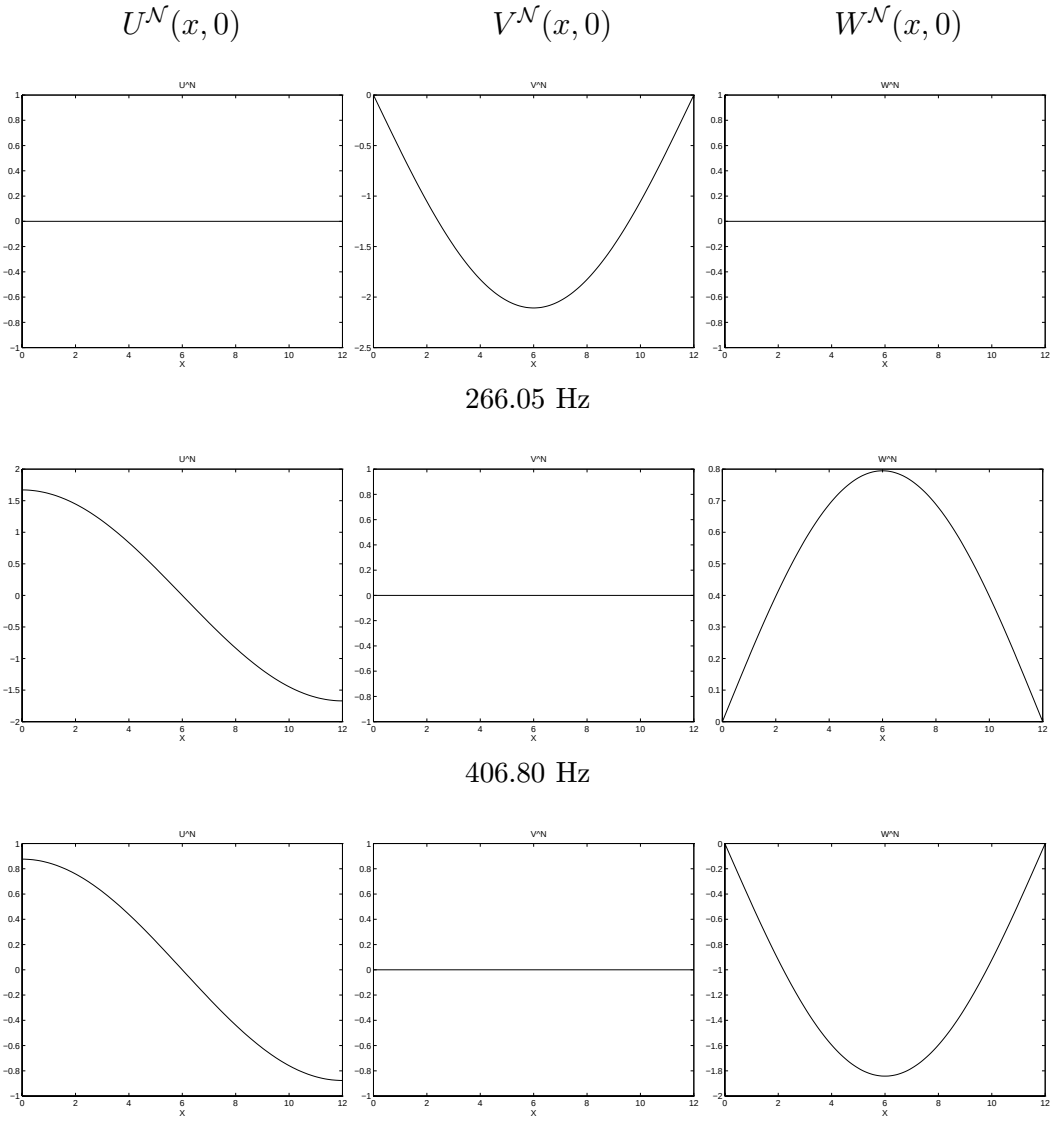

Figure 5.1: Simply supported axisymmetric modes $U^{\mathcal{N}}(x,0), V^{\mathcal{N}}(x,0)$ and $W^{\mathcal{N}}(x,0)$ corresponding to the 266.05, 406.80 and 603.83 Hz natural frequencies $(m=0, n=1)$.

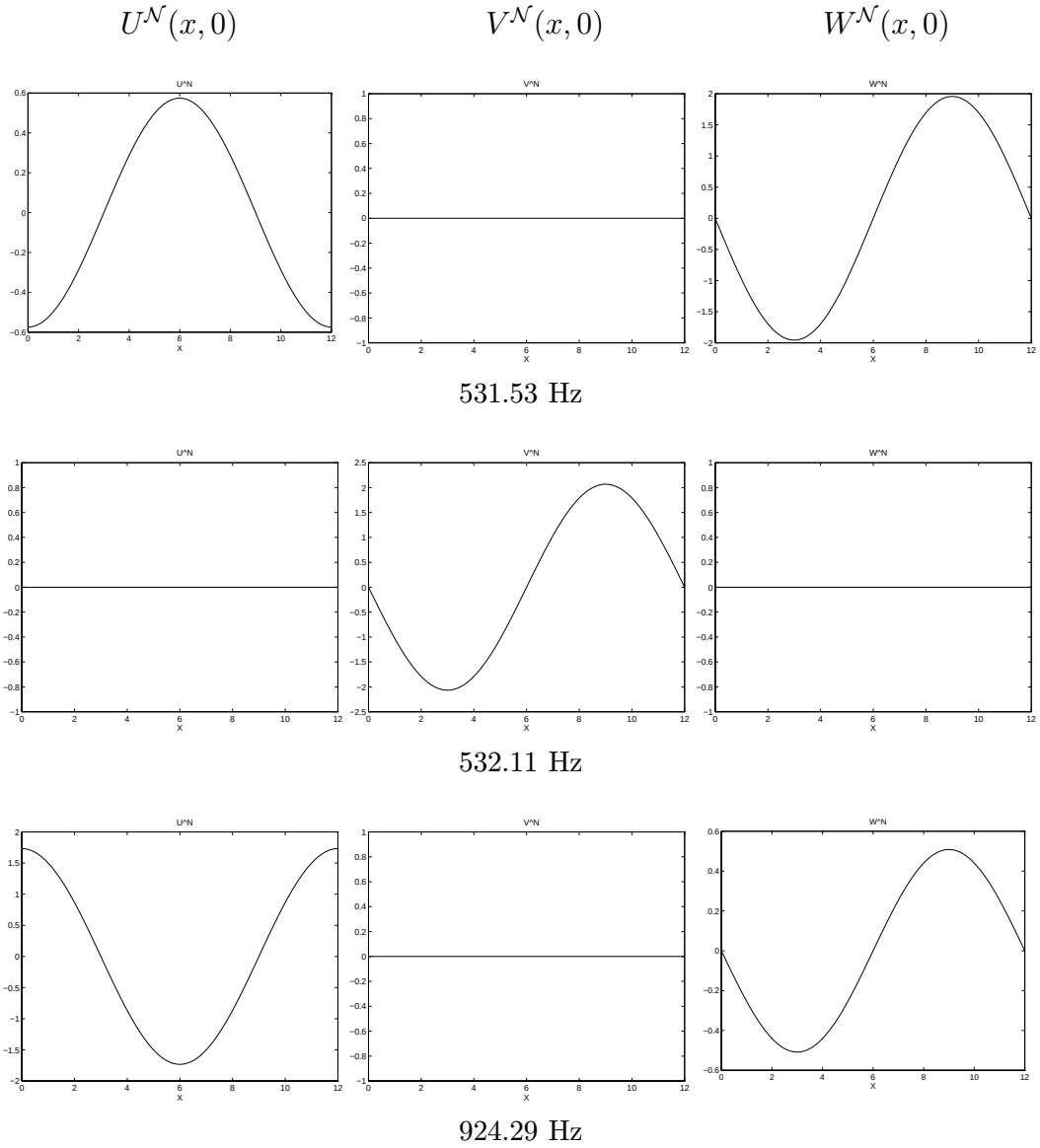

Figure 5.2: Simply supported axisymmetric modes $U^{\mathcal{N}}(x,0), V^{\mathcal{N}}(x,0)$ and $W^{\mathcal{N}}(x,0)$ corresponding to the 531.53, 532.11 and 924.29 Hz natural frequencies $(m=0, n=2)$.

		Linear Spline Approx		
N=8	Approx Freq	267.77	409.40	604.24
	Rel. Error	.646-2	.639-2	.679-3
N=16	Approx Freq	266.48	407.45	603.93
	Rel. Error	.161-2	.160-2	.166-3
	$\frac{\text{Rel. Err. N=16}}{\text{Rel. Err. N=8}}$	4.012	3.993	3.994
N=32	Approx Freq	266.19	406.99	603.87
	Rel. Error	.526-3	.467-3	.662-4
	$\frac{\text{Rel. Err. N=32}}{\text{Rel. Err. N=16}}$	4.020	4.010	4.106

Table 5.4: Linear spline approximates to the simply supported axisymmetric frequencies 266.05, 406.80 and 603.83 Hz with $n = 1$. The observation that the ratios obtained by dividing the relative error by the previous error are approximately 4 illustrates the $\mathcal{O}(h_x^2)$ convergence of the method.

	Analytic	Galerkin
$m = 1, n = 0$	338.75	338.75
$m = 2, n = 0$	677.50	677.50
$m = 3, n = 0$	1016.25	1016.25

Table 5.5: Simply supported analytic and approximate frequencies obtained using $N = 8$ cubic splines.

in the left column of Figure 5.3. Note that only the nonzero longitudinal component of the modes are presented. The right column of Figure5.3 contains longitudinal components of two analytic modes (from (5.11)), which shows agreement with analytic and computed mode shapes.

(iii) General Modes ($\mathbf{m \geq 1, n \geq 1}$)

For the general case, analytic natural frequencies are obtained from (5.6) and approximated using 8 standard cubic splines ($N = 8$) and 3 Fourier modes ($M = 3$).

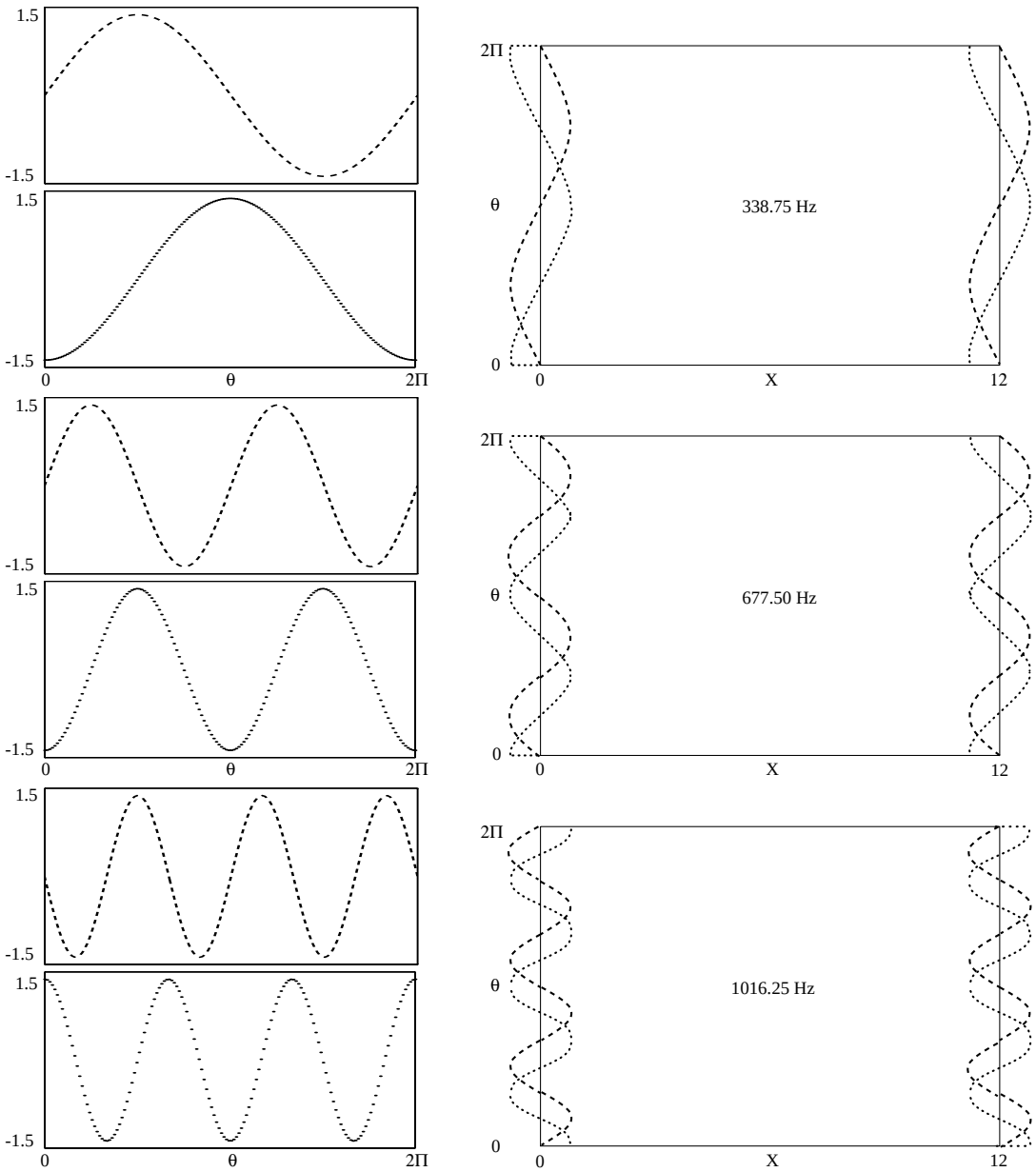

Figure 5.3: Purely extensional modes in the longitudinal direction. Approximate modes in left column $U^{\mathcal{N}}(0,\theta)$ was discretized with $N = 8$ while analytic modes are depicted in right column.

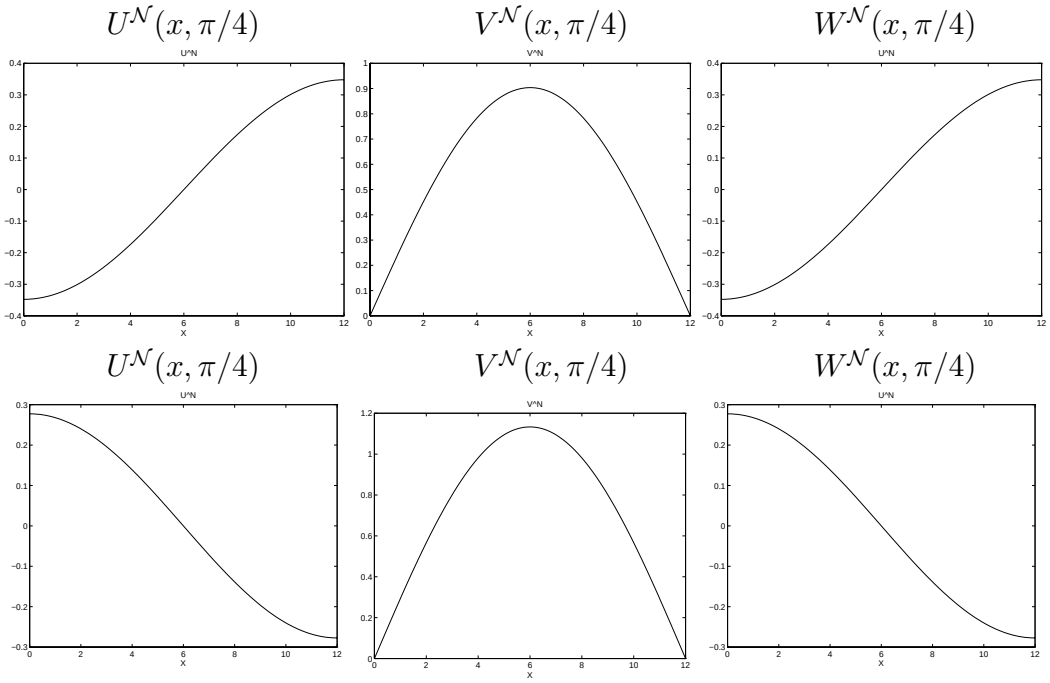

Figure 5.4: Components of the 147.09 Hz modes along the line $\theta = \pi/4$.

In Table 5.6, all frequencies from $m = 0, \ldots, 3$ and $n = 0, \ldots, 5$ are presented (including purely axisymmetric and purely extensional frequencies). The convergence of cubic splines is illustrated in Table 5.7, where frequencies obtained with wave numbers $m = 0, \ldots, 3$, $n = 5$ were computed using two discretization levels $N = 8$ and $N = 16$. A check of the relative errors indicate that the method is converging more quickly than the expected $\mathcal{O}(h_x^4)$ rate.

Modes corresponding to the natural frequencies 147.09, 508.59 and 873.61 (i.e., wave numbers $m = n = 1$) are illustrated by plotting the longitudinal, circumferential and transverse components of the modal displacements at line $\theta = \pi/4$, in Figure 5.4-5.6. The figures illustrate the coupling between the three components of the modal displacements.

Analytic Frequencies				Galerkin Approximates			
$m = 0$				$m = 0$			
$n = 1$	266.05	406.80	603.83	$n = 1$	266.06	406.80	603.83
$n = 2$	531.53	532.11	924.29	$n = 2$	531.53	532.11	924.29
$n = 3$	541.03	798.16	1362.11	$n = 3$	541.03	798.22	1362.19
$n = 4$	543.53	1064.22	1807.86	$n = 4$	543.58	1064.82	1808.81
$n = 5$	544.60	1330.27	2255.52	$n = 5$	544.85	1333.95	2262.44
$m = 1$				$m = 1$			
$n = 0$		338.75		$n = 0$		338.75	
$n = 1$	147.09	508.59	873.61	$n = 1$	147.09	508.59	873.61
$n = 2$	327.96	714.55	1115.55	$n = 2$	327.96	714.44	1115.55
$n = 3$	434.81	909.78	1486.93	$n = 3$	434.83	909.85	1487.00
$n = 4$	483.84	1137.35	1900.34	$n = 4$	483.92	1138.09	1901.13
$n = 5$	507.08	1383.62	2329.09	$n = 5$	507.48	1388.30	2335.07
$m = 2$				$m = 2$			
$n = 0$		677.50		$n = 0$		677.50	
$n = 1$	64.56	755.92	1340.06	$n = 1$	64.56	755.92	1340.06
$n = 2$	187.34	917.53	1521.01	$n = 2$	187.35	917.53	1521.01
$n = 3$	296.26	1100.21	1804.82	$n = 3$	296.28	1100.29	1804.85
$n = 4$	373.46	1300.70	2153.02	$n = 4$	373.61	1301.67	2153.52
$n = 5$	423.98	1519.53	2536.80	$n = 5$	424.54	1521.01	2540.73
$m = 3$				$m = 3$			
$n = 0$		1016.25		$n = 0$		1016.25	
$n = 1$	33.48	1061.88	1858.96	$n = 1$	33.48	1061.88	1858.96
$n = 2$	111.09	1177.72	2001.04	$n = 2$	111.09	1177.73	2001.04
$n = 3$	198.51	1332.12	2225.92	$n = 3$	198.54	1332.21	2225.94
$n = 4$	275.56	1509.99	2514.74	$n = 4$	275.76	1511.08	2515.01
$n = 5$	336.44	1706.31	2848.26	$n = 5$	337.29	1714.42	2850.19

Table 5.6: General frequencies approximated with $N = 8, M = 3$ fully cubic spline basis functions.

$m=0, n=5$			
$N=8$	544.85	1333.95	2262.44
$N=16$	544.60	1330.30	2255.57
Analytic	544.60	1330.27	2255.52
$m=1, n=5$			
$N=8$	507.48	1388.30	2335.07
$N=16$	507.08	1383.66	2329.14
Analytic	507.08	1383.62	2329.09

$m=2, n=5$			
$N=8$	424.54	1521.01	2540.73
$N=16$	423.99	1519.56	2536.84
Analytic	423.98	1519.53	2536.80
$m=3, n=5$			
$N=8$	337.27	1714.42	2850.19
$N=16$	336.45	1706.35	2848.28
Analytic	336.44	1706.31	2848.26

Table 5.7: Accuracy of cubic spline frequency approximation using $N = 8, 16$ and $M = 3$ standard basis functions (with wave numbers $m = 0, \ldots 3, n = 5$).

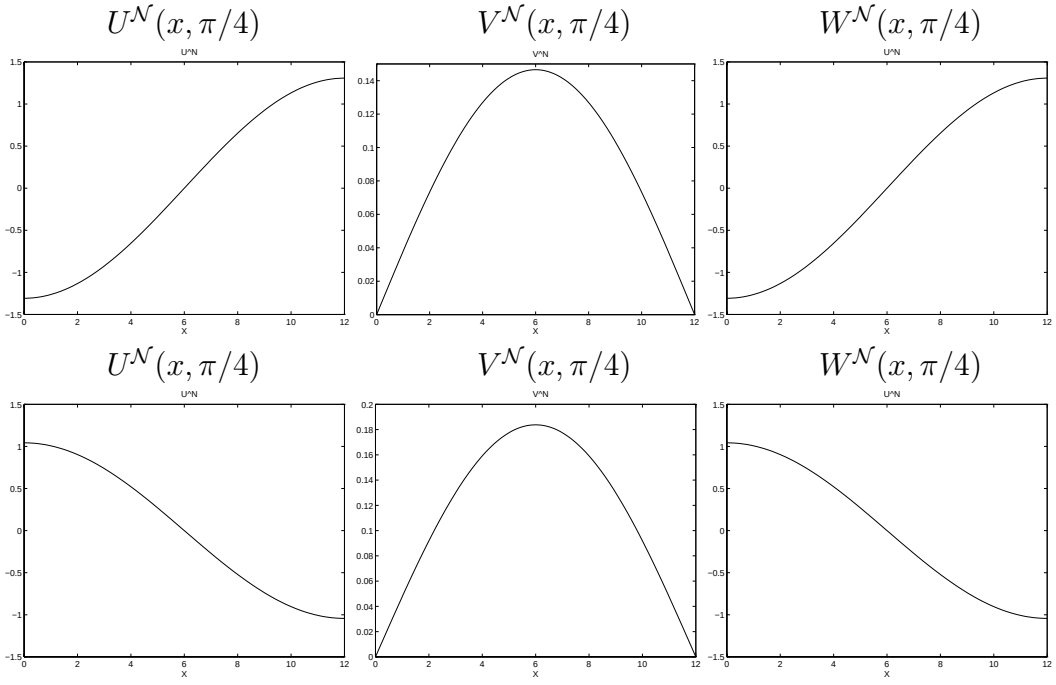

Figure 5.5: Components of the 508.59 Hz modes along the line $\theta = \pi/4$.

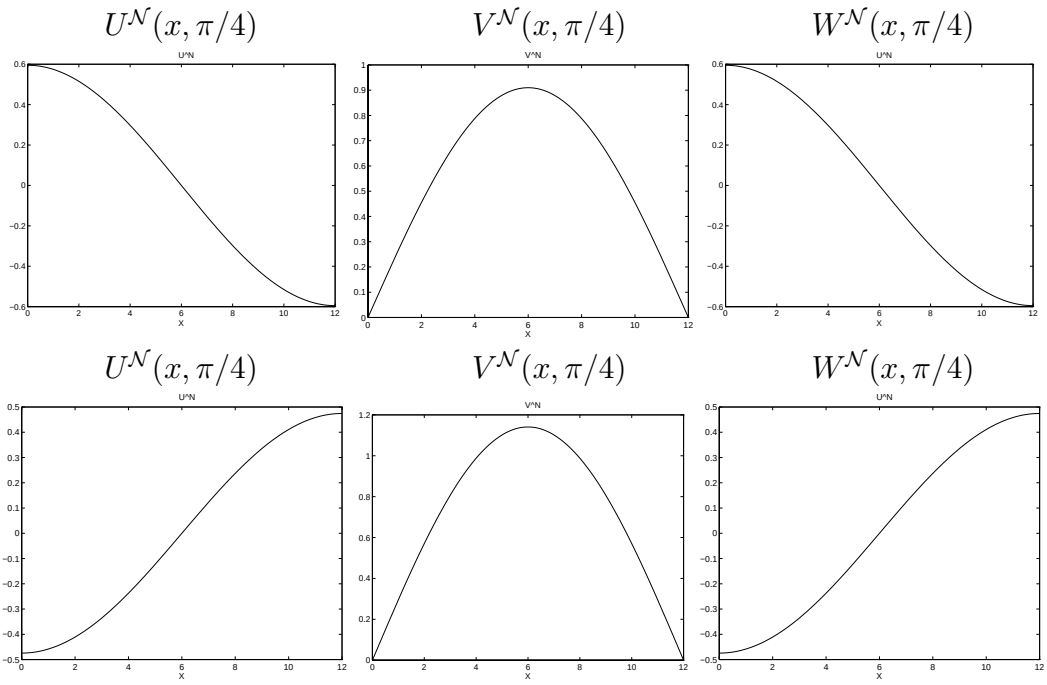

Figure 5.6: Components of the 1873.61 Hz modes along the line $\theta = \pi/4$.

Fixed-Edge shell with no damping, devoid of patches and constant parameters

As in the previous example, natural frequencies are computed by solving the eigenvalue problem (5.8) where basis functions are modified to satisfy the fixed-edge boundary conditions (2.5). In Table 5.8 we summarize the computed axisymmetric frequencies obtained using Fourier/cubic spline basis functions with discretization limits $M = 0$ and $N = 16$. Only the torsional frequencies match with the axisymmetric frequencies of the simply supported shell given in Table 5.3 (the torsional frequencies are boxed to facilitate comparison). The torsional modes, some of which are illustrated in Figure 5.7, are identical with the simply supported case (see Figure 5.1).

While the torsional modes match for the two sets of boundary conditions, this is not true for general modes. We illustrate this in Figures 5.8 and 5.9 where we plot modes corresponding to similar frequencies and wave numbers. Specifically, Figure 5.8 shows modes corresponding to the 541.76 Hz natural frequency of the clamped shell together with the 543.53 Hz modes of the simply supported shell, and Figure 5.9 depicts the modes for the 545.56 Hz fixed-edge and 545.66 Hz simply supported natural frequencies. The plots show that while the qualitative mode shapes are somewhat similar for the two boundary conditions, the fixed-edge shell, unlike the simply supported shell, does not demonstrate the trigonometric relations in its modes. Thus, when modal expansions are employed in applications such as simulations, parameter identification or control, the model must be *consistent* with the physical system.

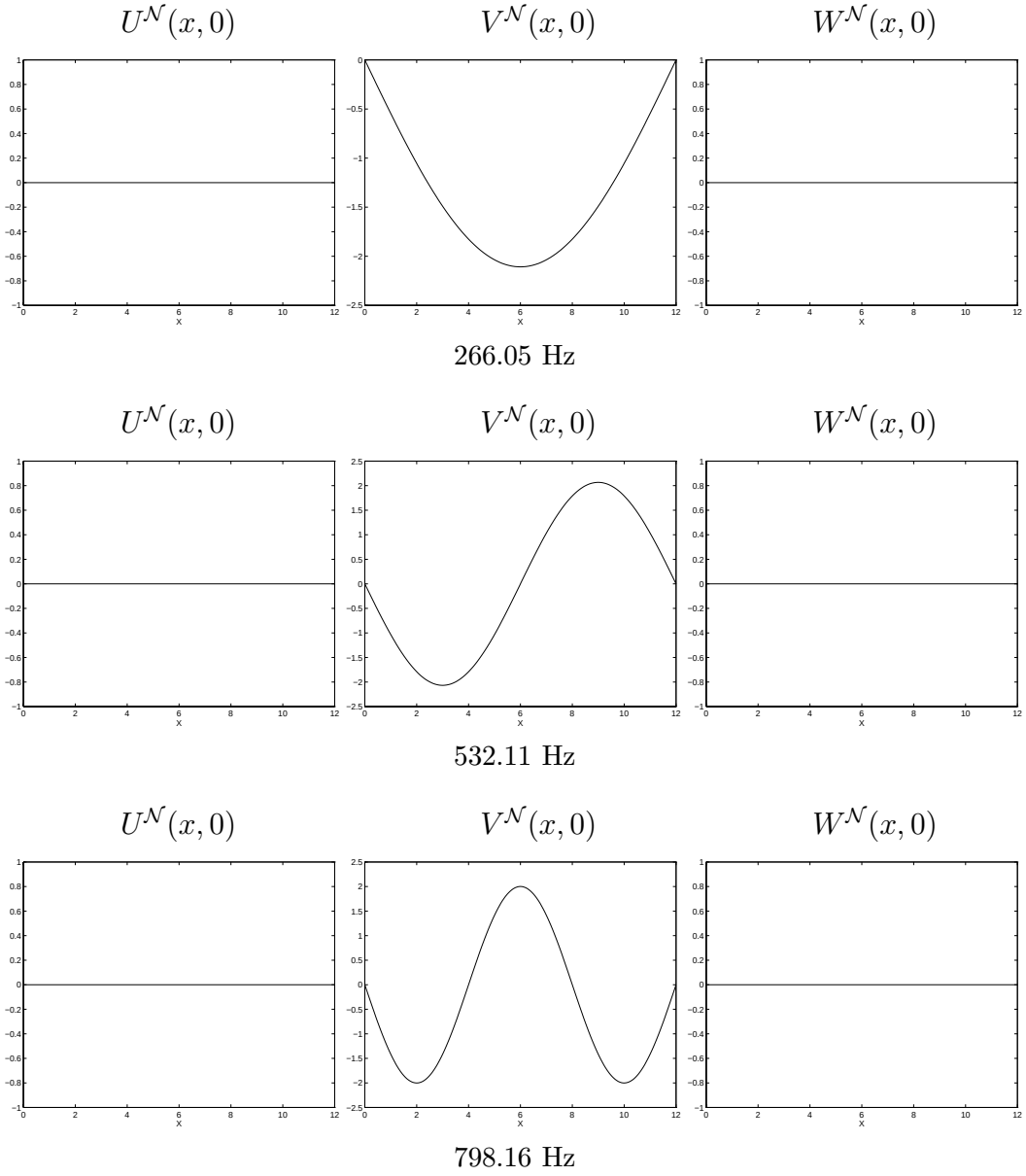

Figure 5.7: Fixed-edge axisymmetric torsional modes $U^{\mathcal{N}}(x,0), V^{\mathcal{N}}(x,0)$ and $W^{\mathcal{N}}(x,0)$ corresponding to the 266.05, 532.11 and 798.16 Hz natural frequencies.

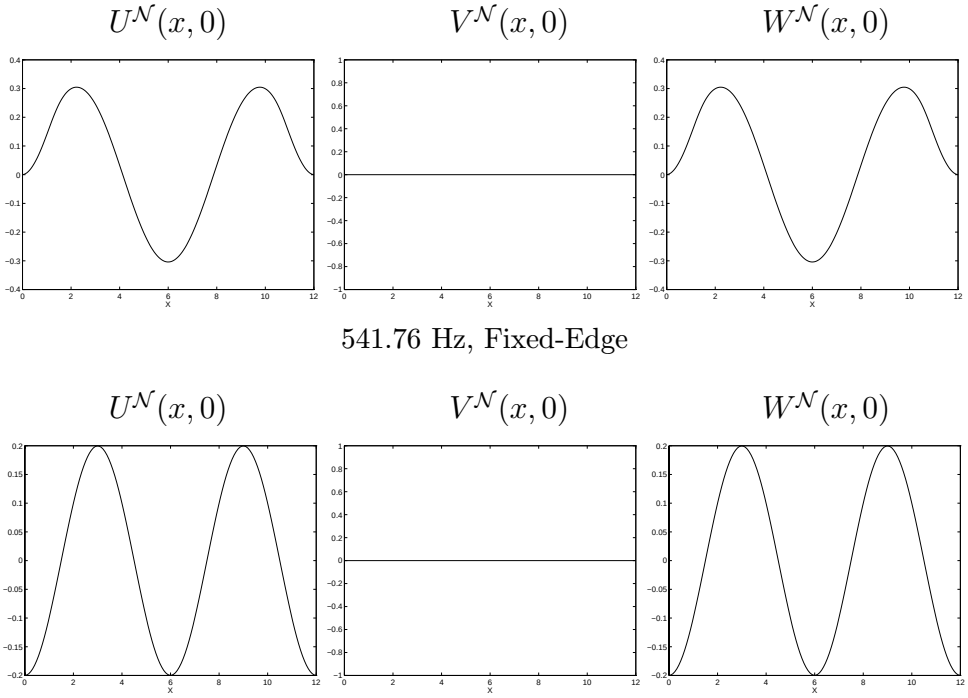

Figure 5.8: Axisymmetric modes $U^{\mathcal{N}}(x,0), V^{\mathcal{N}}(x,0)$ and $W^{\mathcal{N}}(x,0)$ corresponding to the fixed-edge 541.76 Hz frequency and simply supported 543.33 Hz frequency.

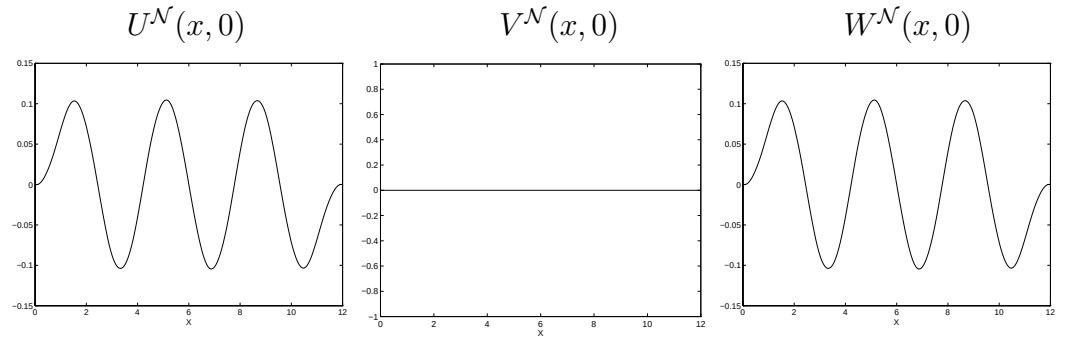

545.56 Hz, Fixed-Edge

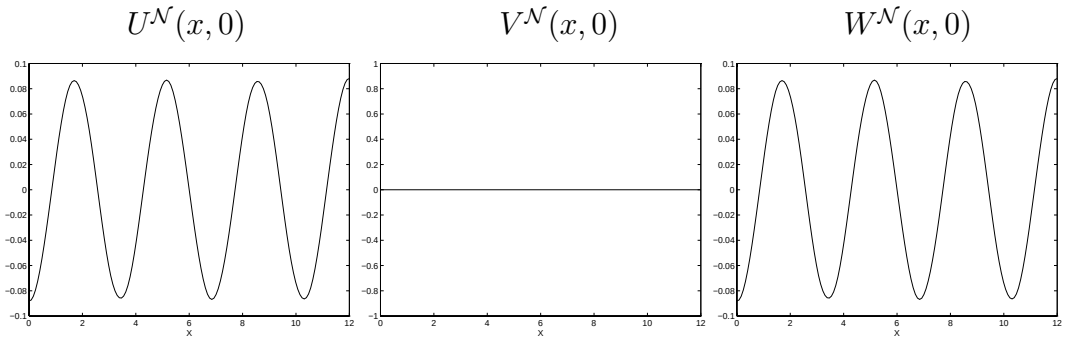

545.66 Hz, Simply Supported

Figure 5.9: Axisymmetric modes $U^{\mathcal{N}}(x,0), V^{\mathcal{N}}(x,0)$ and $W^{\mathcal{N}}(x,0)$ corresponding to the fixed-edge 545.56 Hz frequency and simply supported 545.66 Hz frequency.

Fixed-edge axisymmetric approximate frequencies					
266.05	410.10	532.11	1806.93	1862.80	2129.72
533.22	541.76	543.99	2254.85	2397.95	2669.00
544.96	545.56	546.07	2703.58	2945.38	3153.02
546.69	547.63	549.25	3230.49	3527.16	3603.61
552.18	557.39	565.57	3833.08	4056.54	4119.08
571.17	575.20	599.46	4514.29	4981.08	5167.03
798.16	921.82	1064.22	5172.22	5462.62	5963.62
1330.30	1360.78	1596.45	6480.17	6962.94	8734.17
			8742.91		

Table 5.8: Cubic spline approximates of fixed-edge axisymmetric frequencies obtained with $M = 0$ and $N = 16$.

5.1.2 Uncontrolled Simulations

Numerical examples are presented in this section to further validate the approximation method and to show the expected $\mathcal{O}(h_x^2)$ and $\mathcal{O}(h_x^4)$ convergence of linear and cubic splines, respectively. In the first two examples, known solutions are used to calculate the corresponding force input which are then employed to excite the shell. In the third example, a broadband shell response was obtained by modeling a voltage spike to a pair of identical patches bonded to the inner and outer surfaces of the shell. The excited frequencies are compared with those obtained by solving the matrix eigenvalue problem (5.8) to illustrate the consistency among techniques. Boundary conditions modeling a fixed-edge shell are used in the three examples; shell parameters and coefficients in the English system are given in Table 5.1.

Steady State Solution

Time independent displacements satisfying fixed-edge boundary conditions are taken to be

$$\begin{aligned} u(x,\theta) &= \sin(2\pi x/\ell)\sin(\theta) \\ v(x,\theta) &= \sin(4\pi x/\ell)\sin(2\theta) \\ w(x,\theta) &= [\cos(2\pi x/\ell)-1]\cos(3\theta)\ . \end{aligned} \tag{5.13}$$

Plots of these displacements are shown in Figure 5.10 to illustrate that significant bending deformations are present. The forcing functions given below were obtained by substituting the true solutions (5.13) into the shell equations (2.1), and solving for the functions $\hat{q}_x(x,\theta), \hat{q}_\theta(x,\theta)$ and $\hat{q}_\eta(x,\theta)$, yielding

$$\begin{aligned} \hat{q}_x(x,\theta) &= \frac{Eh}{1-\nu^2}\left[\left(\frac{2\pi}{\ell}\right)^2 \sin\left(2\pi\frac{x}{\ell}\right)\sin(\theta)\right. \\ &\qquad \left. -\frac{\nu 8\pi}{R\ell}\cos\left(4\pi\frac{x}{\ell}\right)\cos(2\theta)+\frac{\nu 2\pi}{R\ell}\sin\left(2\pi\frac{x}{\ell}\right)\cos(3\theta)\right] \\ &- \frac{Eh}{2(1+\nu)}\left[\frac{8\pi}{\ell}\cos\left(4\pi\frac{x}{\ell}\right)\cos(2\theta)-\frac{1}{R}\sin\left(2\pi\frac{x}{\ell}\right)\sin(\theta)\right]\ , \end{aligned} \tag{5.14}$$

$$\begin{aligned} \hat{q}_\theta(x,\theta) &= \frac{Eh}{R(1-\nu^2)}\left[\frac{4}{R}\sin\left(4\pi\frac{x}{\ell}\right)\sin(2\theta)\right. \\ &\qquad \left. +\frac{3}{R\ell}[\cos\left(2\pi\frac{x}{\ell}\right)-1]\sin(3\theta)-\frac{\nu 2\pi}{\ell}\cos\left(2\pi\frac{x}{\ell}\right)\cos(\theta)\right] \\ &+ \frac{Eh}{2(1+\nu)}\left[\left(\frac{4\pi}{\ell}\right)^2\sin\left(4\pi\frac{x}{\ell}\right)\sin(2\theta)-\frac{2\pi}{R\ell}\cos\left(2\pi\frac{x}{\ell}\right)\cos(\theta)\right] \end{aligned} \tag{5.15}$$

and

$$\begin{aligned}
\hat{q}_n(x,\theta) &= \frac{Eh^3}{12(1-\nu^2)}\left[\left(\frac{2\pi}{\ell}\right)^4\cos\left(2\pi\frac{x}{\ell}\right)\cos(3\theta)\right.\\
&\qquad\left.+\frac{9\nu}{R^2}\left(\frac{2\pi}{\ell}\right)^2\cos\left(2\pi\frac{x}{\ell}\right)\cos(3\theta)\right]\\
&+ \frac{Eh^3}{12R^2(1-\nu^2)}\left[\frac{81}{R^2}[\cos\left(2\pi\frac{x}{\ell}\right)-1]\cos(3\theta)\right.\\
&\qquad\left.+9\nu\left(\frac{2\pi}{\ell}\right)^2\cos\left(2\pi\frac{x}{\ell}\right)\cos(3\theta)\right]\\
&+ \frac{Eh^3}{6R^2(1+\nu)}\left[9\left(\frac{2\pi}{\ell}\right)^2\cos\left(2\pi\frac{x}{\ell}\right)\cos(3\theta)\right]\\
&+ \frac{Eh}{R(1-\nu^2)}\left[\frac{2}{R}\sin\left(4\pi\frac{x}{\ell}\right)\cos(2\theta)+\frac{1}{R}[\cos\left(2\pi\frac{x}{\ell}\right)-1]\cos(3\theta)\right.\\
&\qquad\left.+\frac{2\pi\nu}{\ell}\cos\left(2\pi\frac{x}{\ell}\right)\sin(\theta)\right]\ .
\end{aligned}\tag{5.16}$$

Since the problem is time independent, the matrix equation (4.9) reduces to

$$K_E^{\mathcal{N}}\vartheta^{\mathcal{N}} = \hat{F}^{\mathcal{N}}\ ,$$

from which the coefficients $\vartheta^{\mathcal{N}}$ defined in (4.7) are obtained. The approximate solution is then constructed as a linear combination of the basis functions with coefficients from $\vartheta^{\mathcal{N}}$. For the steady state problem, we study two types of axial basis functions: (i) linear splines for u, v and cubic splines for w and (ii) cubic splines for u, v, w. The number of standard splines for the three displacements u, v and w were assumed to be equal and denoted by $N_u = N_v = N_w = N$. To test the expected $\mathcal{O}(h_x^4)$ and $\mathcal{O}(h_x^2)$ convergence rates of the approximations (i) and (ii), respectively, the number of standard cubic splines were doubled from $N = 4, 8$ to 16 (up to $N = 32$ for the mixed linear-cubic spline basis). Due to the nature of the forcing functions (5.14), (5.15) and (5.16), the Fourier limit $M = M_u = M_v = M_w = 3$ was sufficient for resolving the circumferential behavior.

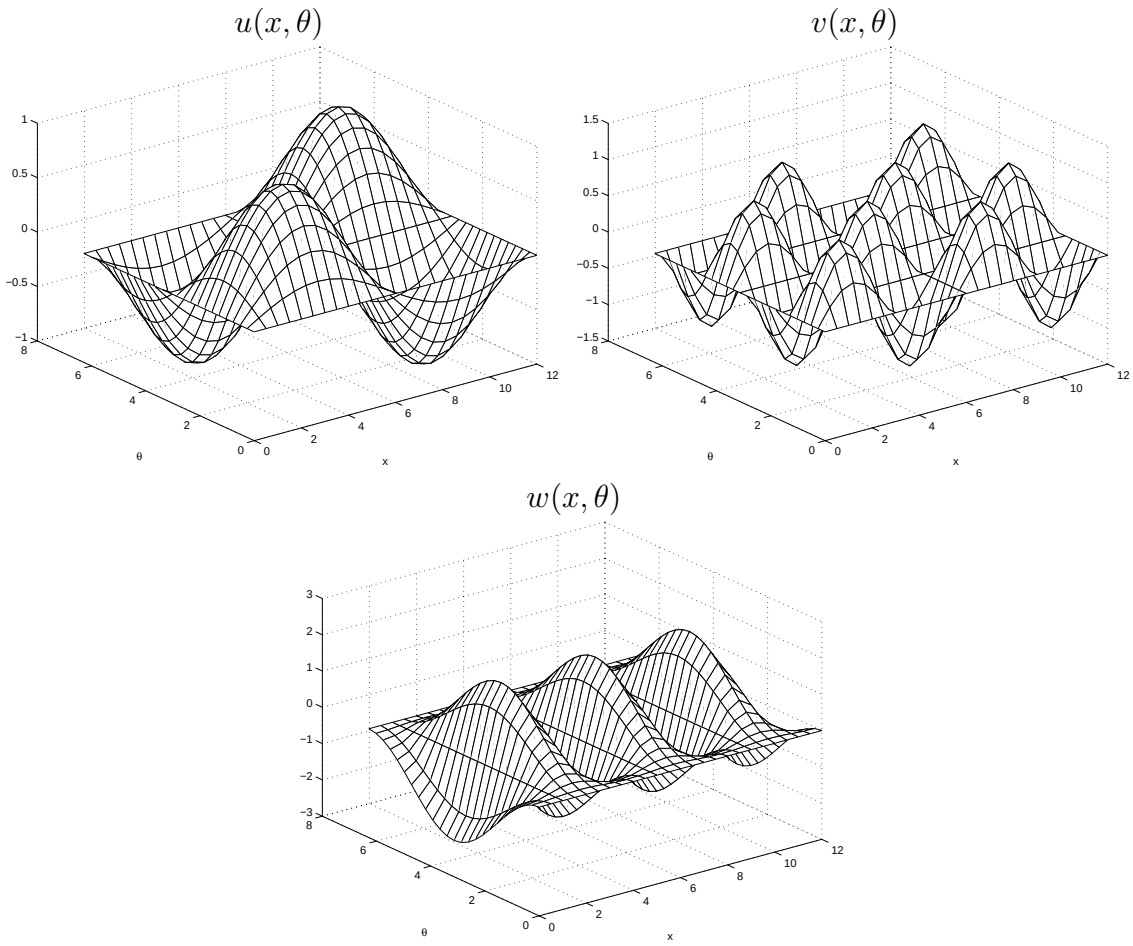

Figure 5.10: True longitudinal, circumferential and transverse displacements for the steady state examples.

	$N=4$	$N=8$	$N=16$	$N=32$
$\mathcal{N}_u=(N_u+1)(2M_u+1)$	35	63	119	231
$\mathcal{N}_v=(N_v-1)(2M_v+1)$	21	49	105	217
$\mathcal{N}_w=(N_w+1)(2M_w+1)$	35	63	119	231
$\mathcal{N}=\mathcal{N}_u+\mathcal{N}_v+\mathcal{N}_w$	91	175	343	679

Table 5.9: Discretization sizes with mixed linear/cubic spline axial basis functions using $M=M_u=M_v=M_w=3$.

(i) Linear Spline Bases for $\mathbf{u}^{\mathcal{N}}$ and $\mathbf{v}^{\mathcal{N}}$, Cubic Spline Basis for $\mathbf{w}^{\mathcal{N}}$

In this example, we analyze the accuracy and convergence of the method as we employ $N=4,8,16$ and 32 standard splines. The number of modified splines in each direction are given in the last column of Table 4.2 where it could be seen that the axial limits, due to modification of standard splines to fit boundary conditions, are given by $\hat{N}_u = N-1, \hat{N}_v = N-1$ and $\hat{N}_w = N-1$. For each discretization level, we obtain the total number of basis functions by multiplying the axial limits $\hat{N}_u, \hat{N}_v, \hat{N}_w$ with the Fourier limit $2M+1$, where $M=3$. The total number of basis functions for the different number of axial splines are summarized in Table 5.9.

In Figures 5.11, 5.12 and 5.13, the approximate displacements in the u, v and w directions, respectively, illustrate the convergence of the approximations as the discretization level increases from $N=4$ to $N=32$. The figures seem to indicate that the computed solution is converged with $N=32$, and this is validated by showing that the absolute errors are small (in comparison with the lesser discretization levels) at $N=32$ (see Table 5.10). We obtain the absolute errors by computing the l_∞-norm of the difference between true and computed solution over 25×25 grid evaluations points (grid points are in x and θ). The expected $\mathcal{O}(h_x^2)$ convergence with this choice of basis functions is illustrated in Table 5.11, where a ratio around 4 results when the absolute error at discretization level N is divided by the absolute error at $2N$.

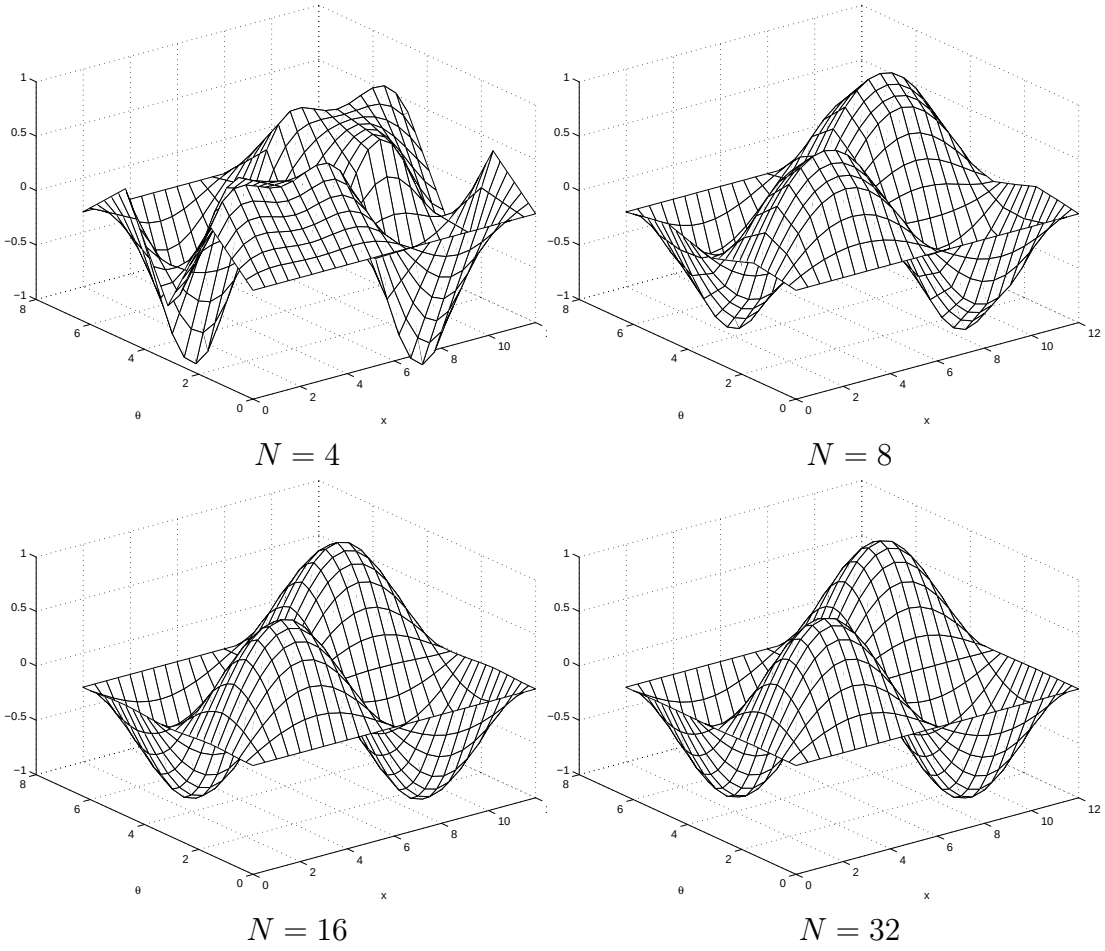

Figure 5.11: Approximate longitudinal displacement $w^{\mathcal{N}}$ with $N = 4, 8, 16$ and 32 using mixed linear and cubic spline axial basis functions for the steady state example.

	$N = 4$	$N = 8$	$N = 16$	$N = 32$
u	5.010×10^{-1}	1.266×10^{-1}	3.277×10^{-2}	7.751×10^{-3}
v	1.580×10^{0}	2.962×10^{-1}	8.313×10^{-2}	2.197×10^{-2}
w	1.864×10^{0}	4.903×10^{-1}	1.236×10^{-1}	3.784×10^{-2}

Table 5.10: Absolute errors in the longitudinal (u), circumferential (v) and transverse displacements (w) with mixed linear and cubic spline axial basis functions for the steady state example.

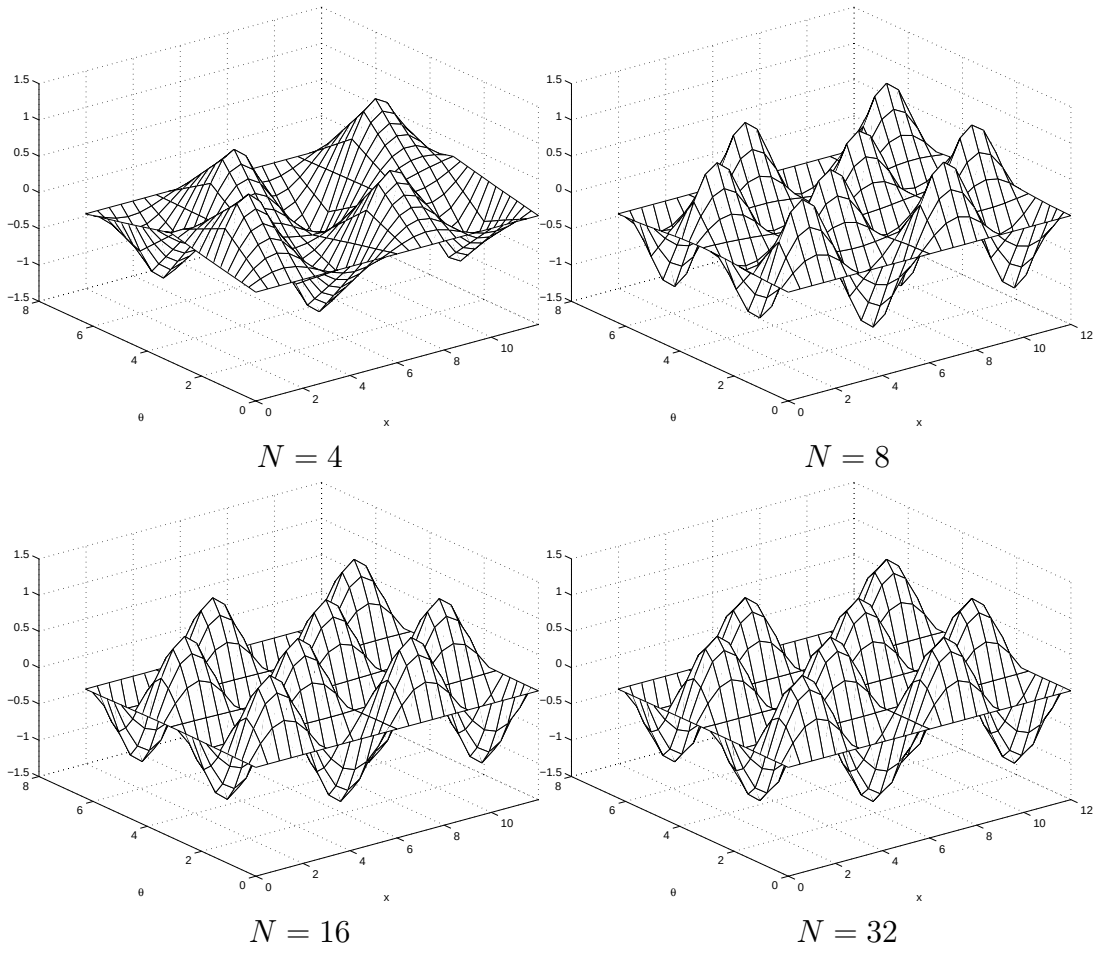

Figure 5.12: Approximate circumferential displacement $v^{\mathcal{N}}$ with $N = 4, 8, 16$ and 32 using mixed linear and cubic spline axial basis functions for the steady state example.

	$\frac{N=4}{N=8}$	$\frac{N=8}{N=16}$	$\frac{N=16}{N=32}$
u	3.956	3.863	4.228
v	5.336	3.563	3.785
w	3.801	3.966	3.268

Table 5.11: $\mathcal{O}(h_x^2)$ convergence with mixed linear/cubic splines, steady state

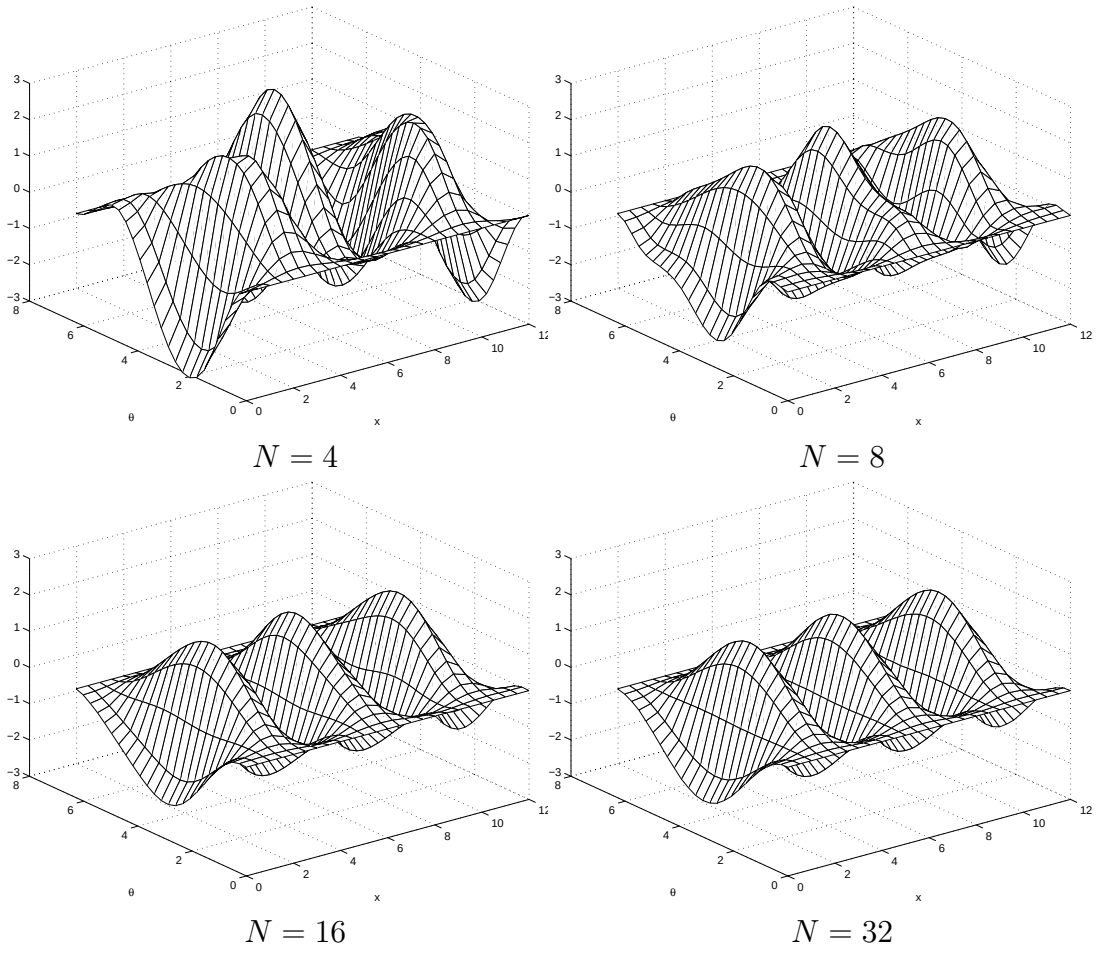

Figure 5.13: Approximate transverse displacement $w^{\mathcal{N}}$ with $N = 4, 8, 16$ and 32 using mixed linear and cubic spline axial basis functions for the steady state example.

	$N = 4$	$N = 8$	$N = 16$
$\mathcal{N}_u = (N_u + 1)(2M_u + 1)$	35	63	119
$\mathcal{N}_v = (N_v + 1)(2M_v + 1)$	35	63	119
$\mathcal{N}_w = (N_v - 1)(2M_w + 1)$	21	49	105
$\mathcal{N} = \mathcal{N}_u + \mathcal{N}_v + \mathcal{N}_w$	91	175	343

Table 5.12: Discretization sizes with cubic spline axial basis functions with $M = M_u = M_v = M_w = 3$.

(ii) Cubic Spline Bases for $\mathbf{u}^{\mathcal{N}}, \mathbf{v}^{\mathcal{N}}$ and $\mathbf{w}^{\mathcal{N}}$

As in the previous example, the total number of axial splines for each direction is given in the last column of Table 4.2. Using the Fourier limit of $M = 3$, we indicate the total number of basis functions for each discretization level $N = 4, 8, 16$ in Table 5.12. Unlike the mixed linear-cubic spline case, the discretization level $N = 32$ was not considered due to the faster convergence and better accuracy of the purely cubic spline basis.

Better accuracy of the method (than with mixed linear/cubic splines) is illustrated in Table 5.13, where absolute errors for each discretization size are summarized. To further illustrate this accuracy, we plot the errors for $N = 4$ in Figure 5.14. Errors for $N = 8$ and $N = 16$ are not given since they are graphically indistinguishable from the coordinate plane as compared with the $N = 4$ error. Ratios of the absolute errors are presented in Table 5.14, where it is seen that all ratios are significantly greater than the 16 expected value for an exact $\mathcal{O}(h_x^4)$ method.

$e_u(x,\theta)$ $e_v(x,\theta)$

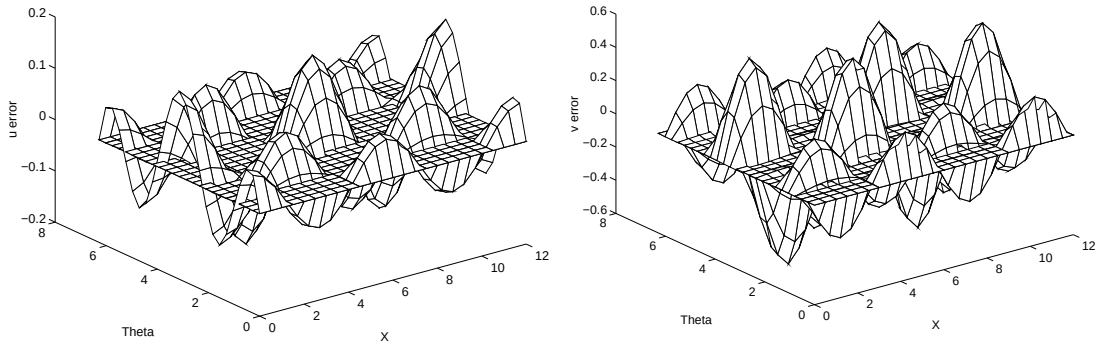

$e_w(x,\theta)$

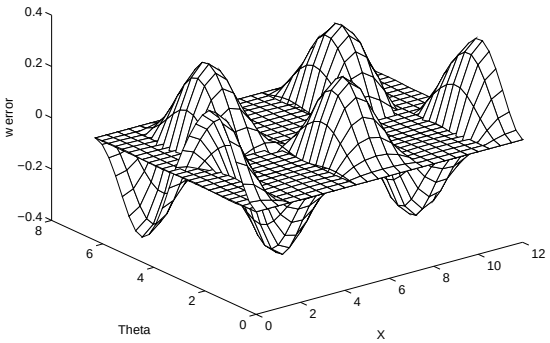

Figure 5.14: Errors e_u, e_v, e_w in the u, v and w directions using cubic spline axial basis functions with $N = 4$ for the steady state example.

	$N = 4$	$N = 8$	$N = 16$
u	1.663×10^{-1}	2.003×10^{-3}	3.936×10^{-5}
v	5.687×10^{-1}	1.501×10^{-2}	6.235×10^{-4}
w	3.136×10^{-1}	4.075×10^{-3}	5.552×10^{-5}

Table 5.13: Absolute errors in the longitudinal (u), circumferential (v) and transverse displacements (w) with cubic spline axial basis functions for the steady state example.

	$\frac{N=4}{N=8}$	$\frac{N=8}{N=16}$
u	83.052	50.888
v	37.899	24.069
w	76.961	73.395

Table 5.14: $\mathcal{O}(h_x^4)$ convergence with cubic splines, steady state.

Time-dependent Solution

A time-dependent solution satisfying the clamped-edge boundary conditions is considered here. The true solutions, chosen as in the previous example to exhibit significant bending deformations, are given by

$$\begin{aligned} u(x,\theta,t) &= t^2 \sin(2\pi x/\ell)\sin(\theta) \\ v(x,\theta,t) &= t^2 \sin(4\pi x/\ell)\sin(2\theta) \\ w(x,\theta,t) &= t^2\Big[\cos(2\pi x/\ell) - 1\Big]\cos(3\theta). \end{aligned}$$

Solving for $\hat{q}_x, \hat{q}_\theta$ and $\hat{q}_\eta$ in the strong form of the equations (2.1) yields the forcing functions

$$\begin{aligned} \hat{q}_x(x,\theta,t) &= 2\rho h \sin\left(2\pi\frac{x}{\ell}\right)\sin(\theta) \\ &+ t^2\left[\frac{4\pi^2 Eh}{\ell^2(1-\nu^2)}\sin\left(2\pi\frac{x}{\ell}\right)\sin(\theta) - \frac{8\pi\nu Eh}{R\ell(1-\nu^2)}\cos\left(4\pi\frac{x}{\ell}\right)\cos(2\theta)\right. \\ &\quad + \frac{2\pi\nu Eh}{R\ell(1-\nu^2)}\sin\left(2\pi\frac{x}{\ell}\right)\cos(3\theta) + \frac{Eh}{2R^2\ell(1+\nu)}\sin\left(2\pi\frac{x}{\ell}\right)\sin(\theta) \\ &\quad \left. - \frac{4\pi Eh}{R\ell(1+\nu)}\cos\left(4\pi\frac{x}{\ell}\right)\cos(2\theta)\right] \\ &+ 2t\left[\frac{4\pi^2 c_D h}{\ell^2(1-\nu^2)}\sin\left(2\pi\frac{x}{\ell}\right)\sin(\theta) - \frac{8\pi\nu c_D h}{R\ell(1-\nu^2)}\cos\left(4\pi\frac{x}{\ell}\right)\cos(2\theta)\right. \\ &\quad + \frac{2\pi\nu c_D h}{R\ell(1-\nu^2)}\sin\left(2\pi\frac{x}{\ell}\right)\cos(3\theta) + \frac{c_D h}{2R^2\ell(1+\nu)}\sin\left(2\pi\frac{x}{\ell}\right)\sin(\theta) \\ &\quad \left. - \frac{4\pi c_D h}{R\ell(1+\nu)}\cos\left(4\pi\frac{x}{\ell}\right)\cos(2\theta)\right] , \end{aligned}$$

$$
\begin{aligned}
\hat{q}_\theta(x,\theta,t) &= 2\rho h \sin\left(4\pi\frac{x}{\ell}\right)\sin(2\theta) \\
&+ \quad t^2\left[\frac{3Eh}{R^2(1-\nu^2)}\left(\cos\left(2\pi\frac{x}{\ell}\right)-1\right)\sin(3\theta)+\frac{4Eh}{R^2(1-\nu^2)}\sin\left(4\pi\frac{x}{\ell}\right)\sin(2\theta)\right. \\
&\qquad +\frac{8\pi^2 Eh}{\ell^2(1+\nu)}\sin\left(4\pi\frac{x}{\ell}\right)\sin(2\theta)-\frac{2\pi\nu Eh}{R\ell(1-\nu^2)}\cos\left(2\pi\frac{x}{\ell}\right)\cos(\theta) \\
&\qquad \left.-\frac{\pi Eh}{R\ell(1+\nu)}\cos\left(2\pi\frac{x}{\ell}\right)\cos(\theta)\right] \\
&+ \quad 2t\left[\frac{3c_D h}{R^2(1-\nu^2)}\left(\cos\left(2\pi\frac{x}{\ell}\right)-1\right)\sin(3\theta)+\frac{4c_D h}{R^2(1-\nu^2)}\sin\left(4\pi\frac{x}{\ell}\right)\sin(2\theta)\right. \\
&\qquad +\frac{8\pi^2 c_D h}{\ell^2(1+\nu)}\sin\left(4\pi\frac{x}{\ell}\right)\sin(2\theta)-\frac{2\pi\nu c_D h}{R\ell(1-\nu^2)}\cos\left(2\pi\frac{x}{\ell}\right)\cos(\theta) \\
&\qquad \left.-\frac{\pi Eh}{R\ell(1+\nu)}\cos\left(2\pi\frac{x}{\ell}\right)\cos(\theta)\right]
\end{aligned}
$$

and

$$
\begin{aligned}
\hat{q}_n(x,\theta,t) &= 2\rho h\left[\cos\left(2\pi\frac{x}{\ell}\right)-1\right] \\
&+ \quad t^2\left[\frac{2\pi\nu Eh}{R\ell(1-\nu^2)}\cos\left(2\pi\frac{x}{\ell}\right)\sin(\theta)+\frac{2Eh}{R^2(1-\nu^2)}\sin\left(4\pi\frac{x}{\ell}\right)\cos(2\theta)\right. \\
&\qquad +\frac{16\pi^4 Eh^3}{12\ell^4(1-\nu^2)}\cos\left(2\pi\frac{x}{\ell}\right)\cos(3\theta)+\frac{3\pi^2\nu Eh^3}{R^2\ell^2(1-\nu^2)}\cos\left(2\pi\frac{x}{\ell}\right)\cos(3\theta) \\
&\qquad +\frac{81Eh^3}{12R^4(1-\nu^2)}\left[\cos\left(2\pi\frac{x}{\ell}\right)-1\right]\cos(3\theta)+\frac{3\pi^2\nu Eh^3}{R^2\ell^2(1-\nu^2)}\cos\left(2\pi\frac{x}{\ell}\right)\cos(3\theta) \\
&\qquad \left.+\frac{6\pi^2 Eh^3}{R^2\ell^2(1+\nu)}\cos\left(2\pi\frac{x}{\ell}\right)\cos(3\theta)+\frac{Eh}{R^2(1-\nu^2)}\left[\cos\left(2\pi\frac{x}{\ell}\right)-1\right]\cos(3\theta)\right] \\
&+ \quad 2t\left[\frac{2\pi\nu c_D h}{R\ell(1-\nu^2)}\cos\left(2\pi\frac{x}{\ell}\right)\sin(\theta)+\frac{2c_D h}{R^2(1-\nu^2)}\sin\left(4\pi\frac{x}{\ell}\right)\cos(2\theta)\right. \\
&\qquad +\frac{16\pi^4 c_D h^3}{12\ell^4(1-\nu^2)}\cos\left(2\pi\frac{x}{\ell}\right)\cos(3\theta)+\frac{3\pi^2\nu c_D h^3}{R^2\ell^2(1-\nu^2)}\cos\left(2\pi\frac{x}{\ell}\right)\cos(3\theta) \\
&\qquad +\frac{81c_D h^3}{12R^4(1-\nu^2)}\left[\cos\left(2\pi\frac{x}{\ell}\right)-1\right]\cos(3\theta)+\frac{3\pi^2\nu c_D h^3}{R^2\ell^2(1-\nu^2)}\cos\left(2\pi\frac{x}{\ell}\right)\cos(3\theta) \\
&\qquad \left.+\frac{6\pi^2 c_D h^3}{R^2\ell^2(1+\nu)}\cos\left(2\pi\frac{x}{\ell}\right)\cos(3\theta)+\frac{c_D h}{R^2(1-\nu^2)}\left[\cos\left(2\pi\frac{x}{\ell}\right)-1\right]\cos(3\theta)\right] .
\end{aligned}
$$

Axial cubic spline basis functions were used in the u, v and w displacements and the resulting total number of basis functions corresponding to discretization levels $N =$

	$\frac{\max Re(-\lambda)}{\min Re(-\lambda)}$
$N = 4$	1.846×10^3
$N = 8$	5.761×10^3
$N = 16$	2.204×10^4

Table 5.15: Stiffness ratios for the system matrix $A^{2\mathcal{N}}$ using fully cubic spline axial basis functions.

$4, 8, 16$ are also indicated by Table 5.12. The large eigenvalue ratio summarized in Table 5.15 illustrates the stiffness of the problem. As mentioned earlier, the ordinary differential equation (4.10) was marched in time using a publicly available software package for solving stiff problems given in [19].

The true solutions at time $T = 1.5\ s$ are plotted in Figure 5.15, while the difference between true and approximate solutions using $N = 4$ are reported in Figure 5.16. As in the time-independent example, the difference between true and numerical solutions using $N = 8$ and $N = 16$ are graphically indistinguishable from the coordinate plane and hence are not given here. In Table 5.16, we give the absolute errors in the longitudinal, circumferential and transverse displacements at $T = 1.5\ s$. The same 25×25 grid evaluation points used in the previous example to compute the absolute errors were employed here. The $\mathcal{O}(h_x^4)$ convergence rate of the method with fully cubic spline axial basis is demonstrated in the error ratios reported in Table 5.17, where again, ratios are significantly greater than the expected value of 16. A comparison between the errors in Table 5.16 and steady-state errors in Table 5.13 indicates that they are of the same magnitude while comparison between Tables 5.17 and 5.14 indicates nearly identical error ratios. Tables 5.17 and 5.16 confirm the validity of the method in the damped, time-dependent problem. Hence with fully cubic spline axial basis, the accuracy contributes to the efficiency of the method through reduced system sizes.

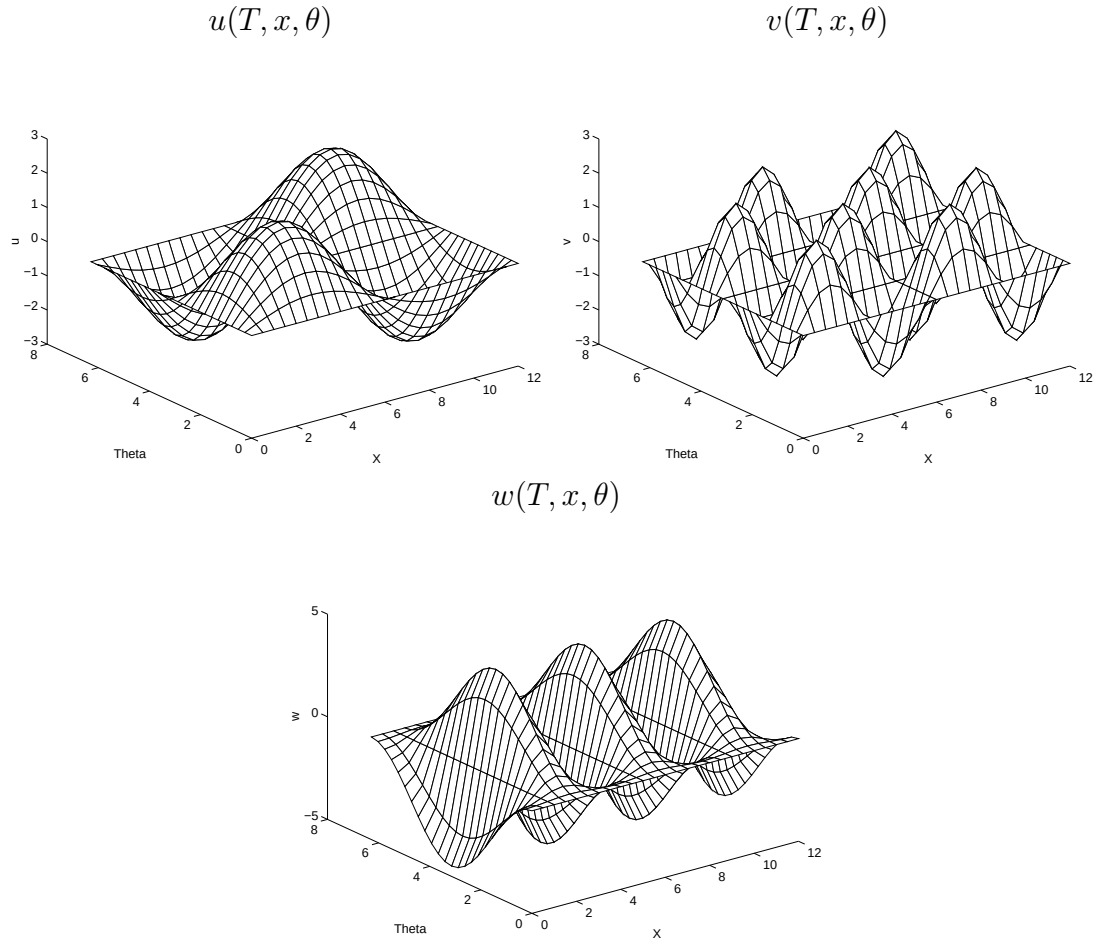

Figure 5.15: True longitudinal, circumferential and transverse displacements for the time dependent example for $T = 1.5$ *sec.*

	$N = 4$	$N = 8$	$N = 16$
u	3.742×10^{-1}	4.506×10^{-3}	8.855×10^{-5}
v	1.280×10^{0}	3.376×10^{-2}	1.403×10^{-3}
w	7.056×10^{-1}	9.169×10^{-3}	1.249×10^{-4}

Table 5.16: Absolute errors in the longitudinal (u), circumferential (v) and transverse displacements (w) with cubic spline axial basis functions for the time dependent example, $T = 1.5$ *sec.*

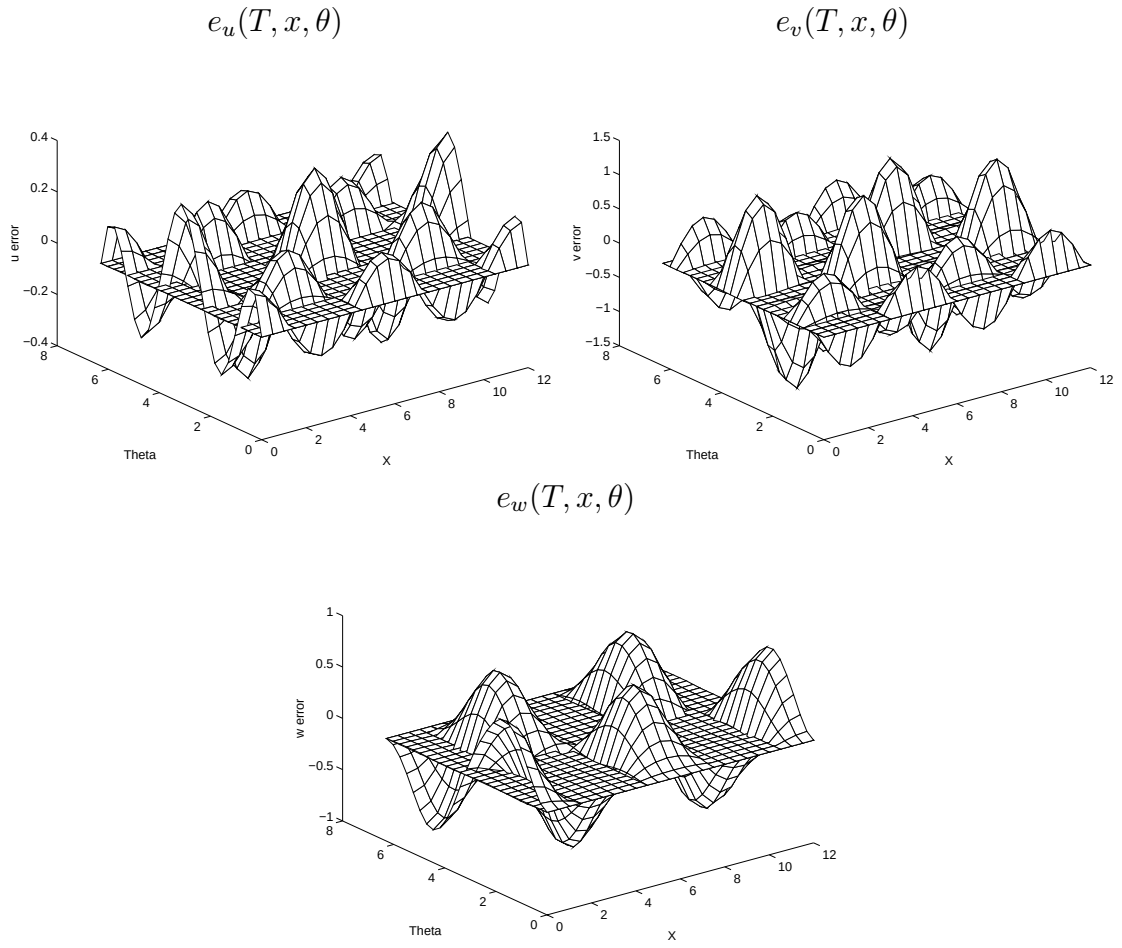

Figure 5.16: Errors e_u, e_v, e_w in the u, v and w directions using cubic spline axial basis functions with $N = 4$ for the time dependent example for $T = 1.5$ *sec.*

	$\frac{N=4}{N=8}$	$\frac{N=8}{N=16}$
u	83.052	50.888
v	37.899	24.069
w	76.961	73.400

Table 5.17: $\mathcal{O}(h_x^4)$ convergence with cubic splines, time dependent, $T = 1.5$ *sec.*

Patch Excitation and Dynamic Simulation without Passive Patch Contributions

In applications, a common method to elicit broadband shell responses to identify parameters or structural damages is to input a triangular voltage spike to the patches. To model such excitation, we consider a single patch pair bonded to the shell with the patch center located at $(x = 6, \theta = \pi/12)$. The patches have dimensions x-length 6 inches and θ-height of $\pi/6$. We then induce a triangular voltage $V_1(t)$, of small duration $T = 0.0001\ s$, to the outer patch as depicted in Figure 5.17. Negative voltage was applied to the inner voltage $V_2(t)$, i.e., $V_2(t) = -V_1(t)$. The out-of-phase voltages were employed to maximize the number of excited frequencies.

After the $t = 0.0001s$ duration of the voltage input (modeling a delta impulse), point displacements at $(\hat{x} = 7.83, \hat{\theta} = 0.89)$ were recorded until $t = 0.5\ s$ as the shell was allowed to vibrate freely (this point lies just outside the $(x, \theta) = (7.5, \pi/6)$ corner of the patch). Time histories of the displacement u at $(\hat{x}, \hat{\theta})$, together with the excited natural frequencies of the shell (obtained by taking the Fourier transform of the displacements), are depicted in Figure 5.18. Peaks in the frequency plots without stars $(*)$ do not contain enough energy to be considered as excited frequencies. The time histories of the circumferential and tangential displacements are given in Figure 5.19 and Figure 5.20, respectively. The excited natural frequencies (i.e., peaks with $(*)$ in the frequency plots) are compared with the natural frequencies (obtained through solving the matrix eigenvalue problem (5.8) for the undamped system) in Table 5.18. As expected, the two sets of frequencies are almost identical since the same discretization limits were used in both cases. The slight differences are due to the Kelvin-Voigt damping and sampling rates in the dynamic simulation.

The Kelvin-Voigt damping used in the previous example was sufficiently large to quickly damp high frequency responses. We consider the case when more of the energy in the shell response is in higher frequencies by using a smaller value of $c_D = 0.0009931891$ and refer to this as the "lightly damped" case. The plots of the time histories and excited frequencies at $(\hat{x}, \hat{\theta})$ are shown in Figures 5.21-5.23. The larger

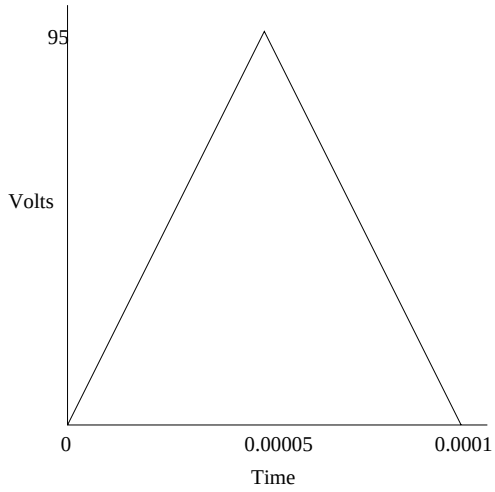

Figure 5.17: Temporal voltage applied to the patch.

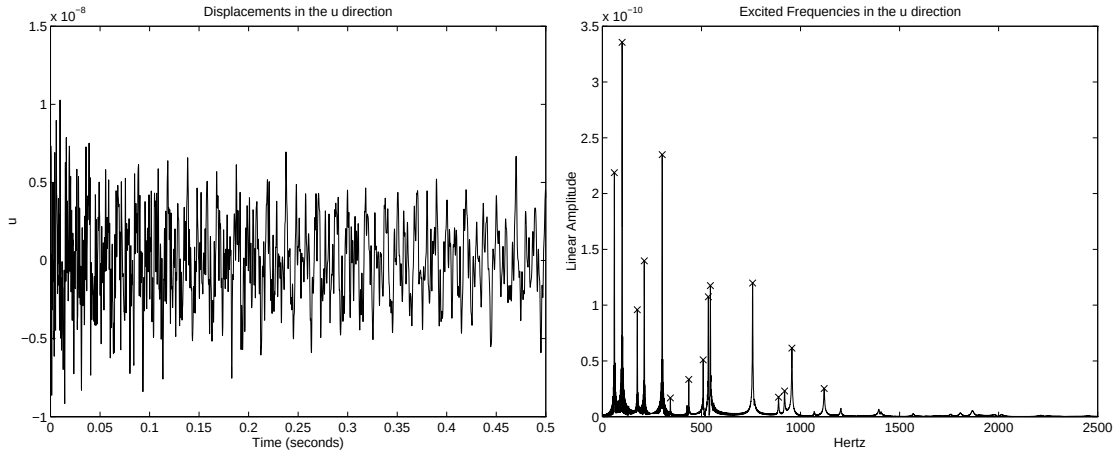

Figure 5.18: Longitudinal displacements and excited frequencies at the point $(\hat{x}, \hat{\theta}) = (7.83, 0.89)$ for the damped shell.

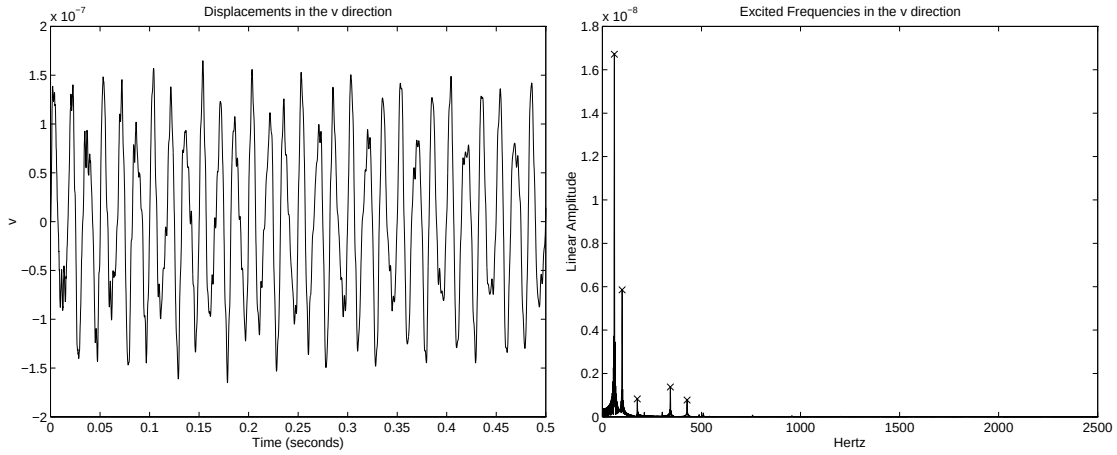

Figure 5.19: Circumferential displacements and excited frequencies at the point $(\hat{x}, \hat{\theta}) = (7.83, 0.89)$ for the damped shell.

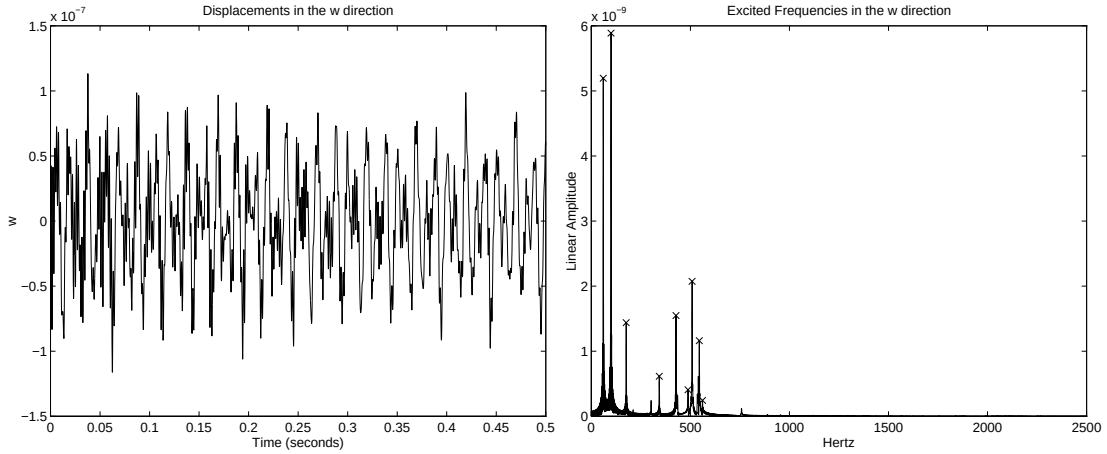

Figure 5.20: Transverse displacements and excited frequencies at the point $(\hat{x}, \hat{\theta}) = (7.83, 0.89)$ for the damped shell.

Dynamically Excited Frequencies		Frequencies from Eigenvalue Problem	
60.1	99.5	60.2	99.5
176.1	211.2	176.0	211.1
301.8	342.7	301.8	342.9
343.0	427.2	342.9	427.4
435.8	488.0	435.8	488.4
508.4	534.7	508.7	534.7
545.0	561.2	544.9	560.6
758.1	889.0	758.2	889.0
919.5	956.4	919.3	956.5
1119.4		1119.2	

Table 5.18: Natural frequencies of the damped shell obtained through dynamic excitation and solution of matrix eigenvalue problem.

number of excited frequencies are compared with natural frequencies of the undamped shell obtained by solving the matrix eigenvalue problem (5.8) in Table 5.19.

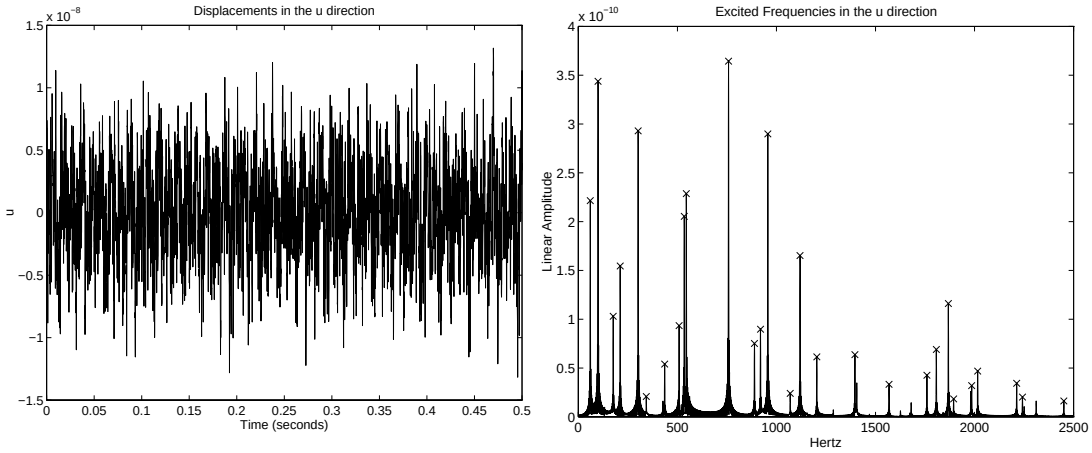

Figure 5.21: Longitudinal displacements and excited frequencies at the point $(\hat{x}, \hat{\theta}) = (7.83, 0.89)$ for the lightly damped shell.

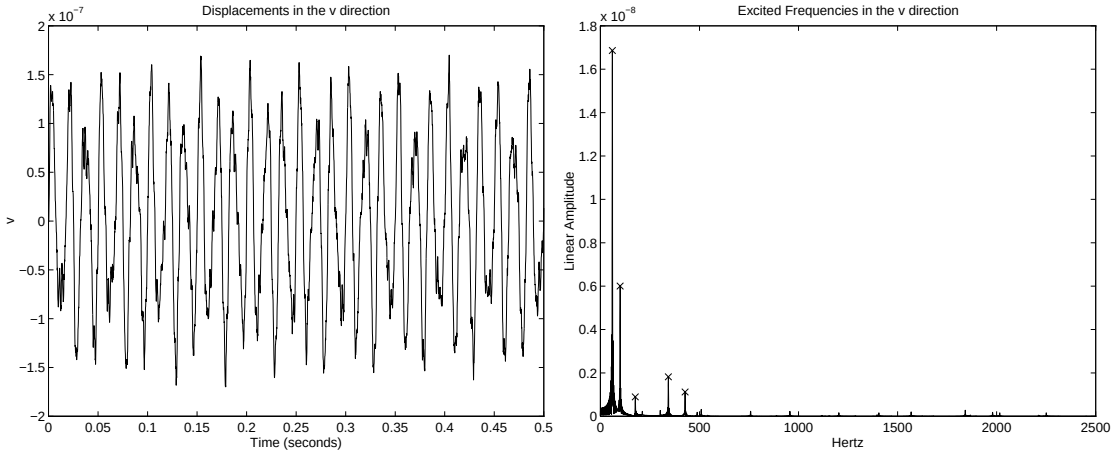

Figure 5.22: Circumferential displacements and excited frequencies at the point $(\hat{x}, \hat{\theta}) = (7.83, 0.89)$ for the lightly damped shell.

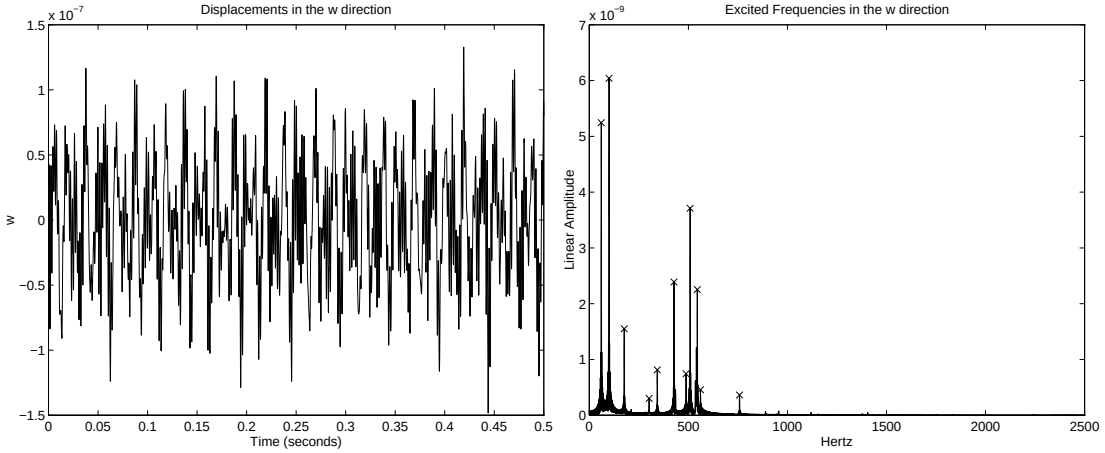

Figure 5.23: Transverse displacements and excited frequencies at the point $(\hat{x}, \hat{\theta}) = (7.83, 0.89)$ for the lightly damped shell.

Dynamically Excited Frequencies		Frequencies from Eigenvalue Problem	
60.1	99.5	60.2	99.5
176.1	211.2	176.0	211.2
301.8	343.0	301.8	343.0
427.2	435.8	427.4	435.8
488.3	508.7	488.4	508.7
534.7	545.0	534.7	544.9
561.2	758.1	560.6	758.2
889.0	919.5	889.0	919.3
956.4	1069.3	956.5	1069.3
1119.1	1203.6	1119.2	1203.5
1396.2	1568.3	1396.1	1568.3
1759.6	1806.9	1759.5	1806.9
1867.7	1894.2	1867.7	1894.1
1985.5	2015.7	1985.5	2015.6
2212.5	2241.8	2212.7	2241.6
2450.6		2450.7	

Table 5.19: Natural frequencies of the lightly damped shell obtained through dynamic excitation and solution of matrix eigenvalue problem.

Excited Frequencies of Shell without Passive Contributions		Excited Frequencies of Shell with Passive Contributions	
292.9	964.4	305.2	988.8
1440.4	1696.8	1513.7	1770.0

Table 5.20: Excited frequencies of the shell with and without passive patch contributions using metric shell constants.

Patch Excitation and Dynamic Simulation Incorporating Passive Patch Contributions

We now investigate the effect of passive patch contributions on the natural frequencies of the shell. Since metric constants, given in Table 5.2, will be used for the rest of the chapter, we use shell and patch parameters given by the table, with the exception that only one patch pair is bonded to the shell. We assume that the identical patch pair is bonded at the center of the shell $(x, \theta) = (\ell/2, 0)$ with dimensions x-length 0.1 m and θ-height $\pi/6$. The same temporal voltage input depicted in Figure 5.17 will be employed. Since a longer shell (1 m as opposed to 12 in) was used in the metric simulations, we expect natural frequencies to be lower. The excited natural frequencies of the shell with and without passive contributions are reported in Table 5.20. The significant difference in the excited frequencies indicate the importance of correct modeling assumptions in parameter estimation and control applications.

5.1.3 LQR Control

The control laws in Chapter 3.5 will be employed in this section to attenuate shell vibrations. To force the shell, we consider a periodic noise source localized near the axial shell center ($x = \ell/2$) and at $\theta = 0$ and $\theta = \pi$ with definition

$$\begin{aligned} \hat{q}_x(x,\theta,t) &= \frac{1}{2} e^{-20(x-\ell/2)^2} \Theta(\theta) g(t) \\ \hat{q}_\theta(x,\theta,t) &= 0 \qquad\qquad , \ \Theta(\theta) = \begin{cases} 1 - e^{-(\theta-\pi/2)^6/2} & , \ 0 \le \theta < \pi \\ 1 - e^{-(\theta-3\pi/2)^6/2} & , \ \pi \le \theta < 2\pi \end{cases} . \\ \hat{q}_\eta(x,\theta,t) &= \frac{1}{200} e^{-20(x-\ell/2)^2} \Theta(\theta) g(t) \end{aligned} \tag{5.17}$$

Time history plots are created by recording displacements at the point p_1 on the shell with coordinates $p_1 = (\hat{x}, \hat{\theta}) = (3\ell/4, \pi/32)$. Control attenuation is illustrated by plotting root mean square (rms) displacements along the lines $L_1 = \{(x,\theta) | 0 \le x \le \ell, \theta = \pi/6\}$ and $L_2 = \{(x,\theta) | x = 3\ell/4, 0 \le \theta \le 2\pi\}$ on the shell. By taking 500 samples at each point on the rms lines, the root mean square displacements on L_1 and L_2 in the longitudinal direction are computed using

$$\begin{aligned} L_1^{rms}(x) &= \sqrt{\frac{1}{500} \sum_{i=0}^{500} u^{\mathcal{N}}(t_i, x, \pi/6)^2} \ , \ 0 \le x \le \ell \\ L_2^{rms}(\theta) &= \sqrt{\frac{1}{500} \sum_{i=0}^{500} u^{\mathcal{N}}(t_i, 3\ell/4, \theta)^2} \ , \ 0 \le \theta \le 2\pi \ . \end{aligned}$$

Rms displacements in the circumferential and transverse directions (v and w) on L_1 and L_2 are calculated similarly. In Figure 5.24, we depict the location of the point p_1, the spatial distribution of the external forcing function (5.17), and location of the lines L_1 and L_2.

Twelve piezoceramic patch pairs to be used as actuators (hence $s = 12$) are bonded to the inner and outer surfaces of the shell. As illustrated in Figure 2.1, the patch pairs were configured in sets of three along the lines $\theta = 0, \pi/2, \pi$ and $3\pi/2$. The physical and material properties of the patches, assumed uniform, together with patch location on the surface of the shell are indicated in Table 5.2. We reiterate that

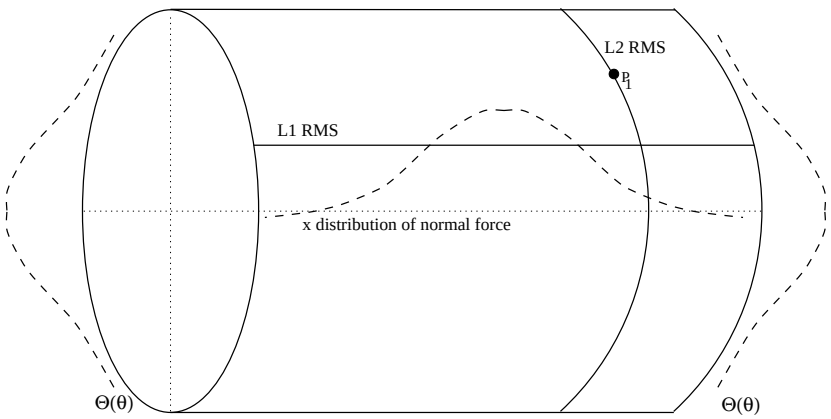

Figure 5.24: Location of the point p_1, rms lines $L_1 = \{(x, \theta)|0 \leq x \leq \ell, \theta = \pi/6\}$ and $L_2 = \{(x, \theta)|x = 3\ell/4, 0 \leq \theta \leq 2\pi\}$ and spatial distribution of the exogenous force.

the voltages to the inner and outer patches in each pair were independent so as to provide capabilities for generating both in-plane forces and bending moments.

Two sizes of patches were considered, the large patches had sizes of $x = 0.2\ m$, $\theta = \pi/3$ while smaller patches had dimensions $x = 0.1\ m$, $\theta = \pi/6$. We point out that issues regarding patch number, placement and size fall outside the scope of this investigation. The two patch sizes were utilized to illustrate the effect of patch sizes on attenuation levels and the fixed number of patches and location were used to demonstrate the capabilities of the control method under uniform conditions.

To reach acceptable levels of accuracy, the discretization sizes of $N = 16$ and $M = 4$ were employed in *all* full order controls. Thus, the first system ode to be marched in time has 666 coefficients (for the fully cubic spline method with fixed-edge boundary conditions).

LQR Control for Shell with No Exogenous Input

Initial input to the shell was provided by the external force (5.17) with temporal component

$$g(t) = \begin{cases} \sin(1000\pi t) & , \quad 0 \leq t < 0.01 \ sec \\ 0 \quad , & \quad t \geq 0.01 \ sec. \end{cases} \tag{5.18}$$

After $t = 0.01$ *sec*, wherein the shell was allowed to freely vibrate, the feedback control law given by Theorem 3.3.1 (i.e., $\bar{U}(t) = -R^{-1}\left(B^{2\mathcal{N}}\right)^T \Pi^{2\mathcal{N}} z^{2\mathcal{N}}(t)$) was employed. Hence we take the time instance $t = 0.01$ were the force g becomes equivalently zero to be $t = 0$ *sec* in the control regime.

In terms of the matrices created in (4.9) and (4.10), the cost functional (3.28) and evolution equation (3.29) are now given by

$$J(U, z_0^{2\mathcal{N}}) = \frac{1}{2}\int_0^\infty \left\{ \left\langle Q^{2\mathcal{N}} z^{2\mathcal{N}}(t), z^{2\mathcal{N}}(t) \right\rangle + \left\langle R^{2s} U(t), U(t) \right\rangle \right\} dt \tag{5.19}$$

subject to the system

$$\begin{aligned} \dot{z}^{2\mathcal{N}}(t) &= A^{2\mathcal{N}} z^{2\mathcal{N}}(t) + B^{2\mathcal{N}} U(t) \\ z^{2\mathcal{N}}(0) &= z_0^{2\mathcal{N}} \ . \end{aligned} \tag{5.20}$$

The matrix $Q^{2\mathcal{N}}$ was taken to be

$$Q^{2\mathcal{N}} = \begin{bmatrix} d_1 I & & & \\ & d_2 I & & \\ & & \ddots & \\ & & & d_6 I \end{bmatrix}_{2\mathcal{N}\times 2\mathcal{N}} \times \begin{bmatrix} K_E^{\mathcal{N}} & \\ & M^{\mathcal{N}} \end{bmatrix}_{2\mathcal{N}\times 2\mathcal{N}} , \tag{5.21}$$

where I is the identity matrix, $M^{\mathcal{N}}$ is the mass matrix and $K_E^{\mathcal{N}}$ denotes the stiffness matrix. The matrix of control weights R^{2s} was taken to be the diagonal matrix $R^{2s} = r \cdot I^{2s\times 2s}$. The parameters $d_i, i = 1, \ldots, 6$ and r were used to maximize attenuation and limit voltage input to the patches to approximately 100 volts rms. In the simulations reported on here, we used $d_i = 10^{13}, i = 1, \ldots, 6$, and $r = 50$. The choice of the weighted mass matrix $Q^{2\mathcal{N}}$ is motivated by energy considerations as detailed in [10].

Passive patch contributions are ignored for this example, hence the convergence and exponential stability of the closed loop are provided by Theorem 3.5.1. Passive patch contributions will be included in the next example.

In Figure 5.25, we present the uncontrolled and controlled time histories at the point p_1, where closed loop dynamics of the shell was computed over the time interval $[0.01, 0.05]$. The left column of the table illustrates attenuation with small $(.1, \pi/6)$ patches while the right column contain the displacements with large $(.2, \pi/3)$ patches. While significant control was obtained with small patches, the attenuation is greatly enhanced by the use of bigger patches. Root mean square displacements on L_1 and L_2 are depicted in Figure 5.26, where it is demonstrated that attenuation is obtained even in regions not covered by the patches.

LQR Control for Shell with Single Frequency Exogenous Input

We now consider the feedback law of Theorem 3.3.2 to attenuate shell dynamics with periodic exogenous force of the form (5.17). The temporal component of (5.17) contains a single 500 Hz frequency given by

$$g(t) = \sin(1000\pi t) \ .$$

To obtain the optimal control minimizing the cost functional (3.38) subject to

$$\begin{aligned} \dot{z}^{2\mathcal{N}}(t) &= \mathcal{A}^{2\mathcal{N}} z^{2\mathcal{N}}(t) + \mathcal{B}^{2\mathcal{N}} U(t) + g^{2\mathcal{N}}(t) \\ z^{2\mathcal{N}}(0) &= z_0^{2\mathcal{N}} \end{aligned} \tag{5.22}$$

(see (3.39)), we first solve the matrix form of the Riccati equation (3.17) and numerically integrate the tracking equation (3.40) from the future time τ back to the present. The optimal control and closed loop solution are then obtained from (3.42) and (3.41).

As in the previous example, the matrix $Q^{2\mathcal{N}}$ is given by (5.21) with $d_i = 10^{13}$. The same R matrix was also used. Both small and large patches were employed, and the effect of passive patch contributions are investigated. Time histories employing small

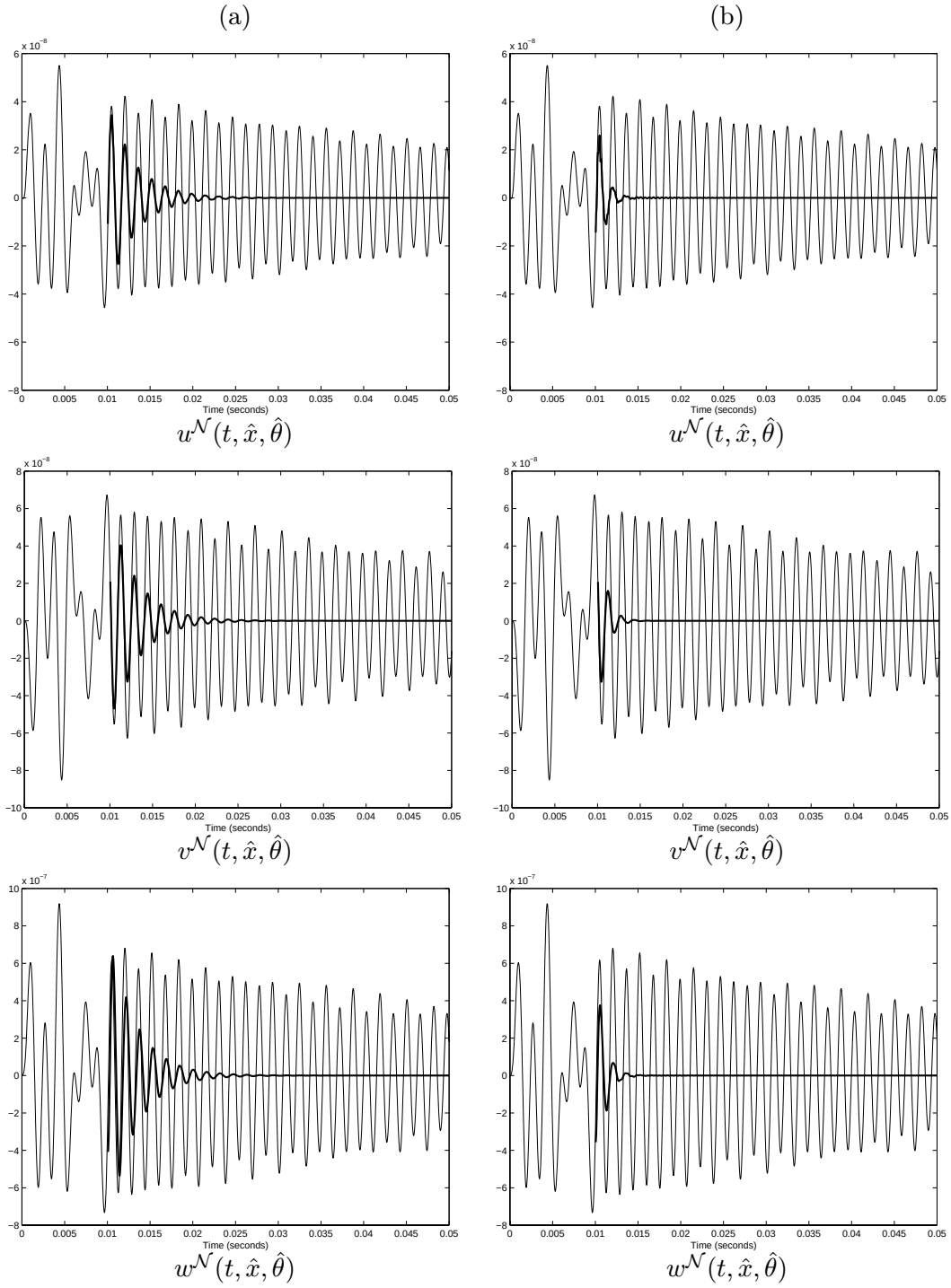

Figure 5.25: Full order uncontrolled (—) and controlled (—) shell displacements at p_1 with control initiated at $t = 0.1s$ using (a) small patches; (b) large patches.

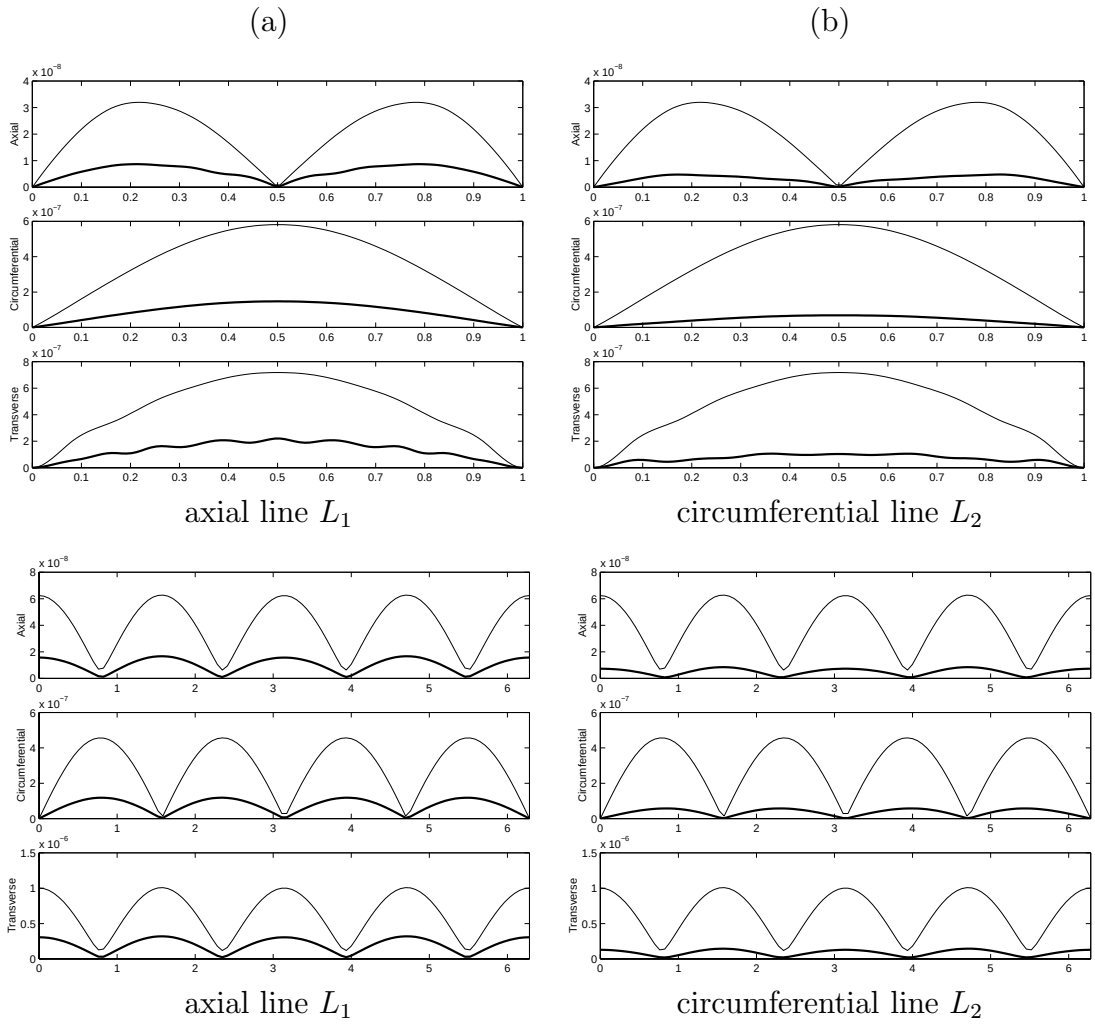

Figure 5.26: Full order root mean square (rms) displacements with control using (a) small, and (b) large patches; — uncontrolled; — controlled.

patches to attenuate the system without passive patch contributions are depicted in the left column of Figure 5.27. Incorporation of passive patch contributions resulted in similar levels of attenuation, and are illustrated in the right column of the same figure. Corresponding rms plots in L_1 and L_2 can be seen in Figure 5.28. Large patch performance on the shell with and without passive patch contributions are given in Figure 5.29 (time histories) and Figure 5.30 (rms plots).

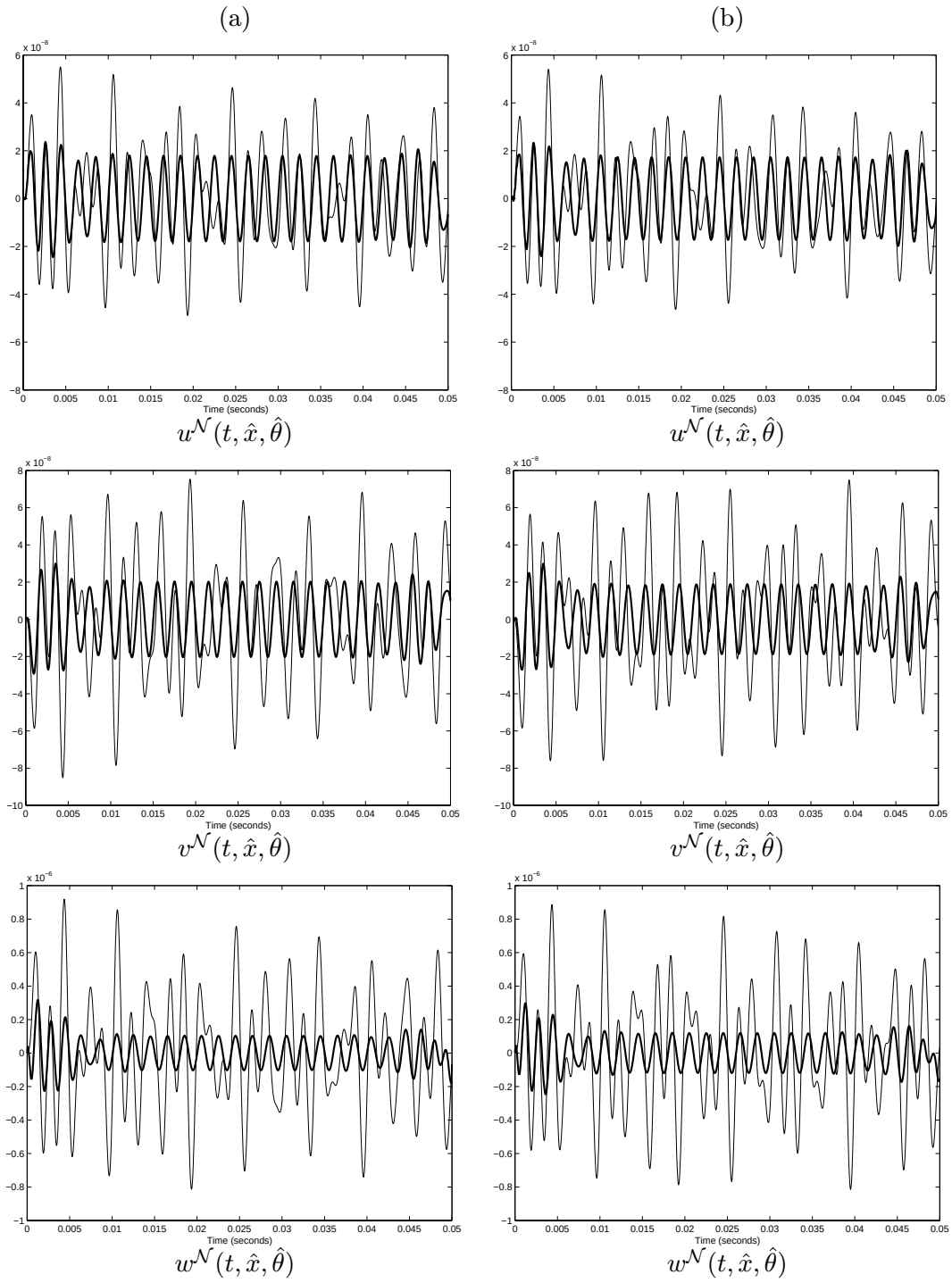

Figure 5.27: Uncontrolled (—) and controlled (—) displacements at p_1; single frequency excitation; with (a) no passive and (b) passive contributions; small patches.

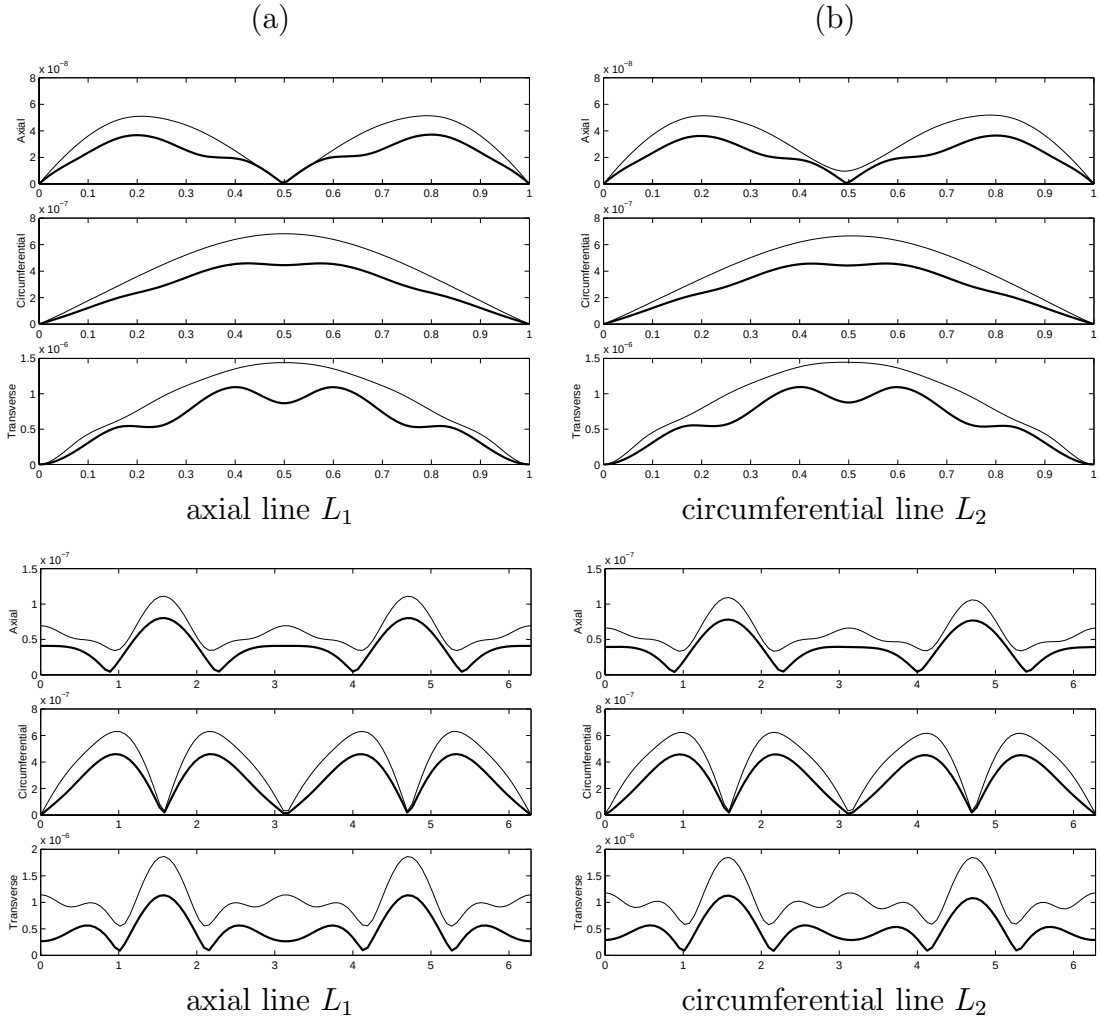

Figure 5.28: Full order root mean square (rms) displacements for shell with single frequency excitation and (a) no passive and (b) passive patch contributions using small patches; — uncontrolled; — controlled.

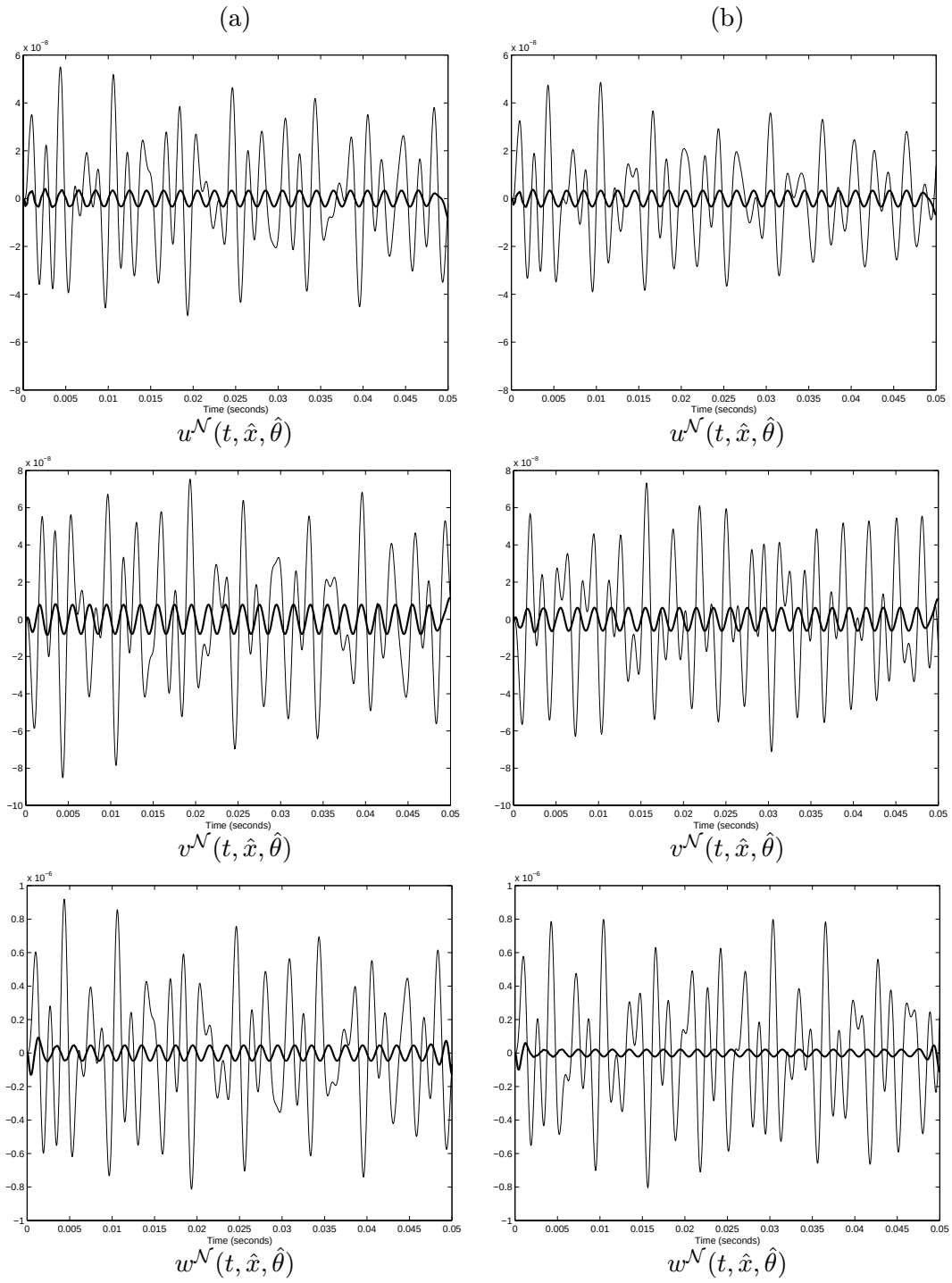

Figure 5.29: Uncontrolled (—) and controlled (—) shell displacements at p_1; single frequency excitation; with (a) no passive and (b) passive contributions; large patches

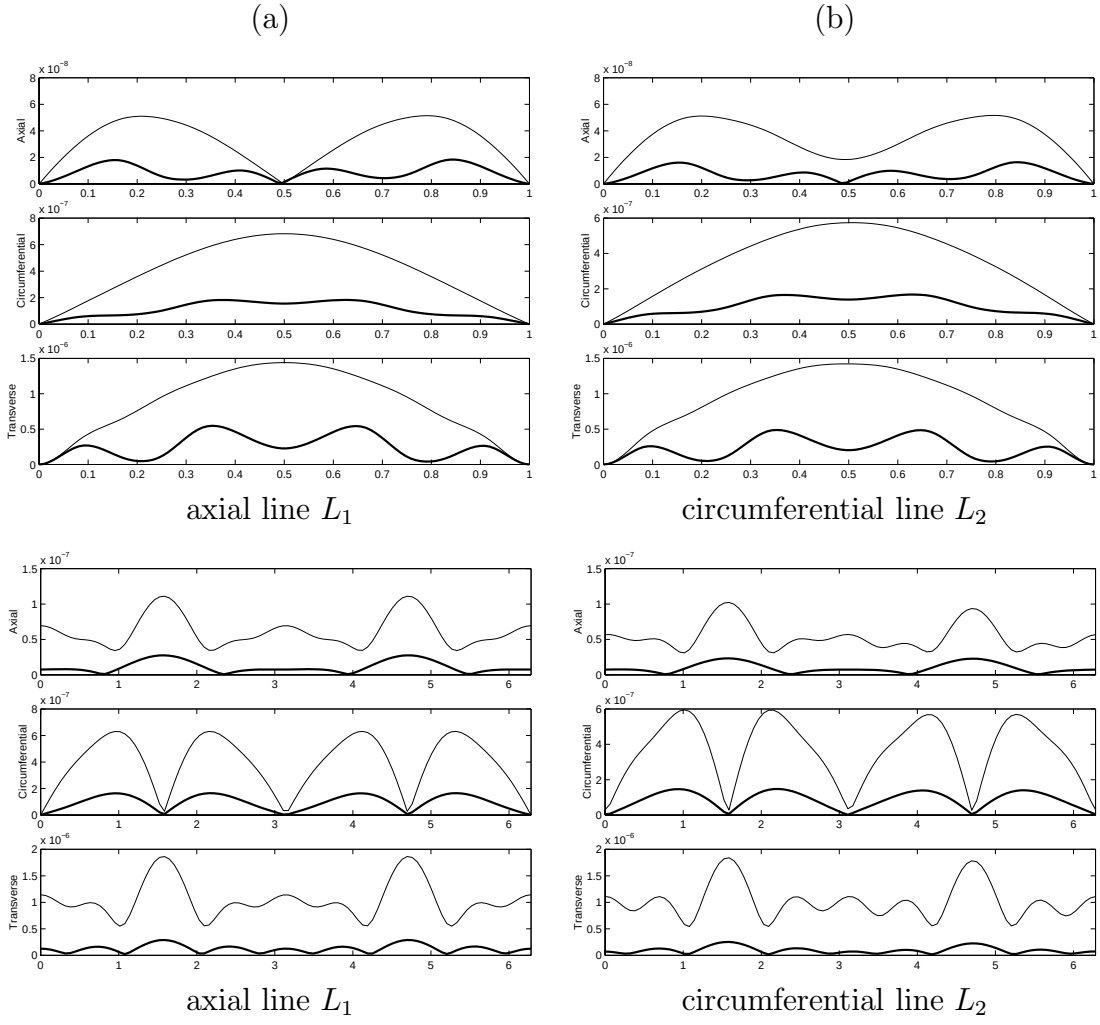

Figure 5.30: Full order root mean square (rms) displacements with single frequency excitation and (a) no passive and (b) passive patch contributions using large patches; — uncontrolled; — controlled.

LQR Control for Shell with Multiple Frequency Exogenous Input

For the final full order control example, we consider (5.17) with five frequencies

$$g(t) = \sin(640\pi t) + \sin(880\pi t) + \sin(1200\pi t) + \sin(1320\pi t) + \sin(1640\pi t)\ . \quad (5.23)$$

Passive patch contributions are ignored, small patches were employed and uncontrolled and controlled displacements at p_1 in the three directions are illustrated in Figure 5.31. Corresponding rms plots in L_1 and L_2 are in Figure 5.32. Attenuation levels in the two figures indicate the effectiveness of the feedback law for broadband responses. We point out that better attenuation is obtained with larger patches (additional plots are in [25, 23]).

We plot the voltages given by (3.42) for the first 6 patch pairs, in Figure 5.33. Due to symmetry, the second six pairs are identical and hence are not given here. It can be seen that voltages to the patch pair 2 is greater than those to patch pairs 1 and 3, and voltages to patch pair 5 are greater than input voltages to pairs 4 and 6. This is due to the heavier concentration of the external forcing function on the shell center. For each patch pair, the voltages appear to be out of phase, which indicates that greater control is needed for the bending moments. In-plane vibrations are also accounted for by the control methodology as illustrated in Figure 5.34, where the magnitude differences are plotted for the first patch pair. The small magnitude differences between inner and outer patches indicate the predominance of bending moments over in-plane forces in the force under consideration.

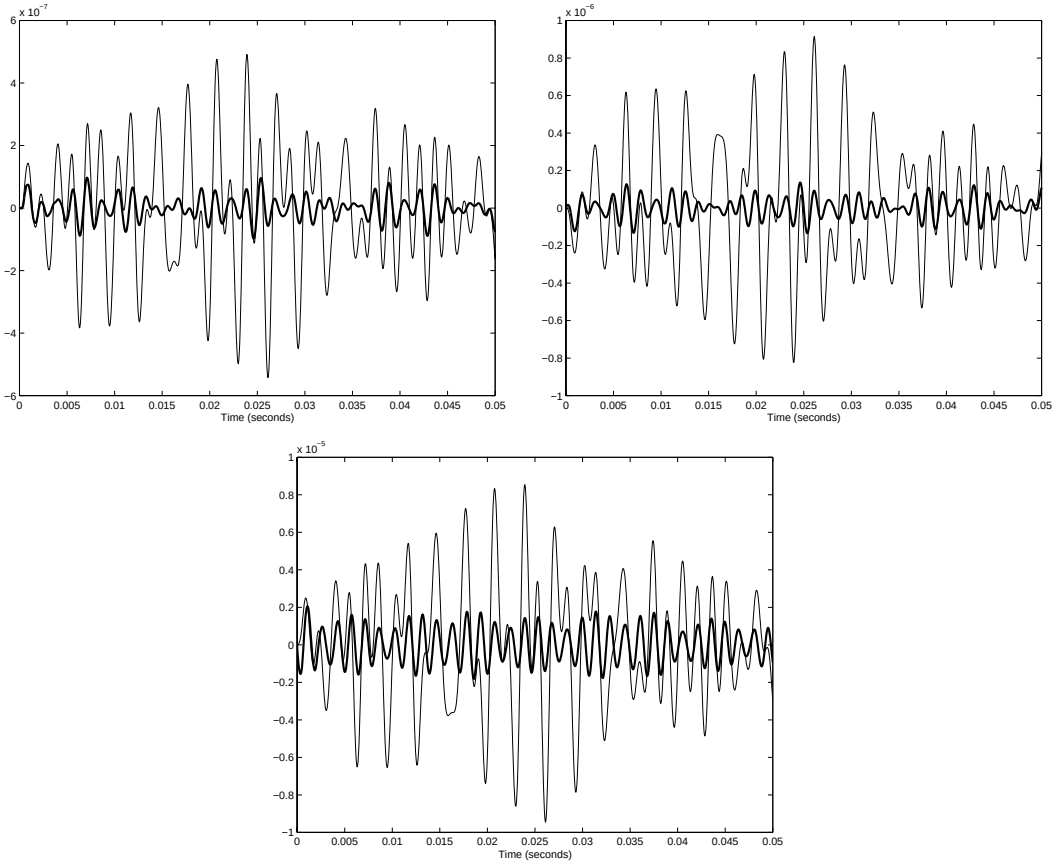

Figure 5.31: Full order uncontrolled (—) and controlled (—) shell displacements at p_1 with multiple frequency using small patches.

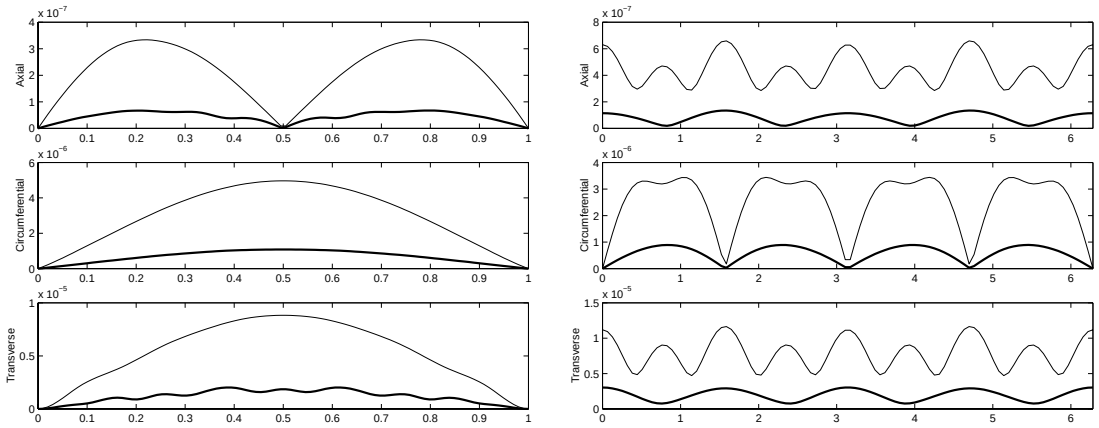

axial line L_1 circumferential line L_2

Figure 5.32: Full order root mean square (rms) displacements with multiple frequency using small patches; — uncontrolled; — controlled.

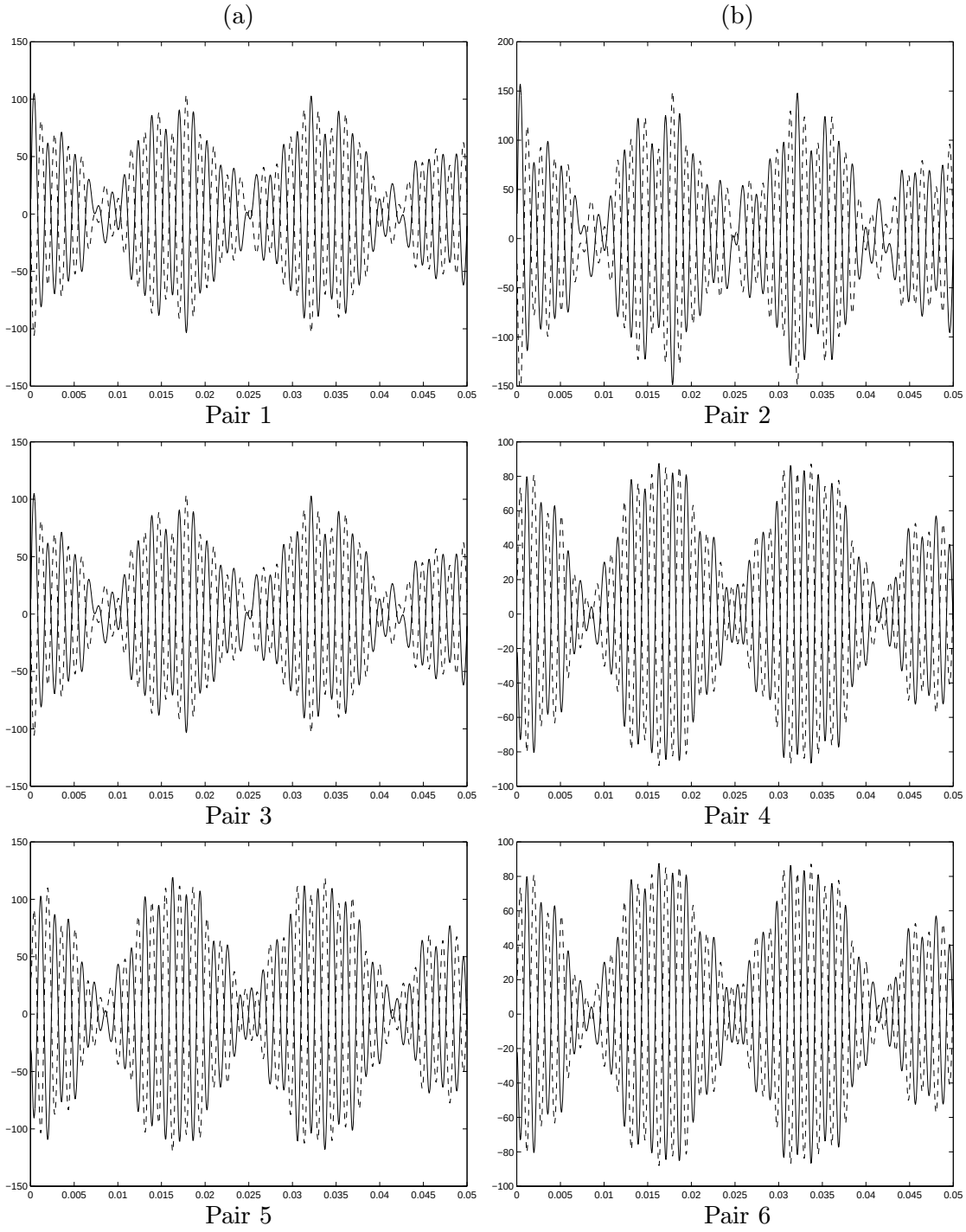

Figure 5.33: Voltages to the inner and outer patches of pairs 1-6 as depicted in Figure 2.1; — outer patch, - - - - inner patch.

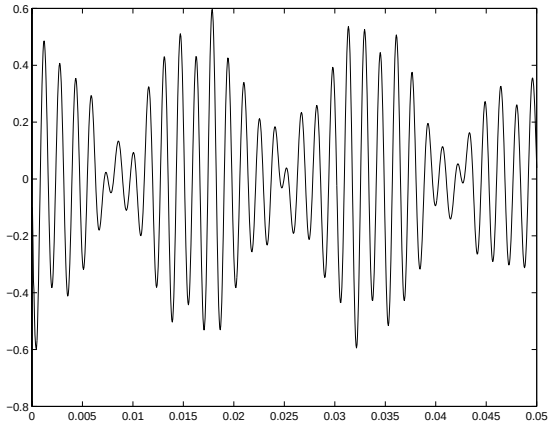

Figure 5.34: Sum of inner and outer voltages to patch pair 1

5.2 Reduced Basis Methods

We first illustrate the use of Lagrange and POD reduced order methods and compare the numerical results with full order uncontrolled approximations. Then attenuation employing reduced order gains in the reduced order model is presented through time histories at the point $p_1 = (\hat{x}, \hat{\theta}) = (3\ell/4, \pi/4)$ and rms plots on L_1 and L_2 (see Figure 5.24). Shell and patch parameters are given in Table 5.2 and small patches $(x = 0.1, \theta = \pi/6)$ were used as actuators. External excitation is modeled by (5.17) with the multifrequency input (5.23). Fixed-edge boundary conditions were employed, and full order simulations, used as a baseline for comparison with reduced order methods were obtained using a discretization level of $M = M_u = M_v = M_w = 4$ and $N = N_u = N_v = N_w = 16$, for a total of $\mathcal{N} = 333$ full order basis elements in the second order system and $2\mathcal{N} = 666$ coefficients in the first order system.

Reduced basis method approximations are compared with full order solutions using the ℓ_1 norm of the difference between the displacements. This is done by taking 500 full and reduced order point displacements at p_1 over the time interval simulation,

and summing the absolute value of the difference between the reduced order and full order dispacements.

5.2.1 Uncontrolled Simulations

Lagrange Reduced Order Method

The Lagrange reduced order method was tested using discretization sizes of $\mathcal{N}_u = \mathcal{N}_v = \mathcal{N}_w = 1, 2, 3$ and 4 ($\mathcal{N} = 3, 6, 9$ and 12). Note that as opposed to the full order method, the same discretization levels could be used for each displacement direction because each reduced basis function (being a full order solution) already satisfies the boundary conditions. We also point out that uniform discretization in the three directions were used for ease in exposition and that the user could choose to do otherwise. For each discretization level, intuition was used to obtain the time instances at which reduced basis functions will be realized to obtain the best approximation. Over the time interval $t \in [0, 0.1]$ s, our experience revealed that the least ℓ_1 errors are obtained with basis functions taken at the time following time instances: (i) $\mathcal{N} = 3, t_i = 0.0333$ s; (ii) $\mathcal{N} = 6, t_i \in \{0.0200, 0.0667\ s\}$; (iii) $\mathcal{N} \in 9, t_i = \{0.0200, 0.0333, 0.0667\ s\}$; (iv) $\mathcal{N} \in 12, t_i = \{0.0200, 0.0500, 0.0.0667, 0.1\ s\}$. It is seen in Table 5.21, where we present the ℓ_1 norm of the difference between full and reduced order approximations, that the ℓ_1 error decreases as the dimension of the Lagrange basis increases. One shortcoming of this method is the tendency of the condition numbers to become very large as the number of basis functions increases. To illustrate this, the condition number κ of the mass matrix $M^{\mathcal{N}}$ and stiffness matrix $K_E^{\mathcal{N}}$ are also reported in Table 5.21.

The time histories at the point p_1 using $\mathcal{N} = 9$ Lagrange basis functions together with trajectories from the full order and POD model (whose implementation will be discussed shortly) are presented in Figure 5.35 below. It could be seen from the plots that the full order, Lagrange and POD approximations are graphically indistinguishable from each other and that the reduced order models give a good

$\mathcal{N}$	$\|udiff\|_{\ell_1}$	$\|vdiff\|_{\ell_1}$	$\|wdiff\|_{\ell_1}$	$\kappa(M^{\mathcal{N}})$	$\kappa(K_E^{\mathcal{N}})$
3	3.23e-05	2.33e-04	6.20e-04	1.4e+00	2.0e+02
6	1.61e-06	1.74e-06	2.55e-05	3.2e+00	1.3e+03
9	5.37e-07	3.83e-07	9.61e-06	8.3e+04	1.8e+05
12	5.32e-08	2.63e-07	3.25e-07	9.7e+05	3.8e+07

Table 5.21: ℓ_1 norm of the difference between full and Lagrange reduced order models and condition numbers of the mass ($M^{\mathcal{N}}$) and stiffness ($K_E^{\mathcal{N}}$) matrices.

approximation to the full order system. Since numerical results with $\mathcal{N} = 6$ and 12 Lagrange basis functions are similar to those with 9 basis functions, the plots are not given here. As shown by the large ℓ_1 error in Table 5.21, the system is not fully approximated with $\mathcal{N} = 3$ basis functions so the displacements are not reported (see [7, p. 10] for illustrations).

POD Reduced Order Method

The POD reduced order method was tested by obtaining $\mathcal{N}_s = 20$ snapshots of the model from which POD basis functions of the form (4.16) are created. As in the Lagrange simulations, $\mathcal{N} = 3, 6, 9$ and 12 discretization levels were employed. In Table 5.23, we note that the ℓ_1 norm of the difference between solutions of the full order and POD reduced order models decreases as the dimension of the reduced basis space increases. Moreover, condition numbers of the mass and stiffness matrices remain small as more basis functions are added. The condition number 1 for all mass matrices $M^{\mathcal{N}}$ in Table 5.23 results from the orthogonality of POD basis functions. We point out that even though the ℓ_1 error of the difference between the full order and Lagrange reduced order method approximations are slightly better as reported in Table 5.21, the basis functions there were chosen, using intuition and trial and error, to give good approximations, and so that level of accuracy is generally much more difficult for users to attain. As mentioned earlier, displacements at the point p_1 using $\mathcal{N} = 9$ POD basis functions, together with full order and Lagrange reduced order

$\mathcal{N}$	% u	% v	% w
3	52.092083	59.426622	54.909536
6	99.895918	99.985078	99.925809
9	99.994818	99.999375	99.993714
12	99.999986	99.999998	99.999773

Table 5.22: Percentage of "energy" in model with complete set of POD elements (i.e., $N_s = 20$) captured by POD reduced basis method.

$\mathcal{N}$	$\|udiff\|_{\ell_1}$	$\|vdiff\|_{\ell_1}$	$\|wdiff\|_{\ell_1}$	$\kappa(M^{\mathcal{N}})$	$\kappa(K_E^{\mathcal{N}})$
3	3.28e-05	2.36e-04	6.31e-04	1.0e+00	1.2e+01
6	1.71e-06	3.66e-06	2.62e-05	1.0e+00	1.0e+03
9	4.03e-07	2.97e-07	7.22e-06	1.0e+00	1.1e+03
12	2.70e-07	2.48e-07	4.84e-06	1.0e+00	1.9e+03

Table 5.23: ℓ_1 norm of the difference between full and POD reduced order models and condition numbers of the mass ($M^{\mathcal{N}}$) and stiffness ($K_E^{\mathcal{N}}$) matrices.

approximations are illustrated in Figure 5.35. As in the Lagrange method, results with $\mathcal{N} = 6$ and 12 are similar to those with $\mathcal{N} = 9$ and hence are not reported. Only $52\%, 59\%$ and 54% of the "energy" in the model with complete set of POD elements in the u, v and w directions, respectively, were captured by the POD method with $\mathcal{N} = 3$ basis functions, indicating poor approximation at this discretization level (see Table 5.22). Hence plots with $\mathcal{N} = 3$ are not given here. The energy percentage increased to 99.9% (for each of the three directions) when $\mathcal{N} = 6$ basis functions were employed and thus, as expected, discretization levels of at least $\mathcal{N} = 6$ provided good approximation to the full order system (see Table 5.23).

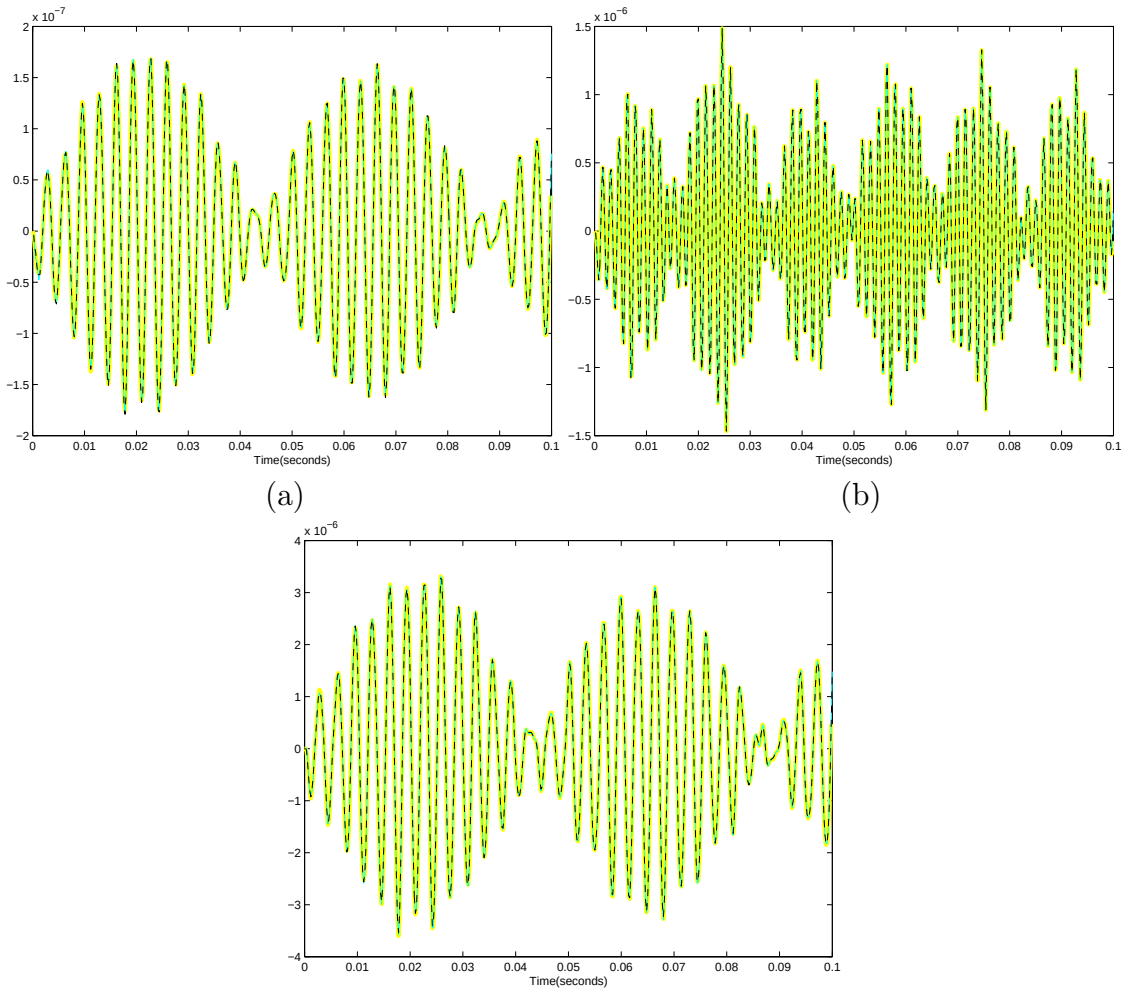

Figure 5.35: Point displacements at $p_1 = (\hat{x}, \hat{\theta}) = (3\ell/4, \pi/4)$; (a) longitudinal $w^{\mathcal{N}}(t, \hat{x}, \hat{\theta})$, (b) circumferential $v^{\mathcal{N}}(t, \hat{x}, \hat{\theta})$, (c) transverse $w^{\mathcal{N}}(t, \hat{x}, \hat{\theta})$; — full order ($\mathcal{N} = 333$), — Lagrange ($\mathcal{N} = 9$), – – POD ($\mathcal{N} = 9$). The graphs are indistinguishable from each other due to the small difference between full order and reduced basis trajectories.

5.2.2 LQR Control

In Figure 5.36, we present full order, uncontrolled and controlled rms displacements together with controlled rms displacements for the Lagrange ($\mathcal{N} = 9$) and POD ($\mathcal{N} = 9$) reduced order models. Uncontrolled and controlled time histories at the point p_1 in the full order, Lagrange and POD reduced order models are depicted in Figure 5.37. We point out that great difficulty was encountered in obtaining full order Riccati solutions due to large matrix dimensions and ill conditioning. Better attenuation is attained with reduced order models (than with full order models) due to smaller matrix dimensions resulting in better conditioning of the mass and stiffness matrices and hence more accurate Riccati solutions.

Displacement and RMS plots with $\mathcal{N} = 6$ and 12 for both Lagrange and POD reduced order models are similar to those reported in Figures 5.37 and 5.36. Although good attenuation was obtained for Lagrange and POD reduced order models using $\mathcal{N} = 3$ basis functions, the full order system was not fully resolved by the reduced order model so results are not presented here.

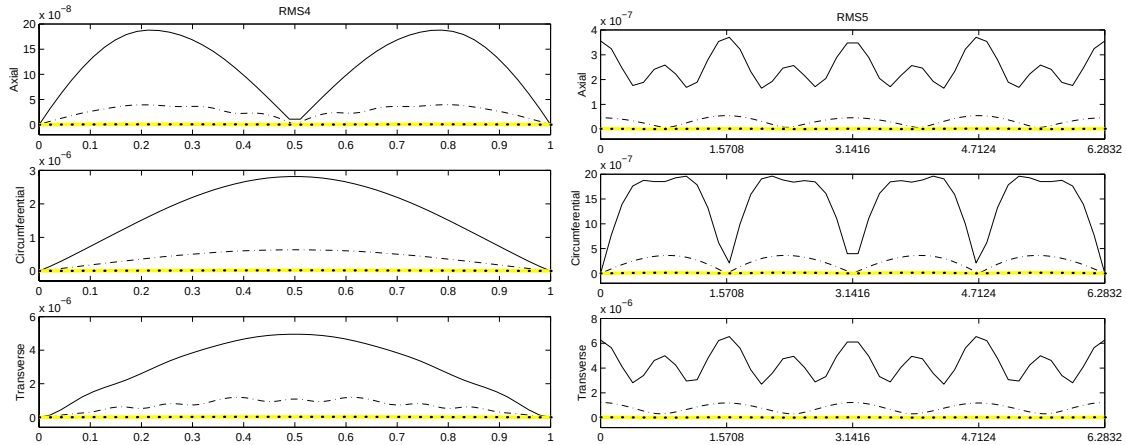

Figure 5.36: Uncontrolled and controlled RMS displacements; — full order uncontrolled ($\mathcal{N} = 333$), – · – full order controlled ($\mathcal{N} = 333$), — Lagrange controlled ($\mathcal{N} = 9$), $\cdots$ POD controlled ($\mathcal{N} = 9$); (a) axial line L_1; (b) circumferential line L_2.

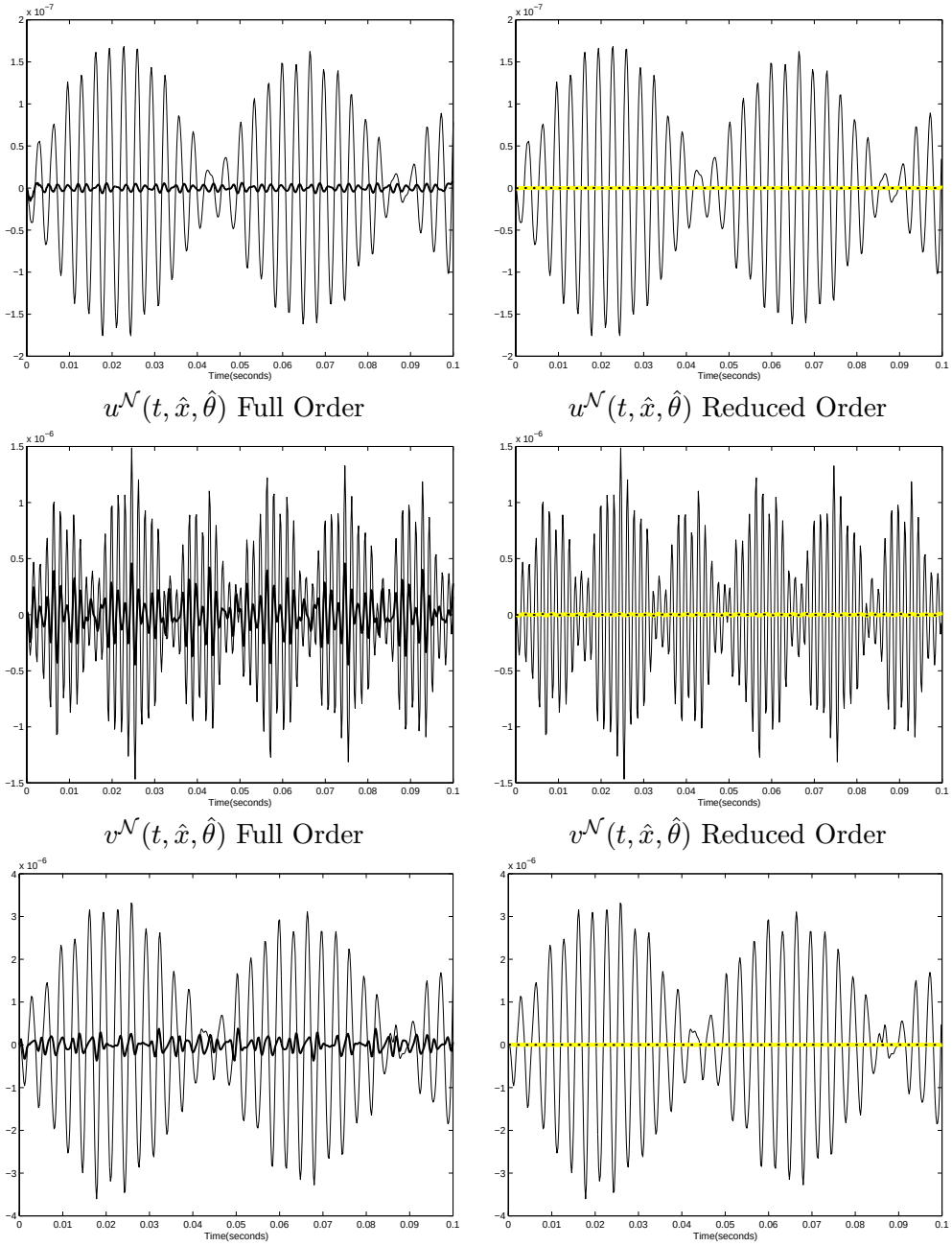

$u^{\mathcal{N}}(t, \hat{x}, \hat{\theta})$ Full Order $u^{\mathcal{N}}(t, \hat{x}, \hat{\theta})$ Reduced Order

$v^{\mathcal{N}}(t, \hat{x}, \hat{\theta})$ Full Order $v^{\mathcal{N}}(t, \hat{x}, \hat{\theta})$ Reduced Order

$w^{\mathcal{N}}(t, \hat{x}, \hat{\theta})$ Full Order $w^{\mathcal{N}}(t, \hat{x}, \hat{\theta})$ Reduced Order

(a) (b)

Figure 5.37: Uncontrolled and controlled displacements at p_1; (a) full order ($\mathcal{N} = 333$): — uncontrolled, — controlled; (b) reduced order: — uncontrolled, — Lagrange controlled ($\mathcal{N} = 9$), $\cdots$ POD controlled ($\mathcal{N} = 9$).

5.3 POD Reduced Order Control Gains Applied in Full Order Model

One primary goal of this research is to develop a method to compute control gains from observations of a physical shell system using a discretized PDE model and implement the computed control gains in real time to the physical system. Numerical results from model reduction techniques given in previous sections indicate the feasibility of real time computation by reducing the number of unknowns without degrading the performance of the model and without losing control authority. While studies of the reduced order controllers applied to the reduced order model dynamics are useful, they do not truly indicate the performance of the controller when applied in practice. To obtain information in this regard, we next investigated the performance of control gains computed from the reduced order model when applied to the full order system. It has been shown through careful analysis of natural frequencies and modes in [24] that the full order system closely approximates the infinite dimensional system. With this assumption, applying the reduced order gains to the full order system is a reasonable way to investigate the anticipated performance of the method when used on an actual physical system. While our early calculations give *some* indication of how a feedback gain based on reduced order models might perform when applied to either the true infinite dimensional system or even a large finite dimensional model, the results are only suggestive. Further evidence will be available once reduced order model based controllers are implemented experimentally.

We illustrate the use of POD reduced order gains in controlling the full order system, but the method we present could be readily adapted for the Lagrange, Hermite or Taylor reduced basis methods.

We denote the full order space by $V^{\mathcal{N}}$ and the POD reduced basis space by $V^{\mathcal{N}_P}$. To employ a POD reduced order based optimal control in the full order equation

$$\dot{z}^{2\mathcal{N}}(t) \;=\; A^{2\mathcal{N}} z^{2\mathcal{N}}(t) + B^{2\mathcal{N}} U(t) + G^{2\mathcal{N}}(t)\;, \tag{5.24}$$

we must find a projection $\hat{P} : \mathbb{R}^{2\mathcal{N}} \to \mathbb{R}^{2\mathcal{N}_P}$ so that we can employ the reduced order feedback gains with full order observations in

$$U(t) = -\left(R^{2s}\right)^{-1}\left(B^{2\mathcal{N}_P}\right)^T\left[\Pi^{2\mathcal{N}_P}\hat{P}z^{2\mathcal{N}}(t) - r^{2\mathcal{N}_P}(t)\right] . \tag{5.25}$$

To this end, note first that the Galerkin approximation $y^{\mathcal{N}}$ (of the solution to (2.7)) is the projection of the infinite dimensional solution y into the finite dimensional subspace $V^{\mathcal{N}}$. Similarly, it follows that $y^{\mathcal{N}_P}$ is the projection of y into $V^{\mathcal{N}_P}$. Denote the projection operator from V into $V^{\mathcal{N}_P}$ by $\mathcal{P}^{\mathcal{N}_P}$ and denote the projection from $V^{\mathcal{N}}$ into $V^{\mathcal{N}_P}$ by $\mathcal{P}^{\mathcal{N}_P}_{V^{\mathcal{N}}}$. Since the same inner products are used in $V, V^{\mathcal{N}}$ and $V^{\mathcal{N}_P}$ and $V^{\mathcal{N}_P} \subset V^{\mathcal{N}} \subset V$, it follows that

$$\mathcal{P}^{\mathcal{N}_P}y^{\mathcal{N}} = \mathcal{P}^{\mathcal{N}_P}_{V^{\mathcal{N}}}y^{\mathcal{N}} = y^{\mathcal{N}_P} \quad \text{for all } y^{\mathcal{N}} \in V^{\mathcal{N}} .$$

This implies that the reduced order state $(y^{\mathcal{N}_P}, \dot{y}^{\mathcal{N}_P}) \in V^{\mathcal{N}_P} \times V^{\mathcal{N}_P}$ is the projection of the full order state $(y^{\mathcal{N}}, \dot{y}^{\mathcal{N}}) \in V^{\mathcal{N}} \times V^{\mathcal{N}}$ from $V^{\mathcal{N}} \times V^{\mathcal{N}}$ into $V^{\mathcal{N}_P} \times V^{\mathcal{N}_P}$, which is equivalent to mapping the vector of basis coefficients $z^{2\mathcal{N}}$ into $z^{2\mathcal{N}_P}$ (the vector $z^{2\mathcal{N}}$ is defined following (3.14)). We obtain this projection by pre-multiplying $z^{2\mathcal{N}}$ by the matrix representation of the projection $\mathcal{P}^{\mathcal{N}_P}_{V^{\mathcal{N}}} \times \mathcal{P}^{\mathcal{N}_P}_{V^{\mathcal{N}}}$ from $V^{\mathcal{N}} \times V^{\mathcal{N}}$ into $V^{\mathcal{N}_P} \times V^{\mathcal{N}_P}$. Denoting the matrix representation of $\mathcal{P}^{\mathcal{N}_P}_{V^{\mathcal{N}}}$ by $\bar{P}^{\mathcal{N}_P}$, then $\hat{P}$ which we use in (5.25) is then given by

$$\hat{P} = \begin{bmatrix} \bar{P}^{\mathcal{N}_P} & \\ & \bar{P}^{\mathcal{N}_P} \end{bmatrix} . \tag{5.26}$$

Note that $\hat{P}$ is the matrix representation of $\mathcal{P}^{\mathcal{N}_P}_{V^{\mathcal{N}}} \times \mathcal{P}^{\mathcal{N}_P}_{V^{\mathcal{N}}}$. The reduced order gains applied in the full order feedback loop, i.e., (5.25) employed in (5.24), yields the full order closed loop

$$\begin{aligned} \dot{z}^{2\mathcal{N}}(t) &= \left[A^{2\mathcal{N}} - B^{2\mathcal{N}}R^{-1}\left(B^{2\mathcal{N}_P}\right)^T\Pi^{2\mathcal{N}_P}\hat{P}\right]z^{2\mathcal{N}}(t) \\ &\quad + B^{2\mathcal{N}}R^{-1}\left(B^{2\mathcal{N}_P}\right)^T r^{2\mathcal{N}_P}(t) + G^{2\mathcal{N}}(t) . \end{aligned} \tag{5.27}$$

The computation and structure of the matrix $\bar{P}^{\mathcal{N}_P} \in \mathbb{R}^{\mathcal{N}_P \times \mathcal{N}}$ is dictated by the component nature of the state $y = (u, v, w)$. The spaces $V^{\mathcal{N}}$ and $V^{\mathcal{N}_P}$ are product

spaces as expressed in (4.1), so the projection $\mathcal{P}_{V^{\mathcal{N}}}^{\mathcal{N}_P}$ has three components

$$\begin{aligned}
\mathcal{P}^{N_P^u} &: \text{span}\,\{\mathcal{B}_{u_i}\}_{i=1}^{\mathcal{N}_u} \to \text{span}\,\{\Phi_{u_i}\}_{i=1}^{N_P} \\
\mathcal{P}^{N_P^v} &: \text{span}\,\{\mathcal{B}_{v_i}\}_{i=1}^{\mathcal{N}_v} \to \text{span}\,\{\Phi_{v_i}\}_{i=1}^{N_P} \\
\mathcal{P}^{N_P^w} &: \text{span}\,\{\mathcal{B}_{w_i}\}_{i=1}^{\mathcal{N}_w} \to \text{span}\,\{\Phi_{w_i}\}_{i=1}^{N_P} \ ,
\end{aligned}$$

where N_p is the number of POD basis functions in the u, v and w directions with basis functions Φ_{u_i}, Φ_{v_i} and Φ_{w_i}, and $\mathcal{N}_u, \mathcal{N}_v$ and $\mathcal{N}_w$ denote full order discretization levels with basis functions $\mathcal{B}_{u_i}, \mathcal{B}_{v_i}$ and $\mathcal{B}_{w_i}$. Denoting the matrix representation of the component projections by $\bar{P}^{N_P^u}$, $\bar{P}^{N_P^v}$ and $\bar{P}^{N_P^w}$, the matrix $\bar{P}^{\mathcal{N}_P}$ has the components

$$\bar{P}^{\mathcal{N}_P} = \begin{bmatrix} \bar{P}^{N_P^u} & & \\ & \bar{P}^{N_P^v} & \\ & & \bar{P}^{N_P^w} \end{bmatrix} .$$

We illustrate the construction of $\bar{P}^{N_P^u}$ and point out that the construction of $\bar{P}^{N_P^v}$ and $\bar{P}^{N_P^w}$ are carried out similarly. For $i = 1, \ldots, N_P$ and any $u^{\mathcal{N}} \in \text{span}\,\{\mathcal{B}_{u_i}\}_{i=1}^{\mathcal{N}_u}$, the projection $\mathcal{P}^{N_P^u}$ satisfies $\left\langle \mathcal{P}^{N_P^u} u^{\mathcal{N}} - u^{\mathcal{N}}, \Phi_{u_i} \right\rangle = 0$. Thus, $\left\langle \mathcal{P}^{N_P^u} u^{\mathcal{N}} - \sum_{j=1}^{\mathcal{N}_u} u_j \mathcal{B}_{u_j}, \Phi_{u_i} \right\rangle = 0$ and it follows that

$$\left\langle \sum_{k=1}^{N_P} (\bar{P}^{N_P^u} \bar{u})_k \Phi_{u_k} - \sum_{j=1}^{\mathcal{N}_u} u_j \mathcal{B}_{u_j}, \Phi_{u_i} \right\rangle = 0 \ , \quad i = 1, \ldots, N_P \ ,$$

where $\bar{u}$ is the vector of coefficients $u_1, \ldots, u_{\mathcal{N}_u}$ in the full order space. The equality $\mathcal{P}^{N_P^u} u^{\mathcal{N}} = \sum_{k=1}^{N_P} (\bar{P}^{N_P^u} \bar{u})_k \Phi_{u_k}$ used above expresses the property of matrix representations where the basis coefficients of the image (i.e., the basis coefficients of $\mathcal{P}^{N_P^u} u^{\mathcal{N}}$ in $\text{span}\,\{\Phi_{u_i}\}_{i=1}^{N_P}$) are obtained by multiplying the matrix representation and the vector of basis coefficients in the domain (i.e., $\bar{P}^{N_P^u} \bar{u}$). We use the linearity properties of the inner product to obtain

$$\sum_{k=1}^{N_P} (\bar{P}^{N_P^u} \bar{u})_k \left\langle \Phi_{u_k}, \Phi_{u_i} \right\rangle = \sum_{j=1}^{\mathcal{N}_u} u_j \left\langle \mathcal{B}_{u_j}, \Phi_{u_i} \right\rangle , \quad i = 1, \ldots, N_P \ .$$

Since this equation is true for $i = 1, \ldots, N_P$, we then form a matrix equation

$$M_1^{N_P \times N_P} (\bar{P}^{N_P^u} \bar{u}) = M_2^{N_P \times \mathcal{N}_u} \bar{u} \ ,$$

where $M_1 \in \mathbb{R}^{N_P \times N_P}$ has components

$$[M_1]_{k,\ell} = \langle \Phi_{u_\ell}, \Phi_{u_k} \rangle \,, \;\; k, \ell = 1, \ldots, N_P \;,$$

and $M_2 \in \mathbb{R}^{N_P \times \mathcal{N}_u}$ has components

$$[M_2]_{k,\ell} = \langle \mathcal{B}_{u_\ell}, \Phi_{u_k} \rangle \,, \;\; \ell = 1, \ldots, N_P, \;\; k = 1, \ldots, \mathcal{N}_u \;.$$

Therefore $\bar{P}^{N_P{}^u} = M_1^{-1} M_2 \in \mathbb{R}^{N_P \times \mathcal{N}_u}$. The other two matrix representations $\bar{P}^{N_P{}^v}$ and $\bar{P}^{N_P{}^w}$ are created similarly. Once these matrices are computed, the matrix $\hat{P} \in \mathbb{R}^{2\mathcal{N}_P \times 2\mathcal{N}}$ is formed and we obtain the full order feedback loop based on reduced order control gains in (5.27).

In Figures 5.38 and 5.39, we present time history and RMS plots when the feedback control based on $\mathcal{N} = 9$ POD basis functions is implemented in the full order system. As might be expected, the resulting attenuation is not as good as when the reduced order control is applied to the reduced order model. However, the overall effectiveness of the feedback control is still quite impressive. Results with $\mathcal{N} = 6$ POD basis functions are similar. Since the system was not resolved with $\mathcal{N} = 3$ POD basis functions (as indicated in Table 3), good attenuation was not obtained (see [7, p. 31]) in the case $\mathcal{N} = 3$.

Somewhat surprisingly, good attenuation using $\mathcal{N} = 12$ POD basis functions *was not* attained. Indeed, computations suggested great difficulty in stabilizing the system based on 12 POD element designs. An analysis of the controllability matrix of the POD reduced order system suggests a possible explanation. *Controllability* is a necessary (but not sufficient) condition for a linear system to be driven to zero starting at any initial state. Linear systems described by the matrices $A^{2\mathcal{N}_P}$ and $B^{2\mathcal{N}_P}$ in the first order linear system (3.14) are *controllable* if the $2\mathcal{N}_P \times 2s\mathcal{N}_P$ controllability matrix $\mathcal{C}(A^{2\mathcal{N}_P}, B^{2\mathcal{N}_P}) = [B|AB|A^2B| \cdots |A^{2\mathcal{N}_P - 1}B]$, where $A \equiv A^{2\mathcal{N}_P}, B \equiv B^{2\mathcal{N}_P}$, has rank $2\mathcal{N}_P$. For systems with rank $\left(\mathcal{C}(A^{2\mathcal{N}_P}, B^{2\mathcal{N}_P})\right) = m \leq 2\mathcal{N}_P$, any initial condition of the state $z^{2\mathcal{N}_P}$ in the m dimensional subspace of $\mathbb{R}^{2\mathcal{N}_P}$ spanned by the columns of $\mathcal{C}(A^{2\mathcal{N}_P}, B^{2\mathcal{N}_P})$ can be driven to zero (see [18]). Generally speaking, the

$\mathcal{N}_P$	rank($\mathcal{C}(A^{2\mathcal{N}_P}, B^{2\mathcal{N}_P})$)/max possible rank
3	4/6
6	4/12
9	6/18
12	6/24

Table 5.24: Ranks of the controllability matrix $\mathcal{C}(A^{2\mathcal{N}_P}, B^{2\mathcal{N}_P})$. The ratios indicate the actual rank over the maximum possible rank of the matrices.

larger the deficit of $\mathcal{C}(A^{2\mathcal{N}_P}, B^{2\mathcal{N}_P})$ from its maximum possible rank, the more difficulty in stabilizing or controlling the linear system (3.19). A summary of the ranks of the controllability matrix for the different numbers of basis functions is given in Table 5.24. Its rank continues to decrease (as more POD elements are used) relative to the maximum possible rank until the system becomes significantly uncontrollable. Therefore, as we increase the number of POD basis functions, the system becomes increasingly more difficult to stabilize. Since stabilizing feedback control in the reduced order model is already more difficult with 12 basis functions than with 9, then stabilizing control in the full order model is likely to be much more difficult.

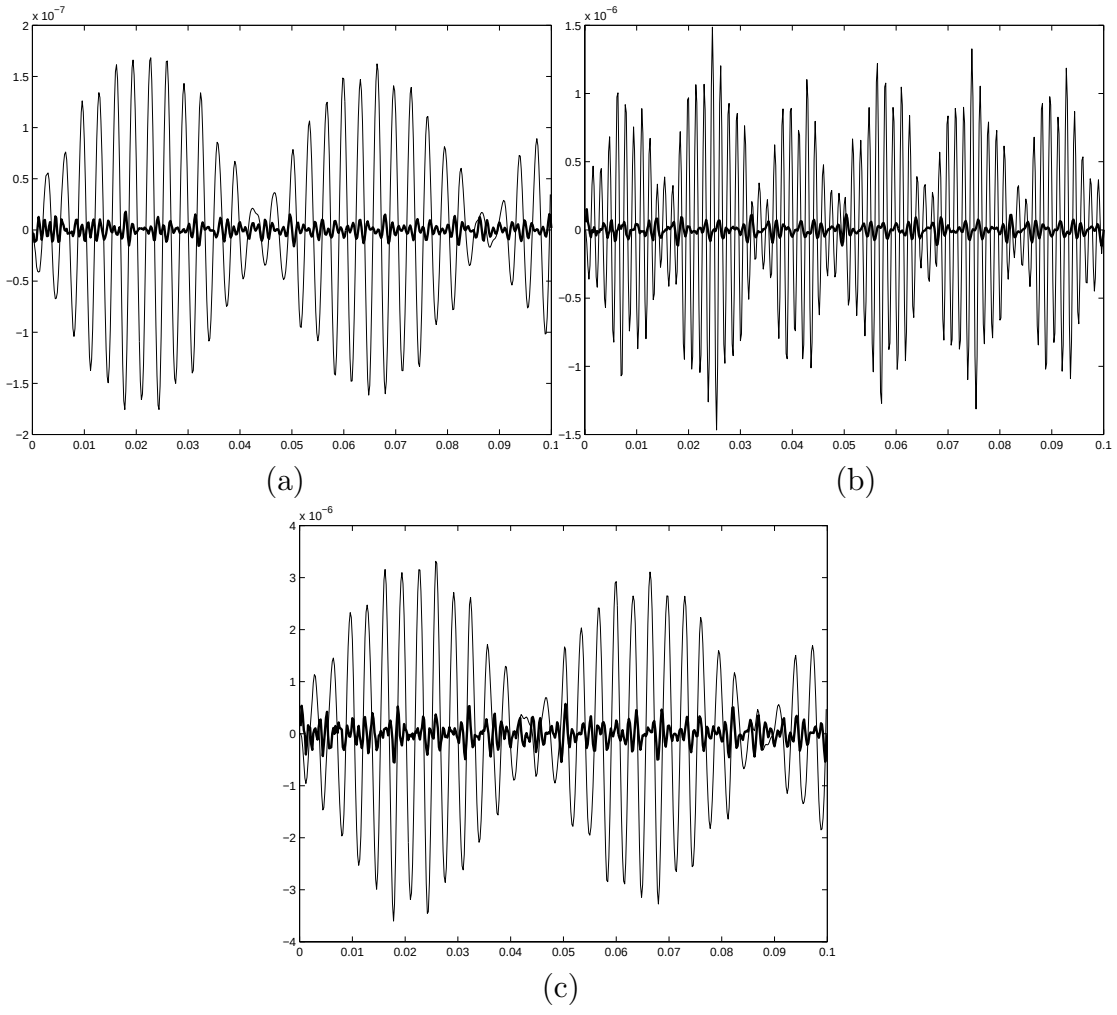

Figure 5.38: Full order uncontrolled and controlled displacements at p_1 with control design based on $\mathcal{N} = 9$ POD basis functions; (a) longitudinal $u^{\mathcal{N}}(t, \hat{x}, \hat{\theta})$, (b) circumferential $v^{\mathcal{N}}(t, \hat{x}, \hat{\theta})$, (c) transverse $w^{\mathcal{N}}(t, \hat{x}, \hat{\theta})$; — uncontrolled, — controlled.

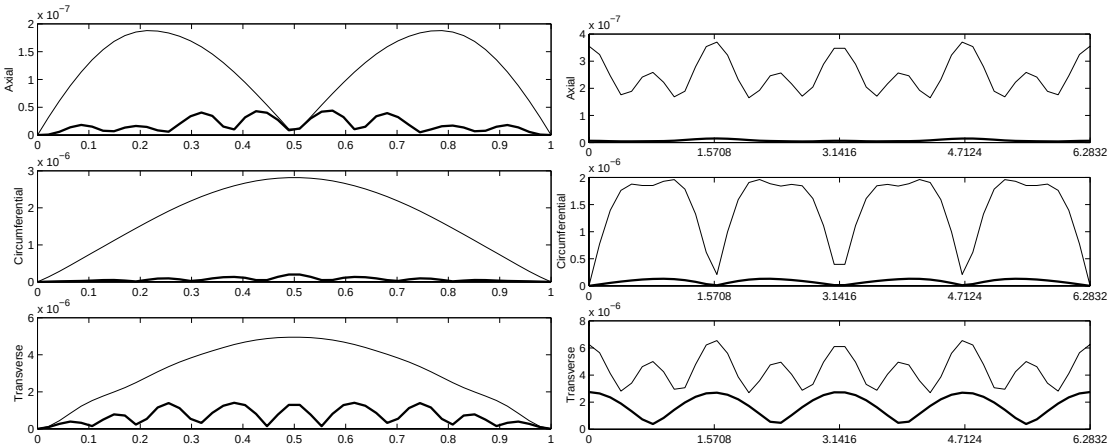

Figure 5.39: Full order uncontrolled and controlled root mean square displacements with control design based on $\mathcal{N} = 9$ POD basis functions; (a) axial line L_1, (b) circumferential line L_2; — uncontrolled, — controlled.

Chapter 6

Conclusions

We presented and implemented a full order Galerkin type numerical method for thin shell models illustrating the following advantages: (i) adapting to different boundary conditions simply involve modification of test functions to fit necessary conditions; (ii) discontinuities in shell and patch parameters, together with localized patch input are easily handled; (iii) fast convergence — $\mathcal{O}(h_x^2)$ with fully cubic spline axial basis functions; (iv) high accuracy leads to smaller matrix sizes (than with linear spline basis functions or finite elements); (v) approximate frequencies and modes agree with analytic thin shell solutions for simply supported boundary conditions and no damping; (vi) semidiscrete system (of the form $\dot{z} = Az + BU + g$) facilitates application of control methodologies. These advantages are all illustrated in the numerical examples in Chapter 5. One advantage of the method that we hope to illustrate in future work is the absence of *locking* which occurs in finite element applications.

LQR control on the system with no exogenous force produced good attenuation levels (Chapter 5.1.3), which agrees with theoretical convergence results in Chapter 3.5. Although theoretical results for convergence of finite dimensional controls of the periodically excited shell is not complete, numerical examples establish the controllability of the shell system with surface mounted piezoceramic patches incorporating passive contributions and strong Kelvin-Voigt damping.

Although the accuracy and fast convergence of the full order method yielded matrix dimensions smaller than those in finite element or finite difference methods, real time computation of the control gains for application in physical systems necessitated the investigation of reduced basis methods. The Lagrange and POD reduced basis methods exhibited convergence to the full order solution as more basis functions were used. It should be noted that there is no systematic way to choose basis elements for the Lagrange reduced basis space. For vibrations with few excited frequencies, it is very probable to get linearly dependent basis functions as more basis elements are chosen. Convergence of the Lagrange reduced basis method will be lost if the user is not careful in selecting the elements. On the other hand, the POD reduced basis method offered a systematic way to choose basis functions which exhibit convergence to the full order solution. Furthermore, linear independence of basis functions is retained and hence the resulting matrices in the finite dimensional system remain well-conditioned, i.e., ill-conditioning that occurs when increasing the Lagrange basis space is not present. Finally, POD reduced order gains were implemented in the full order model as a first step in testing the performance of reduced order gains in controlling physical systems. The attenuation levels attained were very satisfactory.

List of References

[1] R. A. Adams, *Sobolev Spaces*, Academic Press, Inc., New Yor, 1975.

[2] B. Almroth, *Automatic choice of global shape functions in structural analysis*, AIAA Journal, 16 (1978), pp. 525–528.

[3] D. N. Arnold and R. S. Falk, *A uniformly accurate finite element for the Reissner Mindlin plate*, SIAM Journal of Numerical Analysis, 26 (1989), pp. 1276–1290.

[4] D. G. Ashwell and R. H. Gallagher, *Finite Elements for Thin Shells and Curved Members*, John Wiley and Sons, London, 1976.

[5] I. Babuška and M. Suri, *Locking effects in the finite element approximation of elasticity problems*, Numerische Mathematik, 61 (1992), pp. 439–463.

[6] ——, *On locking and robustness in the finite element method*, SIAM Journal of Numerical Analysis, 29 (1992), pp. 1261–1293.

[7] H. T. Banks, R. C. del Rosario, and R. C. Smith, *Reduced order model feedback control design: Computational studies for thin cylindrical shells*, Tech. Rep. CRSC-TR98-25, Center for Research in Scientific Computation, NCSU, Raleigh, June 1998.

[8] H. T. Banks, M. Demetriou, and R. C. Smith, *Utilization of coupling effects in compensator design for structural acoustic systems – numerical examples*, Journal of the Acoustical Society of America, 103 (1998), pp. 872–887.

[9] H. T. Banks, M. A. Demetriou, and R. C. Smith, *An H^∞/minmax periodic control in a 2-d structural acoustic model with piezceramic actuators*, IEEE Transactions on Automatic Control, 41 (1996), pp. 943–959.

[10] H. T. Banks, W. Fang, R. J. Silcox, and R. C. Smith, *Approximation methods for control of acoustic/structure models with piezoceramic actuators*, Journal of Intelligent Material Systems and Structures, 4 (1993), pp. 98–116.

[11] H. T. Banks and K. Ito, *Approximation in LQR problems for infinite dimensional systems with unbounded input operators*, Journal of Mathematical Systems, Estimation, and Control, 7 (1997), pp. 1–34.

[12] H. T. Banks, K. Ito, and Y. Wang, *Well-posedness for damped second order systems with unbounded input operators*, Differential and Integral Equations, 8 (1995), pp. 587–606.

[13] H. T. Banks, R. C. Smith, D. Brown, R. Silcox, and V. Metcalf, *Experimental confirmation of a PDE-based approach to design of feedback controls*, SIAM Journal on Control and Optimization, 35 (1997), pp. 1263–1296.

[14] H. T. Banks, R. C. Smith, and Y. Wang, *Smart Material Structures: Modeling Estimation and Control*, Masson/John Wiley, Paris/Chichester, 1996.

[15] H. T. Banks and Y. Zhang, *Computational methods for a curved beam with piezoceramic patches*, Journal of Intelligent Material Systems and Structures, 8 (1997), pp. 260–278.

[16] G. Berkooz, P. Holmes, and J. Lumley, *The proper orthogonal decomposition in the analysis of turbulent flows*, Annual Review of Fluid Mechanics, 25 (1993), pp. 539–575.

[17] M. Bernadou, *Finite Element Methods for Thin Shell Problems*, John Wiley/Masson, Chichester/Paris, 1996.

[18] W. L. Brogan, *Modern Control Theory*, Prentice Hall, New Jersey, 1991.

[19] P. N. Brown, G. D. Byrne, and C. Hindmarsh, *VODE: A variable coefficient ode solver*, SIAM J. Sci. Stat. Comput., 10 (1989), pp. 1038–1051.

[20] F. Chatelin, *Spectral Approximation of Linear Operators*, Academic Press, New York, 1983.

[21] G. Da Prato, *Syhnthesis of optimal control for an infinite dimensional periodic problem*, SIAM J. Control and Optimizatoin, 25 (1987), pp. 706–714.

[22] R. C. del Rosario and R. C. Smith, *Spline approximation of thin shell dynamics: Numerical examples*, Tech. Rep. CRSC-TR96-5, Center for Research in Scientific Computation, NCSU, Raleigh, 1996.

[23] ——, *LQR control of thin shell dynamics: Formulation and numerical implementation*, Tech. Rep. ICASE Report 97-59, Institute for Computer Applications in Science and Engineering, NASA Langley Research Center, Hampton, 1997. Journal of Intelligent Material Systems and Structures, to apppear.

[24] ——, *Spline approximation of thin shell dynamics*, International Journal for Numerical Methods in Engineering, 40 (1997), pp. 2807–2840.

[25] ——, *LQR conrol of shell vibrations via piezoceramic actuators*, International Series in Numerical Mathematics, 126 (1998), pp. 247–265.

[26] E. Hinton and D. R. J. Owen, *Finite Element Software for Plates and Shells*, Pineridge, Swansea, UK, 1984.

[27] T. J. R. Hughes and E. Hinton, *Finite Element Methods for Plate and Shell Structures*, Pineridge, Swansea, UK, 1986.

[28] T. J. R. Hughes, A. Pifko, and A. Jay, *Nonlinear Finite Element Analysis of Plates and Shells*, American Society of Mechanical Engineers, New York, 1981.

[29] Institute of Electrical and Electronics Engineers, *IEEE Standard on Piezoelectricity*, New York, 1978.

[30] K. Ito and S. S. Ravindran, *A reduced order method for simulation and control of fluid flows*, Tech. Rep. CRSC-TR96-27, Center for Research in Scientific Computation, NCSU, Raleigh, 1996. Journal of Computational Physics, submitted.

[31] ——, *A reduced basis method for control problems governed by PDE*, vol. 126 of International Series in Numerical Mathematics, Birkhäuser Verlag, Basel, 1997. Also CRSC-TR97-1.

[32] H. Kraus, *Thin Elastic Shells: An Introduction to the Theoretical Foundations and the Analysis of their Static and Dynamic Behavior*, Wiley, New York, 1967.

[33] Y. Leino and J. Pitkaänta, *On the membrane locking of $h-p$ finite elements in a cylindrical shell problem*, International Journal for Numerical Methods in Engineering, 37 (1994), pp. 1053–1070.

[34] A. W. Leissa, *Vibrations of shells.* Reprinted by the Acoustical Society of America through the American Institute of Physics, 1973.

[35] A. E. Love, *A Treatise on the Mathematical Theory of Elasticity*, Cambridge University Press, London, 1927.

[36] J. Lumley, *The structure of inhomogenous turbulent flows*, Atmospheric Turbulence and Wave Propagation, (1967), pp. 166–178.

[37] H. Ly and H. Tran, *Proper orthogonal decomposition for flow calculations and optimal control in a horizontal CVD reactor*, Tech. Rep. CRSC-TR98-13, Center for Research in Scientific Computation, NCSU, Raleigh, 1998. Quarterly of Applied Mathematics, to appear.

[38] S. Markuš, *The Mechanics of Vibrations of Cylindrical Shells*, Elsevier, New York, 1988.

[39] D. Nagy, *Modal representation of geometrically nonlinear behavior by the finite element method*, Computers and Structures, 10 (1979), pp. 683–688.

[40] A. Noor, *Recent advances in reduction methods for nonlinear problems*, Computers and Structures, 13 (1981), pp. 31–44.

[41] A. Noor, C. Andersen, and J. Peters, *Reduced basis technique for collapse analysis of shells*, AIAA Journal, 19 (1981), pp. 393–397.

[42] A. Noor and J. Peters, *Reduced basis technique for nonlinear analysis of structures*, AIAA Journal, 18 (1980), pp. 455–462.

[43] A. Pazy, *Semigroups of Linear Operators and Applications to Partial Differential Equations*, Springer-Verlag, New York, 1983.

[44] J. Peterson, *The reduced basis method for incompressible viscous flow calculations*, SIAM Journal on Scientific and Statistical Computing, 10 (1989), pp. 777–786.

[45] J. Pitkaänta, *The problem of membrane locking in finite element analysis of cylindrical shells*, Numerische Mathematik, 61 (1992), pp. 523–542.

[46] G. Prathap, *The Finite Element Method in Structural Mechanics*, Kluwer Academic Publishers, Dordrecht, The Netherlands, 1993.

[47] P. M. Prenter, *Splines and Variational Methods*, Wiley Classics Edition, New York, 1989.

[48] R. E. Showalter, *Hilbert Space Methods for Partial Differential Equations*, Pitman, San Francisco, 1977.

[49] M. Soare, *Application of Finite Difference Equations to Shell Analysis*, Pergamon Press, London, 1967.

[50] W. Soedel, *Vibrations of Shells and Plates*, Marcel Dekker, New York, 1993.

[51] J. Stoer and R. Bulirsch, *Introduction to Numerical Analysis*, Springer-Verlag, New York, 1993.

[52] H. Tanabe, *Equations of Evolution*, Pitman Publishing Ltd., London, 1979.

[53] J. William Weaver and P. Johnston, *Finite Elements for Structural Analysis*, Prentice-Hall, Englewood Cliffs, New Jersey, 1984.

[54] J. Wloka, *Partial Differential Equations*, Cambridge University Press, Cambridge, 1992.

[55] Y. Zhang, *Mathematical Formulation of Vibrations of a Composite Curved Beam Structure: Aluminum Core Material with Viscoelastic Layers, Constraining Layers and Piezoceramic Patches*, PhD thesis, N. C. State University, 1997.

Appendix A

Passive Patch Contributions

$$
\begin{aligned}
M_x &= -\frac{Eh^3}{12(1-\nu^2)}\left[\frac{\partial^2 w}{\partial x^2}+\frac{\nu}{R^2}\frac{\partial^2 w}{\partial \theta^2}\right] \\
&+ \sum_{i=1}^{s}\frac{E_{pe_{1i}}}{(1-\nu_{pe_{1i}}^2)}\left[\frac{a_{2_{1i}}}{2}\left(\frac{\partial u}{\partial x}+\nu_{pe_{1i}}\left(\frac{1}{R}\frac{\partial v}{\partial \theta}+\frac{w}{R}\right)\right)-\frac{a_{3_{1i}}}{3}\left(\frac{\partial^2 w}{\partial x^2}+\frac{\nu_{pe_{1i}}}{R^2}\frac{\partial^2 w}{\partial \theta^2}\right)\right]\chi_{pe_{1i}} \\
&+ \sum_{i=1}^{s}\frac{E_{pe_{2i}}}{(1-\nu_{pe_{2i}}^2)}\left[-\frac{a_{2_{2i}}}{2}\left(\frac{\partial u}{\partial x}+\nu_{pe_{2i}}\left(\frac{1}{R}\frac{\partial v}{\partial \theta}+\frac{w}{R}\right)\right)-\frac{a_{3_{2i}}}{3}\left(\frac{\partial^2 w}{\partial x^2}+\frac{\nu_{pe_{2i}}}{R^2}\frac{\partial^2 w}{\partial \theta^2}\right)\right]\chi_{pe_{2i}} \\
&- \frac{c_D h^3}{12(1-\nu^2)}\frac{\partial}{\partial t}\left[\frac{\partial^2 w}{\partial x^2}+\frac{\nu}{R^2}\frac{\partial^2 w}{\partial \theta^2}\right] \\
&+ \sum_{i=1}^{s}\frac{c_{D_{pe_{1i}}}}{(1-\nu_{pe_{1i}}^2)}\frac{\partial}{\partial t}\left[\frac{a_{2_{1i}}}{2}\left(\frac{\partial u}{\partial x}+\nu_{pe_{1i}}\left(\frac{1}{R}\frac{\partial v}{\partial \theta}+\frac{w}{R}\right)\right)-\frac{a_{3_{1i}}}{3}\left(\frac{\partial^2 w}{\partial x^2}+\frac{\nu_{pe_{1i}}}{R^2}\frac{\partial^2 w}{\partial \theta^2}\right)\right]\chi_{pe_{1i}} \\
&+ \sum_{i=1}^{s}\frac{c_{D_{pe_{2i}}}}{(1-\nu_{pe_{2i}}^2)}\frac{\partial}{\partial t}\left[-\frac{a_{2_{2i}}}{2}\left(\frac{\partial u}{\partial x}+\nu_{pe_{2i}}\left(\frac{1}{R}\frac{\partial v}{\partial \theta}+\frac{w}{R}\right)\right)-\frac{a_{3_{2i}}}{3}\left(\frac{\partial^2 w}{\partial x^2}+\frac{\nu_{pe_{2i}}}{R^2}\frac{\partial^2 w}{\partial \theta^2}\right)\right]\chi_{pe_{2i}}
\end{aligned}
\tag{A.1}
$$

$$
\begin{aligned}
M_\theta &= -\frac{Eh^3}{12(1-\nu^2)}\left[\frac{1}{R^2}\frac{\partial^2 w}{\partial\theta^2}+\nu\frac{\partial^2 w}{\partial x^2}\right] \\
&+ \sum_{i=1}^{s}\frac{E_{pe_{1i}}}{(1-\nu_{pe_{1i}}^2)}\left[\frac{a_{2_{1i}}}{2}\left(\left(\frac{1}{R}\frac{\partial v}{\partial\theta}+\frac{w}{R}\right)+\nu_{pe_{1i}}\frac{\partial u}{\partial x}\right)-\frac{a_{3_{1i}}}{3}\left(\frac{1}{R^2}\frac{\partial^2 w}{\partial\theta^2}+\nu_{pe_{1i}}\frac{\partial^2 w}{\partial x^2}\right)\right]\chi_{pe_{1i}} \\
&+ \sum_{i=1}^{s}\frac{E_{pe_{2i}}}{(1-\nu_{pe_{2i}}^2)}\left[\frac{-a_{2_{2i}}}{2}\left(\left(\frac{1}{R}\frac{\partial v}{\partial\theta}+\frac{w}{R}\right)+\nu_{pe_{2i}}\frac{\partial u}{\partial x}\right)-\frac{a_{3_{2i}}}{3}\left(\frac{1}{R^2}\frac{\partial^2 w}{\partial\theta^2}+\nu_{pe_{2i}}\frac{\partial^2 w}{\partial x^2}\right)\right]\chi_{pe_{2i}} \\
&- \frac{c_D h^3}{12(1-\nu^2)}\frac{\partial}{\partial t}\left[\frac{1}{R^2}\frac{\partial^2 w}{\partial\theta^2}+\nu\frac{\partial^2 w}{\partial x^2}\right] \\
&+ \sum_{i=1}^{s}\frac{c_{D_{pe_{1i}}}}{(1-\nu_{pe_{1i}}^2)}\frac{\partial}{\partial t}\left[\frac{a_{2_{1i}}}{2}\left(\left(\frac{1}{R}\frac{\partial v}{\partial\theta}+\frac{w}{R}\right)+\nu_{pe_{1i}}\frac{\partial u}{\partial x}\right)-\frac{a_{3_{1i}}}{3}\left(\frac{1}{R^2}\frac{\partial^2 w}{\partial\theta^2}+\nu_{pe_{1i}}\frac{\partial^2 w}{\partial x^2}\right)\right]\chi_{pe_{1i}} \\
&+ \sum_{i=1}^{s}\frac{c_{D_{pe_{2i}}}}{(1-\nu_{pe_{2i}}^2)}\frac{\partial}{\partial t}\left[\frac{-a_{2_{2i}}}{2}\left(\left(\frac{1}{R}\frac{\partial v}{\partial\theta}+\frac{w}{R}\right)+\nu_{pe_{2i}}\frac{\partial u}{\partial x}\right)-\frac{a_{3_{2i}}}{3}\left(\frac{1}{R^2}\frac{\partial^2 w}{\partial\theta^2}+\nu_{pe_{2i}}\frac{\partial^2 w}{\partial x^2}\right)\right]\chi_{pe_{2i}}
\end{aligned}
\tag{A.2}
$$

$$
\begin{aligned}
M_{x\theta} &= M_{\theta x} = -\frac{Eh^3}{12R(1+\nu)}\frac{\partial^2 w}{\partial x\partial\theta} \\
&+ \sum_{i=1}^{s}E_{pe_{1i}}\left[\frac{a_{2_{1i}}}{4(1+\nu_{pe_{1i}})}\left(\frac{\partial v}{\partial x}+\frac{1}{R}\frac{\partial u}{\partial\theta}\right)-\frac{a_{3_{1i}}}{6(1+\nu_{pe_{1i}})}\left(\frac{2}{R}\frac{\partial^2 w}{\partial x\partial\theta}\right)\right]\chi_{pe_{1i}} \\
&+ \sum_{i=1}^{s}E_{pe_{2i}}\left[-\frac{a_{2_{2i}}}{4(1+\nu_{pe_{2i}})}\left(\frac{\partial v}{\partial x}+\frac{1}{R}\frac{\partial u}{\partial\theta}\right)-\frac{a_{3_{2i}}}{6(1+\nu_{pe_{2i}})}\left(\frac{2}{R}\frac{\partial^2 w}{\partial x\partial\theta}\right)\right]\chi_{pe_{2i}} \\
&- \frac{c_D h^3}{12R(1+\nu)}\frac{\partial}{\partial t}\left[\frac{\partial^2 w}{\partial x\partial\theta}\right] \\
&+ \sum_{i=1}^{s}c_{D_{pe_{1i}}}\frac{\partial}{\partial t}\left[\frac{a_{2_{1i}}}{4(1+\nu_{pe_{1i}})}\left(\frac{\partial v}{\partial x}+\frac{1}{R}\frac{\partial u}{\partial\theta}\right)-\frac{a_{3_{1i}}}{6(1+\nu_{pe_{1i}})}\left(\frac{2}{R}\frac{\partial^2 w}{\partial x\partial\theta}\right)\right]\chi_{pe_{1i}} \\
&+ \sum_{i=1}^{s}c_{D_{pe_{2i}}}\frac{\partial}{\partial t}\left[-\frac{a_{2_{2i}}}{4(1+\nu_{pe_{2i}})}\left(\frac{\partial v}{\partial x}+\frac{1}{R}\frac{\partial u}{\partial\theta}\right)-\frac{a_{3_{2i}}}{6(1+\nu_{pe_{2i}})}\left(\frac{2}{R}\frac{\partial^2 w}{\partial x\partial\theta}\right)\right]\chi_{pe_{2i}}
\end{aligned}
\tag{A.3}
$$

$$
\begin{aligned}
N_\theta &= \frac{Eh}{(1-\nu^2)}\left[\frac{1}{R}\frac{\partial v}{\partial \theta}+\frac{w}{R}+\nu\frac{\partial u}{\partial x}\right] \\
&+ \sum_{i=1}^{s}\frac{E_{pe_{1i}}}{(1-\nu_{pe_{1i}}^2)}\left[h_{pe_{1i}}\left(\frac{1}{R}\frac{\partial v}{\partial \theta}+\frac{w}{R}+\nu_{pe_{1i}}\frac{\partial u}{\partial x}\right)-\frac{a_{2_{1i}}}{2}\left(\frac{1}{R^2}\frac{\partial^2 w}{\partial \theta^2}+\nu_{pe_{1i}}\frac{\partial^2 w}{\partial x^2}\right)\right]\chi_{pe_{1i}} \\
&+ \sum_{i=1}^{s}\frac{E_{pe_{2i}}}{(1-\nu_{pe_{2i}}^2)}\left[h_{pe_{2i}}\left(\frac{1}{R}\frac{\partial v}{\partial \theta}+\frac{w}{R}+\nu_{pe_{2i}}\frac{\partial u}{\partial x}\right)+\frac{a_{2_{2i}}}{2}\left(\frac{1}{R^2}\frac{\partial^2 w}{\partial \theta^2}+\nu_{pe_{2i}}\frac{\partial^2 w}{\partial x^2}\right)\right]\chi_{pe_{2i}} \\
&+ \frac{c_D h}{(1-\nu^2)}\frac{\partial}{\partial t}\left[\frac{1}{R}\frac{\partial v}{\partial \theta}+\frac{w}{R}+\nu\frac{\partial u}{\partial x}\right] \\
&+ \sum_{i=1}^{s}\frac{c_{D_{pe_{1i}}}}{(1-\nu_{pe_{1i}}^2)}\frac{\partial}{\partial t}\left[h_{pe_{1i}}\left(\frac{1}{R}\frac{\partial v}{\partial \theta}+\frac{w}{R}+\nu_{pe_{1i}}\frac{\partial u}{\partial x}\right)-\frac{a_{2_{1i}}}{2}\left(\frac{1}{R^2}\frac{\partial^2 w}{\partial \theta^2}+\nu_{pe_{1i}}\frac{\partial^2 w}{\partial x^2}\right)\right]\chi_{pe_{1i}} \\
&+ \sum_{i=1}^{s}\frac{c_{D_{pe_{2i}}}}{(1-\nu_{pe_{2i}}^2)}\frac{\partial}{\partial t}\left[h_{pe_{2i}}\left(\frac{1}{R}\frac{\partial v}{\partial \theta}+\frac{w}{R}+\nu_{pe_{2i}}\frac{\partial u}{\partial x}\right)+\frac{a_{2_{2i}}}{2}\left(\frac{1}{R^2}\frac{\partial^2 w}{\partial \theta^2}+\nu_{pe_{2i}}\frac{\partial^2 w}{\partial x^2}\right)\right]\chi_{pe_{2i}}
\end{aligned}
\tag{A.4}
$$

$$
\begin{aligned}
N_{x\theta} &= N_{\theta x} = \frac{Eh}{2(1+\nu)}\left[\frac{\partial v}{\partial x}+\frac{1}{R}\frac{\partial u}{\partial \theta}\right] \\
&+ \sum_{i=1}^{s}E_{pe_{1i}}\left[\frac{h_{pe_{1i}}}{2(1+\nu_{pe_{1i}})}\left(\frac{\partial v}{\partial x}+\frac{1}{R}\frac{\partial u}{\partial \theta}\right)-\frac{a_{2_{1i}}}{4(1+\nu_{pe_{1i}})}\left(\frac{2}{R}\frac{\partial^2 w}{\partial x \partial \theta}\right)\right]\chi_{pe_{1i}} \\
&+ \sum_{i=1}^{s}E_{pe_{2i}}\left[\frac{h_{pe_{2i}}}{2(1+\nu_{pe_{2i}})}\left(\frac{\partial v}{\partial x}+\frac{1}{R}\frac{\partial u}{\partial \theta}\right)+\frac{a_{2_{2i}}}{4(1+\nu_{pe_{2i}})}\left(\frac{2}{R}\frac{\partial^2 w}{\partial x \partial \theta}\right)\right]\chi_{pe_{2i}} \\
&+ \frac{c_D h}{2(1+\nu)}\frac{\partial}{\partial t}\left[\frac{\partial v}{\partial x}+\frac{1}{R}\frac{\partial u}{\partial \theta}\right] \\
&+ \sum_{i=1}^{s}c_{D_{pe_{1i}}}\frac{\partial}{\partial t}\left[\frac{h_{pe_{1i}}}{2(1+\nu_{pe_{1i}})}\left(\frac{\partial v}{\partial x}+\frac{1}{R}\frac{\partial u}{\partial \theta}\right)-\frac{a_{2_{1i}}}{4(1+\nu_{pe_{1i}})}\left(\frac{2}{R}\frac{\partial^2 w}{\partial x \partial \theta}\right)\right]\chi_{pe_{1i}} \\
&+ \sum_{i=1}^{s}c_{D_{pe_{2i}}}\frac{\partial}{\partial t}\left[\frac{h_{pe_{2i}}}{2(1+\nu_{pe_{2i}})}\left(\frac{\partial v}{\partial x}+\frac{1}{R}\frac{\partial u}{\partial \theta}\right)+\frac{a_{2_{2i}}}{4(1+\nu_{pe_{2i}})}\left(\frac{2}{R}\frac{\partial^2 w}{\partial x \partial \theta}\right)\right]\chi_{pe_{2i}}
\end{aligned}
\tag{A.5}
$$

Appendix B

V inner product definition

We define the inner product on V to be $< \phi, \psi >_{V_E} = \sum_{i=1}^{16} I_i(\phi, \psi)$, where I_1 and I_2 are defined in Chapter 3. The remaining terms $I_3, \ldots, I_{16}$ are defined below. Note that $\phi = (u, v, w)$ and $\psi = (\eta_1, \eta_2, \eta_3)$.

$$I_3(\phi,\psi) = \int_0^{2\pi}\int_0^{\ell} \frac{Eh}{2(1+\nu)}\left[\frac{\partial v}{\partial x} + \frac{1}{R}\frac{\partial u}{\partial \theta}\right]\overline{\frac{\partial \eta_1}{\partial \theta}}dxd\theta \tag{B.1}$$

$$\begin{aligned} I_4(\phi,\psi) &= \sum_{i=1}^{s}\int_{\theta_{1_{1i}}}^{\theta_{2_{1i}}}\int_{x_{1_{1i}}}^{x_{2_{1i}}} E_{pe_{1i}}\left[\frac{h_{pe_{1i}}}{2(1+\nu_{pe_{1i}})}\left(\frac{\partial v}{\partial x} + \frac{1}{R}\frac{\partial u}{\partial \theta}\right)\right. \\ &\qquad \left. - \frac{a_{2_{1i}}}{2R(1+\nu_{pe_{1i}})}\frac{\partial^2 w}{\partial x \partial \theta}\right]\overline{\frac{\partial \eta_1}{\partial \theta}}dxd\theta \\ &+ \sum_{i=1}^{s}\int_{\theta_{1_{2i}}}^{\theta_{2_{2i}}}\int_{x_{1_{2i}}}^{x_{2_{2i}}} E_{pe_{2i}}\left[\frac{h_{pe_{2i}}}{2(1+\nu_{pe_{2i}})}\left(\frac{\partial v}{\partial x} + \frac{1}{R}\frac{\partial u}{\partial \theta}\right)\right. \\ &\qquad \left. + \frac{a_{2_{2i}}}{2R(1+\nu_{pe_{2i}})}\frac{\partial^2 w}{\partial x \partial \theta}\right]\overline{\frac{\partial \eta_1}{\partial \theta}}dxd\theta \end{aligned} \tag{B.2}$$

$$I_5(\phi,\psi) = \int_0^{2\pi}\int_0^{\ell} \frac{Eh}{(1-\nu^2)}\left[\frac{1}{R}\frac{\partial v}{\partial \theta} + \frac{w}{R} + \nu\frac{\partial u}{\partial x}\right]\overline{\frac{\partial \eta_2}{\partial \theta}}dxd\theta \tag{B.3}$$

$$I_6(\phi,\psi) = \sum_{i=1}^{s}\int_{\theta_{1_{1i}}}^{\theta_{2_{1i}}}\int_{x_{1_{1i}}}^{x_{2_{1i}}} \frac{E_{pe_{1i}}}{(1-\nu_{pe_{1i}}^2)}\left[h_{pe_{1i}}\left(\frac{1}{R}\frac{\partial v}{\partial \theta} + \frac{w}{R} + \nu_{pe_{1i}}\frac{\partial u}{\partial x}\right)\right.$$

$$- \frac{a_{2_{1i}}}{2}\left(\frac{1}{R^2}\frac{\partial^2 w}{\partial\theta^2} + \nu_{pe_{1i}}\frac{\partial^2 w}{\partial x^2}\right)\Bigg]\overline{\frac{\partial\eta_2}{\partial\theta}}dxd\theta$$

$$+ \sum_{i=1}^{s}\int_{\theta_{1_{2i}}}^{\theta_{2_{2i}}}\int_{x_{1_{2i}}}^{x_{2_{2i}}}\frac{E_{pe_{2i}}}{(1-\nu_{pe_{2i}}^2)}\left[h_{pe_{2i}}\left(\frac{1}{R}\frac{\partial v}{\partial\theta} + \frac{w}{R} + \nu_{pe_{2i}}\frac{\partial u}{\partial x}\right)\right. \tag{B.4}$$

$$\left. + \frac{a_{2_{2i}}}{2}\left(\frac{1}{R^2}\frac{\partial^2 w}{\partial\theta^2} + \nu_{pe_{2i}}\frac{\partial^2 w}{\partial x^2}\right)\right]\overline{\frac{\partial\eta_2}{\partial\theta}}dxd\theta$$

$$I_7(\phi,\psi) = \int_0^{2\pi}\int_0^{\ell}\frac{EhR}{2(1+\nu)}\left[\frac{\partial v}{\partial x} + \frac{1}{R}\frac{\partial u}{\partial\theta}\right]\overline{\frac{\partial\eta_2}{\partial\theta}}dxd\theta \tag{B.5}$$

$$I_8(\phi,\psi) = \sum_{i=1}^{s}\int_{\theta_{1_{1i}}}^{\theta_{2_{1i}}}\int_{x_{1_{1i}}}^{x_{2_{1i}}}E_{pe_{1i}}R\left[\frac{h_{pe_{1i}}}{2(1+\nu_{pe_{1i}})}\left(\frac{\partial v}{\partial x} + \frac{1}{R}\frac{\partial u}{\partial\theta}\right)\right.$$

$$\left. - \frac{a_{2_{1i}}}{2R(1+\nu_{pe_{1i}})}\frac{\partial^2 w}{\partial x\partial\theta}\right]\overline{\frac{\partial\eta_2}{\partial x}}dxd\theta$$

$$+ \sum_{i=1}^{s}\int_{\theta_{1_{2i}}}^{\theta_{2_{2i}}}\int_{x_{1_{2i}}}^{x_{2_{2i}}}E_{pe_{2i}}R\left[\frac{h_{pe_{2i}}}{2(1+\nu_{pe_{2i}})}\left(\frac{\partial v}{\partial x} + \frac{1}{R}\frac{\partial u}{\partial\theta}\right)\right. \tag{B.6}$$

$$\left. + \frac{a_{2_{2i}}}{2R(1+\nu_{pe_{2i}})}\frac{\partial^2 w}{\partial x\partial\theta}\right]\overline{\frac{\partial\eta_2}{\partial x}}dxd\theta$$

$$I_9(\phi,\psi) = \int_0^{2\pi}\int_0^{\ell}\frac{Eh}{(1-\nu^2)}\left[\frac{1}{R}\frac{\partial v}{\partial\theta} + \frac{w}{R} + \nu\frac{\partial u}{\partial x}\right]\overline{\eta_3}dxd\theta \tag{B.7}$$

$$I_{10}(\phi,\psi) = \sum_{i=1}^{s}\int_{\theta_{1_{1i}}}^{\theta_{2_{1i}}}\int_{x_{1_{1i}}}^{x_{2_{1i}}}\frac{E_{pe_{1i}}}{(1-\nu_{pe_{1i}}^2)}\left[h_{pe_{1i}}\left(\frac{1}{R}\frac{\partial v}{\partial\theta} + \frac{w}{R} + \nu_{pe_{1i}}\frac{\partial u}{\partial x}\right)\right.$$

$$\left. - \frac{a_{2_{1i}}}{2}\left(\frac{1}{R^2}\frac{\partial^2 w}{\partial\theta^2} + \nu_{pe_{1i}}\frac{\partial^2 w}{\partial x^2}\right)\right]\overline{\eta_3}dxd\theta$$

$$+ \sum_{i=1}^{s}\int_{\theta_{1_{2i}}}^{\theta_{2_{2i}}}\int_{x_{1_{2i}}}^{x_{2_{2i}}}\frac{E_{pe_{2i}}}{(1-\nu_{pe_{2i}}^2)}\left[h_{pe_{2i}}\left(\frac{1}{R}\frac{\partial v}{\partial\theta} + \frac{w}{R} + \nu_{pe_{2i}}\frac{\partial u}{\partial x}\right)\right. \tag{B.8}$$

$$\left. + \frac{a_{2_{2i}}}{2}\left(\frac{1}{R^2}\frac{\partial^2 w}{\partial\theta^2} + \nu_{pe_{2i}}\frac{\partial^2 w}{\partial x^2}\right)\right]\overline{\eta_3}dxd\theta$$

$$I_{11}(\phi,\psi) = \int_0^{2\pi}\int_0^{\ell}\frac{Eh^3R}{12(1-\nu^2)}\left[\frac{\partial^2 w}{\partial x^2} + \frac{\nu}{R^2}\frac{\partial^2 w}{\partial\theta^2}\right]\overline{\frac{\partial^2\eta_3}{\partial x^2}}dxd\theta \tag{B.9}$$

$$
\begin{aligned}
I_{12}(\phi,\psi) &= \sum_{i=1}^{s}\int_{\theta_{1_{1i}}}^{\theta_{2_{1i}}}\int_{x_{1_{1i}}}^{x_{2_{1i}}} -\frac{E_{pe_{1i}}R}{(1-\nu_{pe_{1i}}^2)}\left[\frac{a_{2_{1i}}}{2}\left(\frac{\partial u}{\partial x}+\nu_{pe_{1i}}\left(\frac{1}{R}\frac{\partial v}{\partial\theta}+\frac{w}{R}\right)\right)\right.\\
&\qquad \left.-\frac{a_{3_{1i}}}{3}\left(\frac{\partial^2 w}{\partial x^2}+\frac{\nu_{pe_{1i}}}{R^2}\frac{\partial^2 w}{\partial\theta^2}\right)\right]\overline{\frac{\partial^2\eta_3}{\partial x^2}}dxd\theta\\
&+ \sum_{i=1}^{s}\int_{\theta_{1_{2i}}}^{\theta_{2_{2i}}}\int_{x_{1_{2i}}}^{x_{2_{2i}}} -\frac{E_{pe_{2i}}R}{(1-\nu_{pe_{2i}}^2)}\left[-\frac{a_{2_{2i}}}{2}\left(\frac{\partial u}{\partial x}+\nu_{pe_{2i}}\left(\frac{1}{R}\frac{\partial v}{\partial\theta}+\frac{w}{R}\right)\right)\right. \qquad \text{(B.10)}\\
&\qquad \left.-\frac{a_{3_{2i}}}{3}\left(\frac{\partial^2 w}{\partial x^2}+\frac{\nu_{pe_{2i}}}{R^2}\frac{\partial^2 w}{\partial\theta^2}\right)\right]\overline{\frac{\partial^2\eta_3}{\partial x^2}}dxd\theta
\end{aligned}
$$

$$
I_{13}(\phi,\psi) = \int_0^{2\pi}\int_0^{\ell}\frac{Eh^3}{12R(1-\nu^2)}\left[\frac{1}{R^2}\frac{\partial^2 w}{\partial\theta^2}+\nu\frac{\partial^2 w}{\partial x^2}\right]\overline{\frac{\partial^2\eta_3}{\partial\theta^2}}dxd\theta \qquad \text{(B.11)}
$$

$$
\begin{aligned}
I_{14}(\phi,\psi) &= \sum_{i=1}^{s}\int_{\theta_{1_{1i}}}^{\theta_{2_{1i}}}\int_{x_{1_{1i}}}^{x_{2_{1i}}} -\frac{E_{pe_{1i}}}{R(1-\nu_{pe_{1i}}^2)}\left[\frac{a_{2_{1i}}}{2}\left(\frac{1}{R}\frac{\partial v}{\partial\theta}+\frac{w}{R}+\nu_{pe_{1i}}\frac{\partial u}{\partial x}\right)\right.\\
&\qquad \left.-\frac{a_{3_{1i}}}{3}\left(\frac{1}{R^2}\frac{\partial^2 w}{\partial\theta^2}+\nu_{pe_{1i}}\frac{\partial^2 w}{\partial x^2}\right)\right]\overline{\frac{\partial^2\eta_3}{\partial\theta^2}}dxd\theta\\
&+ \sum_{i=1}^{s}\int_{\theta_{1_{2i}}}^{\theta_{2_{2i}}}\int_{x_{1_{2i}}}^{x_{2_{2i}}} -\frac{E_{pe_{2i}}}{R(1-\nu_{pe_{2i}}^2)}\left[-\frac{a_{2_{2i}}}{2}\left(\frac{1}{R}\frac{\partial v}{\partial\theta}+\frac{w}{R}+\nu_{pe_{2i}}\frac{\partial u}{\partial x}\right)\right. \qquad \text{(B.12)}\\
&\qquad \left.-\frac{a_{3_{2i}}}{3}\left(\frac{1}{R^2}\frac{\partial^2 w}{\partial\theta^2}+\nu_{pe_{2i}}\frac{\partial^2 w}{\partial x^2}\right)\right]\overline{\frac{\partial^2\eta_3}{\partial\theta^2}}dxd\theta
\end{aligned}
$$

$$
I_{15}(\phi,\psi) = +\int_0^{2\pi}\int_0^{\ell}\frac{Eh^3}{6R(1+\nu)}\frac{\partial^2 w}{\partial x\partial\theta}\overline{\frac{\partial^2\eta_3}{\partial x\partial\theta}}dxd\theta \qquad \text{(B.13)}
$$

$$
\begin{aligned}
I_{16}(\phi,\psi) &= \sum_{i=1}^{s}\int_{\theta_{1_{1i}}}^{\theta_{2_{1i}}}\int_{x_{1_{1i}}}^{x_{2_{1i}}} -2E_{pe_{1i}}\left[\frac{a_{2_{1i}}}{4(1+\nu_{pe_{1i}})}\left(\frac{\partial v}{\partial x}+\frac{1}{R}\frac{\partial u}{\partial\theta}\right)\right.\\
&\qquad \left.-\frac{a_{3_{1i}}}{3R(1+\nu_{pe_{1i}})}\frac{\partial^2 w}{\partial x\partial\theta}\right]\overline{\frac{\partial^2\eta_3}{\partial x\partial\theta}}dxd\theta\\
&+ \sum_{i=1}^{s}\int_{\theta_{1_{2i}}}^{\theta_{2_{2i}}}\int_{x_{1_{2i}}}^{x_{2_{2i}}} -2E_{pe_{2i}}\left[-\frac{a_{2_{2i}}}{4(1+\nu_{pe_{2i}})}\left(\frac{\partial v}{\partial x}+\frac{1}{R}\frac{\partial u}{\partial\theta}\right)\right. \qquad \text{(B.14)}\\
&\qquad \left.-\frac{a_{3_{2i}}}{3R(1+\nu_{pe_{2i}})}\frac{\partial^2 w}{\partial x\partial\theta}\right]\overline{\frac{\partial^2\eta_3}{\partial x\partial\theta}}dxd\theta
\end{aligned}
$$

Appendix C

Weak Form and Matrix Components

C.1 Circumferential Displacement

The complete weak form of the second equation in (2.7), is obtained by adding damping terms to the equation below. The damping terms are created by rewriting each term in (C.1) containing the stiffness coefficients $E, E_{pe_{1i}}$ or $E_{pe_{2i}}$ and replacing them with damping coefficients $c_D, c_{D_{pe_{1i}}}$ or $c_{D_{pe_{2i}}}$, respectively.

$$
\begin{aligned}
& \int_{\Gamma_0} \rho_s h R \frac{\partial^2 v^{\mathcal{N}}}{\partial t^2} B_{v_j} d\gamma \\
+ \quad & \sum_{i=1}^{s} \int_{\Gamma_{pe_{1i}}} \rho_{pe_{1i}} h_{pe_{1i}} R \frac{\partial^2 v^{\mathcal{N}}}{\partial t^2} B_{v_j} d\gamma + \sum_{i=1}^{s} \int_{\Gamma_{pe_{2i}}} \rho_{pe_{2i}} h_{pe_{2i}} R \frac{\partial^2 v^{\mathcal{N}}}{\partial t^2} B_{v_j} d\gamma \\
+ \quad & \int_{\Gamma_0} \frac{Eh}{(1-\nu^2)} \left[\frac{1}{R} \frac{\partial v^{\mathcal{N}}}{\partial \theta} + \frac{w^{\mathcal{N}}}{R} + \nu \frac{\partial u^{\mathcal{N}}}{\partial x} \right] \frac{\partial \mathcal{B}_{v_j}}{\partial \theta} d\gamma \\
+ \quad & \sum_{i=1}^{s} \int_{\Gamma_{pe_{1i}}} \frac{E_{pe_{1i}}}{(1-\nu_{pe_{1i}}^2)} \left[h_{pe_{1i}} \left(\frac{1}{R} \frac{\partial v^{\mathcal{N}}}{\partial \theta} + \frac{w^{\mathcal{N}}}{R} + \nu_{pe_{1i}} \frac{\partial u^{\mathcal{N}}}{\partial x} \right) \right. \\
& \qquad \left. - \frac{a_{2_{1i}}}{2} \left(\frac{1}{R^2} \frac{\partial^2 w^{\mathcal{N}}}{\partial \theta^2} + \nu_{pe_{1i}} \frac{\partial^2 w^{\mathcal{N}}}{\partial x^2} \right) \right] \frac{\partial \mathcal{B}_{v_j}}{\partial \theta} d\gamma \\
+ \quad & \sum_{i=1}^{s} \int_{\Gamma_{pe_{2i}}} \frac{E_{pe_{2i}}}{(1-\nu_{pe_{2i}}^2)} \left[h_{pe_{2i}} \left(\frac{1}{R} \frac{\partial v^{\mathcal{N}}}{\partial \theta} + \frac{w^{\mathcal{N}}}{R} + \nu_{pe_{2i}} \frac{\partial u^{\mathcal{N}}}{\partial x} \right) \right. \\
& \qquad \left. + \frac{a_{2_{2i}}}{2} \left(\frac{1}{R^2} \frac{\partial^2 w^{\mathcal{N}}}{\partial \theta^2} + \nu_{pe_{2i}} \frac{\partial^2 w^{\mathcal{N}}}{\partial x^2} \right) \right] \frac{\partial \mathcal{B}_{v_j}}{\partial \theta} d\gamma \qquad \text{(C.1)} \\
+ \quad & \int_{\Gamma_0} \frac{EhR}{2(1+\nu)} \left[\frac{\partial v^{\mathcal{N}}}{\partial x} + \frac{1}{R} \frac{\partial u^{\mathcal{N}}}{\partial \theta} \right] \frac{\partial \mathcal{B}_{v_j}}{\partial x} d\gamma
\end{aligned}
$$

$$
\begin{aligned}
&+ \sum_{i=1}^{s} \int_{\Gamma_{pe_{1i}}} E_{pe_{1i}} R \left[\frac{h_{pe_{1i}}}{2(1+\nu_{pe_{1i}})} \left(\frac{\partial v^{\mathcal{N}}}{\partial x} + \frac{1}{R} \frac{\partial u^{\mathcal{N}}}{\partial \theta} \right) \right. \\
&\qquad \left. - \frac{a_{2_{1i}}}{2R(1+\nu_{pe_{1i}})} \frac{\partial^2 w^{\mathcal{N}}}{\partial x \partial \theta} \right] \frac{\partial \mathcal{B}_{v_j}}{\partial x} d\gamma \\
&+ \sum_{i=1}^{s} \int_{\Gamma_{pe_{2i}}} E_{pe_{2i}} R \left[\frac{h_{pe_{2i}}}{2(1+\nu_{pe_{2i}})} \left(\frac{\partial v^{\mathcal{N}}}{\partial x} + \frac{1}{R} \frac{\partial u^{\mathcal{N}}}{\partial \theta} \right) \right. \\
&\qquad \left. + \frac{a_{2_{2i}}}{2R(1+\nu_{pe_{2i}})} \frac{\partial^2 w^{\mathcal{N}}}{\partial x \partial \theta} \right] \frac{\partial \mathcal{B}_{v_j}}{\partial x} d\gamma \\
&= \int_{\Gamma_0} R q_\theta B_{v_j} d\gamma + \sum_{i=1}^{s} \int_{\Gamma_{pe_{1i}}} (N_\theta)_{pe_{1i}} \frac{\partial B_{v_j}}{\partial \theta} d\gamma + \sum_{i=1}^{s} \int_{\Gamma_{pe_{2i}}} (N_\theta)_{pe_{2i}} \frac{\partial B_{v_j}}{\partial \theta} d\gamma
\end{aligned}
$$

By considering the Galerkin expansions (4.2) and letting the basis functions $\mathcal{B}_{v_j}$ range from $l = 1, \ldots \mathcal{N}_v$, the following matrix components are created.

1. $$
\begin{aligned}
[V_M]_{l,k}^{\mathcal{N}_v \times \mathcal{N}_v} &= \int_0^{2\pi} \int_0^{\ell} \rho h R \mathcal{B}_{v_k}(x,\theta) \mathcal{B}_{v_l}(x,\theta) dx d\theta \\
&+ \sum_{i=1}^{s} \int_{\theta_{1_{1i}}}^{\theta_{2_{1i}}} \int_{x_{1_{1i}}}^{x_{2_{1i}}} \rho_{pe_{1i}} h_{pe_{1i}} R \mathcal{B}_{v_k}(x,\theta) \mathcal{B}_{v_l}(x,\theta) dx d\theta \\
&+ \sum_{i=1}^{s} \int_{\theta_{1_{2i}}}^{\theta_{2_{2i}}} \int_{x_{1_{2i}}}^{x_{2_{2i}}} \rho_{pe_{2i}} h_{pe_{2i}} R \mathcal{B}_{v_k}(x,\theta) \mathcal{B}_{v_l}(x,\theta) dx d\theta
\end{aligned}
$$

2. $$[V_{21}]_{l,k}^{\mathcal{N}_v \times \mathcal{N}_v} = \int_0^{2\pi} \int_0^{\ell} \frac{Eh}{R(1-\nu^2)} \frac{\partial}{\partial \theta} \mathcal{B}_{v_k}(x,\theta) \frac{\partial}{\partial \theta} \mathcal{B}_{v_l}(x,\theta) dx d\theta$$

3. $$[W_{21}]_{l,k}^{\mathcal{N}_v \times \mathcal{N}_w} = \int_0^{2\pi} \int_0^{\ell} \frac{Eh}{R(1-\nu^2)} \mathcal{B}_{w_k}(x,\theta) \frac{\partial}{\partial \theta} \mathcal{B}_{v_l}(x,\theta) dx d\theta$$

4. $$[U_{21}]_{l,k}^{\mathcal{N}_v \times \mathcal{N}_u} = \int_0^{2\pi} \int_0^{\ell} \frac{Eh\nu}{1-\nu^2} \frac{\partial}{\partial x} \mathcal{B}_{u_k}(x,\theta) \frac{\partial}{\partial \theta} \mathcal{B}_{v_l}(x,\theta) dx d\theta$$

5. $$[V_{22}]_{l,k}^{\mathcal{N}_v \times \mathcal{N}_v} = \int_0^{2\pi} \int_0^{\ell} \frac{EhR}{2(1+\nu)} \frac{\partial}{\partial x} \mathcal{B}_{v_k}(x,\theta) \frac{\partial}{\partial x} \mathcal{B}_{v_l}(x,\theta) dx d\theta$$

6. $$[U_{22}]_{l,k}^{\mathcal{N}_v \times \mathcal{N}_u} = \int_0^{2\pi} \int_0^{\ell} \frac{Eh}{2(1+\nu)} \frac{\partial}{\partial \theta} \mathcal{B}_{u_k}(x,\theta) \frac{\partial}{\partial x} \mathcal{B}_{v_l}(x,\theta) dx d\theta$$

7. $$[V_{23}]_{l,k}^{\mathcal{N}_v \times \mathcal{N}_v} = \sum_{i=1}^{s} \int_{\theta_{1_{1i}}}^{\theta_{2_{1i}}} \int_{x_{1_{1i}}}^{x_{2_{1i}}} \frac{E_{pe_{1i}} h_{pe_{1i}}}{R(1-\nu_{pe_{1i}}^2)} \frac{\partial}{\partial \theta} \mathcal{B}_{v_k}(x,\theta) \frac{\partial}{\partial \theta} \mathcal{B}_{v_l}(x,\theta) dx d\theta$$

8. $$[W_{22}]_{l,k}^{\mathcal{N}_v \times \mathcal{N}_w} = \sum_{i=1}^{s} \int_{\theta_{1_{1i}}}^{\theta_{2_{1i}}} \int_{x_{1_{1i}}}^{x_{2_{1i}}} \frac{E_{pe_{1i}} h_{pe_{1i}}}{R(1-\nu_{pe_{1i}}^2)} \mathcal{B}_{w_k}(x,\theta) \frac{\partial}{\partial \theta} \mathcal{B}_{v_l}(x,\theta) dx d\theta$$

9. $$[U_{23}]_{l,k}^{\mathcal{N}_v \times \mathcal{N}_u} = \sum_{i=1}^{s} \int_{\theta_{1_{1i}}}^{\theta_{2_{1i}}} \int_{x_{1_{1i}}}^{x_{2_{1i}}} \frac{E_{pe_{1i}} h_{pe_{1i}} \nu_{pe_{1i}}}{1-\nu_{pe_{1i}}^2} \frac{\partial}{\partial x} \mathcal{B}_{u_k}(x,\theta) \frac{\partial}{\partial \theta} \mathcal{B}_{v_l}(x,\theta) dx d\theta$$

10. $$[W_{23}]_{l,k}^{\mathcal{N}_v\times\mathcal{N}_w} = \sum_{i=1}^{s}\int_{\theta_{1_{1i}}}^{\theta_{2_{1i}}}\int_{x_{1_{1i}}}^{x_{2_{1i}}} -\frac{E_{pe_{1i}}a_{2_{1i}}}{2R^2(1-\nu_{pe_{1i}}^2)}\frac{\partial^2}{\partial\theta^2}\mathcal{B}_{w_k}(x,\theta)\frac{\partial}{\partial\theta}\mathcal{B}_{v_l}(x,\theta)dxd\theta$$

11. $$[W_{24}]_{l,k}^{\mathcal{N}_v\times\mathcal{N}_w} = \sum_{i=1}^{s}\int_{\theta_{1_{1i}}}^{\theta_{2_{1i}}}\int_{x_{1_{1i}}}^{x_{2_{1i}}} -\frac{E_{pe_{1i}}\nu_{pe_{1i}}a_{2_{1i}}}{2(1-\nu_{pe_{1i}}^2)}\frac{\partial^2}{\partial x^2}\mathcal{B}_{w_k}(x,\theta)\frac{\partial}{\partial\theta}\mathcal{B}_{v_l}(x,\theta)dxd\theta$$

12. $$[V_{24}]_{l,k}^{\mathcal{N}_v\times\mathcal{N}_v} = \sum_{i=1}^{s}\int_{\theta_{1_{2i}}}^{\theta_{2_{2i}}}\int_{x_{1_{2i}}}^{x_{2_{2i}}} \frac{E_{pe_{2i}}h_{pe_{2i}}}{R(1-\nu_{pe_{2i}}^2)}\frac{\partial}{\partial\theta}\mathcal{B}_{v_k}(x,\theta)\frac{\partial}{\partial\theta}\mathcal{B}_{v_l}(x,\theta)dxd\theta$$

13. $$[W_{25}]_{l,k}^{\mathcal{N}_v\times\mathcal{N}_w} = \sum_{i=1}^{s}\int_{\theta_{1_{2i}}}^{\theta_{2_{2i}}}\int_{x_{1_{2i}}}^{x_{2_{2i}}} \frac{E_{pe_{2i}}h_{pe_{2i}}}{R(1-\nu_{pe_{2i}}^2)}\mathcal{B}_{w_k}(x,\theta)\frac{\partial}{\partial\theta}\mathcal{B}_{v_l}(x,\theta)dxd\theta$$

14. $$[U_{24}]_{l,k}^{\mathcal{N}_v\times\mathcal{N}_u} = \sum_{i=1}^{s}\int_{\theta_{1_{2i}}}^{\theta_{2_{2i}}}\int_{x_{1_{2i}}}^{x_{2_{2i}}} \frac{E_{pe_{2i}}h_{pe_{2i}}\nu_{pe_{2i}}}{1-\nu_{pe_{2i}}^2}\frac{\partial}{\partial x}\mathcal{B}_{u_k}(x,\theta)\frac{\partial}{\partial\theta}\mathcal{B}_{v_l}(x,\theta)dxd\theta$$

15. $$[W_{26}]_{l,k}^{\mathcal{N}_v\times\mathcal{N}_w} = \sum_{i=1}^{s}\int_{\theta_{1_{2i}}}^{\theta_{2_{2i}}}\int_{x_{1_{2i}}}^{x_{2_{2i}}} \frac{E_{pe_{2i}}a_{2_{2i}}}{2R^2(1-\nu_{pe_{2i}}^2)}\frac{\partial^2}{\partial\theta^2}\mathcal{B}_{w_k}(x,\theta)\frac{\partial}{\partial\theta}\mathcal{B}_{v_l}(x,\theta)dxd\theta$$

16. $$[W_{27}]_{l,k}^{\mathcal{N}_v\times\mathcal{N}_w} = \sum_{i=1}^{s}\int_{\theta_{1_{2i}}}^{\theta_{2_{2i}}}\int_{x_{1_{2i}}}^{x_{2_{2i}}} \frac{E_{pe_{2i}}\nu_{pe_{2i}}a_{2_{2i}}}{2(1-\nu_{pe_{2i}}^2)}\frac{\partial^2}{\partial x^2}\mathcal{B}_{w_k}(x,\theta)\frac{\partial}{\partial\theta}\mathcal{B}_{v_l}(x,\theta)dxd\theta$$

17. $$[V_{25}]_{l,k}^{\mathcal{N}_v\times\mathcal{N}_v} = \sum_{i=1}^{s}\int_{\theta_{1_{1i}}}^{\theta_{2_{1i}}}\int_{x_{1_{1i}}}^{x_{2_{1i}}} \frac{E_{pe_{1i}}h_{pe_{1i}}R}{2(1+\nu_{pe_{1i}})}\frac{\partial}{\partial x}\mathcal{B}_{v_k}(x,\theta)\frac{\partial}{\partial x}\mathcal{B}_{v_l}(x,\theta)dxd\theta$$

18. $$[U_{25}]_{l,k}^{\mathcal{N}_v\times\mathcal{N}_u} = \sum_{i=1}^{s}\int_{\theta_{1_{1i}}}^{\theta_{2_{1i}}}\int_{x_{1_{1i}}}^{x_{2_{1i}}} \frac{E_{pe_{1i}}h_{pe_{1i}}}{2(1+\nu_{pe_{1i}})}\frac{\partial}{\partial\theta}\mathcal{B}_{u_k}(x,\theta)\frac{\partial}{\partial x}\mathcal{B}_{v_l}(x,\theta)dxd\theta$$

19. $$[W_{28}]_{l,k}^{\mathcal{N}_v\times\mathcal{N}_w} = -\frac{E_{pe_{1i}}a_{2_{1i}}}{2(1+\nu_{pe_{1i}})}\frac{\partial^2}{\partial x\partial\theta}\mathcal{B}_{w_k}(x,\theta)\frac{\partial}{\partial x}\mathcal{B}_{v_l}(x,\theta)dxd\theta$$

20. $$[V_{26}]_{l,k}^{\mathcal{N}_v\times\mathcal{N}_v} = \sum_{i=1}^{s}\int_{\theta_{1_{2i}}}^{\theta_{2_{2i}}}\int_{x_{1_{2i}}}^{x_{2_{2i}}} \frac{E_{pe_{2i}}h_{pe_{2i}}R}{2(1+\nu_{pe_{2i}})}\frac{\partial}{\partial x}\mathcal{B}_{v_k}(x,\theta)\frac{\partial}{\partial x}\mathcal{B}_{v_l}(x,\theta)dxd\theta$$

21. $$[U_{26}]_{l,k}^{\mathcal{N}_v\times\mathcal{N}_u} = \sum_{i=1}^{s}\int_{\theta_{1_{2i}}}^{\theta_{2_{2i}}}\int_{x_{1_{2i}}}^{x_{2_{2i}}} \frac{E_{pe_{2i}}h_{pe_{2i}}}{2(1+\nu_{pe_{2i}})}\frac{\partial}{\partial\theta}\mathcal{B}_{u_k}(x,\theta)\frac{\partial}{\partial x}\mathcal{B}_{v_l}(x,\theta)dxd\theta$$

22. $$[W_{29}]_{l,k}^{\mathcal{N}_v\times\mathcal{N}_w} = \sum_{i=1}^{s}\int_{\theta_{1_{2i}}}^{\theta_{2_{2i}}}\int_{x_{1_{2i}}}^{x_{2_{2i}}} \frac{E_{pe_{2i}}a_{2_{2i}}}{2(1+\nu_{pe_{2i}})}\frac{\partial^2}{\partial x\partial\theta}\mathcal{B}_{w_k}(x,\theta)\frac{\partial}{\partial x}\mathcal{B}_{v_l}(x,\theta)dxd\theta$$

23. $$[F_v(t)]_l = \int_0^{2\pi}\int_0^{\ell} R\hat{q}_\theta(t,\theta,x)\mathcal{B}_{v_l}(\theta,x)dxd\theta$$

24. $$[B_v]_l^{\mathcal{N}_u\times 1} = \sum_{i=1}^{s}\int_{\theta_{1_{1i}}}^{\theta_{2_{1i}}}\int_{x_{1_{1i}}}^{x_{2_{1i}}} R(N_\theta)_{pe_{1i}}\frac{\partial\mathcal{B}_{ul}}{\partial\theta}dxd\theta$$
$$+\sum_{i=1}^{s}\int_{\theta_{1_{2i}}}^{\theta_{2_{2i}}}\int_{x_{1_{2i}}}^{x_{2_{2i}}} R(N_\theta)_{pe_{2i}}\frac{\partial\mathcal{B}_{ul}}{\partial\theta}dxd\theta$$

C.2 Transverse Displacement

Similar to the longitudinal (4.3) and circumferential (C.1) equations, the full form of the weak equations describing the transverse displacements are obtained by adding damping terms to the following equation.

$$
\begin{aligned}
& \int_{\Gamma_0} R\rho_s h \frac{\partial^2 w^{\mathcal{N}}}{\partial t^2} B_{w_j} d\gamma \\
+ & \sum_{i=1}^{s} \int_{\Gamma_{pe_{1i}}} \rho_{pe_{1i}} h_{pe_{1i}} \frac{\partial^2 w^{\mathcal{N}}}{\partial t^2} B_{w_j} d\gamma + \sum_{i=1}^{s} \int_{\Gamma_{pe_{2i}}} \rho_{pe_{2i}} h_{pe_{2i}} \frac{\partial^2 w^{\mathcal{N}}}{\partial t^2} B_{w_j} d\gamma \\
+ & \int_{\Gamma_0} \frac{Eh}{(1-\nu^2)} \left[\frac{1}{R} \frac{\partial v^{\mathcal{N}}}{\partial \theta} + \frac{w^{\mathcal{N}}}{R} + \nu \frac{\partial u^{\mathcal{N}}}{\partial x} \right] B_{w_j} d\gamma \\
+ & \sum_{i=1}^{s} \int_{\Gamma_{pe_{1i}}} \frac{E_{pe_{1i}}}{(1-\nu_{pe_{1i}}^2)} \left[h_{pe_{1i}} \left(\frac{1}{R} \frac{\partial v^{\mathcal{N}}}{\partial \theta} + \frac{w^{\mathcal{N}}}{R} + \nu_{pe_{1i}} \frac{\partial u^{\mathcal{N}}}{\partial x} \right) \right. \\
& \qquad \left. - \frac{a_{2_{1i}}}{2} \left(\frac{1}{R^2} \frac{\partial^2 w^{\mathcal{N}}}{\partial \theta^2} + \nu_{pe_{1i}} \frac{\partial^2 w^{\mathcal{N}}}{\partial x^2} \right) \right] B_{w_j} d\gamma \\
+ & \sum_{i=1}^{s} \int_{\Gamma_{pe_{2i}}} \frac{E_{pe_{2i}}}{(1-\nu_{pe_{2i}}^2)} \left[h_{pe_{2i}} \left(\frac{1}{R} \frac{\partial v^{\mathcal{N}}}{\partial \theta} + \frac{w^{\mathcal{N}}}{R} + \nu_{pe_{2i}} \frac{\partial u^{\mathcal{N}}}{\partial x} \right) \right. \\
& \qquad \left. + \frac{a_{2_{2i}}}{2} \left(\frac{1}{R^2} \frac{\partial^2 w^{\mathcal{N}}}{\partial \theta^2} + \nu_{pe_{2i}} \frac{\partial^2 w^{\mathcal{N}}}{\partial x^2} \right) \right] B_{w_j} d\gamma \\
+ & \int_{\Gamma_0} \frac{Eh^3 R}{12(1-\nu^2)} \left[\frac{\partial^2 w}{\partial x^2} + \frac{\nu}{R^2} \frac{\partial^2 w}{\partial \theta^2} \right] \frac{\partial^2 B_{w_j}}{\partial x^2} d\gamma \\
- & \sum_{i=1}^{s} \int_{\Gamma_{pe_{1i}}} \frac{E_{pe_{1i}} R}{(1-\nu_{pe_{1i}}^2)} \left[\frac{a_{2_{1i}}}{2} \left(\frac{\partial u^{\mathcal{N}}}{\partial x} + \nu_{pe_{1i}} \left(\frac{1}{R} \frac{\partial v^{\mathcal{N}}}{\partial \theta} + \frac{w^{\mathcal{N}}}{R} \right) \right) \right. \\
& \qquad \left. - \frac{a_{3_{1i}}}{3} \left(\frac{\partial^2 w^{\mathcal{N}}}{\partial x^2} + \frac{\nu_{pe_{1i}}}{R^2} \frac{\partial^2 w}{\partial \theta^2} \right) \right] \frac{\partial^2 B_{w_j}}{\partial x^2} d\gamma \\
- & \sum_{i=1}^{s} \int_{\Gamma_{pe_{2i}}} \frac{E_{pe_{2i}} R}{(1-\nu_{pe_{2i}}^2)} \left[-\frac{a_{2_{2i}}}{2} \left(\frac{\partial u^{\mathcal{N}}}{\partial x} + \nu_{pe_{2i}} \left(\frac{1}{R} \frac{\partial v^{\mathcal{N}}}{\partial \theta} + \frac{w^{\mathcal{N}}}{R} \right) \right) \right. \\
& \qquad \left. - \frac{a_{3_{2i}}}{3} \left(\frac{\partial^2 w^{\mathcal{N}}}{\partial x^2} + \frac{\nu_{pe_{2i}}}{R^2} \frac{\partial^2 w}{\partial \theta^2} \right) \right] \frac{\partial^2 B_{w_j}}{\partial x^2} d\gamma \qquad \text{(C.2)} \\
+ & \int_{\Gamma_0} \frac{Eh^3}{12R(1-\nu^2)} \left[\frac{1}{R^2} \frac{\partial^2 w}{\partial \theta^2} + \nu \frac{\partial^2 w}{\partial x^2} \right] \frac{\partial^2 B_{w_j}}{\partial \theta^2} d\gamma \\
- & \sum_{i=1}^{s} \int_{\Gamma_{pe_{1i}}} \frac{E_{pe_{1i}}}{R(1-\nu_{pe_{1i}}^2)} \left[\frac{a_{2_{1i}}}{2} \left(\left(\frac{1}{R} \frac{\partial v^{\mathcal{N}}}{\partial \theta} + \frac{w^{\mathcal{N}}}{R} \right) + \nu_{pe_{1i}} \frac{\partial u^{\mathcal{N}}}{\partial x} \right) \right.
\end{aligned}
$$

$$
\begin{aligned}
& -\frac{a_{3_{1i}}}{3}\left(\frac{1}{R^2}\frac{\partial^2 w}{\partial\theta^2}+\nu_{pe_{1i}}\frac{\partial^2 w}{\partial x^2}\right)\Bigg]\frac{\partial^2 B_{w_j}}{\partial\theta^2}d\gamma \\
- & \sum_{i=1}^{s}\int_{\Gamma_{pe_{2i}}}\frac{E_{pe_{2i}}}{R(1-\nu_{pe_{2i}}^2)}\left[-\frac{a_{2_{2i}}}{2}\left(\left(\frac{1}{R}\frac{\partial v^{\mathcal{N}}}{\partial\theta}+\frac{w^{\mathcal{N}}}{R}\right)+\nu_{pe_{2i}}\frac{\partial u^{\mathcal{N}}}{\partial x}\right)\right. \\
& \left. -\frac{a_{3_{2i}}}{3}\left(\frac{1}{R^2}\frac{\partial^2 w}{\partial\theta^2}+\nu_{pe_{2i}}\frac{\partial^2 w}{\partial x^2}\right)\right]\frac{\partial^2 B_{w_j}}{\partial\theta^2}d\gamma \\
+ & \int_{\Gamma_0}\frac{Eh^3}{6R(1+\nu)}\frac{\partial^2 w}{\partial x\partial\theta}\frac{\partial^2 B_{w_j}}{\partial x\partial\theta}d\gamma \\
- & \sum_{i=1}^{s}\int_{\Gamma_{pe_{1i}}}2E_{pe_{1i}}\left[\frac{a_{2_{1i}}}{4(1+\nu_{pe_{1i}})}\left(\frac{\partial v^{\mathcal{N}}}{\partial x}+\frac{1}{R}\frac{\partial u^{\mathcal{N}}}{\partial\theta}\right)\right. \\
& \left. -\frac{a_{3_{1i}}}{3R(1+\nu_{pe_{1i}})}\frac{\partial^2 w}{\partial x\partial\theta}\right]\frac{\partial^2 B_{w_j}}{\partial x\partial\theta}d\gamma \\
- & \sum_{i=1}^{s}\int_{\Gamma_{pe_{2i}}}2E_{pe_{2i}}\left[\frac{-a_{2_{2i}}}{4(1+\nu_{pe_{2i}})}\left(\frac{\partial v^{\mathcal{N}}}{\partial x}+\frac{1}{R}\frac{\partial u^{\mathcal{N}}}{\partial\theta}\right)\right. \\
& \left. -\frac{a_{3_{2i}}}{3R(1+\nu_{pe_{2i}})}\frac{\partial^2 w}{\partial x\partial\theta}\right]\frac{\partial^2 B_{w_j}}{\partial x\partial\theta}d\gamma \\
= & \int_{\Gamma_0}q_n B_{w_j}Rd\gamma+\sum_{i=1}^{s}\int_{\Gamma_{pe_{1i}}}\left\{R(M_x)_{pe_{1i}}\frac{\partial^2 B_{w_j}}{\partial x^2}+\frac{1}{R}(M_\theta)_{pe_{1i}}\frac{\partial^2 B_{w_j}}{\partial\theta^2}\right\}d\gamma \\
+ & \sum_{i=1}^{s}\int_{\Gamma_{pe_{2i}}}\left\{R(M_x)_{pe_{2i}}\frac{\partial^2 B_{w_j}}{\partial x^2}+\frac{1}{R}(M_\theta)_{pe_{2i}}\frac{\partial^2 B_{w_j}}{\partial\theta^2}\right\}d\gamma
\end{aligned}
$$

The matrix compoments are as follows.

1. $[W_M]_{l,k}^{\mathcal{N}_w\times\mathcal{N}_w}=\int_0^{2\pi}\int_0^{\ell}\rho hR\mathcal{B}_{w_k}(x,\theta)\mathcal{B}_{w_l}(x,\theta)dxd\theta$
$$
\begin{aligned}
& + \sum_{i=1}^{s}\int_{\theta_{1_{1i}}}^{\theta_{2_{1i}}}\int_{x_{1_{1i}}}^{x_{2_{1i}}}\rho_{pe_{1i}}h_{pe_{1i}}R\mathcal{B}_{w_k}(x,\theta)\mathcal{B}_{w_l}(x,\theta)dxd\theta \\
& + \sum_{i=1}^{s}\int_{\theta_{1_{2i}}}^{\theta_{2_{2i}}}\int_{x_{1_{2i}}}^{x_{2_{2i}}}\rho_{pe_{2i}}h_{pe_{2i}}R\mathcal{B}_{w_k}(x,\theta)\mathcal{B}_{w_l}(x,\theta)dxd\theta
\end{aligned}
$$
2. $[V_{31}]_{l,k}^{\mathcal{N}_w\times\mathcal{N}_v}=\int_0^{2\pi}\int_0^{\ell}\frac{Eh}{R(1-\nu^2)}\frac{\partial}{\partial\theta}\mathcal{B}_{v_k}(x,\theta)\mathcal{B}_{w_l}(x,\theta)dxd\theta$
3. $[W_{31}]_{l,k}^{\mathcal{N}_w\times\mathcal{N}_w}=\int_0^{2\pi}\int_0^{\ell}\frac{Eh}{R(1-\nu^2)}\mathcal{B}_{w_k}(x,\theta)\mathcal{B}_{w_l}(x,\theta)dxd\theta$
4. $[U_{31}]_{l,k}^{\mathcal{N}_w\times\mathcal{N}_u}=\int_0^{2\pi}\int_0^{\ell}\frac{Eh\nu}{1-\nu^2}\frac{\partial}{\partial x}\mathcal{B}_{u_k}(x,\theta)\mathcal{B}_{w_l}(x,\theta)dxd\theta$

5. $[W_{32}]_{l,k}^{\mathcal{N}_w\times\mathcal{N}_w} = \int_0^{2\pi}\int_0^{\ell} \frac{Eh^3R}{12(1-\nu^2)}\frac{\partial^2}{\partial x^2}\mathcal{B}_{w_k}(x,\theta)\frac{\partial^2}{\partial x^2}\mathcal{B}_{w_l}(x,\theta)dxd\theta$

6. $[W_{33}]_{l,k}^{\mathcal{N}_w\times\mathcal{N}_w} = \int_0^{2\pi}\int_0^{\ell} \frac{Eh^3\nu}{12R(1-\nu^2)}\frac{\partial^2}{\partial \theta^2}\mathcal{B}_{w_k}(x,\theta)\frac{\partial^2}{\partial x^2}\mathcal{B}_{w_l}(x,\theta)dxd\theta$

7. $[W_{34}]_{l,k}^{\mathcal{N}_w\times\mathcal{N}_w} = \int_0^{2\pi}\int_0^{\ell} \frac{Eh^3}{12R^3(1-\nu^2)}\frac{\partial^2}{\partial \theta^2}\mathcal{B}_{w_k}(x,\theta)\frac{\partial^2}{\partial \theta^2}\mathcal{B}_{w_l}(x,\theta)dxd\theta$

8. $[W_{35}]_{l,k}^{\mathcal{N}_w\times\mathcal{N}_w} = \int_0^{2\pi}\int_0^{\ell} \frac{Eh^3\nu}{12R(1-\nu^2)}\frac{\partial^2}{\partial x^2}\mathcal{B}_{w_k}(x,\theta)\frac{\partial^2}{\partial \theta^2}\mathcal{B}_{w_l}(x,\theta)dxd\theta$

9. $[W_{36}]_{l,k}^{\mathcal{N}_w\times\mathcal{N}_w} = \int_0^{2\pi}\int_0^{\ell} \frac{Eh^3}{6R(1+\nu)}\frac{\partial^2}{\partial x\partial \theta}\mathcal{B}_{w_k}(x,\theta)\frac{\partial^2}{\partial x\partial \theta}\mathcal{B}_{w_l}(x,\theta)dxd\theta$

10. $[V_{32}]_{l,k}^{\mathcal{N}_w\times\mathcal{N}_v} = \sum_{i=1}^{s}\int_{\theta_{1_{1i}}}^{\theta_{2_{1i}}}\int_{x_{1_{1i}}}^{x_{2_{1i}}} \frac{E_{pe_{1i}}h_{pe_{1i}}}{R(1-\nu_{pe_{1i}}^2)}\frac{\partial}{\partial \theta}\mathcal{B}_{v_k}(x,\theta)\mathcal{B}_{w_l}(x,\theta)dxd\theta$

11. $[W_{37}]_{l,k}^{\mathcal{N}_w\times\mathcal{N}_w} = \sum_{i=1}^{s}\int_{\theta_{1_{1i}}}^{\theta_{2_{1i}}}\int_{x_{1_{1i}}}^{x_{2_{1i}}} \frac{E_{pe_{1i}}h_{pe_{1i}}}{R(1-\nu_{pe_{1i}}^2)}\mathcal{B}_{w_k}(x,\theta)\mathcal{B}_{w_l}(x,\theta)dxd\theta$

12. $[U_{32}]_{l,k}^{\mathcal{N}_w\times\mathcal{N}_u} = \sum_{i=1}^{s}\int_{\theta_{1_{1i}}}^{\theta_{2_{1i}}}\int_{x_{1_{1i}}}^{x_{2_{1i}}} \frac{E_{pe_{1i}}h_{pe_{1i}}\nu_{pe_{1i}}}{(1-\nu_{pe_{1i}}^2)}\frac{\partial}{\partial x}\mathcal{B}_{u_k}(x,\theta)\mathcal{B}_{w_l}(x,\theta)dxd\theta$

13. $[W_{38}]_{l,k}^{\mathcal{N}_w\times\mathcal{N}_w} = \sum_{i=1}^{s}\int_{\theta_{1_{1i}}}^{\theta_{2_{1i}}}\int_{x_{1_{1i}}}^{x_{2_{1i}}} -\frac{E_{pe_{1i}}a_{2_{1i}}}{2R^2(1-\nu_{pe_{1i}}^2)}\frac{\partial^2}{\partial \theta^2}\mathcal{B}_{w_k}(x,\theta)\mathcal{B}_{w_l}(x,\theta)dxd\theta$

14. $[W_{39}]_{l,k}^{\mathcal{N}_w\times\mathcal{N}_w} = \sum_{i=1}^{s}\int_{\theta_{1_{1i}}}^{\theta_{2_{1i}}}\int_{x_{1_{1i}}}^{x_{2_{1i}}} -\frac{E_{pe_{1i}}\nu_{pe_{1i}}a_{2_{1i}}}{2(1-\nu_{pe_{1i}}^2)}\frac{\partial^2}{\partial x^2}\mathcal{B}_{w_k}(x,\theta)\mathcal{B}_{w_l}(x,\theta)dxd\theta$

15. $[V_{33}]_{l,k}^{\mathcal{N}_w\times\mathcal{N}_v} = \sum_{i=1}^{s}\int_{\theta_{1_{2i}}}^{\theta_{2_{2i}}}\int_{x_{1_{2i}}}^{x_{2_{2i}}} \frac{E_{pe_{2i}}h_{pe_{2i}}}{R(1-\nu_{pe_{2i}}^2)}\frac{\partial}{\partial \theta}\mathcal{B}_{v_k}(x,\theta)\mathcal{B}_{w_l}(x,\theta)dxd\theta$

16. $[W_{310}]_{l,k}^{\mathcal{N}_w\times\mathcal{N}_w} = \sum_{i=1}^{s}\int_{\theta_{1_{2i}}}^{\theta_{2_{2i}}}\int_{x_{1_{2i}}}^{x_{2_{2i}}} \frac{E_{pe_{2i}}h_{pe_{2i}}}{R(1-\nu_{pe_{2i}}^2)}\mathcal{B}_{w_k}(x,\theta)\mathcal{B}_{w_l}(x,\theta)dxd\theta$

17. $[U_{33}]_{l,k}^{\mathcal{N}_w\times\mathcal{N}_u} = \sum_{i=1}^{s}\int_{\theta_{1_{2i}}}^{\theta_{2_{2i}}}\int_{x_{1_{2i}}}^{x_{2_{2i}}} \frac{E_{pe_{2i}}h_{pe_{2i}}\nu_{pe_{2i}}}{(1-\nu_{pe_{2i}}^2)}\frac{\partial}{\partial x}\mathcal{B}_{u_k}(x,\theta)\mathcal{B}_{w_l}(x,\theta)dxd\theta$

18. $[W_{311}]_{l,k}^{\mathcal{N}_w\times\mathcal{N}_w} = \sum_{i=1}^{s}\int_{\theta_{1_{2i}}}^{\theta_{2_{2i}}}\int_{x_{1_{2i}}}^{x_{2_{2i}}} \frac{E_{pe_{2i}}a_{2_{2i}}}{2R^2(1-\nu_{pe_{2i}}^2)}\frac{\partial^2}{\partial \theta^2}\mathcal{B}_{w_k}(x,\theta)\mathcal{B}_{w_l}(x,\theta)dxd\theta$

19. $[W_{312}]_{l,k}^{\mathcal{N}_w\times\mathcal{N}_w} = \sum_{i=1}^{s}\int_{\theta_{1_{2i}}}^{\theta_{2_{2i}}}\int_{x_{1_{2i}}}^{x_{2_{2i}}} \frac{E_{pe_{2i}}\nu_{pe_{2i}}a_{2_{2i}}}{2(1-\nu_{pe_{2i}}^2)}\frac{\partial^2}{\partial x^2}\mathcal{B}_{w_k}(x,\theta)\mathcal{B}_{w_l}(x,\theta)dxd\theta$

20. $[U_{34}]_{l,k}^{\mathcal{N}_w\times\mathcal{N}_u} = \sum_{i=1}^{s}\int_{\theta_{1_{1i}}}^{\theta_{2_{1i}}}\int_{x_{1_{1i}}}^{x_{2_{1i}}} -\frac{E_{pe_{1i}}Ra_{2_{1i}}}{2(1-\nu_{pe_{1i}}^2)}\frac{\partial}{\partial x}\mathcal{B}_{u_k}(x,\theta)\frac{\partial^2}{\partial x^2}\mathcal{B}_{w_l}(x,\theta)dxd\theta$

21. $[V_{34}]_{l,k}^{\mathcal{N}_w\times\mathcal{N}_v} = \sum_{i=1}^{s}\int_{\theta_{1_{1i}}}^{\theta_{2_{1i}}}\int_{x_{1_{1i}}}^{x_{2_{1i}}} -\frac{E_{pe_{1i}}\nu_{pe_{1i}}a_{2_{1i}}}{2(1-\nu_{pe_{1i}}^2)}\frac{\partial}{\partial \theta}\mathcal{B}_{v_k}(x,\theta)\frac{\partial^2}{\partial x^2}\mathcal{B}_{w_l}(x,\theta)dxd\theta$

22. $$[W_{313}]_{l,k}^{\mathcal{N}_w\times\mathcal{N}_w} = \sum_{i=1}^{s}\int_{\theta_{1_{1i}}}^{\theta_{2_{1i}}}\int_{x_{1_{1i}}}^{x_{2_{1i}}} -\frac{E_{pe_{1i}}\nu_{pe_{1i}}a_{2_{1i}}}{2(1-\nu_{pe_{1i}}^2)}\mathcal{B}_{w_k}(x,\theta)\frac{\partial^2}{\partial x^2}\mathcal{B}_{w_l}(x,\theta)dxd\theta$$

23. $$[W_{314}]_{l,k}^{\mathcal{N}_w\times\mathcal{N}_w} = \sum_{i=1}^{s}\int_{\theta_{1_{1i}}}^{\theta_{2_{1i}}}\int_{x_{1_{1i}}}^{x_{2_{1i}}} \frac{E_{pe_{1i}}Ra_{3_{1i}}}{3(1-\nu_{pe_{1i}}^2)}\frac{\partial^2}{\partial x^2}\mathcal{B}_{w_k}(x,\theta)\frac{\partial^2}{\partial x^2}\mathcal{B}_{w_l}(x,\theta)dxd\theta$$

24. $$[W_{315}]_{l,k}^{\mathcal{N}_w\times\mathcal{N}_w} = \sum_{i=1}^{s}\int_{\theta_{1_{1i}}}^{\theta_{2_{1i}}}\int_{x_{1_{1i}}}^{x_{2_{1i}}} \frac{E_{pe_{1i}}\nu_{pe_{1i}}a_{3_{1i}}}{3R(1-\nu_{pe_{1i}}^2)}\frac{\partial^2}{\partial\theta^2}\mathcal{B}_{w_k}(x,\theta)\frac{\partial^2}{\partial x^2}\mathcal{B}_{w_l}(x,\theta)dxd\theta$$

25. $$[U_{35}]_{l,k}^{\mathcal{N}_w\times\mathcal{N}_u} = \sum_{i=1}^{s}\int_{\theta_{1_{2i}}}^{\theta_{2_{2i}}}\int_{x_{1_{2i}}}^{x_{2_{2i}}} \frac{E_{pe_{2i}}Ra_{2_{2i}}}{2(1-\nu_{pe_{2i}}^2)}\frac{\partial}{\partial x}\mathcal{B}_{u_k}(x,\theta)\frac{\partial^2}{\partial x^2}\mathcal{B}_{w_l}(x,\theta)dxd\theta$$

26. $$[V_{35}]_{l,k}^{\mathcal{N}_w\times\mathcal{N}_v} = \sum_{i=1}^{s}\int_{\theta_{1_{2i}}}^{\theta_{2_{2i}}}\int_{x_{1_{2i}}}^{x_{2_{2i}}} \frac{E_{pe_{2i}}\nu_{pe_{2i}}a_{2_{2i}}}{2(1-\nu_{pe_{2i}}^2)}\frac{\partial}{\partial\theta}\mathcal{B}_{v_k}(x,\theta)\frac{\partial^2}{\partial x^2}\mathcal{B}_{w_l}(x,\theta)dxd\theta$$

27. $$[W_{316}]_{l,k}^{\mathcal{N}_w\times\mathcal{N}_w} = \sum_{i=1}^{s}\int_{\theta_{1_{2i}}}^{\theta_{2_{2i}}}\int_{x_{1_{2i}}}^{x_{2_{2i}}} \frac{E_{pe_{2i}}\nu_{pe_{2i}}a_{2_{2i}}}{2(1-\nu_{pe_{2i}}^2)}\mathcal{B}_{w_k}(x,\theta)\frac{\partial^2}{\partial x^2}\mathcal{B}_{w_l}(x,\theta)dxd\theta$$

28. $$[W_{317}]_{l,k}^{\mathcal{N}_w\times\mathcal{N}_w} = \sum_{i=1}^{s}\int_{\theta_{1_{2i}}}^{\theta_{2_{2i}}}\int_{x_{1_{2i}}}^{x_{2_{2i}}} \frac{E_{pe_{2i}}Ra_{3_{2i}}}{3(1-\nu_{pe_{2i}}^2)}\frac{\partial^2}{\partial x^2}\mathcal{B}_{w_k}(x,\theta)\frac{\partial^2}{\partial x^2}\mathcal{B}_{w_l}(x,\theta)dxd\theta$$

29. $$[W_{318}]_{l,k}^{\mathcal{N}_w\times\mathcal{N}_w} = \sum_{i=1}^{s}\int_{\theta_{1_{2i}}}^{\theta_{2_{2i}}}\int_{x_{1_{2i}}}^{x_{2_{2i}}} \frac{E_{pe_{2i}}\nu_{pe_{2i}}a_{3_{2i}}}{3R(1-\nu_{pe_{2i}}^2)}\frac{\partial^2}{\partial\theta^2}\mathcal{B}_{w_k}(x,\theta)\frac{\partial^2}{\partial x^2}\mathcal{B}_{w_l}(x,\theta)dxd\theta$$

30. $$[V_{36}]_{l,k}^{\mathcal{N}_w\times\mathcal{N}_v} = \sum_{i=1}^{s}\int_{\theta_{1_{1i}}}^{\theta_{2_{1i}}}\int_{x_{1_{1i}}}^{x_{2_{1i}}} -\frac{E_{pe_{1i}}a_{2_{1i}}}{2R^2(1-\nu_{pe_{1i}}^2)}\frac{\partial}{\partial\theta}\mathcal{B}_{v_k}(x,\theta)\frac{\partial^2}{\partial\theta^2}\mathcal{B}_{w_l}(x,\theta)dxd\theta$$

31. $$[W_{319}]_{l,k}^{\mathcal{N}_w\times\mathcal{N}_w} = \sum_{i=1}^{s}\int_{\theta_{1_{1i}}}^{\theta_{2_{1i}}}\int_{x_{1_{1i}}}^{x_{2_{1i}}} -\frac{E_{pe_{1i}}a_{2_{1i}}}{2R^2(1-\nu_{pe_{1i}}^2)}\mathcal{B}_{w_k}(x,\theta)\frac{\partial^2}{\partial\theta^2}\mathcal{B}_{w_l}(x,\theta)dxd\theta$$

32. $$[U_{36}]_{l,k}^{\mathcal{N}_w\times\mathcal{N}_u} = \sum_{i=1}^{s}\int_{\theta_{1_{1i}}}^{\theta_{2_{1i}}}\int_{x_{1_{1i}}}^{x_{2_{1i}}} -\frac{E_{pe_{1i}}\nu_{pe_{1i}}a_{2_{1i}}}{2R(1-\nu_{pe_{1i}}^2)}\frac{\partial}{\partial x}\mathcal{B}_{u_k}(x,\theta)\frac{\partial^2}{\partial\theta^2}\mathcal{B}_{w_l}(x,\theta)dxd\theta$$

33. $$[W_{320}]_{l,k}^{\mathcal{N}_w\times\mathcal{N}_w} = \sum_{i=1}^{s}\int_{\theta_{1_{1i}}}^{\theta_{2_{1i}}}\int_{x_{1_{1i}}}^{x_{2_{1i}}} \frac{E_{pe_{1i}}a_{3_{1i}}}{3R^3(1-\nu_{pe_{1i}}^2)}\frac{\partial^2}{\partial\theta^2}\mathcal{B}_{w_k}(x,\theta)\frac{\partial^2}{\partial\theta^2}\mathcal{B}_{w_l}(x,\theta)dxd\theta$$

34. $$[W_{321}]_{l,k}^{\mathcal{N}_w\times\mathcal{N}_w} = \sum_{i=1}^{s}\int_{\theta_{1_{1i}}}^{\theta_{2_{1i}}}\int_{x_{1_{1i}}}^{x_{2_{1i}}} \frac{E_{pe_{1i}}\nu_{pe_{1i}}a_{3_{1i}}}{3R(1-\nu_{pe_{1i}}^2)}\frac{\partial^2}{\partial x^2}\mathcal{B}_{w_k}(x,\theta)\frac{\partial^2}{\partial\theta^2}\mathcal{B}_{w_l}(x,\theta)dxd\theta$$

35. $$[V_{37}]_{l,k}^{\mathcal{N}_w\times\mathcal{N}_v} = \sum_{i=1}^{s}\int_{\theta_{1_{2i}}}^{\theta_{2_{2i}}}\int_{x_{1_{2i}}}^{x_{2_{2i}}} \frac{E_{pe_{2i}}a_{2_{1i}}}{2R^2(1-\nu_{pe_{2i}}^2)}\frac{\partial}{\partial\theta}\mathcal{B}_{v_k}(x,\theta)\frac{\partial^2}{\partial\theta^2}\mathcal{B}_{w_l}(x,\theta)dxd\theta$$

36. $$[W_{322}]_{l,k}^{\mathcal{N}_w\times\mathcal{N}_w} = \sum_{i=1}^{s}\int_{\theta_{1_{2i}}}^{\theta_{2_{2i}}}\int_{x_{1_{2i}}}^{x_{2_{2i}}} \frac{E_{pe_{2i}}a_{2_{1i}}}{2R^2(1-\nu_{pe_{2i}}^2)}\mathcal{B}_{w_k}(x,\theta)\frac{\partial^2}{\partial\theta^2}\mathcal{B}_{w_l}(x,\theta)dxd\theta$$

37. $$[U_{37}]_{l,k}^{\mathcal{N}_w\times\mathcal{N}_u} = \sum_{i=1}^{s}\int_{\theta_{1_{2i}}}^{\theta_{2_{2i}}}\int_{x_{1_{2i}}}^{x_{2_{2i}}} \frac{E_{pe_{2i}}\nu_{pe_{2i}}a_{2_{1i}}}{2R(1-\nu_{pe_{2i}}^2)}\frac{\partial}{\partial x}\mathcal{B}_{u_k}(x,\theta)\frac{\partial^2}{\partial\theta^2}\mathcal{B}_{w_l}(x,\theta)dxd\theta$$

38. $$[W_{323}]_{l,k}^{\mathcal{N}_w\times\mathcal{N}_w} = \sum_{i=1}^{s}\int_{\theta_{1_{2i}}}^{\theta_{2_{2i}}}\int_{x_{1_{2i}}}^{x_{2_{2i}}} \frac{E_{pe_{2i}}a_{3_{2i}}}{3R^3(1-\nu_{pe_{2i}}^2)}\frac{\partial^2}{\partial\theta^2}\mathcal{B}_{w_k}(x,\theta)\frac{\partial^2}{\partial\theta^2}\mathcal{B}_{w_l}(x,\theta)dxd\theta$$

39. $$[W_{324}]_{l,k}^{\mathcal{N}_w\times\mathcal{N}_w} = \sum_{i=1}^{s}\int_{\theta_{1_{2i}}}^{\theta_{2_{2i}}}\int_{x_{1_{2i}}}^{x_{2_{2i}}} \frac{E_{pe_{2i}}\nu_{pe_{2i}}a_{3_{2i}}}{3R(1-\nu_{pe_{2i}}^2)}\frac{\partial^2}{\partial x^2}\mathcal{B}_{w_k}(x,\theta)\frac{\partial^2}{\partial\theta^2}\mathcal{B}_{w_l}(x,\theta)dxd\theta$$

40. $$[V_{38}]_{l,k}^{\mathcal{N}_w\times\mathcal{N}_v} = \sum_{i=1}^{s}\int_{\theta_{1_{1i}}}^{\theta_{2_{1i}}}\int_{x_{1_{1i}}}^{x_{2_{1i}}} -\frac{E_{pe_{1i}}a_{2_{1i}}}{2(1+\nu_{pe_{1i}})}\frac{\partial}{\partial x}\mathcal{B}_{v_k}(x,\theta)\frac{\partial^2}{\partial x\partial\theta}\mathcal{B}_{w_l}(x,\theta)dxd\theta$$

41. $$[U_{38}]_{l,k}^{\mathcal{N}_w\times\mathcal{N}_u} = \sum_{i=1}^{s}\int_{\theta_{1_{1i}}}^{\theta_{2_{1i}}}\int_{x_{1_{1i}}}^{x_{2_{1i}}} -\frac{E_{pe_{1i}}a_{2_{1i}}}{2R(1+\nu_{pe_{1i}})}\frac{\partial}{\partial\theta}\mathcal{B}_{u_k}(x,\theta)\frac{\partial^2}{\partial x\partial\theta}\mathcal{B}_{w_l}(x,\theta)dxd\theta$$

42. $$[W_{325}]_{l,k}^{\mathcal{N}_w\times\mathcal{N}_w} = \sum_{i=1}^{s}\int_{\theta_{1_{1i}}}^{\theta_{2_{1i}}}\int_{x_{1_{1i}}}^{x_{2_{1i}}} \frac{2E_{pe_{1i}}a_{3_{1i}}}{3R(1+\nu_{pe_{1i}})}\frac{\partial^2}{\partial x\partial\theta}\mathcal{B}_{w_k}(x,\theta)\frac{\partial^2}{\partial x\partial\theta}\mathcal{B}_{w_l}(x,\theta)dxd\theta$$

43. $$[V_{39}]_{l,k}^{\mathcal{N}_w\times\mathcal{N}_v} = \sum_{i=1}^{s}\int_{\theta_{1_{2i}}}^{\theta_{2_{2i}}}\int_{x_{1_{2i}}}^{x_{2_{2i}}} \frac{E_{pe_{2i}}a_{2_{1i}}}{2(1+\nu_{pe_{2i}})}\frac{\partial}{\partial x}\mathcal{B}_{v_k}(x,\theta)\frac{\partial^2}{\partial x\partial\theta}\mathcal{B}_{w_l}(x,\theta)dxd\theta$$

44. $$[U_{39}]_{l,k}^{\mathcal{N}_w\times\mathcal{N}_u} = \sum_{i=1}^{s}\int_{\theta_{1_{2i}}}^{\theta_{2_{2i}}}\int_{x_{1_{2i}}}^{x_{2_{2i}}} \frac{E_{pe_{2i}}a_{2_{1i}}}{2R(1+\nu_{pe_{2i}})}\frac{\partial}{\partial\theta}\mathcal{B}_{u_k}(x,\theta)\frac{\partial^2}{\partial x\partial\theta}\mathcal{B}_{w_l}(x,\theta)dxd\theta$$

45. $$[W_{326}]_{l,k}^{\mathcal{N}_w\times\mathcal{N}_w} = \sum_{i=1}^{s}\int_{\theta_{1_{2i}}}^{\theta_{2_{2i}}}\int_{x_{1_{2i}}}^{x_{2_{2i}}} \frac{2E_{pe_{2i}}a_{3_{2i}}}{3R(1+\nu_{pe_{2i}})}\frac{\partial^2}{\partial x\partial\theta}\mathcal{B}_{w_k}(x,\theta)\frac{\partial^2}{\partial x\partial\theta}\mathcal{B}_{w_l}(x,\theta)dxd\theta$$

46. $$[F_w(t)]_l^{\mathcal{N}_w\times 1} = \int_0^{2\pi}\int_0^{\ell} R\hat{q}_n(t,\theta,x)\mathcal{B}_{w_l}(\theta,x)dxd\theta$$

47. $$[B_w]_l^{\mathcal{N}_w\times 1} = -\sum_{i=1}^{s}\int_{\theta_{1_{1i}}}^{\theta_{2_{1i}}}\int_{x_{1_{1i}}}^{x_{2_{1i}}}\left[R(M_x)_{pe_{1i}}\frac{\partial^2\mathcal{B}_{w_l}}{\partial x^2} - \frac{1}{R}(M_\theta)_{pe_{1i}}\frac{\partial^2\mathcal{B}_{w_l}}{\partial\theta^2}\right]dxd\theta$$
$$-\sum_{i=1}^{s}\int_{\theta_{1_{2i}}}^{\theta_{2_{2i}}}\int_{x_{1_{2i}}}^{x_{2_{2i}}}\left[R(M_x)_{pe_{2i}}\frac{\partial^2\mathcal{B}_{w_l}}{\partial x^2} - \frac{1}{R}(M_\theta)_{pe_{2i}}\frac{\partial^2\mathcal{B}_{w_l}}{\partial\theta^2}\right]dxd\theta$$